QUANTUM MEDIATED EFFECTIVE INTERACTIONS FOR SPATIALLY COMPLEX SYSTEMS

A Dissertation

Presented to the Faculty of the Graduate School

of Cornell University

in Partial Fulfillment of the Requirements for the Degree of

Doctor of Philosophy

by

Shivam Ghosh

May 2015

QUANTUM MEDIATED EFFECTIVE INTERACTIONS FOR SPATIALLY COMPLEX SYSTEMS

Shivam Ghosh, Ph.D.

Cornell University 2015

Magnetic interactions between classical or quantum spin degrees of freedom in a condensed matter system are mediated by particles, which come in two flavors, fermions or bosons. Such a magnetic system can be put on a discrete lattice and one can ask about the nature of the ground state resulting from minimizing the magnetic interactions. More often than not, a ground state, defined by specifying the spin orientation or the spin state at every site on the discrete lattice, is complex. Complex meaning that the spin arrangement in real space is complicated or the ground state has properties (excitations) that are not common place.

The origin of this complexity can be attributed to the nature of the discrete lattice on which the spins live, the nature of the mediating quantum particle - fermion versus a boson, and to the nature of the spins themselves - classical versus quantum. In this thesis, we present examples of how non-trivial, spatially (both real and spin space) complex ground states can arise due to quantum (fermion/boson) mediated interactions between spin degrees of freedom.

Chapters 2, 3, 4 and 7 solve model Hamiltonians for quantum spins, where the interactions are boson mediated, and the resulting ground states are spatially complex - meaning that they break translational invariance (some states in Chapter 7 also break time reversal invariance). Chapters 4 and 5 introduce and solve model Hamiltonians for classical spin degrees of freedom, where the interactions are fermion mediated, and the resulting ground states have complex and beautiful spin arrangements in both real and spin space.

To solve the model Hamiltonians in this thesis and to arrive at spatially complex ground states, our central technique is to use Effective Hamiltonians - which under certain approximations, are a good mimicry of model Hamiltonians. The true usefulness of Effective Hamiltonians lies in the fact that they are much easier to solve, compared to the model Hamiltonians. To solve these Effective Hamiltonians, we develop a host of new numerical and theoretical tools. Each of these tools are more generic than the specific problems they have been applied to in this thesis, and a discerning reader will immediately see their broader applicability to a variety of other problems in condensed matter physics.

BIOGRAPHICAL SKETCH

Shivam Ghosh was born on July 1, 1986 to Indian parents: Dr. Ashish Ghosh (father) and Dr. Nandini Ghosh (mother), in the small north-eastern town of Gorakhpur, India. Shivam attended the local St. Paul's School from 1990-2002. During his penultimate years in high school, Shivam developed a keen interest in mathematics and physics. In spite of a poor score(86/100) in maths in his high school exams, Shivam went on to pursue mathematics and science in 11th and 12th grade (senior secondary school) at Delhi Public School R. K. Puram (New Delhi) from 2002-2004.

Shivam was attracted to the beauty and simplicity of Physics in his final year at school in Delhi and after failed attempts to qualify for a good engineering college, decided to pursue B.S.c. (Hons.) (undergraduate degree with major in Physics) in Physics from St. Stephen's College, Delhi. From 2004-2007, Shivam took fundamental courses in Physics and was fortunate to have an ensemble of very inspiring and dedicated teachers - the best that he will have in his school life.

After three splendid years at St. Stephen's college, Shivam went on to pursue a second bachelors and masters in Physics at University of Cambridge, UK, from 2007-2009. Although disappointed by the style of teaching at Cambridge, Shivam learnt a lot from his classmates, who were all very eager and excited about Physics. During his time at Cambridge, Shivam did a numerical project in computational physics which opened his eyes to the world of simulations and computer programming.

Having done well at Cambridge (a First), Shivam was offered a graduate fellowship to Cornell University, U.S.A. to pursue a graduate degree in Physics. Shivam started graduate school in Physics, at Cornell, in 2009 and completed

his P.h.D. in the winter of 2014. In graduate school, Shivam developed a keen interest in modeling physical systems and using quantitative methods and simulations to make predictive estimates. In spite of a number of successful projects in graduate school, Shivam became acutely aware of the isolation and disconnect that working on a remote Physics problem brings and a search for more collaborative projects brought him to try a finance internship at J. P. Morgan Chase in New York City, in the summer of 2014.

Shivam was pleasantly surprised at the transferability of his academic skills to an industrial setting and enjoyed the two months that he spent at the bank. After briefly returning to school in the Fall of 2014 to wrap up the final chapters of this P.h.D. thesis, Shivam started working in a full time role at J. P. Morgan Chase, in January 2015, and is currently a research associate at the bank.

For my parents: Nandini and Ashish

ACKNOWLEDGMENTS

The last five years at Cornell have not only made me somewhat of an expert in a few specialized areas of physics, but have also greatly transformed me as a person. In particular, I have learnt to think critically about problems (not just related to physics), I have learnt to collaborate with people and to value the richness of differing perspectives, I have learnt to value friendships and even learnt to enjoy being in a place like Ithaca.

For these learning experiences, I would like to raise a toast to my colleagues and friends in the physics department. In particular, Hitesh (Hitesh Changlani), from whom, I probably learnt more physics and methods, than I did, even from my advisor. To Sumi (Sumiran Pujari), who is the most chilled and laid back person I have ever met. To Zach, for being funny. To my batch mates (in no particular order): Ines, Jesse, Mihir, Kartik and Thomas, for teaching me so much and whose parallel P.h.D. journeys has often brought perspective to my own experience at Cornell.

I would like to raise another round of toast to my advisor Chris Henley, who, by the time that this note is written, will probably not be able to read most of it. Irrespective, I would like to thank him for his support and encouragement. Over the years, a gradual peeling of the different layers of his personality, has not just revealed a brilliant academician, but also a person who cares deeply for the well being of his students and always wants the very best for them. I wish Chris the very best and hope that he allows me to help, in whichever way I can, as he fights a challenging personal battle.

I would also like to thank Mike (Michael Lawler) for all the ideas, discussions and important collaborations in Chapters 5,6 and 7 of this thesis and for agreeing to be a member of my graduate committee. Mike has been a constant

source for ideas and support, especially during the past couple of years. In the same vein, I would also like to thank Mukund (Mukund Vengalattore) for agreeing to be on my committee and whose ultra-cold atoms class has been one of the most fun classes I have attended at Cornell.

I would like to buy the next round of drinks for Pat (Patrick O' Brien), my collaborator at Binghamton for all the ideas and discussions related to Chapter 5 of this thesis. Thank you Pat for coming to Ithaca so many times to collaborate and I hope to see you in NYC soon.

To my friends who made Ithaca brighter than New York. Kartik: for all the binge drinking and stories at Chapter House, Shreesha: for bearing all my tantrums and gossip, Moni: for throwing tantrums and elaichi chai, Divya: for bringing some calm to the mad house and for the dinners that never happened, Priyanka: for hanging out, Ajay: for generating gossip and the bike ride that is still waiting to happen, Mihir: for listening to all my 'devta' stories, Kshitij: for bearing with all the unwashed cups, Javad: for jogging my imagination with all the political drama and to Jesse (Jesse Silverberg): for fireworks and your enthusiasm and spirit.

To my friends at Cambridge, who, spookily, made me feel as if I never left the city: Nandini, Parul, Anam and Umang.

My teachers at St. Stephen's College for giving me something to be passionate about in my early 20's: Dr. Vikram Vyas, Dr. Abhinav Gupta, Dr. Bikram Phookun and Dr. Sanjay Kumar.

To Manoj (Manoj Gopalakrishnan) for an inspiring summer of bio-physics research.

Finally, a last round of drinks for my parents: Nandini and Ashish, for always standing by me and for instilling in me, the importance of a good educa-

tion. Also, for their ever-evolving expectations which I have always strived to live up to, except for the latest one: marriage, which might be a tough nut to crack. To my brother Ragho (Raghav Ghosh): for all the fun winters spent at his place in Delhi and for being with my parents, when I could not.

And to Nandini, my best friend, for always being there.

TABLE OF CONTENTS

LIST OF TABLES

LIST OF FIGURES

CHAPTER 1

QUANTUM MEDIATED INTERACTIONS IN CONDENSED MATTER SYSTEMS

1.1 Introduction

Interacting quantum condensed matter systems have an enormous number of degrees of freedom[1]. The large state space of such systems makes them intractable for theoretical or numerical investigations, unless certain simplifications, based on firm physical grounds, are made. Furthermore, the different degrees of freedom in a quantum system also interact with each other, giving rise to a complex set of low energy states and non-trivial excitations.

In most cases, we are interested in a low energy effective description of a physical system. This is because at low energies, corresponding to low temperatures, quantum effects dominate which are otherwise smeared out by thermal fluctuations at higher temperatures. A low energy effective description then refers to a systematic elimination of all, except a few relevant degrees of freedom. The remnant degrees of freedom sometimes have more composite and complex forms, compared to their identities before the elimination. The remnant degrees of freedom also have new renormalized interactions between them.

Before we go on to present a common example of deriving low energy effective descriptions, we note that each sub-section in this chapter corresponds to a chapter of the thesis. The layout of the sub-sections is such, that within each

[1] of the order of an Avogadro number of atoms $\sim 10^{23}$

sub-section, we present the main problem, the methods developed to solve the problem and the central results.

A common example is the large interaction limit of the Hubbard model[1] on a discrete lattice. The Hubbard model[1] is a model of interacting electrons which have a hopping amplitude t on the lattice and also an on site potential that penalizes double occupancy of electrons at a site. The penalty cost of this double occupancy is U. The number of electrons that we want to put in to the system is up to us, and is referred to as the filling of the system. A special limit of this model is in the very large U/t limit, at half filling, where every site on the lattice is singly occupied by an electron. In this limit, hopping of an electron from one site to another costs a large energy U, since the other site is already occupied by an electron. However, virtual second order hopping processes generate an effective short-ranged spin exchange Hamiltonian give by:

$$\mathcal{H}_{eff} = J \sum_{\langle i,j \rangle} \mathbf{S}_i \cdot \mathbf{S}_j \tag{1.1}$$

where $\mathbf{S}_i$ are electron spin operators and J is called an exchange interaction, given by $J \equiv 4t^2/U$ in terms of the parameters of our original microscopic Hubbard model.

The Effective Hamiltonian in (1.1) therefore arises from a systematic elimination of the electron kinetic degrees of freedom. The effective interaction J is obtained by considering virtual second order charge fluctuation processes, where an electron from a site, temporarily hops to its neighboring site paying an energy cost U, and returns back to its original site, generating an effective

spin-spin exchange interaction in the process. The electronic charge degrees of freedom are therefore eliminated, and an effective low energy description of the system is in terms of remnant spin degrees of freedom of an electron.

The form of the effective interaction J in (1.1) crucially depends on the nature of the quantum particles mediating the interaction between electron spins on the lattice. In the case of the large U/t limit of the Hubbard model, the quantum particles mediating the interactions are electrons and the resulting effective interaction J in (1.1) is short ranged - it only connects neighboring sites i, j on the lattice.

The effective low-energy remnant degrees of freedom (spins in (1.1)) are easy to find in the case of the Hubbard model. For a more complicated microscopic model or a relatively simple model on a complicated real space lattice, identification of the relevant degrees of freedom might not be straightforward.

The central premise of this thesis is to identify the low energy relevant degrees of freedom and to derive Effective Hamiltonians, like the one in (1.1), for microscopic quantum models on complicated spatial geometries. The methods and techniques, both theoretical and numerical, developed in this thesis are more generic than the problems they have been applied to in the next six chapters. Taken together, the ideas and techniques developed in the rest of this thesis, will hopefully find applications in a variety of interesting problems in condensed matter physics.

We next turn to discussing some specific examples of quantum mediated interactions in magnetic systems on spatially complex lattices.

1.2 Emergent Spin Excitations in a Bethe Lattice at Percolation

As a first example of spatial complexity and effective Hamiltonians, we study the low energy excitation spectrum of quantum spin half Heisenberg Hamiltonian on a diluted Bethe lattice percolation cluster[2, 3, 4]. The system was numerically[3] found to have an anomalous scaling of the lowest energy spin gap with the number of sites in the system. The origin of a new set of low energy excitations was attributed to the interactions between dangling or locally unpaired spins on the lattice. The dangling spins arise due to the presence of sub-lattice imbalance on a diluted Bethe lattice percolation cluster[4]. An Effective Hamiltonian capturing the interactions between these emergent spin moments was previously reported[4] and the couplings between the emergent moments were found to be exponentially decaying with the separation between moments. In this thesis, we address a more specific question of relating the presence of the dangling spin moments on the cluster to the local cluster geometry.

The algorithm used for locating the presence of local unpaired moments for a given realization of a diluted percolation cluster at the percolation threshold is similar in spirit to the classical monomer-dimer model introduced by Wang and Sandvik[3]. The greedy algorithm in Section 2.2 outlines a valence-bond framework for obtaining a maximal dimer covering configuration of the cluster by pairing up nearest neighbor spins in to singlets. The spins left unpaired in the maximal dimer covering configuration are then identified to be the dangling emergent moments on the cluster.

Chapter 2 also links the count of these dangling emergent moments with the number of states making up the anomalously low energy quasi-degenerate

set of spin excitations on a percolation cluster. The algorithm furthermore also predicts the presence of spin one excitations which occur when two mobile dangling spins belonging to the same sub-lattice come within two lattice spacings of each other. The results of Chapter 2 provide the first instance, in this thesis, of how a spatially complex lattice geometry can lead to non-trivial excitation spectra and presence of emergent spin degrees of freedom.

1.3 Non-Uniform Schwinger Bosons

Despite the presence of quantum magnetic and non-magnetic impurities being an intrinsic part of experimental condensed matter systems, mean field techniques to deal with such impurities are virtually non existent in literature. Chapter 3 aims to provide a mean field description of Heisenberg spin half magnets on spatially diluted lattices in the presence of non-magnetic site and bond impurities. The optimization method developed in Chapter 3 to obtain the ground state spin correlations and the energy of a quantum spin-half Heisenberg antiferromagnet (HAF) will be applied to study quantum spins on diluted lattices in Chapter 4 and also to uncover non-uniform mean field states of the Schwinger Boson mean field theory on the Kagome lattice in Chapter 7.

The search for spatially non-uniform mean field solutions of the HAF is done by mapping the HAF Hamiltonian to Schwinger bosons[5, 6, 7] and framing the constraints of the resulting mean field theory as an optimization problem in the mean field parameters: the bond amplitudes and the on-site chemical potentials. Methods for obtaining solutions to this constrained optimization problem for both bipartite and non-bipartite lattices is discussed in Section 3.4.

The SBMFT correlations and the mean field energy obtained from the optimal solution to the constrained optimization problem are found to be in excellent agreement with numerical exact diagonalization and branched cluster Density Matrix Renormalization Group (DMRG) algorithms[8]. The method is universally applicable to magnetic spin-half systems with quenched site and/or bond dilution and also to search for spatially non-uniform symmetry breaking mean field solutions of HAF on uniform frustrated lattices like the Kagome (see Chapter 7).

1.4 Anomalous Bosonic Excitations in Diluted Heisenberg Antiferromagnets

Chapter 4 aims to explain the origin of the anomalous[2] low energy excitations of the HAF on diluted square and Bethe lattices in a mean field description. Previous work [3, 4] established the low energy spectrum of excitations to the presence of emergent dangling moments on the cluster and the splittings in the energy spectra to interactions between these emergent moments. However, the exact mechanism of how a locally unpaired dangling spin decouples from the rest of the cluster to behave as an independent spin half degree of freedom remained unanswered in these publications. Another question of interest was the role of dangling emergent excitations in the propagation and sustenance of long range Neel order on the cluster. Chapter 4 provides answers, supported by concrete evidence, to both these questions within the framework of Schwinger Boson mean field theory applied to lattices with quenched random dilution (See

[2] an anomalous excitation in this context is defined to be one where the excitation spin gap has a scaling exponent with the system size of 2[3, 2, 4]

Chapter 3).

Section 4.3 adapts the Schwinger boson mean field theory constrained optimization framework of Sections 3.4 and 3.5 to the diluted square and Bethe lattice geometries. The variational parameters of the Schwinger Boson mean field theory[5, 7] are the bond variables living on all links of the cluster and the on-site chemical potentials. These extensive (in the system size) mean field parameters are optimized to meet the self-consistent constraints required for the mapping of the HAF to the Schwinger Boson mean field theory (see Section 3.2). The optimal values of the mean field parameters, along with the single particle frequencies and wave-functions allow us to form a mean field interpretation of lowest energy spin excitations of the HAF on a diluted percolation geometry.

Within SBMFT, each emergent dangling spin on the percolation cluster is characterized as a localized excitation with a characteristic single particle bosonic wave-function and an anomalously[3] low frequency. Section 4.4 shows how the geometric disorder of a percolation cluster manifests itself in the distribution of the mean field parameters leading to localized single particle modes with almost zero frequencies.

Section 4.5 further shows that there is a spectrum of anomalously low frequencies present in SBMFT similar to the exact spectrum from exact diagonalization or Density matrix Renormalization group calculations[4]. This low energy spectra arises from interactions between the single particle modes associated with dangling spins on the cluster. Section 4.5 also highlights how these interactions lead to delocalized single particle modes, which are identified to be the analogues of the uniform Goldstone modes found on a regular lattice,

[3]defined to be at least an order of magnitude lower than the continuum of single particle SBMFT frequencies

on a percolation cluster. Non uniform SBMFT therefore provides a complete and consistent (with exact calculations, see Section 4.8) picture of the lowest energy spin excitations on a percolation cluster which other traditional mean field theories like Spin Wave Theory, would have failed to capture (see Section 4.6).

1.5 Phase Diagram of the Kondo Lattice Model on the Kagome Lattice

Chapter 5 presents an example of a toy lattice model where quantum interactions, mediated by fermions, lead to complex (both in real and in spin space) classical spin orders. The Kondo Lattice Model (KLM) is a model of itinerant fermions interacting locally with classical spins living on a Kagome lattice. The goal is to find all classical spin configurations required to map out the phase diagram of KLM as a function of the electronic filling (the number of fermions on the Kagome lattice) and the strength of the Kondo coupling between the fermions and the local classical moments.

The techniques used to map out the phase diagram are the Luttinger-Tisza and Monte-Carlo methods in the weak coupling limit[4] and exact fermionic diagonalization in the limit of strong Kondo coupling. The weak coupling techniques are used on an Effective Hamiltonian, an approximation of KLM energy when the strength of the Kondo coupling is smaller than the bandwidth of itinerant electrons, found by integrating out the fermions via second order perturbation theory (see Section 5.3). The resulting Effective Hamiltonian is known

[4]the strength of the coupling is measured in terms of a dimensionless ratio of the strength of the local Kondo coupling to the band-width of the itinerant electrons

as the RKKY Hamiltonian[9, 10] and has the functional form of quadratic classical spin operators of the Heisenberg form with coupling coefficients that are long-ranged in real space and also oscillate in sign as a function of the electronic filling (see Section 5.3.3). Details of the Luttinger-Tisza and Monte-Carlo methods are outlined in Sections 5.4.1 and 5.5.1, respectively.

In the limit of strong coupling, the ground state classical spin orders of KLM for any filling, are calculated variationally by assembling a data-base of spin orders found in the RKKY limit via the weak coupling techniques. This data base also includes some commensurate classical orders whose ordering wave-vector lies at a special, high symmetry point in the Kagome first Brillouin zone. Exact fermionic diagonalization is done on all members of this data base and the lowest energy classical spin configuration is approximated to be the ground state of the KLM model(see Section 5.6).

The phase diagram of KLM, shown in Fig.5.15, is rich and complex with many participating spin orders. In the weak coupling RKKY limit of the model, incommensurate (ordering wave-vector of the classical spin order is not at a special high symmetry location in the zone) and non-coplanar(classical spin vectors in spin space do not all lie in a plane) orders are favored. Most of these orders, in the weak coupling limit, are driven by subtle nesting effects of the Fermi surface of the itinerant electrons as detailed in Sections 5.4.2 and 5.4.3. As we proceed from weak to stronger Kondo coupling strengths, many of the classical spin orders remain non-coplanar, but switch to being pre-dominantly commensurate instead of incommensurate. The collection of classical spin orders found in Chapter 5 are examples of complex systems in both real and spin space, arising due to quantum (fermion) mediated interactions. This is in contrast to the

diluted HAF of Chapters 2 and 4 where complexity was in real space (percolation clusters) and the quantum mediated interactions were bosonic (non-linear spin waves or mediated through Schwinger Bosons).

1.6 State Selection in the Double Exchange model on the Kagome lattice

A particularly interesting limit of the Kondo Lattice Model (introduced in Section 1.5 and defined in Chapter 5) is the limit of infinite coupling between the spin of the itinerant band of electrons and the local classical moments. Chapter 6 discusses this limit of Hund's coupling in the context of state-selection between the three-coloring 120 degree [11] states on the Kagome lattice. In the infinite Hund's coupling limit, the KLM becomes a simple hopping model of fermions, with complex hopping amplitudes dependent on the Berry phases and angles between classical spins on the lattice[12]. This hopping Hamiltonian, called the Double Exchange model, in the presence of a nearest neighbor super exchange interaction, can induce state-selection between degenerate 3 coloring states on the Kagome lattice. The lifting of the degeneracy, as a function of electronic filling, between the three coloring ground states of the classical nearest neighbor Heisenberg model on the frustrated Kagome lattice, is the main question of interest in Chapter 6.

The lifting of the degeneracy between the 3 coloring states on the Kagome lattice is studied via an Effective Hamiltonian approach outlined in Section 6.3. The spin of the itinerant fermions, in the presence of infinite Hund's coupling, follows the background classical spin texture on the lattice. This induces a non-

trivial Berry phase to the phase of the hopping amplitudes, making these amplitudes complex in general. Electrons hopping around closed loops on the Kagome lattice lead to loop fluxes. The total energy, at every filling, obtained by summing over the single particle energies up to that filling, can be expressed as a loop expansion in terms of fluxes through loops on the lattice with filling dependent expansion coefficients. Section 6.3 outlines a procedure for calculating these "universal" loop expansion coefficients that are independent of the classical spin background configuration and are only a function of the electronic filling.

Section 6.4 studies the problem of state-selection between three degenerate classical 3 coloring states on the Kagome lattice, induced by the Double Exchange Hamiltonian. The non-coplanar and complex *Cuboc1*[13, 14] state is found to be selected for two disjoint filling intervals. The Effective Hamiltonian shows that the lifting of degeneracy occurs via length six hexagonal and bowties loops on the Kagome lattice. The Double Exchange model, unlike quantum and thermal selection effects which favor the coplanar 3 coloring states, selects the non-coplanar and complex *Cuboc1* state.

1.7 Non-uniform Saddle Points and Z_2 Excitations on the Kagome Lattice

The final Chapter of this thesis continues the theme of spatial complexity by searching and finding spatially complex non-uniform mean field solutions of the nearest neighbor Heisenberg Anti-ferromagnet on the Kagome lattice. Chapter 7 uses the optimization mechanism developed in Chapter 3 to carry

out an unbiased search for low energy saddle point solutions in the spin liquid regime of the Schwinger Boson Mean Field Theory on the Kagome lattice[7, 15]. The motivation behind this search is to find spontaneously symmetry broken solutions that would be elusive within the assumptions of uniform mean field parameters[15] and the Projective Symmetry Group[16]. The Chapter also displays the power and diversity of the optimization mechanism of Chapter 3 in the numerical realization of Z_2 topological excitations which have only been predicted in theory[17], but never before realized in a numerical or a real experiment.

The central technique used in Chapter 7 is the constrained optimization algorithm developed in Chapter 3, to numerically solve the Schwinger Boson mean field equations, allowing the optimal mean field parameters to take on non-uniform values. The $Sp(N)$ formalism of the non-linear optimization algorithm (see Section 3.4.2) is used to start the optimizer from several different initial conditions. The optimal solution(s) with the lowest cost is then characterized via the distribution of the optimal mean field parameters and the gauge invariant $U(1)$ fluxes[18, 19] through even length loops on the lattice. Because of the exponentially large number of saddle point solutions on the Kagome lattice and the freedom of the mean field bond parameters to take on complex values, all non-uniform saddle point search calculations are restricted to a lattice of $3 \times 4^2 = 48$ sites.

The results of the search algorithm are discussed in Section 7.4. The lowest energy mean field solution, on a 48 site lattice, is found to spontaneously break the three fold orientational symmetry of the lattice and is much lower in energy than the uniform solution found by Sachdev[15]. This lowest energy solution is

triply degenerate (each configuration from the degenerate family corresponding to stronger bond amplitudes along a given orientation compared to bond amplitudes in the other two orientations), has uniform on-site chemical potentials and has zero fluxes through hexagonal and rhombus loops on the lattice. This lowest energy solution, called the "striped state", was also found on a 36 site lattice by Misguich[19]. The striped state is the simplest of the spatially complex low energy manifold of saddle point solutions on the Kagome lattice, most of which have non-uniform configurations of bond amplitudes and time reversal symmetry breaking chiral fluxes[20] through even length loops on the lattice.

Non-trivial topological excitations of a Z_2 spin liquid are realized in a numerical experiment in Section 7.5. The three topological excitations - the bosonic spinon, the magnetic vison and the bound state of the spinon and the vison called an ε fermionic spinon are realized within the Schwinger Boson mean field theory. The vison is created by starting the optimizer from an initial condition which has two hexagonal loops on the lattice threading a flux of π and finding the nearest saddle point solution that retains this two vison configuration. Furthermore, the lowest single particle bosonic spinon wave-functions are found to be localized around the two visons indicating a bound vison-bosonic spinon state and a numerical realization of the ε fermionic spinon. Central to the realization of all three topological quasiparticles is the freedom of the Schwinger boson mean field parameters to take on spatially non-uniform values. Section 7.5 therefore concludes the thesis with the final example of the richness of physical phenomenon obtained by the commingling of quantum interactions with spatial complexity.

BIBLIOGRAPHY

[1] P. Fazekas and P. W. Anderson, Philos. Mag. 30, 23 (1974).

[2] L. Wang and A. W. Sandvik, Phys. Rev. Lett. **97**, 117204 (2006).

[3] L. Wang and A. W. Sandvik, Phys. Rev. B **81**, 054417 (2010).

[4] H. J. Changlani, S. Ghosh, S. Pujari, and C. L. Henley, Phys. Rev. Lett. **111**, 157201 (2013).

[5] A. Auerbach and D. P. Arovas, Phys. Rev. Lett. **61**, 617 (1988).

[6] N. Read and S. Sachdev, Phys. Rev. Lett. **66**, 1773 (1991).

[7] A. Auerbach, Interacting Electrons and Quantum Magnetism, Springer (1997).

[8] H. J. Changlani, S. Ghosh, C. L. Henley, and A. M. Läuchli, Phys. Rev. B **87**, 085107 (2013).

[9] M. A. Ruderman and C. Kittel, Phys. Rev. **96**, 99 (1954).

[10] K. Yosida, Phys. Rev. **106**, 893 (1957).

[11] C. L. Henley, Phys. Rev. B **80**, 180401 (2009).

[12] P. Anderson and H. Hasegawa, Phys. Rev. **100**, 675 (1955).

[13] L. Messio, C. Lhuillier, and G. Misguich, Phys. Rev. B **87**, 125127 (2013).

[14] J.-C. Domenge, P. Sindzingre, C. Lhuillier, and L. Pierre, Phys. Rev. B **72**, 024433 (2005).

[15] S. Sachdev, Phys. Rev. B **45**, 12377 (1992).

[16] F. Wang and A. Vishwanath, Phys. Rev. B **74**, 174423 (2006).

[17] A. Essin and M. Hermele, Phys. Rev. B **87**, 104406 (2013).

[18] O. Tchernyshyov, R. Moessner, and S. L. Sondhi, EPL (Europhysics Letters) **73**, 278 (2006).

[19] G. Misguich, Phys. Rev. B **86**, 245132 (2012).

[20] L. Messio, C. Lhuillier, and G. Misguich, Phys. Rev. B **87**, 125127 (2013).

CHAPTER 2

EMERGENT SPIN EXCITATIONS IN A BETHE LATTICE AT PERCOLATION

The text and main results of this Chapter have been published. The published document can be found at Phys. Rev. Lett. 111, 157201 (2013). This Chapter expands one particular Section of the paper to which the author of this thesis made significant contributions. This Section is called: *Locating dangling degrees of freedom in real space*. The Figures in this chapter will have some overlap with Figures in the published version and also with the thesis of Hitesh J. Changlani (at http://www.lassp.cornell.edu/clh/Theses/hjc_thesis_final.pdf).The author acknowledges contributions from Hitesh J. Changlani, Sumiran Pujari and Christopher L. Henley

2.1 Diluted Heisenberg Anti-ferromagnets

We study the spin half Heisenberg anti-ferromagnet on a percolation cluster. The Hamiltonian is given by:

$$\mathcal{H}_{heis} = J \sum_{\langle i,j \rangle} \mathbf{S}_i \cdot \mathbf{S}_j \tag{2.1}$$

where $\mathbf{S}_{i(j)}$ are Pauli spin half operators, J is the uniform Heisenberg exchange constant on the bonds of the percolation cluster and $\langle i, j \rangle$ refers to pairs of nearest neighbor sites on the lattice.

A percolation cluster is obtained by diluting or removing sites with a certain probability p from a regular lattice. The regular lattice that we consider in this

study is the Bethe lattice of coordination three[1]. The lattice is bipartite and there is no frustration. Furthermore, there is a critical value of the probability p, at which the cluster undergoes a classical phase transition, called a percolation transition, from an infinitely connected lattice to a series of disconnected finite lattices. A quantum spin model, such as (7.1), can not have long range order beyond this critical value of the percolation threshold $p = p_c$. We study the nearest neighbor Heisenberg model (7.1) exactly at this critical value of the percolation threshold.

The primary aim of this Chapter is to show that the lowest energy excitations of the Heisenberg model on a percolation cluster have a scaling exponent (with system size N_s) different from what is expected from Heisenberg spin systems on uniform lattices. Before discussing these low energy non-trivial excitations, it is important to state that the excitations of a quantum anti-ferromagnet on a regular lattice, like the uniform square lattice, are Quantum Rotor states. The energy of these rotor states is given by:

$$E_{rotor} = \frac{S(S+1)}{2N_s\chi} \tag{2.2}$$

where S is the spin quantum number of the state, N_s is the number of sites on the lattice and χ is the magnetic susceptibility[2]. The set of Quantum rotor states therefore form a tower of states in the finite size many body spectrum of the quantum anti-ferromagnet on a regular uniform lattice and each state in the tower is labeled by its spin quantum number S.

The other very important thing to note about the Quantum Rotor states is that they scale as $1/N_s$ and therefore vanish in the thermodynamic limit. The

super-position of these degenerate (in the thermodynamic limit) Quantum Rotor states gives rise to the Neel order on the lattice[2].

Wang and Sandvik[3, 4] observed an *anomalous* scaling of the spin gap $\Delta_{\ell ow}$ [1] on a square lattice percolation cluster. Instead of the expected scaling of $\Delta_{\ell ow} \sim N_s^{-1}$ (corresponding to the Anderson tower of states), they found a scaling exponent closer to two: $\Delta_{\ell ow} \sim N_s^{-2}$. Wang and Sandvik[3, 4] postulated that the *anomalously* low energy excitations came from places in the cluster where there was local sub-lattice imbalance - an excess of sites belonging to one sub-lattice over sites belonging to the other kind of sub-lattice, giving rise to locally unpaired spins on the cluster which were called *dangling spins*. This is possible in percolation clusters, even though the cluster may be globally balanced (have an equal number of sites belonging to each of the two sub-lattices).

We extended this argument on the Bethe lattice percolation cluster[5] and showed the presence of an entire spectrum of almost degenerate states with *anomalously* low energies, meaning that all states within the quasidegenerate spectrum had an exponent greater than one (and close to two) in the scaling of their finite size gap as a function of the number of sites on the lattice. We further connected the quantum numbers of states from within the quasidegenerate spectrum to the cluster geometry, by studying the low energy spectra from Exact Diagonalization and Branched cluster Density Matrix Renormalization Group[1, 5], of thousands of clusters generated at the percolation threshold.

Figure 2.1 shows three bipartite[2] 18 site percolation clusters. Sites are colored red and green to indicate the sub-lattice that they belong to. Dashed ovals

[1] Spin gap refers to the $S_0 \rightarrow S_0 + 1$ excitation gap, where S_0 is the ground state spin quantum number

[2] A bipartite lattice is one in which every site can be colored black or white uniquely, identifying it with one of the even or odd sublattices

encircling pairs of spins correspond to a maximal dimer covering of the cluster and such a covering does not include all sites. Sites left out of a maximal dimer covering of the cluster are called dangling spins and are shown in the Figure by black circles. Cluster one therefore has two dangling spin, cluster two has 4 dangling spin halves and cluster three has 2 dangling spin halves and a dangling spin one. The spin one is an emergent composite excitation formed of two spin halves[5].

The number of states and the quantum numbers of the low energy spectrum have a strong connection to the cluster geometry and the number of dangling spins on the cluster. It was empirically observed that the number of states N_{QD} making up the quasidegenerate spectrum was related to the number n_d of dangling spins on the cluster via the relation:

$$N_{QD} = 2^{n_d} \tag{2.3}$$

which strongly suggested that each dangling spin behaved like an emergent spin half excitation and a low energy effective description of the system could be obtained by coupling these dangling spin degrees of freedom in a rotationally invariant manner (since the quasidegenerate spectrum does not break spin rotational invariance and each state within the spectrum has well defined spin quantum numbers).

This was indeed verified in our calculations[5], where we showed via an Effective Hamiltonian approach, that each dangling spin behaves as an emergent spin half excitation and interacts via a Heisenberg exchange Hamiltonian with other emergent spin half degrees of freedom on the cluster. The effective

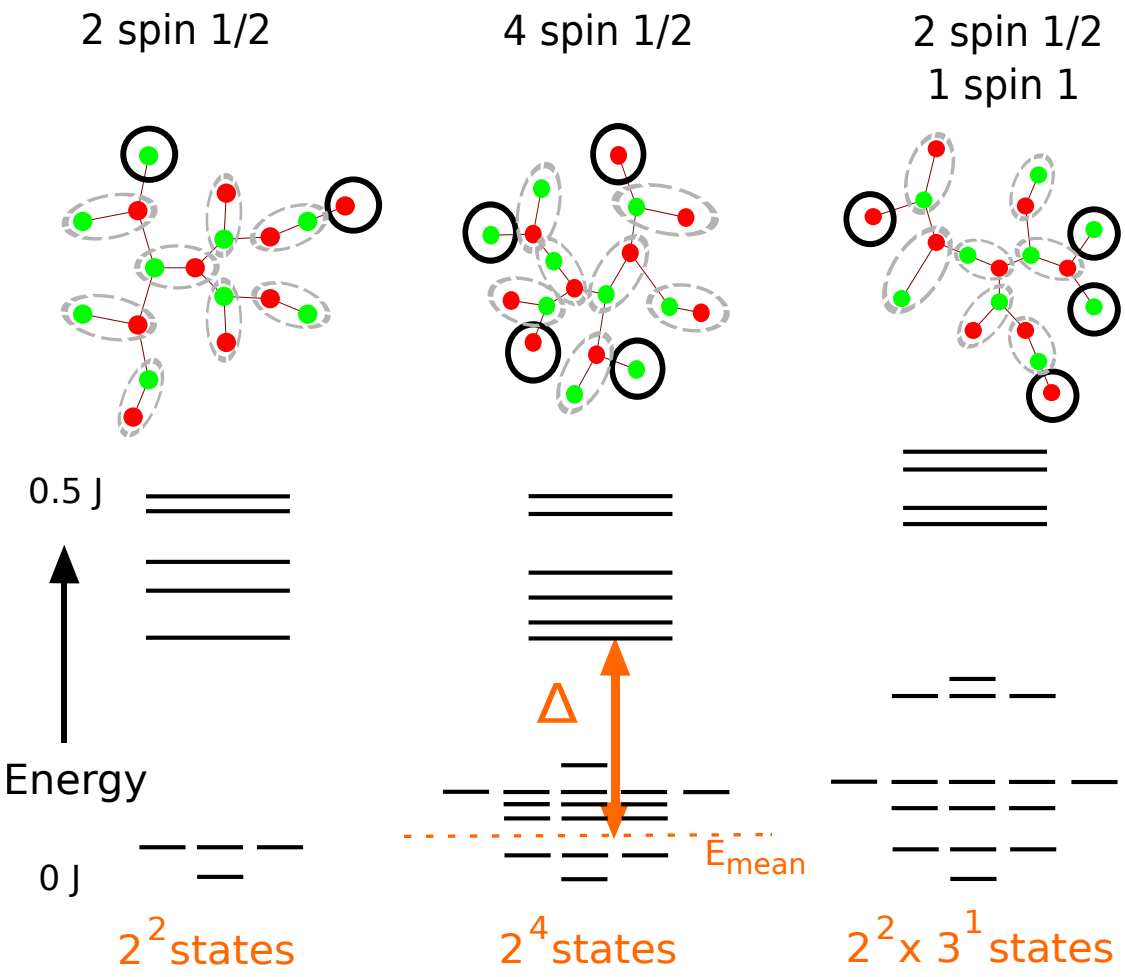

Figure 2.1: Percolation clusters (obtained from diluting a coordination three Bethe lattice at the percolation threshold) and their low energy spectrum. In each of the three 18 site clusters, red and green dots indicated the sub-lattice type of each site. Dashed grey ovals on each cluster, encircle pairs of spins that are strongly dimerized. The black circles indicate locations of dangling spins on the cluster. The energy spectra, for all three clusters, shows a series of states separated from the higher energy Quantum Rotor spectrum. The number of states in the low energy spectra is related to the count of dangling spins on the cluster. The relation is: # states = 2^{n_d}, where n_d is the number of dangling spins on the cluster. The third cluster has a slightly different relation coming from the presence of spin one excitations on the cluster (see [5]). Also, shown is the measure Δ of the energy separation between the mean energy E_{mean} of the QD states and the lowest energy Quantum Rotor state

couplings in the Heisenberg exchange Hamiltonian decay exponentially in the separation between two dangling spins[5]. The reader is also suggested to read Chapter 4 for a more detailed discussion of the emergent spin half degrees of freedom and their characterization within Schwinger Boson Mean Field Theory.

Since the geometry of the cluster plays a crucial role in deciding the nature of low energy excitations, we next describe a purely geometrical algorithm for predicting the count and the nature of excitations on a percolation cluster.

2.2 A geometrical algorithm for locating dangling spins in real space

In this Section we present a geometrical algorithm for counting the number of dangling spins on a diluted Bethe lattice percolation cluster. We present the algorithm and then discuss its application on a specific percolation cluster in detail.

The geometric algorithm is based within the framework of a quantum monomer-dimer model. We imagine that the wave function is a product of valence bonds in which the N_s spins on the cluster are paired (dimerized) into singlets to the maximum extent possible (optimal configuration). Even when even and odd sites are balanced globally, there remain some uncovered sites, i.e. monomers, due to local sub-lattice imbalances. These are spin-$1/2$ degrees of freedom and (within this picture) represent the dangling spins. There are multiple ways to optimally place the monomers; the actual wave function is imagined to be a superposition of these ways.

Our geometric algorithm, based on the valence bond framework, finds one element from the set of optimal dimerizations of the cluster and then attempts to find other elements of the set by locally replacing monomers with adjacent dimers. Wang and Sandvik [3] have a similar classical monomer-dimer model for locating locally unpaired spins on the lattice. Contrary to their method, we give greater attention to the relation between a locally unpaired spin and the local geometric features of the cluster. In spirit, the is a "greed" algorithm which tries to place dimers wherever possible (to obtain an optimal dimerization pattern), working from the outer sites inwards on the cluster.

Given any cluster, there are two operations which cut it down to a smaller cluster or clusters, such that all optimal dimerizations on the smaller cluster(s) are in 1-to-1 correspondence with some of the dimerizations on the larger one. The first operation is that whenever two sites have coordination 1 or 2, we can remove both (given the dimerization on the smaller cluster, just insert another dimer to get the dimerization on the larger one).

The second operation is that whenever we find a pair of adjacent sites with respective coordinations 3 and 1 (a "prong"), we can always place a dimer on that pair, which fragments the rest into two subclusters; a very common special case is the fork, at which we can arbitrarily choose either side to be the prong. These two operations can be used recursively till only isolated sites remain, each corresponding to one monomer in the original cluster. Furthermore, any other optimal dimerization is accessible from the special one we constructed, by repeatedly exchanging a monomer with an adjacent dimer.

A monomer can thus "hop" to sites on the lattice via such local monomer-dimer rearrangements. Our rule of thumb is that two monomers (belonging to

the same sub-lattice) form a spin 1 moment if and only if they can approach to the minimal separation of two lattice constants.

We now show the working of the algorithm in the specific instance of the cluster shown in Fig. 2.2(a). The first step of the algorithm is to locate bonds on the lattice that have sites with coordinations one and two. These bonds are colored orange in the Fig.2.2(a). These bonds are trimmed and removed from the cluster. The trimmed bond pairs are stored before being trimmed. The trimmed cluster is shown in Fig.2.2(b).

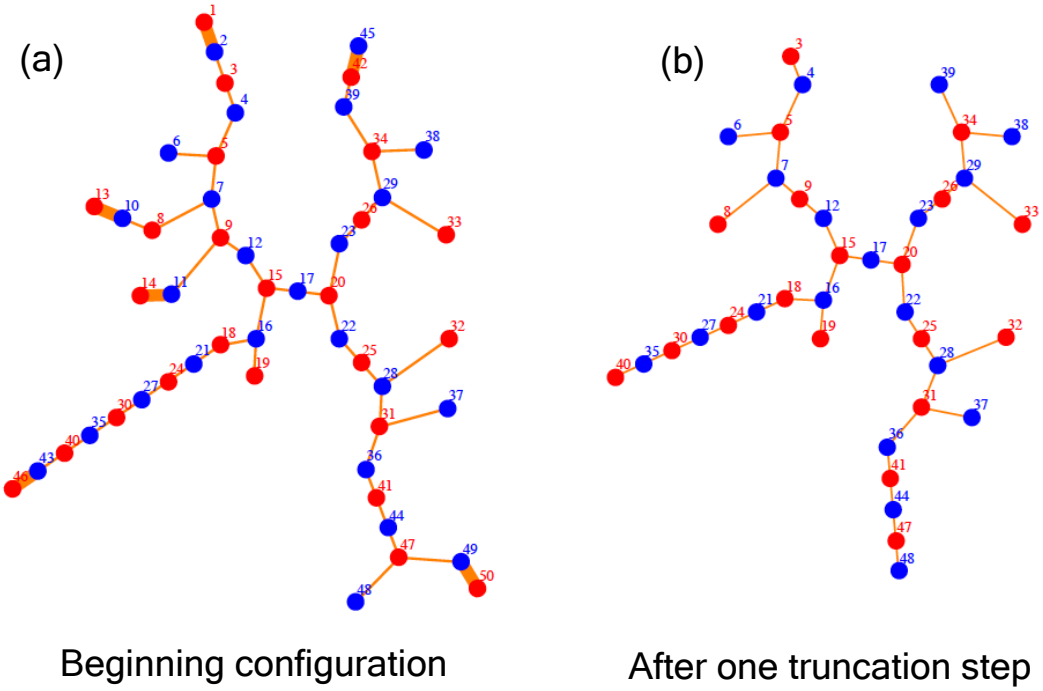

Figure 2.2: Demonstration of the geometric algorithm for finding dangling spins on the cluster (a) A diluted Bethe lattice percolation cluster. Each site has a colored disc in red or blue corresponding to the sub-lattice type of the lattice site. Bonds to be trimmed are shown via thick orange lines (see text). (b) Cluster after the bonds in orange in (a) have been trimmed from the lattice

The algorithm then searches for the presence of forks on the cluster. These are geometrical features of the cluster that look like a fork and consist of a triad of three sites. One of the sites in the triad has coordination three and the other

two have coordination one.

Fig2.3(c) shows a fork at sites $38, 39, 34$. Sites $38, 39$ have a coordination of one and site 34 has coordination three. A monomer always gets trapped when a fork is encountered, since a maximal dimer covering can (arbitrarily) correspond to dimerizing only one of the two, completely equivalent, bonds of the fork. Dimerizing one of the two bonds, then leaves an unpaired coordination one site or a monomer.

For example, we can dimerize bonds $(34, 39)$ and that would create a monomer at site 38. The dimerized bond is again stored and the monomer site number is also recorded. Fig.2.3(d) shows the cluster after bonds in orange in Fig.2.3(c) have been removed.

The iteration steps corresponding to locating and trimming of bonds with sites of coordination one and two and of forks is repeated, until we end up with a linear chain or a fork containing three sites. Some of the intermediate cluster configurations during the iterations steps is shown in Fig.2.4(e)-(h). Panels (e) and (g) show bonds to be trimmed highlighted in orange, and clusters (f) and (h) correspond to cluster configurations after the trimming.

Fig.2.5(i) shows the penultimate step of the algorithm, the last fork to be trimmed is highlighted in orange. The fork is trimmed, the trimmed bonds and the monomer are recorded, and the resulting trimmed cluster is seen in Fig.2.5(j). Once the cluster reduces to a straight line, it is trivial to find whether it has any monomers. Lines with an even number of sites can be completely dimerized and therefore contain zero monomers, whereas straight lines with an odd number of sites will have a single monomer, than can "hop" to sites belong-

ing to the same sub-lattice along the chain. The trimmed cluster in Fig.2.5(j) has an odd number of sites and the algorithm gathers another monomer.

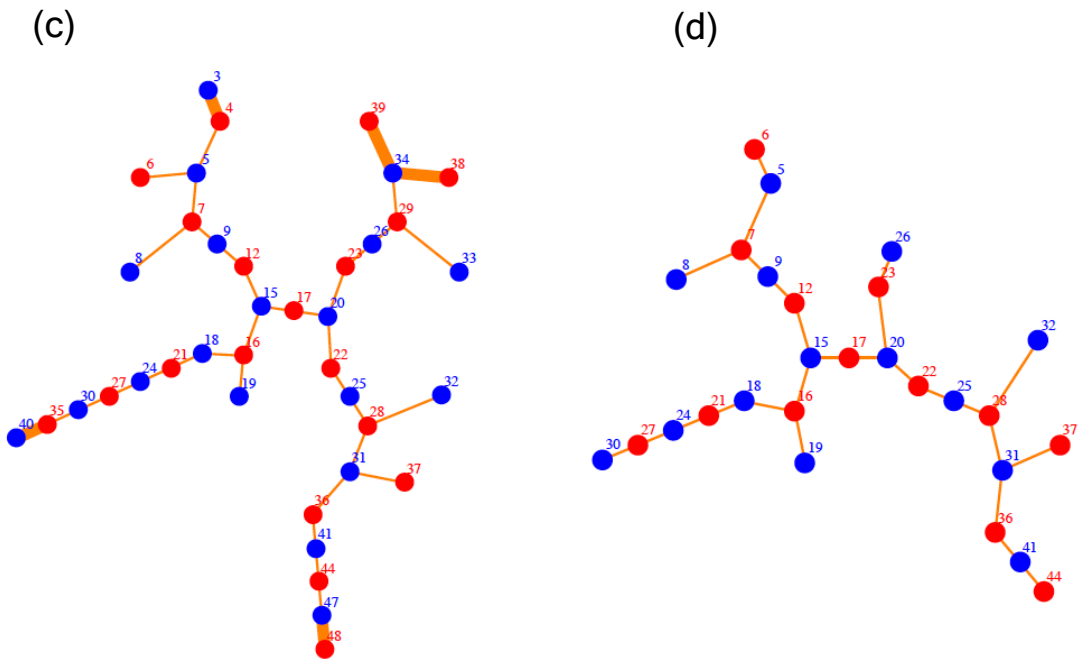

Figure 2.3: (c) A geometrical feature called a fork is formed by the sites $34, 38, 39$. (d) Trimmed cluster after bonds in (c) have been removed

At the end of the algorithm we have a list of bonds that have been trimmed and correspond to a single maximal dimer covering of the cluster. We also have a list of the monomer locations on the cluster, which are sites left unpaired in the maximal dimer covering configuration. The count of the monomers gives us the number of dangling spins n_d on the cluster.

Starting from a single maximal dimer covering configuration of the cluster, we can access the entire set of maximal dimer coverings. This is done by a local update algorithm that shuffles a dimer to an adjacent bond, making the monomer hop to a new location. Once the complete set of maximal dimer configurations of the cluster have been obtained, we find out all possible sites that a monomer can hop to and delocalize. Two monomers belonging to the same

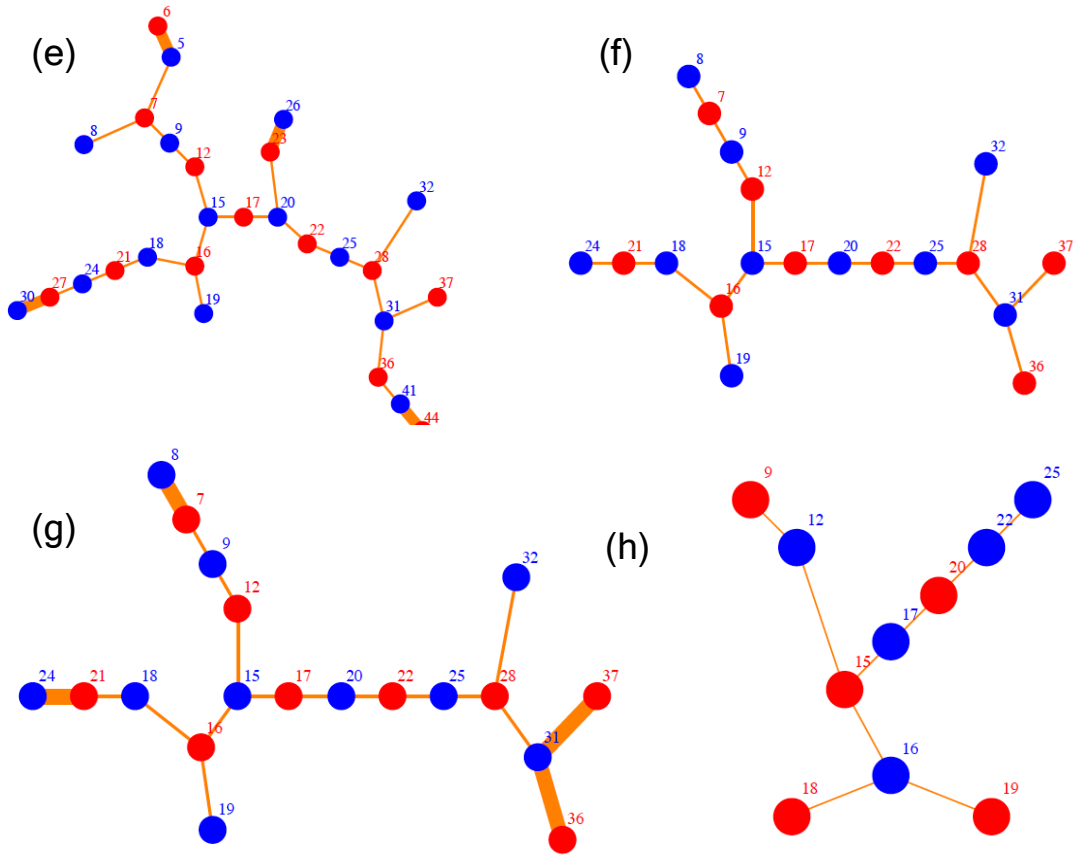

Figure 2.4: Cluster configurations corresponding to the intermediate steps of the geometrical algorithm. Panels (e),(g) highlight bonds and fork(s) that have been identified to be trimmed (removed) from the cluster and panels (f),(h) show the cluster configurations after the trimming step is over

sub-lattice form a spin one excitation, if via delocalization, they can come within two lattice spacings of each other. In this manner, we can classify the number of emergent spin half $n_{1/2}$ and spin onc n_1 excitations on the cluster. The number of states N_{QD} calculated via[3]:

$$N_{QD} = 2^{n_{1/2}} 3^{n_1} \tag{2.4}$$

can be tallied against the number of low lying states from exact numeri-

[3]The factors of 2 and 3 in (2.4) come from the two-fold and three fold degeneracy of the z component of spin angular momentum states in a spin half and spin one excitation, respectively

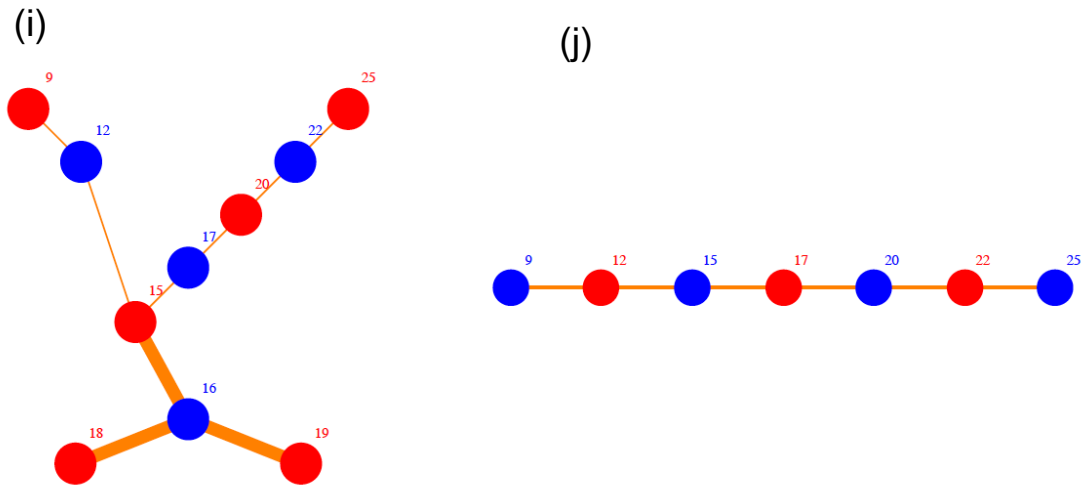

Figure 2.5: Cluster configurations corresponding to the final steps of the algorithm. (i) Cluster with the last fork to be trimmed, highlighted in orange (j) cluster after the fork in (i) is trimmed becomes a straight line and the algorithm stops

cal calculations. Both estimates of N_{QD} are in excellent agreement with one another[5].

2.3 Conclusion

Quantum magnets on diluted lattices are an idea playground for exploring the interplay between quantum fluctuations and geometric disorder. The lowest energy excitations in a spin half Heisenberg model on diluted Bethe and square lattices are highly non-trivial and emergent. In this chapter we have outlined a purely geometrical algorithm for finding the number of these low lying emergent spin excitations on a percolation cluster. Predictions from the algorithm are in good agreement with the number of such excitations obtained from exact numerics[5]. Further details about these emergent excitations and a mean field description of their characterization and interactions with other similar excita-

tions on the cluster, are discussed in great detail in Chapter 4. Interested readers are strongly encouraged to continue on to Chapter 4.

BIBLIOGRAPHY

[1] H. J. Changlani, S. Ghosh, C. L. Henley, and A. M. Läuchli, Phys. Rev. B **87**, 085107 (2013).

[2] P. Anderson, Phys. Rev. **86**, 694 (1952).

[3] L. Wang and A. W. Sandvik, Phys. Rev. B **81**, 054417 (2010).

[4] L. Wang and A. W. Sandvik, Phys. Rev. Lett. **97**, 117204 (2006).

[5] H. J. Changlani, S. Ghosh, S. Pujari, and C. L. Henley, Phys. Rev. Lett. **111**, 157201 (2013).

CHAPTER 3

NON-UNIFORM SCHWINGER BOSONS

3.1 Mean-field theories for Heisenberg Spins

The earliest and the most successful mean-field description of ordered states of Heisenberg quantum magnets was the Spin Wave Theory [1]. Linear Spin wave theory (LSWT) adds quantum fluctuations to a classical ferromagnetic or antiferromagnetic ordered state via Holstein Primakoff bosons[2]. LSWT works well in cases where magnetic long range order exists and the classical order is *a priori* known.

LSWT cannot be applied if the initial antiferromagnetic state is not known, as is true in the case of frustrated magnets, or when the presence of a small spin and low system dimensionality can invalidate the spin wave expansion due to enhanced quantum fluctuations. The first (theoretical and false) instance of enhanced quantum fluctuations leading to a quantum disordered magnetic state was the 'quantum spin liquid' for spin half, reported by Fazekas and Anderson[3], on the two dimensional triangular lattice. LSWT fails to capture such magnetically disordered phases, found most commonly in short-ranged Hamiltonians in dimensions less than or equal to two at finite temperatures, where Mermin-Wagner theorem predicts an absence of order [4].

In particular, both the presence of a small spin $S = 1/2$ and low ($d = 2$) system dimensionality was found in the high-temperature superconductor La_2CuO_4 which was experimentally (via powder neutron diffraction)shown to have long range antiferromagnetic Neel order [5]. Interest in this material in the late 1980's

led to a revival of mean field theories of $S = 1/2$ quantum magnets in two spatial dimensions which could fit the experimental structure factor curves of La_2CuO_4. Unlike the one dimensional Heisenberg $S = 1/2$ chain, which at that time was known to lack magnetic order, the fate of the $S = 1/2$ square lattice anti-ferromagnet was unsettled.

Furthermore, an agreement with experimental data on La_2CuO_4 and comparison with numerics [6] required a formalism which preserved spin rotational SU(2) invariance. Linear Spin Wave theory (and $1/S$ corrections) assume an ordered state for the spin wave expansion and therefore explicitly break $\mathrm{SU}(2)$ rotational invariance. The earliest effort to find a rotationally invariant mean field theory for Heisenberg spins was in the form of modified Linear Spin wave theory by Takahashi in 1987 [7]. Takahashi added bosonic (Holstein-Primakoff) fluctuations to the Neel antiferromagnetic state on the square lattice with the constraint of a vanishing total z component of the spin angular momentum $\mathbf{S}^z_{tot} = 0$. The constraint matches the physical Hilbert space of the bosons to the quantum states of the spin Hamiltonian. While Takahashi's theory was successful in replicating the Bethe ansatz solution for $S = 1/2$ in one dimension, the theory broke rotational invariance and the assumption of a vanishing $\mathbf{S}^z_{tot} = 0$ was forced and *ad hoc* at best.

Arovas and Auerbach in 1988 made Takahashi's spin wave theory more systematic and introduced a spin rotationally invariant theory of Heisenberg antiferromagnets which they called Schwinger Boson Mean Field Theory (SBMFT). The theory is able to describe both ordered and magnetically disordered phases and has been generalized to frustrated lattices by Read and Sachdev [8]. Since the early $1990's$ SBMFT has proven to be a versatile tool in mapping out quali-

tative phase diagrams of Heisenberg spins on both bipartite and frustrated lattices.

We now briefly describe the organization of this chapter. In Section3.2 we discuss the mapping of a Heisenberg spin half to Schwinger bosons and the resultant mean field Hamiltonian. The SBMFT Hamiltonian along with a set of constraints will be shown to qualitatively capture many properties of singlet many body ground states of Heisenberg spin Hamiltonians. Next in Section 3.3 , we show an application of SBMFT and the solution to the mean field equations for a linear $S = 1/2$ Heisenberg chain. We then go on to develop a generalized scheme for a systematic and unbiased search of non-uniform mean field solutions of SBMFT and describe an optimization algorithm for finding self-consistent mean field solutions with a large number of parameters in Section3.4 . Finally, in Sections 3.5 and 3.6 we discuss technical details regarding the implementation of the algorithm and the linear algebra routines used for carrying out different steps of the optimization algorithm.

3.2 Setting up the Schwinger Boson Mean Field Theory

We begin with the Heisenberg Hamiltonian which is a short ranged interaction between $S = 1/2$ spin degrees of freedom living on a lattice. The Hamiltonian is given by

$$\mathcal{H} = J \sum_{\langle ij \rangle} \mathbf{S}_i \cdot \mathbf{S}_j \tag{3.1}$$

where the indices i, j label sites in real space, $J > 0$ for the antiferromagnetic

case and $\mathbf{S}_{i,j}$ are SU(2) spin half operators. Each spin is mapped to two 'flavors' of Schwinger bosons via [9] as shown in Fig.3.1:

$$\mathbf{S}_i^+ = a_i^\dagger b_i, \qquad \mathbf{S}_i^- = b_i^\dagger a_i, \qquad \mathbf{S}_i^z = \frac{1}{2}(a_i^\dagger a_i - b_i^\dagger b_i) \tag{3.2}$$

Expressing (3.1) in terms of the Schwinger representation in (3.2) we get the following Hamiltonian:

$$\mathcal{H}_{Schwinger} = -\frac{J}{2}\sum_{\langle ij\rangle}\left(Q_{ij}^\dagger Q_{ij} - 2S^2\right) \tag{3.3}$$

where we introduce bond variables $Q_{ij} = a_i a_j + b_i b_j$ [1]. The Hamiltonian $\mathcal{H}_{Schwinger}$ is an interacting theory of two flavors of bosons and is quartic in the bosonic operators. To convert (3.3) in to a non-interacting theory (quadratic in the bosonic flavors) we do a large N(flavor) expansion which we describe next.

The large-N expansion is a standard trick to create a small perturbative expansion parameter in a theory where there is no small parameter and when the theory is tractable and easily soluble in the $N \to \infty$ limit. A small parameter allows us to organize an interacting theory as a power series in the operators. Each term in the series is preceded by a power of the small expansion parameter and is therefore smaller than the previous term. This allows the possibility of convergence of such an expansion. A standard example is Spin wave theory where the small parameter is $1/S$. An expansion in $1/S$ allows us to filter out a quadratic, non-interacting Hamiltonian to leading order[2].

[1] Q_{ij} is anti-symmetric in the spatial indices $i \leftrightarrow j$, in general. On a bipartite lattice, we can do a spin rotation that changes $a_j \to -b_j$ and $b_j \to a_j$ for $j \in$ sublattice B allowing us to make Q_{ij} symmetric in the spatial indices [9]

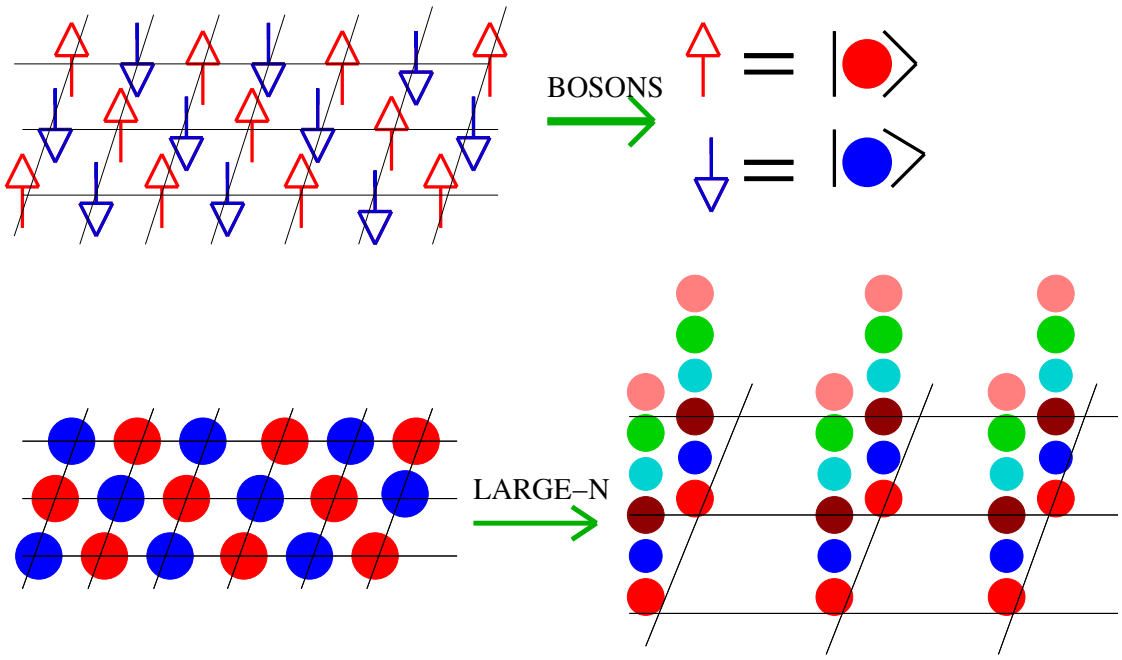

Figure 3.1: Mapping of SU(2) antiferromagnets to Schwinger Bosons. Top: Neel state of S=1/2 antiferromagnet shown on square lattice with red(up) $S_z = 1/2$ and blue (down) $S_z = -1/2$ arrows; also shown is the mapping to two flavors of Schwinger bosons shown via red and blue discs. Bottom: Large flavor(N) expansion: from two flavors (red and blue) of Schwinger Bosons to 'N' flavors on each site. Each boson flavor is shown by a differently colored disc. Generalization of the SU(2) group to a larger symmetry SU(N) theory reveals a small expansion parameter $1/N$(see text Section 3.2)

In the case of the Schwinger bosons, such an expansion parameter is obtained by extending the symmetry group of the Heisenberg Hamiltonian from SU(2) to SU(N) by going from the two flavors in (3.2) to N flavors of bosons as shown in Fig.3.1. To leading order in $1/N$, we can therefore decouple the interacting bosonic theory (3.3) in to a non-interacting quadratic mean field Hamiltonian.

Using Wick's theorem, we can decouple the interacting terms in $\mathcal{H}_{Schwinger}$(3.3) in to antiferromagnetic and/or ferromagnetic channels where the dominant short-

ranged interactions are anti-ferromagnetic and ferromagnetic, respectively[10]. Instead of doing the most generic case where de-coupling terms corresponding to both kinds (anti-ferromagnetic and ferromagnetic) interactions are retained, we are going to de-couple (3.3) *only* in the anti-ferromagnetic channel. This de-coupling *only* in the anti-ferromagnetic channel reduces the number of mean field parameters and makes the calculation more efficient and tractable. Following Wick's theorem, we get:

$$Q_{ij}^{\dagger}Q_{ij} \cong \langle Q_{ij}^{\dagger}\rangle Q_{ij} + Q_{ij}^{\dagger}\langle Q_{ij}\rangle - |Q_{ij}|^2 \tag{3.4}$$

where the averages $\langle ...\rangle$ are taken in the mean field state. Using the above decoupling in (3.3), the mean field Hamiltonian for the bosons can be written as follows[9]:

$$\mathcal{H}_{MF} = \sum_{\langle ij\rangle,m} \left(Q_{ij}^{*} b_i^m b_j^m + Q_{ij} b_i^{m\dagger} b_j^{m\dagger} \right) - \sum_{i=1,m=1}^{i=N_s,m=N} \lambda_i (b_i^{m\dagger} b_i^m - S) + \sum_{\langle ij\rangle} JS^2 \tag{3.5}$$

where the boson flavor index m goes from 1 to N, the number of sites are indicated by N_s and a set of Lagrange multipliers $\{\lambda_i\}$ are introduced to enforce the constraint of a fixed number of bosons (equal to spin length S) per site. At the mean field level, bosons of different flavors do not interact with each other and the Hamiltonian in (3.5) is a sum of N identical copies of a single flavor Hamiltonian given by:

$$\mathcal{H}_{MF}^{m} = \boldsymbol{\beta}^{\dagger} \begin{pmatrix} \mathbf{\Lambda} & \mathbf{Q} \\ \mathbf{Q}^{\dagger} & \mathbf{\Lambda} \end{pmatrix} \boldsymbol{\beta} + \frac{1}{J} \sum_{i<j} |Q_{ij}|^2 - \left(S + \frac{1}{2} \right) \sum_i \lambda_i \tag{3.6}$$

where $\boldsymbol{\beta}$ is a vector given by $\boldsymbol{\beta}^T = (b_{1m}, ..., b_{N_s m}, b^\dagger_{i1}, ..., b^\dagger_{N_s m})$. The matrix $\mathbf{\Lambda}$ is diagonal in the site basis with entries given by Lagrange multipliers $\mathbf{\Lambda}_{ij} = \lambda_i \delta_{ij}/2$ which enforce the 'number constraint' on the bosons $\sum_m \langle b^\dagger_{im} b_{im} \rangle_{MF} = NS$, which is only satisfied on *average* [2]. All Lagrange multipliers are real. The matrix $\mathbf{Q}$ has entries that are complex (in general), off diagonal and given by $Q_{ij} = \sum_m \langle b_{im} b_{jm} \rangle$. The mean field solution is a self-consistent solution in the $\{Q_{ij}\}$ meaning that the bond amplitudes input to the Hamiltonian(3.6) should agree with the amplitudes computed self-consistently, i.e. $Q_{ij} = \langle Q_{ij} \rangle$

The set of Lagrange multipliers $\{\lambda_i\}$ act as on-site potential for the bosons and in general can have different values on every site. The set of bond variables $\{Q_{ij}\}$ are 'pairing amplitudes' for the bosons and in general can be long-ranged. The set of Lagrange multipliers and the bond variables taken together $\{\lambda_i, Q_{ij}\}$ form an **Ansatz** and a mean-field solution to the Schwinger Boson Hamiltonian (3.6). To arrive at the mean field solution, we need to meet the following two constraints discussed earlier:

$$\begin{aligned} \textbf{Number constraint}&: \langle n_i \rangle = \langle b^\dagger_i b_i \rangle = S \\ \textbf{Bond constraint}&: Q_{ij} = \langle Q_{ij} \rangle = \langle b_i b_j \rangle \end{aligned} \tag{3.7}$$

The **Ansatz** that satisfied the boson 'number constraint' and the self-consistent 'bond constraint' (3.7) is called an optimal **Ansatz**: $\{\lambda^*_i, Q^*_{ij}\}$. The standard route to finding the optimal **Ansatz** is to carry out a Bogoliubov diagonalization of the Hamiltonian (3.6) to obtain the set of single particle frequencies and eigen-modes. The modes are used to compute expectations for the number operator n_i

[2] This maps the Hilbert space of the spin operator into that of the bosons. Boson number fluctuations about the average constraint of NS bosons per site lead to *spurious* factors of $3/2$ in spin-spin correlations [11]

and the bond operators Q_{ij} in the mean field state. Using these expectations we arrive at two constraint equations (3.7) which need to be simultaneously solved for the optimal **Ansatz**. We show how these different steps work in the case of the $S = 1/2$ Heisenberg chain in the next section.

3.3 SBMFT applied to $S = 1/2$ Heisenberg chain

In this section we present an example of the application of SBMFT in the simplest setting possible - the $S = 1/2$ Heisenberg chain and show how SBMFT predicts the lack of long range magnetic order [3].

We discuss the translationally invariant $S = 1/2$ linear Heisenberg chain with periodic boundary conditions in this Section and discuss the more complex cases of translationally non-invariant systems in Section 3.4. For the $S = 1/2$ linear chain with periodic boundary conditions we invoke translational invariance to define the following bosonic operators in momentum space:

$$\begin{aligned} a_i &= \frac{1}{\sqrt{N_s}} \sum_{\mathbf{k}} a_{\mathbf{k}} e^{-i\mathbf{k}\cdot\mathbf{R}_i} \\ a_i^\dagger &= \frac{1}{\sqrt{N_s}} \sum_{\mathbf{k}} a_{\mathbf{k}}^\dagger e^{\mathbf{k}\cdot\mathbf{R}_i} \end{aligned} \tag{3.8}$$

where $\mathbf{R}_i$ is the position vector of site i and $\mathbf{k} = 2\pi m/L$ for integral $m = (-L/2, ..., -L/2-1)$ for an even site chain of length La (a is the lattice constant). Translational invariance also implies a uniform **Ansatz** $\lambda_i = \lambda$ and $Q_{ij} = Q$ and in terms of the above momentum space operators $\mathcal{H}_{MF}^m$ can be rewritten as [9]

[3] this result was already known in 1988[12] when SBMFT was introduced and served as a benchmark for the accuracy of the theory

$$\mathcal{H}_{MF} = \sum_{\mathbf{k}} \left[\lambda a^{\dagger}_{\mathbf{k}} a_{\mathbf{k}} + \frac{1}{2} zQ \cos(\mathbf{k}a) \left(a^{\dagger}_{\mathbf{k}} a^{\dagger}_{-\mathbf{k}} + a_{\mathbf{k}} a_{-\mathbf{k}} \right) \right] + N_s \frac{zQ^2}{2J} - N_s S\lambda \quad (3.9)$$

The quadratic Hamiltonian (3.9) can be diagonalized to obtain the single Bogoliubov quasiparticle spectrum with the following transformation:

$$\begin{pmatrix} a_{\mathbf{k}} \\ a^{\dagger}_{-\mathbf{k}} \end{pmatrix} = \begin{pmatrix} u_{\mathbf{k}} & v_{\mathbf{k}} \\ v_{\mathbf{k}} & u_{\mathbf{k}} \end{pmatrix} \begin{pmatrix} \alpha_{\mathbf{k}} \\ \alpha^{\dagger}_{-\mathbf{k}} \end{pmatrix} \quad (3.10)$$

where the coeffcients of the transformation $\{u_{\mathbf{k}}, v_{\mathbf{k}}\}$ are determined by requiring the Bogoliubov quasiparticle operators to follow the bosonic commutation relations $[\alpha_{\mathbf{p}}, \alpha^{\dagger}_{\mathbf{q}}] = \delta_{\mathbf{p},\mathbf{q}}$. The commutation relation constraint implies a relationship $u^2_{\mathbf{k}} - \mathbf{v}^2_{\mathbf{k}} = 1$ and the simplest functional forms for parametrizing the transformation coefficients is $u_{\mathbf{k}} = \cosh\theta_{\mathbf{k}}$ and $v_{\mathbf{k}} = \sinh\theta_{\mathbf{k}}$.

The transformation to Bogoliubov quasiparticle operators (3.10) can be plugged in to $\mathcal{H}_{MF}$ (3.9) with the requirement of a normal diagonal form [4] of the mean field Hamiltonian (3.9) in terms of the quasiparticle operators $\alpha_{\mathbf{k}}, \alpha^{\dagger}_{\mathbf{k}}$. The mean field Hamiltonian (3.9) is diagonal in the new basis of quasiparticle operators and the mean field energy per flavor at zero temperature is given by

$$\frac{\langle \mathcal{H}_{MF} \rangle}{N} = e_{MF} = \sum_{\mathbf{k}} \frac{\hbar\omega_{\mathbf{k}}}{2} + \frac{zQ^2}{2J} - N_s \left(S + \frac{1}{2} \right) \lambda \quad (3.11)$$

The set of quasiparticle frequencies $\omega_{\mathbf{k}}$ are given by

[4] A normal diagonal form requires a choice of $\theta_{\mathbf{k}}$ such that *anomalous* terms like $\sim \alpha\alpha, \alpha^{\dagger}\alpha^{\dagger}$ vanish

$$\omega_{\mathbf{k}} = \sqrt{\lambda^2 - (zQ\cos(\mathbf{k}))^2} \tag{3.12}$$

where z is the coordination number of the spatially uniform lattices (two for the one dimensional chain). As a reminder, the set of equations (3.9),(3.10) and (3.11) are *only* valid for the special case of spatially uniform lattices. The generalization of these equations to spatially non-uniform lattices will be discussed in Section 3.4.

The spectrum is plotted in Fig.3.2 as a function of the mode index number in the first Brillouin zone. The curves shown are for different values of the ratio of the mean-field parameters defined $x \equiv zQ/\lambda$. As x approaches 1, the single particle spectral gap begins to close in at the zone center and the zone boundaries. Closing of the single particle boson frequency leads to Bose condensation of the bosons in to this lowest mode $\omega_{\mathbf{k}=0,\pi}$ and is the signal of long range order within SBMFT. Does this mean that SBMFT predicts long range magnetic order for the $S = 1/2$ Heisenberg chain?

The answer is no. In fact it predicts the opposite. A choice of mean field parameters that allow the single particle gap to close it by itself a necessary, but not a sufficient condition for long range order. The mean field parameters also need to satisfy the self-consistent equations given by the constraints (3.7). In particular, the number constraint is obtained by $\partial e_{MF}/\partial\lambda$ and gives

$$\frac{1}{N}\sum_{\mathbf{k}} \frac{1}{\sqrt{1-(\cos(k))^2}} = 2S_c + 1 \tag{3.13}$$

and in one dimension the integral on the left hand side is divergent and there is no solution to the above equation for $x = 1$. Thus the critical size of the

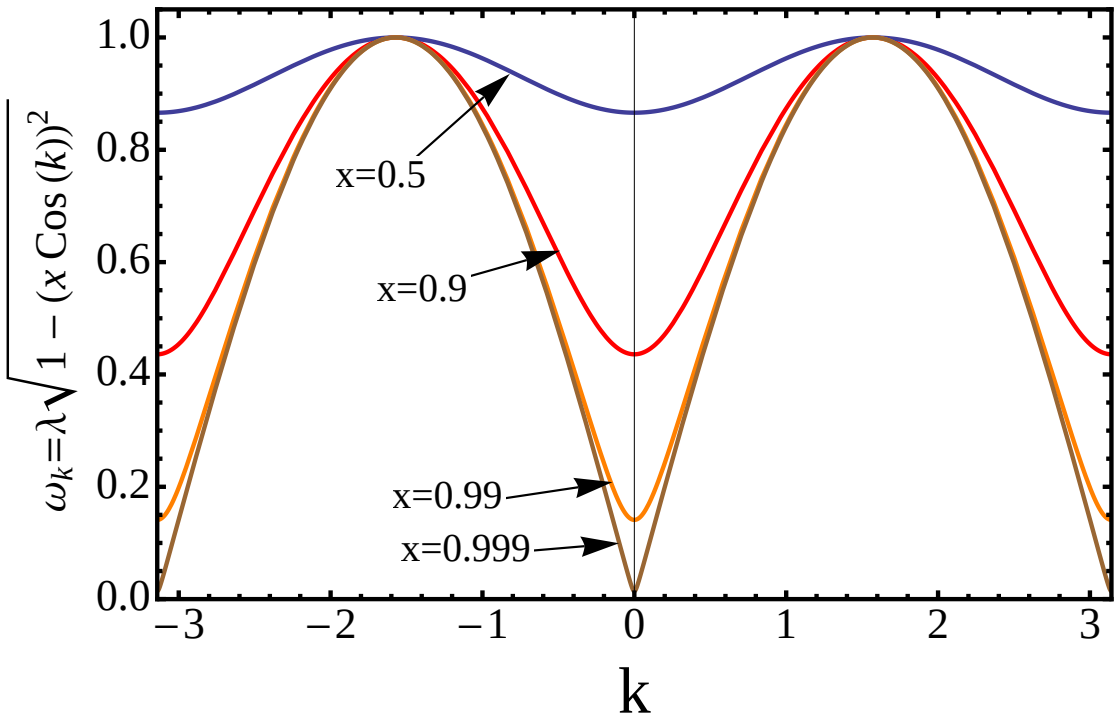

Figure 3.2: Single particle SBMFT spectrum for a Heisenberg $S = 1/2$ chain with periodic boundary conditions. The bosonic frequencies $\omega_k = \lambda\sqrt{1-(x\cos(ka))^2}$ is plotted against the mode index number m, where $k = 2\pi m/L$. The different curves are for different values of the mean field Hamiltonian (3.9) parameter $x \equiv zQ/\lambda$. As $x \to 1$ the dispersion goes to zero at the zone center ($\mathbf{k} = 0$) and at the zone corners ($\mathbf{k} = \pi$)

spin S_c (at which the gap (3.12) closes as the ratio of zQ to λ approaches one) is divergent. In two and three dimensions, solutions to (3.13) exist for finite values of S_c[9] and SBMFT thus predicts long range order for spin sizes exceeding S_c.

There are two other ways within SBMFT to predict S_c and to check whether SBMFT self-consistently allows for the existence of long range magnetic order. The first is to introduce a condensate field as a non zero expectation value of one of the bosonic flavors [13, 14]. This condensate field enters as another variational parameter in the SBMFT equations and the space of solutions can be checked for the existence of a mean field **Ansatz** that allows for the closing of the single particle spectrum and a non zero condensate field.

A second probe for long range order is to weakly break the symmetry between the different flavors by switching on a small magnetic field [11]. The magnetic field lowers the frequency of a single flavor mode. Bosons condense in to this mode and one can again check for the critical spin length for which a macroscopic condensate builds up in the lowered single particle frequency. Both probes give consistent results for the value of the critical spin length S_c required for the onset of long range magnetic order.

3.4 Generalization of SBMFT to search for non-uniform solutions

The number of mean field parameters in SBMFT build up to a large number very quickly if one wants to allow for condensate fields[13] and additional pairing amplitudes[14]. In particular, *assumption* of a uniform ansatz, like for the uniform Heisenberg chain of the previous Section, prevents an unbiased exploration of SBMFT mean field solutions which might want to *spontaneously* break spatial or chiral symmetries [10, 15]. A larger number of variational parameters are essential in cases where dilution or presence of disorder breaks spatial symmetries and destroys equivalence between sites[16]. In this section, we discuss a numerical implementation of SBMFT that allows for a larger space of mean field parameters and allows for an unbiased exploration of the space of SBMFT solutions.

We describe a numerical algorithm for an unbiased search of SBMFT solutions optimized with a large number of mean field parameters. We outline separate implementations for the two kinds of large N extensions: SU(N) and Sp(N)

models in the sub-sections below.

3.4 .1 SU(N) algorithm

To generalize the applicability of SBMFT to spatially non-uniform lattices and to search for spontaneously symmetry broken SBMFT solutions on uniform lattices we outline an algorithm that generalizes the equations (3.9), (3.10) and (3.11) to incorporate site and/or bond dependent mean field parameters.

The algorithm described below is carried out for very many initial starting points of the mean field parameters to map out the basin of attraction of the mean field solutions:

Step 1: Choose an initial starting guess for the mean field parameters $\{\lambda_i^{init}, Q_{ij}^{init}\}$. With these parameters the optimizer Levenberg Marquardt[17] is called.

Step 2: The optimizer in this step diagonalizes the Hamiltonian matrix $\mathbf{M}$:

$$\mathbf{M} = \begin{pmatrix} \mathbf{\Lambda} & \mathbf{Q} \\ \mathbf{Q} & \mathbf{\Lambda} \end{pmatrix} \tag{3.14}$$

Diagonalization is done by introducing a transformation matrix $\mathbf{P}$ such that $\mathbf{P}^\dagger\mathbf{M}\mathbf{P}$ is diagonal. This transformation matrix also relates the bosonic operators $\boldsymbol{\beta}$ to the Bogoliubov quasiparticle operators $\boldsymbol{\alpha}^T = (\alpha_1, ...\alpha_{N_s}, \alpha_1^\dagger, ..., \alpha_{N_s}^\dagger)$ where $\alpha_m(\alpha_m^\dagger)$ destroy (create) a quasi-particle in the single mode m. The matrix $\mathbf{P}$ relates $\boldsymbol{\beta}$ to $\boldsymbol{\alpha}$ via $\boldsymbol{\beta} = \mathbf{P}\boldsymbol{\alpha}$ and can be explicitly written out as:

$$\begin{pmatrix} \mathbf{b} \\ \mathbf{b}^\dagger \end{pmatrix} = \begin{pmatrix} \mathbf{U} & \mathbf{V} \\ \mathbf{V}^* & \mathbf{U}^* \end{pmatrix} \begin{pmatrix} \boldsymbol{\alpha} \\ \boldsymbol{\alpha}^\dagger \end{pmatrix} \tag{3.15}$$

where the matrices $\mathbf{U}, \mathbf{V}$ contain the Bogoliubov coefficients analogous to the transformation coefficients $\{u_{\mathbf{k}}, v_{\mathbf{k}}\}$ in the uniform case (3.10). In addition, the bosonic operators $\alpha_m, \alpha_n^\dagger$ also need to satisfy the commutation relations $[\alpha_m, \alpha_n^\dagger] = \delta_{m,n}$. A straightforward diagonalization of $\mathbf{M}$ does not enforce the constraint of bosonic commutation relations[5] and we instead need to diagonalize the matrix $\mathbf{JM}$ where $\mathbf{J}$ is given by

$$\mathbf{J} = \begin{pmatrix} \mathbf{1} & 0 \\ 0 & -\mathbf{1} \end{pmatrix} \tag{3.16}$$

where $\mathbf{1}$ is the $N_s \times N_s$ identity matrix. The matrix $\mathbf{JM}$ is non-Hermitian but has real eigenvalues for large enough values of $\mathbf{\Lambda}$. The optimizer therefore solves the following eigenvalue equation by calling the LAPACK routine **dgeev** [18] for diagonalizing a general (non-Hermitian) matrix:

$$\begin{pmatrix} \mathbf{\Lambda} & \mathbf{Q} \\ -\mathbf{Q} & -\mathbf{\Lambda} \end{pmatrix} \begin{pmatrix} \mathbf{u}_n \\ \mathbf{v}_n^* \end{pmatrix} = \omega_n \begin{pmatrix} \mathbf{u}_n \\ \mathbf{v}_n^* \end{pmatrix} \tag{3.17}$$

The eigenvalues come in positive and negative pairs $\{\pm\omega_n\}$ and the eigen vectors are the column entries of the transformation matrix $\mathbf{P}$.

Step 3: Once diagonalization is done, the optimizer computes the boson density n_i using the Bogoliubov coefficient matrices $\mathbf{U}$ and $\mathbf{V}$. We outline the

[5] this is unlike the case of non-interacting fermions where diagonalizing the Hermitian Hamiltonian matrix preserves fermionic commutation relations

calculation below:

$$
\begin{aligned}
n_i = \langle b_i^\dagger b_i \rangle &= \langle \sum_{m,n} (v_{in}^* a_n + u_{in}^* a_n^\dagger)(u_{im} a_m + v_{im} a_m^\dagger) \rangle \\
&= \sum_{m,n} v_{in}^* v_{im} \langle a_n a_m^\dagger \rangle = \sum_{m,n} v_{in}^* v_{im} \delta_{m,n} = \sum_{n=1}^{n=N_s} |v_{in}|^2
\end{aligned}
\tag{3.18}
$$

where we use the fact $\langle \alpha_n \alpha_m^\dagger \rangle = \delta_{m,n}$ since the mean field state is the vacuum of the Bogoliubov quasparticles. The optimizer computes the boson density at every site and uses it to compute a cost function: $C_\lambda = \sum_{i=1}^{i=N_s} (n_i - S)^2$ to check whether the number constraint (3.7) has been met. If C_λ is above a tolerance $\epsilon_\lambda \sim 10^{-19}$ the optimizer makes the next best guess for the set λ_i based on the gradient of the C_λ with respect to the $\{\lambda_i\}$[17] and returns to **Step 2**. If the cost meets the tolerance criterion, the optimizer proceeds on to **Step 4**.

Step 4: The optimizer now computes the self-consistent value of the pairing amplitude or the bond variables Q_{ij} as follows:

$$
\begin{aligned}
\langle Q_{ij} \rangle = \langle b_i b_j \rangle &= \langle \sum_{m,n} (u_{in} a_n + v_{in} a_n^\dagger)(u_{jm} a_m + v_{jm} a_m^\dagger) \rangle \\
&= \sum_{m,n} u_{in} v_{jm} \langle a_n a_m^\dagger \rangle = (\mathbf{UV})_{ij}^T
\end{aligned}
\tag{3.19}
$$

The mean field bond variables are used to compute another cost function $C_Q = \sum_{i<j} (Q_{ij} - \langle Q_{ij} \rangle)^2$ [6] which comes along with its own tolerance $\epsilon_Q \sim 10^{-16}$. This tolerance ensures that the bond constraint (3.7) has been met. The optimizer exits the loop if the tolerance is met, else it calls **Step 2** with the updated bond variables.

[6] one can in general allow for further ranged bond variables Q_{ij} and the cost function needs to be summed over all such amplitudes for a self-consistent solution

Step 5: Once the optimizer exits the loop the mean field energy and spin-spin correlations can be calculated. The mean field energy is given in (3.11) and we show below the computation of the correlations.

The spin-spin correlation expression $\langle \mathbf{S}_i \cdot \mathbf{S}_j \rangle$ differs depending on whether sites $i, j \in$ sublattice A or B. First note that, spin rotational invariance requires us to only compute the correlation $\langle \mathbf{S}_i^+ \mathbf{S}_j^- \rangle$. Using the definitions of $\mathbf{S}_i^{\pm}$ [7], it is easy to show that $\langle \mathbf{S}_i \cdot \mathbf{S}_j \rangle = 3\langle S_i^+ S_j^- \rangle / 2$. We therefore proceed to compute $\langle S_i^+ S_j^- \rangle$ for $i, j \in A(B)$ using (3.2)

$$
\begin{aligned}
\langle S_i^+ S_j^- \rangle &= \langle a_i^\dagger b_i b_j^\dagger a_j \rangle \\
&= \langle a_i^\dagger a_j \rangle \langle b_i b_j^\dagger \rangle \\
&= \left(\sum_{m,n} \langle (u_{in}^* \alpha_n^\dagger + v_{in}^* \alpha_n)(u_{jm} \alpha_m + v_{jm} \alpha_m^\dagger) \rangle \right) * \\
&\quad \left(\sum_{m,n} \langle (u_{in} \alpha_n + v_{in} \alpha_n^\dagger)(u_{jm}^* \alpha_m^\dagger + v_{jm}^* \alpha_m) \rangle \right) \\
&= \left(\sum_n v_{in}^* v_{jn} \right) \left(\sum_n u_{in} u_{jn}^* \right) \\
&= (\mathbf{V}^* \mathbf{V}^\dagger)_{ij} * (\mathbf{U} \mathbf{U}^\dagger)_{ij}
\end{aligned}
\tag{3.20}
$$

where the matrices $\mathbf{U}, \mathbf{V}$ of Bogoliubov coefficients is defined in (3.15). In a similar manner we can compute the spin correlations $\langle \mathbf{S}_i \cdot \mathbf{S}_j \rangle$ for $i \in A$ and $j \in B$ keeping in mind the sub-lattice rotation of the spin operators on sublattice B which transforms $a_j \to -b_j$, $b_j \to a_j$

[7] $S_i^{\pm} = S_i^x \pm i S_i^y$

$$
\begin{aligned}
\langle S_i^+ S_j^- \rangle &= -\langle a_i^\dagger b_i a_j^\dagger b_j \rangle \\
&= -\langle a_i^\dagger a_j^\dagger \rangle \langle b_i b_j \rangle \\
&= \left(\sum_{m,n} \langle (u_{in}^* \alpha_n^\dagger + v_{in}^* \alpha_n)(u_{jm}^* \alpha_m^\dagger + v_{jm}^* \alpha_m) \rangle \right) * \\
&\quad \left(\sum_{m,n} \langle (u_{in} \alpha_n + v_{in} \alpha_n^\dagger)(u_{jm} \alpha_m + v_{jm} \alpha_m^\dagger) \rangle \right) \\
&= \left(\sum_n v_{in}^* u_{jn}^* \right) \left(\sum_n u_{in} v_{jn} \right) \\
&= (\mathbf{V}^* \mathbf{U}^\dagger)_{ij} * (\mathbf{U} \mathbf{V}^T)_{ij}
\end{aligned}
\tag{3.21}
$$

Both correlations (3.20),(3.21) computed within SBMFT are over-estimated from the real (exact many-body) calculations by a factor of $2S(S+1)$ [9] which is $3/2$ for $S = 1/2$. For agreement with many-body numerics we therefore need to normalize both correlations by this *ad-hoc* factor (in practice the the spin -spin correlations are $3/2$ times the correlations in (3.20) and exactly cancel the *ad-hoc* $3/2$ factor).

Figure 3.3 shows a cartoon of the main steps of the optimization algorithm described in this section. We briefly comment now on the complexity of the optimizer. The computational complexity grows as the number of mean field parameters $\{\lambda_i, Q_{ij}\}$ in the system. For the Bethe lattice, with only nearest neighbor bonds, the number of mean field parameters are $2N_s - 1 \sim N_s$. The most expensive component of the algorithm is the repeated evaluation of the cost function C_λ which requires diagonalization of a $2N_s \times 2N_s$ matrix (3.14) and scales as $\sim N_s^3$. Thus the complexity goes as $N_s^3 \tau_\lambda \tau_Q$ where τ_λ is the typical number of steps for the optimizer to reach the tolerance criterion for C_λ (typical values of $\tau_\lambda \sim 1000$ for $N_s = 100$) and τ_Q is the number of self-consistent steps

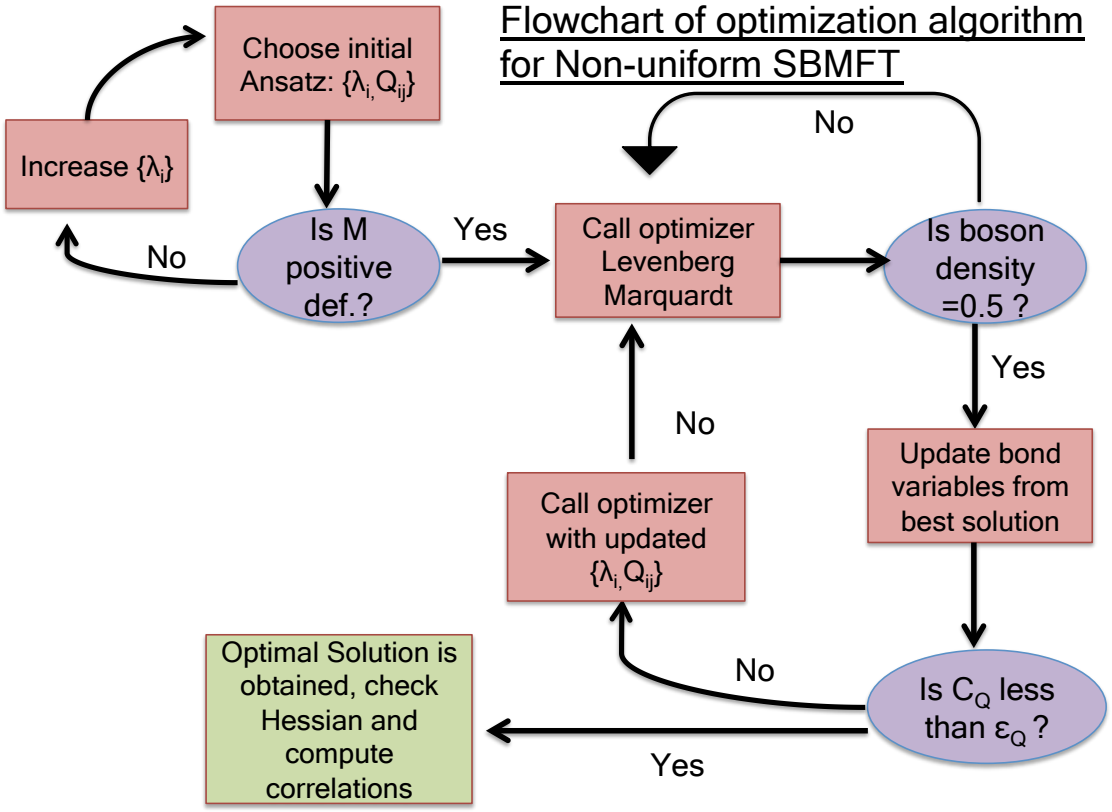

Figure 3.3: Numerical algorithm to find optimal set of parameters $\{\lambda_i^*, Q_{ij}^*\}$ within non-uniform SBMFT. The cost functions C_Q, C_λ measure deviation from the constraints (3.7) associated with self-consistent bond amplitudes and a fixed boson density on every site, respectively. Each cost function needs to meet a tolerance set by $\epsilon_{Q(\lambda)}$. The matrix $\mathbf{M}$ refers to the "Hamiltonian" matrix (3.14) that needs to be para-diagonalized at every call of the optimizer 'Levenberg Marquardt' to obtain the single particle bosonic spectrum of frequencies and eigen-modes

to meet the ϵ_Q criterion (typically $\sim 20 - 30$ for $N_s = 100$).

The SU(N) formalism is valid for bipartite lattices and in general allows for complex values of the bond amplitudes Q_{ij}. A more general approach (valid even on frustrated lattices[8, 13]) extends the symmetry group of the spins from SU(2) to Sp(N) and is described next.

3.4 .2 Sp(N) formalism

Read and Sachdev [8] generalized Arovas and Auerbach's [11] Schwinger boson construction to frustrated lattices. The symmetry group for the large N expansion for frustrated lattices is Sp(N)[19]. The optimization algorithm for 3.3 for Sp(N) non-uniform SBMFT is exactly similar to the SU(N) formalism Section 3.4 .1 except for specific implementation details which we outline below.

The Sp(N) mapping to two species $\uparrow, \downarrow$ of bosons analogous to (3.2) is given by:

$$\mathbf{S}_i^+ = b_{i\uparrow}^\dagger b_{i\downarrow}, \qquad \mathbf{S}_i^- = b_{i\downarrow}^\dagger b_{i\uparrow}, \qquad \mathbf{S}_i^z = \frac{1}{2}(b_{i\uparrow}^\dagger b_{i\uparrow} - b_{i\downarrow}^\dagger b_{i\downarrow}) \tag{3.22}$$

where $b_{\uparrow(\downarrow)}$ are two species of bosons corresponding to a *single* flavor (two flavors in SU(N) correspond to a single Sp(N) flavor). The mean field Hamiltonian is expressed in terms of the Lagrange multipliers λ_i which enforce the constraint:

$$n_i = \sum_{\sigma=\uparrow,\downarrow} \langle b_{i\sigma}^\dagger b_{i\sigma} \rangle = 2S = \kappa \tag{3.23}$$

and bond amplitudes Q_{ij} (complex in general) given by

$$Q_{ij} = \frac{1}{2}(b_{i\uparrow} b_{j\downarrow} - b_{i\downarrow} b_{i\uparrow}) \tag{3.24}$$

The Hamiltonian is given by:

$$\mathcal{H}_{Sp} = \boldsymbol{\beta}^\dagger \mathbf{M}_{Sp} \boldsymbol{\beta} + \sum_{ij} J|Q_{ij}|^2 + (1+\kappa) \sum_{i=1}^{N_s} \lambda_i \tag{3.25}$$

where $\boldsymbol{\beta}^T = (b_{1\uparrow}, .., b_{N_s\uparrow}, b^\dagger_{1\downarrow}, .., b^\dagger_{N_s\downarrow})$ and the Hamiltonian matrix is given by

$$\mathbf{M}_{Sp} = \begin{pmatrix} -\mathbf{\Lambda} & J\mathbf{Q} \\ -J\mathbf{Q}^* & -\mathbf{\Lambda} \end{pmatrix} \tag{3.26}$$

where $\mathbf{\Lambda}_{ij} = \delta_{ij}\lambda_i$ and $\mathbf{Q}$ is an anti-symmetric matrix of bond variables(3.24) . The matrix $\mathbf{M}_{Sp}$ resembles the $\mathbf{SU}(N)$ matrix (3.14) except for the anti-symmetric matrix $\mathbf{Q}$ [8].

The optimizer diagonalizes the $2N_s \times 2N_s$ matrix M_{Sp} by finding a matrix of Bogoliubov coefficients $\mathbf{P}$: $\boldsymbol{\beta} = \mathbf{P}\boldsymbol{\alpha}$ such that $\mathbf{P}^\dagger\mathbf{M}\mathbf{P} = \bar{\mathrm{M}}$. $\bar{\mathrm{M}}$ is a diagonal matrix containing the single particle boson frequencies $\{\omega_n\}$. In addition, for the new Bogoliubov operators $\alpha_n, \alpha^\dagger_m$ to satisfy the bosonic commutation relations $[\alpha_n, \alpha^\dagger_m] = \delta_{n,m}$, the optimizer also needs to ensure $\mathbf{P}^\dagger\mathbf{J}\mathbf{P} = \mathbf{J}$ where $\mathbf{J}$ is a diagonal matrix of ones and minus ones defined earlier(3.16) (This diagonal matrix $\mathbf{J}$ should not be confused with the notation of the uniform Heisenberg coupling amplitude of Eq. (3.1), which is a scalar). The optimizer meets these requirements using the follow algorithm for **Step2** of the algorithm.

Step 2(a): As a first step towards diagonalizing the Hamiltonian matrix (7.3) we carry out a Cholesky decomposition of $\mathbf{M}$ is done by finding a $N_s \times N_s$ matrix $\mathbf{K}$ such that $\mathbf{M} = \mathbf{K}^\dagger\mathbf{K}$

Step 2(b): The second step towards diagonalizing the Hamiltonian matrix M_{Sp} (7.3) is to find a unitary matrix $\mathbf{U}$: $\mathbf{U}^\dagger\mathbf{U} = 1$ such that $\mathbf{L} = \mathbf{U}^\dagger\mathbf{K}\mathbf{J}\mathbf{K}^\dagger\mathbf{U}$ is di-

[8] For a frustrated lattice, we can not do a sublattice rotation to make Q_{ij} symmetric as in the SU(N) case

agonal. The matrix **U** then contains the eigen-vectors of $\mathbf{KJK}^{\dagger}$ matrix arranged along the columns. The matrices **K** and **U** will be used to build the transformation matrix **P** that links the bare bosonic operators β to the Bogoliubov quasi-particle operators.

Step 2(c): The single particle frequencies are the diagonal values of $\bar{\mathbf{M}} = \mathbf{J} \cdot \mathbf{L}$ and come in pairs $\{\pm\omega_n\}$. The N_s positive frequencies are the single particle bosonic dispersion. The transformation matrix **P** is given by $\mathbf{P} = \mathbf{K}^{-1}\mathbf{U}\bar{\mathbf{M}}^{1/2}$.

The optimizer then continues on to **Step 3** of the algorithm as described in 3.4 .1. The spin-spin correlations have a slightly more tedious computation than the SU(N) formalism and we show below how to compute them using the transformation matrix **P**.

The transformation matrix **P** can be expressed in terms of four $N_s \times N_s$ matrices as follows:

$$\mathbf{P} = \begin{pmatrix} \mathbf{A} & \mathbf{B} \\ \mathbf{C} & \mathbf{D} \end{pmatrix} \tag{3.27}$$

Using rotational invariance again, it suffices to compute the expectation $\langle S_i^+ S_j^- \rangle$ to get the spin-spin correlations. Using the **Sp**(N) mapping, this expectation can be expressed in terms of the bosonic operators as follows:

$$\begin{aligned}\langle S_i^+ S_j^- \rangle &= \langle b_{i\uparrow}^\dagger b_{i\downarrow} b_{j\downarrow}^\dagger b_{j\uparrow} \rangle \\ &= 2\langle b_{i\uparrow}^\dagger b_{i\downarrow} \rangle \langle b_{j\downarrow}^\dagger b_{j\uparrow} \rangle + \langle b_{i\uparrow}^\dagger b_{j\downarrow}^\dagger \rangle \langle b_{i\downarrow} b_{j\uparrow} \rangle + \langle b_{i\uparrow}^\dagger b_{j\uparrow} \rangle \langle b_{i\downarrow} b_{j\downarrow}^\dagger \rangle + \langle b_{i\downarrow} b_{j\downarrow}^\dagger \rangle \langle b_{i\uparrow}^\dagger b_{j\uparrow} \rangle + \\ &\quad \langle b_{i\downarrow} b_{j\uparrow} \rangle \langle b_{i\uparrow}^\dagger b_{j\downarrow}^\dagger \rangle \end{aligned} \tag{3.28}$$

where all expectations $\langle ... \rangle$ are taken in the mean field ground state - the vacuum of the Bogoliubov quasiparticles. The decoupling of the $S_i^+ S_i^-$ operator in (3.28) is general and includes both the symmetric (ferromagnetic) and anti-symmetric (anti-ferromagnetic) channels. Both symmetric and anti-symmetric refer to the sign of the decoupling terms with respect to an interchange of the spatial indices. Because of our assumption about retaining only the anti-ferromagnetic correlations in the ground state of the AFM Heisenberg model, the expectations corresponding to ferromagnetic correlations in (3.28) will vanish.

Each expectation can be expressed in terms of the transformation matrices in (3.27). The decoupling of the spin operators above is done only in the anti-symmetric channel which captures the dominant anti-ferromagnetic correlations in the ground state of the Heisenberg spin model. It is also possible to decouple in the symmetric ferromagnetic channel[10]. However, for the sake of simplicity we will consider only the anti-symmetric channel. The only expectations that vanish are $\langle b_{i\uparrow}^\dagger b_{i\downarrow} \rangle$ and $\langle b_{j\downarrow}^\dagger b_{j\uparrow} \rangle$ both of which correspond to on-site spin flip excitations not allowed by the mean field Hamiltonian (7.2). The other terms in (3.28) have the following expectations:

$$
\begin{aligned}
\langle b^{\dagger}_{i\uparrow} b^{\dagger}_{j\downarrow} \rangle \langle b_{i\downarrow} b_{j\uparrow} \rangle &= (\mathbf{B}^{*}\mathbf{D}^{T})_{ij} * (\mathbf{D}^{*}\mathbf{B}^{T})_{ij} \\
\langle b^{\dagger}_{i\uparrow} b_{j\uparrow} \rangle \langle b_{i\downarrow} b^{\dagger}_{j\downarrow} \rangle &= (\mathbf{B}^{*}\mathbf{B}^{T})_{ij} * (\mathbf{D}^{*}\mathbf{D}^{T})_{ij} \\
\langle b_{i\downarrow} b^{\dagger}_{j\downarrow} \rangle \langle b^{\dagger}_{i\uparrow} b_{j\uparrow} \rangle &= (\mathbf{D}^{*}\mathbf{D}^{T})_{ij} * (\mathbf{B}^{*}\mathbf{B}^{T})_{ij} \\
\langle b_{i\downarrow} b_{j\uparrow} \rangle \langle b^{\dagger}_{i\uparrow} b^{\dagger}_{j\downarrow} \rangle &= (\mathbf{D}^{*}\mathbf{B}^{T})_{ij} * (\mathbf{B}^{*}\mathbf{D}^{T})_{ij}
\end{aligned}
\tag{3.29}
$$

The spin-spin correlation can therefore be expressed as:

$$
\langle \mathbf{S}_i \cdot \mathbf{S}_j \rangle = 3 \left[(\mathbf{B}^{*}\mathbf{D}^{T})_{ij} * (\mathbf{D}^{*}\mathbf{B}^{T})_{ij} + (\mathbf{D}^{*}\mathbf{D}^{T})_{ij} * (\mathbf{B}^{*}\mathbf{B}^{T})_{ij} \right] \tag{3.30}
$$

Unlike the $SU(N)$ spin-spin correlations where the SBMFT correlators(3.20),(3.21) need to be multiplied by an overall factor of $3/2$ to agree with numerical exact diagonalization[9] or DMRG [14] calculations, the Sp(N) correlations are not plagued by factors of $3/2$ allowing for direct comparison with exact numerical calculations. Fig.3.4 shows a comparison between spin-spin correlations at successive stages of the self-consistent Q_{ij} iteration cycle with exact DMRG calculations. The lattice chosen is a $N_s = 50$ site Bethe lattice cluster at percolation threshold. A site is chosen on the cluster at random and spin correlations between the chosen site and all other sites on the cluster is shown on a Log scale. The optimizer converges to a stable saddle-point solution after $9\ Q_{ij} cycle$ iterations. Agreement between DMRG correlations and SBMFT measurements improves as we lower the C_Q cost with each successive iteration. The converged solution (9^{th} iteration) shows better agreement with DMRG results for short distance correlations compared to long distance spin-spin interactions.

Both formalisms described in this section allow for an unbiased search of non-uniform SBMFT solutions. The search crucially depends on having a robust

optimizer that can seek solutions satisfying the mean field constraints (3.7) and we next describe a set of tricks for computationally efficient optimization.

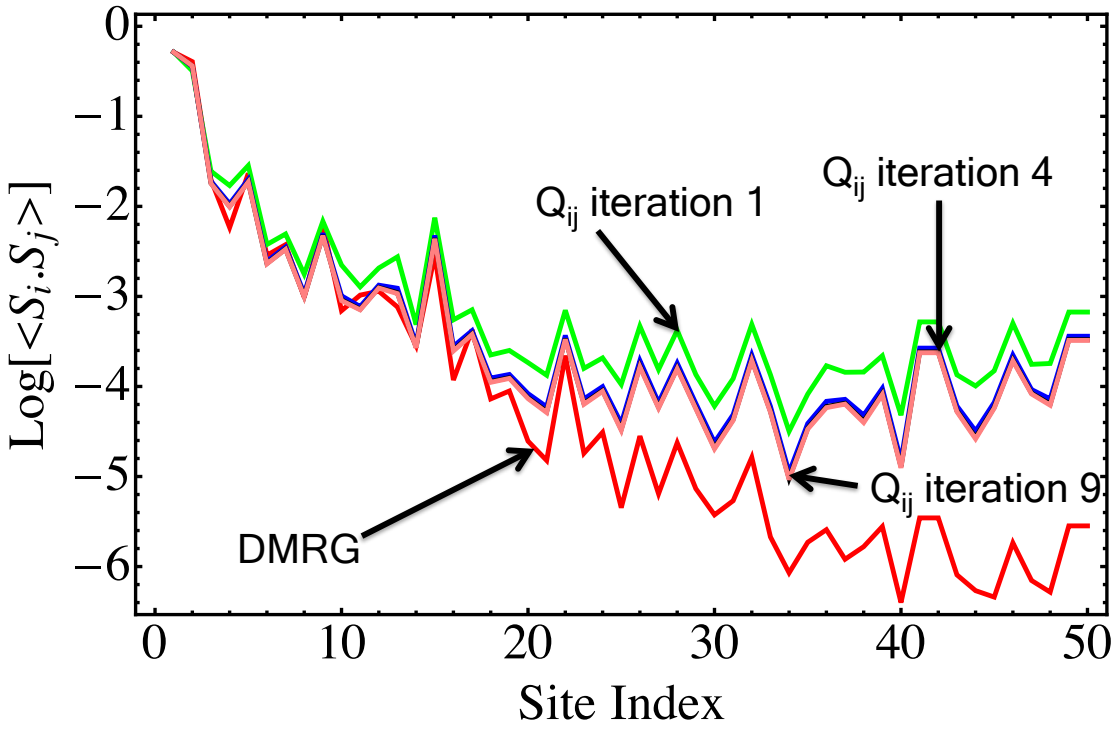

Figure 3.4: Comparison of spin-spin correlations at different Q_{ij} iteration cycles with DMRG results. Correlations are for a $N_s = 50$ site Bethe lattice at the percolation threshold. Correlations are between a single site (chosen at random) on the cluster and all other sites. The optimizer converges to a stable saddle-point solution at the 9^{th} iteration. Short distance correlations are in better agreement than long distance spin-spin interactions.

3.5 Optimization tricks

Optimizers need to be tailored to the specific problems they are trying to solve and the efficiency and speed depends crucially on a physical understanding of the problem. For SBMFT optimizations we use two kinds of optimizers - Levenberg Marquardt and Nelder Mead.

Levenberg Marquardt is a gradient based algorithm and works by computing numerically, the derivatives of the cost or objective function at different points in parameter space. The algorithm then proceeds along the direction of greatest descent (largest negative slope in parameter space) until it reaches a local minimum. The gradient based algorithm works very well for convex objective functions with a single minimum. However, for non-convex functions or several closely spaced, almost degenerate minimas, the optimizer needs to be restarted with several initial guesses to test the robustness (to initial starting conditions and against other local or global minimas) of the optimal optimizer solution.

Nelder Mead, unlike the Levenberg Marquardt algorithm, is not a gradient based algorithm and works well for problems where the first order derivative of the cost or objective function, with respect to variational parameters, cannot be written down in a closed or analytic form. Nelder Mead is also efficient, in comparison to Levenberg Marquardt, in cases where it is numerically expensive to evaluate derivatives.

Since evaluation of numerical derivatives is relatively cheap for the number constraint (3.7) objective function in SBMFT, we use the Levenberg Marquardt algorithm for all SBMFT optimizations. The Nelder Mead serves as an independent check for optimization results obtained from Levenberg Marquardt, but is computationally more expensive for large system sizes (N_s>20) sites.

3.5 .1 Reducing the number of mean field parameters

As argued previously in Section3.4 , the computational complexity of the optimizer scales as $\sim N_s^3 \tau_Q \tau_\lambda$, where N_s is the number of lattice sites, τ_Q is the number of steps for convergence of the self-consistent Q_{ij} iteration (see Section 1.4.1 and Figure 1.3) and τ_λ is the number of iterations required to meet the number constraint (3.7). For a given lattice size N_s, the number of self-consistent iteration steps τ_Q to update the bond variables and the number of iterations τ_λ required to meet the number constraint(3.7) depend on the number of mean field parameters $\{Q_{ij}, \lambda_i\}$. The optimizer steps increase with the number of $\{Q_{ij}\}$. To reduce the number of bond variables, it is usually sufficient to keep *only* up to nearest neighbor Q_{ij} and to ignore longer range bond amplitudes, if spin-spin correlations in the ground state are dominantly anti-ferromagnetic[9]. We can reduce the number of bond amplitudes further by invoking two further constraints motivated by logical necessities on the distribution of Q_{ij}: *symmetry* and *gauge invariance*.

Exact symmetries of the lattice can constrain the mean field parameters to take the same values on symmetry equivalent bonds or lattice sites reducing the number of mean field parameters. Such symmetries on Bethe lattices at percolation correspond to forks where the tip sites are equivalent and related by a reflection symmetry and in the case of pure-Bethe lattice corresponds to a ring of sites at a given generation[14]. At percolation, the number of forks scales as N_s and we therefore see a considerable reduction in the number of parameters. However, before reducing the number of parameters it is important to ensure that the SBMFT ground state on small enough lattices does not *spontaneously*

[9] empirically spin-spin correlations are found to agree well in both formalisms by retaining only nearest neighbor Q_{ij}

violate space group symmetries. In case it does, as in the case of the kagome lattice [15], we can no longer reduce the mean field parameters on symmetry grounds.

For lattices with loops, the mean field SBMFT energy (3.11) depends on gauge invariant fluxes through loops on the lattice. The flux through an even length loop ℓ comprising of sites $i, j, k, ...n$ is given by [20]:

$$\Phi_\ell = \arg(Q_{ij} * (-Q^*_{jk})Q_{k\ell}...(-Q^*_{ni})) \tag{3.31}$$

The gauge invariant flux (6.10) allows us to fix a certain fraction of the bonds $\{Q_{ij}\}$ as real allowing a reduction in phase drifts as noted by Misguich [15]. We use this technique on the Kagome lattice to explore the low energy SBMFT saddle-points. Finally, on lattices without loops like the Bethe lattice at percolation, the fluxes are not defined and we can therefore choose all Q_{ij} to be real.

3.5 .2 Initial guess for the optimizer

As in all optimization problems an informed initial guess leads to faster convergence. While it is easy to give the optimizer an initial guess based on lattice symmetries discussed in the previous section or from many-body calculations [10] we normally avoid doing so unless we encounter slow convergence for large lattices or considerable complex drifts in the bond amplitudes.

Starting with a uniform initial guess of the mean field parameters allows

[10] A guess for the ground state $\{Q_{ij}\}$ pattern can be obtained via spin-spin correlations from many body calculations like Exact Diagonalization on small lattices or DMRG. Since $\langle \mathbf{S}_i \cdot \mathbf{S}_j \propto Q^2_{ij} \rangle$ the correlations allow for an informed initial guess for the bond amplitudes

for an unbiased exploration of the low energy SBMFT solutions and an estimate of the basin of attraction of the low energy saddle point solutions. The optimizer has greater sensitivity to the accuracy of the initial guess of the Lagrange multipliers compared to the starting guess for the bond amplitudes. A reason for this is that it is important to start exploration from a region in parameter space where the matrix $\mathbf{M}$ (3.14) is positive-definite. Starting with uniform large enough $\mathbf{\Lambda}$(typically $\lambda > zQ$ where z is the average coordination of the lattice sites) ensures that the eigen-values of $\mathbf{M}$ are real and come in pairs: $\{\pm\omega_n\}$.

In spite of starting from a positive definite $\mathbf{M}$ the optimizer can still fail to meet the ϵ_λ criterion (3.7). This happens most frequently for three reasons. Firstly, the number of initial starting guesses might be too small and this is easily resolved by increasing the set of initial seeds for the optimizer.

Secondly, in situations where there are small differences in bond amplitudes for nearest neighbor bonds, the optimizer might fail to minimize C_λ to low enough values. In this case we relax the number constraint (3.7) slightly (increase tolerance), find a set of Lagrange multipliers and compute the $\{Q_{ij}\}$ using the self-consistent equations (3.19). The optimizer is now called with an initial seed of the bond amplitudes and tries to minimize C_Q, keeping the Lagrange multipliers constant. The optimal set might violate the number constraint, in which case we again start the optimizer with an initial seed consisting of the Lagrange multipliers keeping the bond amplitudes constant. This iterative minimization procedure, where we alternately optimize C_Q and C_λ costs, works well once we are close to a saddle point and the tolerances are below a certain threshold (typically $\epsilon_Q, \epsilon_\lambda \sim 10^{-4}$).

Finally, the optimizer might also fail due to inaccuracy in the computation of

the numerical derivatives required for determining the step sizes in parameter space by the Levenberg Marquardt algorithm. We discuss this case in greater detail next.

3.5 .3 Computation of Jacobian

The optimizer decides on the step size in parameter space depending on the Jacobian - the matrix of first derivatives of the cost functions with respect to the mean field parameters. Levenberg Marquardt allows the user to choose from one of two options for evaluating numerical derivatives. The forward difference method is faster but less accurate whereas the central difference is more accurate but also slower. Since there are typically $\tau_\lambda \sim 1000$ steps the optimizer needs to take at each cycle of the optimization to meet the tolerance criterion for C_λ, the computation of the Jacobian matrix needs to be optimized.

For cases in which the optimizer convergence is slow we provide the Jacobian matrix as an input to the optimizer. The GSL library **gsl_deriv_central** allows efficient (order N_s^2. N_s is the number of sites in the system) computation of the Jacobian matrix given a cost function. A manual input of the Jacobian matrix is found to speed calculations by $5 - 8\%$ for system sizes up to $N_s = 100$ sites.

3.5 .4 Relaxing constraints

Relaxing the tolerances ϵ_Q and ϵ_λ for the self-consistent bond amplitudes and the boson densities per site (see (3.7)) also helps the optimizer speed up.

In many cases setting a high $\epsilon_\lambda \sim 10^{-4} - 10^{-611}$ for the first few iteration steps and then bringing it down to $\epsilon_\lambda \sim 10^{-19}$ guides the optimizer towards the low energy saddle points. During the Sp(N) optimization we also allow the matrix **M** to lose positive-definiteness by a small amount (quantified by the difference in the magnitudes of the positive and negative frequency branches). The optimal set of mean field parameters $\{\lambda_i^*, Q_{ij}^*\}$ are always checked to correspond to a positive definite **M**.

3.6 Optimizer settings and libraries

In this section we describe some typical optimizer settings and enumerate the different kinds of LAPACK subroutines used by the optimizer. Optimizer settings are shown in 3.1 for finding saddle point solutions on Bethe lattice percolation clusters and on the Kagome lattice. The Kagome lattice due to a high density of almost degenerate saddle points requires Jacobian evaluations with greater precision and also a larger number of iteration steps itmax for the ϵ_λ tolerance to be met. The optimizer allows two kinds of precision settings for Jacobian evaluation. The LM_DIFF_DELTA approximates a numerical Jacobian matrix using forward differences whereas the setting $-$LM_DIFF_DELTA approximates the Jacobian using central differences and is therefore more accurate.

We use standard LAPACK libraries for linear algebra calculations. Some common subroutines used for matrix diagonalization, Cholesky decomposition

[11]Reminder: ϵ_Q is the tolerance criterion for the C_Q bond constraint cost in (3.7) and has dimensions of [ϵ_Q]=Energy^2. An estimate for the maximum value that C_Q can have, can be obtained by setting $Q_{ij} \sim 1$ and the target $\langle Q_{ij} \rangle = 0$ in (3.7), which gives $\epsilon_Q = 1$

Settings	Description	SU(2) Bethe percolation	Sp(1) Kagome
$\mathbf{p}$	Initial guess $\{\lambda_i^{init}\}$	$\mathbf{p}_i \in (2, 3)$	$\mathbf{p}_i \in (-3, -2.5)$
$\mathbf{x}$	Measurement vector	$\mathbf{x}_i = S = 0.5$	$\mathbf{x}_i = \kappa = 1$
m	Dimension $\mathbf{p}$	N_s	N_s
n	Dimension $\mathbf{x}$	N_s	N_s
opts[4]	Jacobian evaluation	LM_DIFF_DELTA	-LM_DIFF_DELTA
itmax	Max. # iterations	1000	5000
$\mathbf{Q}^{init}$	Initial guess for $\{Q_{ij}^{init}\}$	$Q_{ij} \in (-0.6, -0.5)$	$Q_{ij} \in (-0.6, -0.55)$

Table 3.1: Optimizer settings for computing SBMFT ground states for Bethe lattice percolation clusters and Kagome lattice for the Levenberg Marquardt routine $dlvemar\_dif()$ [17]

LAPACK routine	Description/Use
zpotrf	Cholesky decomposition of $\mathbf{M}_{Sp}$
zheev	Eigenvalues and vectors of complex Hermitian matrix $\mathbf{M}_{Sp}$
zgetrf	LU factorization of matrix $\mathbf{K}$ (for evaluating $\mathbf{K}^{-1}$)
zgetri	Inverse of $\mathbf{K}$
dgeev	Eigenvalue and vectors of real matrix $\mathbf{M}$

Table 3.2: List of LAPACK subroutines for different matrix operations used in the optimizer cycle

and computing matrix inverse operations is enlisted in Table3.2.

BIBLIOGRAPHY

[1] P. W. Anderson, Phys. Rev. **83**, 1260 (1951).

[2] T. Holstein and H. Primakoff, Phys. Rev. **58**, 1098 (1940).

[3] P. Fazekas and P. W. Anderson, Philos. Mag. 30, 23 (1974).

[4] N. D. Mermin and H. Wagner, Phys. Rev. Lett. **17**, 1133 (1966).

[5] D. Vaknin, S. K. Sinha, D. E. Moncton, D. C. Johnston, J. M. Newsam, C. R. Safinya, and H. E. King, Phys. Rev. Lett. **58**, 2802 (1987).

[6] J. B. Oitmaa, Canadian Journal of Physics **56**, 897 (1978).

[7] M. Takahashi, Phys. Rev. Lett. **58**, 168 (1987).

[8] N. Read and S. Sachdev, Phys. Rev. Lett. **66**, 1773 (1991).

[9] A. Auerbach, Interacting Electrons and Quantum Magnetism, Springer (1997).

[10] L. Messio, C. Lhuillier, and G. Misguich, Phys. Rev. B **87**, 125127 (2013).

[11] A. Auerbach and D. P. Arovas, Phys. Rev. Lett. **61**, 617 (1988).

[12] Landau and Lifshitz - 'Statistical Physics', Sec. 149, Pergamon, Oxford, 1958.

[13] S. Sachdev, Phys. Rev. B **45**, 12377 (1992).

[14] H. J. Changlani, S. Ghosh, C. L. Henley, and A. M. Läuchli, Phys. Rev. B **87**, 085107 (2013).

[15] G. Misguich, Phys. Rev. B **86**, 245132 (2012).

[16] H. J. Changlani, S. Ghosh, S. Pujari, and C. L. Henley, Phys. Rev. Lett. **111**, 157201 (2013).

[17] L. . users.ics.forth.gr/ lourakis/levmar/, The Journal of Chemical Physics **77**, 5562 (1982).

[18] LAPACK, LAPACK library (1997).

[19] Subir Sachdev, *Quantum Phase Transitions*, Cambridge University Press, 1999.

[20] O. Tchernyshyov, R. Moessner, and S. L. Sondhi, EPL (Europhysics Letters) **73**, 278 (2006).

CHAPTER 4

ANOMALOUS BOSONIC EXCITATIONS IN DILUTED HEISENBERG ANTIFERROMAGNETS

4.1 Emergent excitations in condensed matter systems

The contents of the chapter are in the process of being converted in to a manuscript to be submitted to Physical Review B. The author acknowledges contributions from Hitesh J. Changlani and Christopher L. Henley in research related to the contents of the chapter.

A phenomenon very common in interacting condensed matter systems is that of *emergence*. Emergence refers to the act of a few effective degrees of freedom, with emergent symmetries, being able to adequately describe the low energy excitations of a physical system. Interaction, between these emergent degrees of freedom, is captured in an Effective low energy Hamiltonian, by a systematic truncation or elimination of the higher energy degrees of freedom.

There are many ways of realizing emergent degrees of freedom. An interesting place to look for them is in frustrated magnets. Frustrated magnets have an extensive ground state degeneracy and therefore lack long range magnetic order. The $S = 1/2$ Heisenberg Hamiltonian on the Kagome lattice has emergent spinon degrees of freedom. Spinons are *fractional* excitations carrying the spin but not the charge of the electron. On the Kagome lattice they behave as Z_2 excitations[1] and therefore have a symmetry entirely different (although lower) than the parent Heisenberg Hamiltonian.

Yet another example of emergence in frustrated magnets are magnetic monopoles

in spin ice compounds[2, 3]. Spin ice is a classical state of Ising spins on a pyrochlore lattice with a large number of degenerate ground states, very similar to the frustration in the Kagome lattice. All ground state configurations correspond to a specific constraint imposed on each tetrahedra of the pyrochlore lattice. Violation of these constraints create tetrahedra with net "charges" or magnetic monopoles. The low energy description of spin ice is therefore in terms of emergent monopoles and power law interactions between them.

Presence of disorder also creates emergent spin degrees of freedom. A removed site or a vacancy was shown to have a local magnetic moment in the Kitaev model on the honeycomb lattice[4]. Presence of static or quenched disorder was also seen to give rise to novel low energy excitations in quantum $S = 1/2$ magnets, diluted to the percolation threshold, on the square lattice. Wang and Sandvik[5, 6] observed that the presence of sub-lattice imbalance: an excess of sites belonging to sublattice A(B) over sublattice B(A), in a local region of the cluster, could lead to local spin degrees of freedom. These local spin degree of freedom gave rise to singlet-triplet gaps much lower in energy than the typical gaps expected from quantum rotor excitations[5, 6, 7].

The spins arising out of local sub-lattice imbalance were shown to behave like emergent $S = 1/2$ spin excitations and, interacted with other similar degrees of freedom, through Heisenberg exchange couplings to give rise to an *anomalously* low in energy set of almost degenerate states called the Quasi Degenerate spectrum[7]. It is also known that Neel order survives on percolation clusters all the way up to the percolation threshold[8]. Diluted magnets therefore provide an example of emergent spin excitations with SU(2) spin rotational invariance arising in a Neel ordered background!

The purpose of this chapter is two fold. Firstly, we would like to test the machinery of Chapter 3 on diluted percolation clusters. The presence of geometric disorder on percolation clusters breaks translational symmetry and allows for non-uniform saddle point SBMFT solutions. Secondly, using SBMFT we want to characterize these emergent spin excitations and attempt to explain, at a mean field level, why each localized emergent moment arises and is associated with *anomalously* low energies.

The organization of the chapter is as follows: In Section4.2 we motivate the use of non-uniform SBMFT to study the nature of single particle bosonic excitations on diluted magnets. This set of single particle SBMFT modes and mean field parameters are provided an interpretation in Section 4.3. Section 4.4 provides an explanation for how strong non-linearities in the distribution of mean field parameters leads to an *anomalous* lowering of single particle bosonic frequencies and a localization of the corresponding wave-functions. In Section 4.5, we relate the number of low energy modes in SBMFT to the dangling spin count on the cluster. Section 4.6 shows the failure of Linear and Hartree-Fock Spin Wave theory to capture the *anomalous* excitations seen within SBMFT. Section 4.7 puts SBMFT calculations on diluted magnets on a solid footing by benchmarking the calculations against exact numerics. Section 4.8 extends the scope of SBMFT, beyond being able to replicate ground state properties, to probe excited states using the Single Mode Approximation. The Conclusion of the chapter is provided in Section 4.9 .

4.2 Using SBMFT to probe emergent moments

In this section we provide a brief recap of important results required to understand the emergent spin excitations on diluted magnets and also provide motivation for using SBMFT as a tool for probing these excitations.

We begin by showing a typical percolation cluster with local regions with sublattice imbalance. Figure4.1 shows a Bethe lattice cluster obtained by diluting a regular Bethe lattice, with coordination three, up to the percolation threshold p_c for the Bethe lattice. The cluster is bipartite as shown by the red (sublattice A) and blue (sublattice B) coloring of sites. The figure also shows two regions encircled in brown contours where there is an excess of sites belonging to one sublattice over sites belonging to the other kind of sublattice. The excess spin, indicated by blue(up) and red(down) arrows, is left unpaired or dangling on the cluster. Each encircled local region is the center of an emergent spin excitation which was shown to have the quantum numbers of a SU(2) magnet[7].

Numerically exact DMRG calculations[7] showed that locally balanced parts of the cluster were strongly dimerized. Presence of strong dimerization leads to exponentially decaying spin-spin correlations and these parts of the cluster should therefore be magnetically disordered. In fact, within DMRG it was shown that several kinds of modes associated with a dangling spin were found to decay exponentially as one moved away from the dangling centers in to the locally balanced regions. Thus, each emergent local moment is effectively disconnected from the cluster and a network of such moments interact via exponentially decaying Heisenberg couplings[7].

A good mean field description of these emergent spin excitations, therefore,

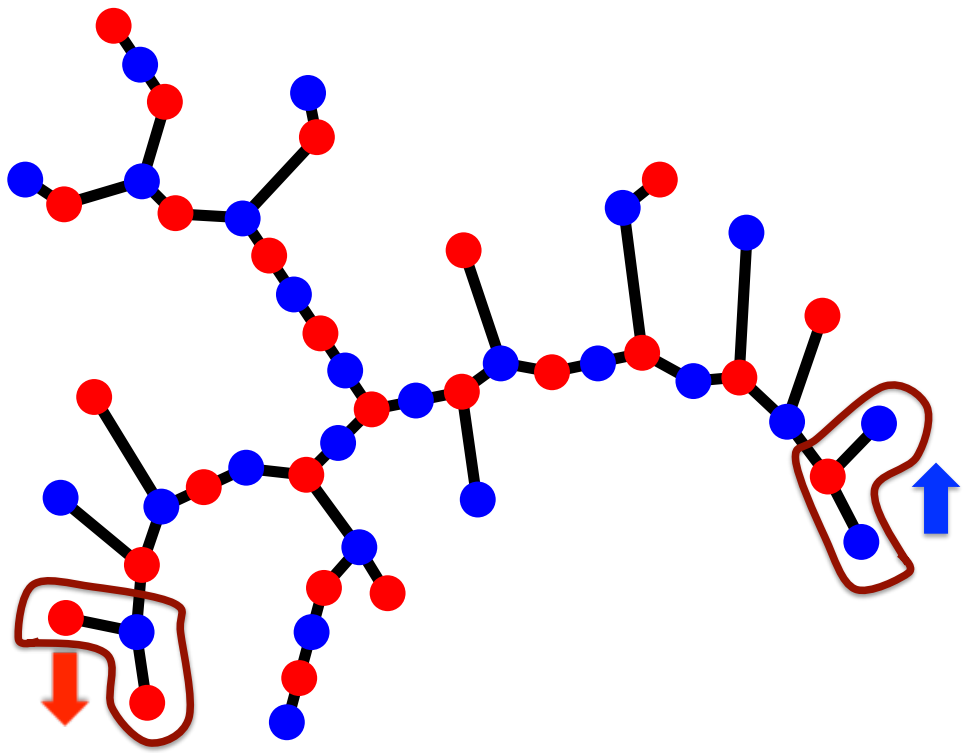

Figure 4.1: Bethe lattice percolation cluster with two dangling spins. The cluster has $N_s = 50$ sites and is bipartite as shown by the red (sublattice A) and blue (sublattice) coloring of sites. Two regions with local sublattice imbalance - excess number of sites belonging to one sublattice over the other sublattice, are shown encircled in brown contours. The excess dangling spin in each locally imbalanced region is shown by arrows. The color of the arrows indicates the excess sublattice type of the imbalance in each dangling region

needs to answer three important questions. Firstly, it needs to explain the *anomalous* lowering of energies associated with each such local moment. Secondly, it needs to capture the co-existence of these local dangling degrees of freedom with locally balanced regions on the cluster, which exhibit strong nearest neighbor spin dimerization. And, finally, the mean field theory also needs to provide a framework for the role that these emergent spin excitations play in the

propagation of long range Neel order on the cluster[8]. We will now show that Schwinger Boson Mean Field theory (SBMFT) offers a single unified framework for answering all three questions.

The rotational symmetry of SBMFT is expected to play a crucial role in the characterization of emergent spins since we already know that each local moment has an emergent SU(2) symmetry in a Neel ordered background. An SBMFT perspective on the dangling spins will be to associate an *anomalously* low frequency and a corresponding localized mode with every local emergent degree of freedom. The localized bosonic mode with an almost zero frequency is the signature of a local Bose condensate[9].The set of bond parameters $\{Q_{ij}\}$ are directly proportional to the spin-spin correlations and will therefore provide a distinction between locally balanced regions from regions with sublattice imbalance. Finally, on clusters with long range magnetic order, bosons condense in to the lowest single particle SBMFT mode(s), and the spatial profile of these mode(s) on the lattice will provide direct evidence for the role that different spins on the cluster play in the existence of long range order.

4.3 SBMFT parameters and single particle modes

In this Section we use the SBMFT machinery, developed in Chapter 3, to find non-uniform SBMFT solutions on percolation clusters. We show that the emergent moments have well defined characteristic signatures in the single particle frequencies and spatial mode profiles within SBMFT. We show that these signatures are generic to both Bethe and square lattice percolation clusters. The organization of this Section is as follows: in Section 4.3.1 we introduce the map-

ping of the Heisenberg spin half to two flavors of bosons[10] via SBMFT, we then outline the optimization details for finding non-uniform solutions to the SBMFT equations on percolation clusters in sub-section 4.3.2 and finally, in sub-section 4.3.3, we show the nature of single particle SBMFT frequencies and modes on both Bethe and square lattice percolation clusters.

4.3 .1 Mapping Heisenberg Hamiltonian to a bosonic mean field Hamiltonian via SBMFT

This Section is a brief recap of Section 3.2 about setting up the Schwinger Boson mean field equations. The nearest neighbor spin half Heisenberg antiferromagnet is mapped to two flavors of bosons via (3.2). The resulting bosonic Hamiltonian is quartic in the bosonic operators and is decoupled by extending the number of flavors of bosons from two to N, and in the limit of large N, using $1/N$ as a small expansion parameter, the SBMFT Hamiltonian is given by:

$$\mathcal{H}^m_{MF} = \boldsymbol{\beta}^\dagger \begin{pmatrix} \mathbf{\Lambda} & \mathbf{Q} \\ \mathbf{Q}^\dagger & \mathbf{\Lambda} \end{pmatrix} \boldsymbol{\beta} + \frac{1}{J}\sum_{i<j} |Q_{ij}|^2 - \left(S + \frac{1}{2}\right)\sum_i \lambda_i \tag{4.1}$$

where $\boldsymbol{\beta}$ is a vector given by $\boldsymbol{\beta}^T = (b_{1m}, ..., b_{N_s m}, b^\dagger_{1m}, ..., b^\dagger_{N_s m})$. The matrix $\mathbf{\Lambda}$ is diagonal in the site basis with entries given by Lagrange multipliers $\mathbf{\Lambda}_{ij} = \lambda_i \delta_{ij}/2$ which enforce the 'number constraint' on the bosons $\sum_m \langle b^\dagger_{im} b_{im}\rangle_{MF} = NS$, which is only satisfied on *average* [1]. The matrix $\mathbf{Q}$ has entries that are all off

[1]This maps the Hilbert space of the spin operator to that of the bosons. Boson number fluctuations about the average constraint of NS bosons per site lead to *spurious* factors of $3/2$ in spin-spin correlations [11]

diagonal and given by $Q_{ij} = J\sum_m \langle b_{im} b_{jm}\rangle$[2]. The mean field solution is a self-consistent solution in the $\{Q_{ij}\}$ meaning that the bond amplitudes input to the Hamiltonian(3.6) should agree with the amplitudes computed self-consistently, i.e. $Q_{ij} = \langle Q_{ij}\rangle$.

At the mean field level, all bosonic flavors (labeled by 'm' in (4.1)), are decoupled and the mean field Hamiltonian is given by N copies of the single particle Hamiltonian (4.1). Diagonalizing (4.1) gives rise to a set of single particle frequencies $\{\omega_n\}$ and modes $\{u_{in}, v_{in}\}$. The mean field energy, for each flavor m, is given by:

$$\langle \mathcal{H}^m_{MF}\rangle = e_{MF} = \sum_{n=1}^{N_s} \frac{\hbar\omega_n}{2} + e_{classical} \tag{4.2}$$

where the term $e_{classical}$ depends only on classical fields $\{Q_{ij}, \lambda_i\}$ and is given by:

$$e_{classical} = \frac{1}{j}\sum_{i<j} |Q^2_{ij}| - \left(S + \frac{1}{2}\right)\sum_{i=1}^{N_s} \lambda_i \tag{4.3}$$

We next discuss how to find self-consistent saddle point solutions, satisfying the constraints in (3.7), using the optimization techniques developed in Chapter 3.

[2]This expression for Q is only valid in the $SU(N)$ case where a sub-lattice rotation allows us to re-define the bond variables Q_{ij} such that the boson flavors decouple[10]

4.3 .2 Solving the SBMFT equations on a percolation cluster

We now provide some specific implementation details for applying non-uniform SBMFT mechanism of Chapter 3 to percolation clusters. We make the assumption of retaining only nearest neighbor bond amplitudes Q_{ij} (3.7),(4.1) and set all other bond variables to zero. This assumption on the bond variables, as we will see, is going to make longer distance correlations less accurate compared to shorted ranged spin-spin interactions, this *assumption* also reduces the number of mean field parameters and leads to faster convergence of the optimization algorithm. For small clusters of size $N_s = 20$, we retain all possible bond amplitudes and verify that truncation to nearest neighbor bond amplitudes does not *qualitatively* change the longer ranged correlations. Finally, the absence of loops on Bethe lattice percolation clusters, allows us to choose all bond variables to be real.

All initial starting guesses to the optimizer are completely unbiased and we do not make any assumptions on the distribution of the mean field parameters based on lattice symmetries or otherwise. As argued earlier, the lack of loops on the Bethe lattice percolation clusters also allows us to choose all $\{Q_{ij}\}$ to be real. The optimizer is run on an ensemble of clusters drawn from the percolation threshold with a $\epsilon_\lambda = 10^{-19}$, $\epsilon_Q = 10^{-16}$. We next look at the optimized saddle-point solutions obtained by the optimizer.

Before discussing the optimizer results we briefly comment on the delicate interplay involved in trying to minimize the mean field energy e_{MF}(3.11),(4.2) as a function of the variational parameters $\{\lambda_i, Q_{ij}\}$. e_{MF} can be expressed as a sum of the quantum zero point energies obtained by summing over vacuum fluctuations of the quasiparticle modes and a classical term $e_{classical}$ (4.2),(4.3).

We will now show that the quantum and classical parts of the mean field energy compete in the choice of the mean field parameters.

The quantum zero point energies want to maximize the bond amplitudes and minimize the value of the Lagrange multipliers (4.1). To see this, we note that for a uniform one dimensional Heisenberg chain the frequencies are momentum dependent and given by $\omega_k = \sqrt{\lambda^2 - (zQ\cos k)^2}$, where z is the coordination number of the lattice ($z = 2$ for the chain) and λ and Q are the mean field parameters. A Taylor expansion in $x = Q^2/\lambda^2$ shows that $\omega_k \equiv \lambda - cQ^2/\lambda$ (c is a coordination dependent constant independent of λ, Q) and therefore zero point energies are minimized when Q is maximal and λ is minimal[3].

The classical term $e_{classical}$ (4.3), on the other hand, would like the Q to be minimal and the Lagrange multipliers to be maximum. Thus the quantum and classical contributions to the mean field energy (4.2) want to drive the mean field parameters in opposite directions and the optimal solution calls for a careful optimization of the variational parameters.

4.3 .3 SBMFT saddle point solutions on a percolation cluster

Fig. 4.2(a) shows the distribution of the mean field parameters for the $N_s = 50$ site percolation cluster of Fig.4.1. The thickness of the bonds is proportional to $Q^*_{ij} - \min\{Q^*_{ij}\}$ (we subtract off the minimum to increase the contrast between small and large bonds) and the radius of the discs is proportional to λ^*_i.

The distribution of $\{\lambda^*_i\}$ is proportional to the local coordination of every

[3]the dependence of ω_k on λ, Q changes for non-uniform percolation clusters, however for small six site 'bowtie' cluster we confirm that similar Taylor expansions can be carried out

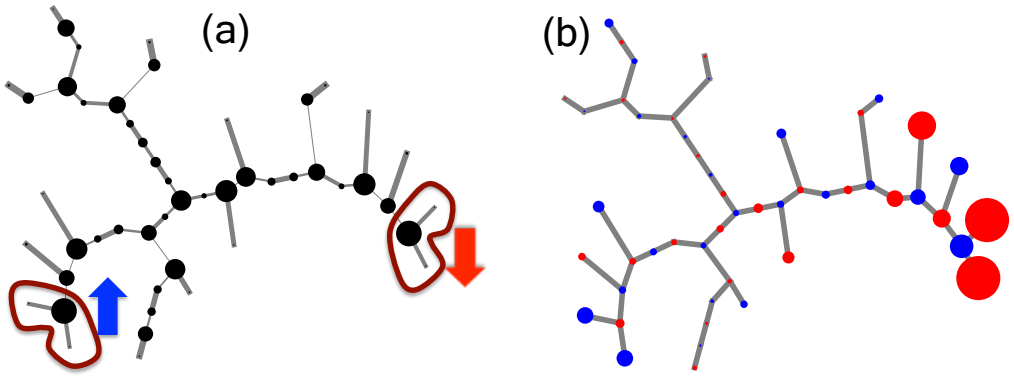

Figure 4.2: Distribution of mean field parameters and lowest wave-function on the Bethe lattice percolation cluster of Fig.4.1. (a) The Lagrange multipliers $\{\lambda_i^*\}$ are proportional to the radius of the discs and the thickness of the bonds is proportional to $Q_{ij}^* - \min\{Q_{ij}^*\}$. Three site regions containing dangling spins are encircled by brown contours. Small red and blue arrows show the sublattice type of each dangling spin (b) Amplitude of the lowest single particle wave function shown on the cluster with magnitude proportional to the radius of the discs. The sign of the wave function is encoded in the red and blue colors. The pattern is staggered

site: sites with coordination one have the smallest $\lambda_i^* \sim 0.5$ and sites with coordination three have the largest $\lambda_i^* \sim 2.5$, as can be seen in Fig.4.2. The $\{\lambda_i^*\}$ field acts like an on-site disordered potential for the bosons. The lowest single particle wave-functions avoid sites with the largest on-site potential. Fig.4.2(b) shows the lowest single particle eigen-mode, the radius of the discs is again proportional to the amplitude of the wave-function $\{u_{i0}, v_{i0}\}$ and the colors red(positive) and blue(negative) encode the sign of the wave function. Comparing Fig.4.2 (a) and (b) we can see that sites with the largest on-site potentials have the lowest amplitude of the single particle wave-functions. Bosons have the highest amplitude of being on sites with the lowest on-site potentials.

If the non-uniform Lagrange multipliers in SBMFT represent a disordered potential landscape for the bosons, what role do the bond amplitudes play?

The distribution of optimal $\{Q^*_{ij}\}$ is a prescription for identifying pairs of spins with the strongest spin-spin correlations. The nearest neighbor spin correlations are proportional to the pairing amplitudes: $\langle \mathbf{S}_i \cdot \mathbf{S}_j \rangle = 3Q^{*2}_{ij}/2$; therefore the mean field ground state exhibits strong dimerization (pairing of nearest neighbor spins in to singlets[4]). This is consistent with exact DMRG calculations[7].

The pattern of $\{Q^*_{ij}\}$ on the cluster provides a recipe for dimerizing spins on the lattice and locating sites with dangling spins. Bonds with the strongest amplitude of Q_{ij} are dimerized until we arrive at a maximal nearest neighbor dimer covering of the cluster. Sites with spins left unpaired or dangling are then the locations of the emergent degrees of freedom.

For example, carrying out the dimerization exercise for the cluster in Fig.4.2 pairs up all spins on the cluster except one spin each in the two encircled regions of three sites each. Each such region is called a 'fork' and has two 'tip' sites with coordination one and a 'mid-point' site with coordination three. The two tip sites are equivalent (related by reflection symmetry of the lattice) and therefore have equal bond amplitudes on links connecting the tip sites to the mid-point of the fork. However, a nearest neighbor dimerization can only include one of the tips leaving the other site unpaired or dangling. Thus each of the two encircled regions in Fig.4.2(a) contain one dangling spin. The dangling spins are on opposite sub-lattices, shown by red and blue arrows.

We will now show that each such emergent spin comes with a localized bosonic mode and an *anomalously* low frequency, which is much lower than the typical scale of frequencies on a cluster with no dangling spins. A single particle eigen-mode exponentially localized on the emergent spin is seen in Fig.4.2(b).

[4]The dimerization is not perfect on the Bethe lattice, the strongest dimer bonds have a spin-spin correlation of -0.67 compared to -0.75 for a perfect singlet state between two spins

The mode corresponds to the lowest single particle frequency ω_0 and has maximal amplitude on the dangling spin on the right fork of the cluster. The second highest mode on the cluster, ω_1, has a similar exponentially localized mode centered on the dangling spin in the left fork of the cluster. Each of the two lowest frequency mode amplitudes $\{u_{i0(1)}, v_{i,0(1)}\}$ decay exponentially as a function of the separation away from the dangling spins. These profiles are shown in Fig.4.3 where the mode amplitudes (magnitude) are plotted as a function of the separation away from the dangling centers.

The spatial profiles of the two lowest frequency SBMFT modes are expected to decay exponentially as a function of separation from the dangling spins. The reason is that as we move away from the dangling spin, the cluster becomes locally balanced and exhibits strong dimerization [7]. These "inert" parts of the cluster behave as though they were locally gapped - since it requires a finite energy to break the dimers and create a spin excitation. Any wave-function passing through these inert, gapped regions will decay exponentially.

The mode amplitudes are fit to an exponentially decaying function of separation away from the dangling spins, and the decay constants are extracted. Before doing the fit we address a special property of the eigen-functions. The eigenfunctions of the Schwinger boson Hamiltonian are of length twice the number of sites $2N_s$(3.17) and therefore we need to map it to a vector of length equal to the number of sites on the lattice N_s to obtain a *physical* mode. It is easy to show that the eigen-value equation(3.17) can be converted to a $N_s \times N_s$ matrix equation with eigenmodes of length N_s, given by linear combinations of $\{u_{in}, v_{in}\}$ and frequencies given by $\{\omega_n^2\}$[12]. In the case of the two lowest modes the linear combinations are trivial since these two wave-functions have the special

feature that $u_{in} = 0$ for $i \in$ sublattice B and $v_{in} = 0$ for $i \in$ sublattice A. Thus a mode vector $\psi_{n=0,1} = u_{in} \pm v_{in}$ (with normalization) is of length N_s and can be used to extract the decay constants. The magnitude of the mode amplitudes is fit to the following function:

$$\psi_{i,n} = c_n + a_n e^{-(d_i - d_n^*)/\xi_n} \tag{4.4}$$

where d_i is the distance away from the dangling spins located at d_n^*, $\{c_n, a_n, \xi_n\}$ are mode dependent coefficients[5]. The best fit curves to the mode amplitudes are shown in Fig.4.3 and corresponding values of the fit coefficients are shown in Table4.1. For both modes the fit coefficients are very similar and consistent with the (almost) symmetric geometric arrangement of the two forks with respect to the rest of the cluster.

A similar study of fitting the mode amplitudes to exponential functions can be carried out for an ensemble of clusters at the percolation threshold. Using the geometrical algorithm described in Chapter 3, we scan an ensemble of size $N_s = 50$ clusters and filter out clusters with two dangling spins. We then run the optimizer on these clusters and obtain the spectrum of single particle frequencies and eigen-modes. Each mode amplitude is fitted to an exponential function(4.4) and the decay constant extracted. The average decay constant over the entire ensemble of clusters is found to be $\langle \xi \rangle_{dis} \sim 3 \pm 0.2$ lattice spacings.

The decay constants ξ_n of approximately three lattice spacings is also close to the decay length scale of effective mediated interactions between the dangling

[5]The coefficient $c_n(N_s)$ is expected to scale with the system size and will be zero in the thermodynamic limit. The exact functional form of how $c_n(N_s)$ decays with the system size N_s is not known

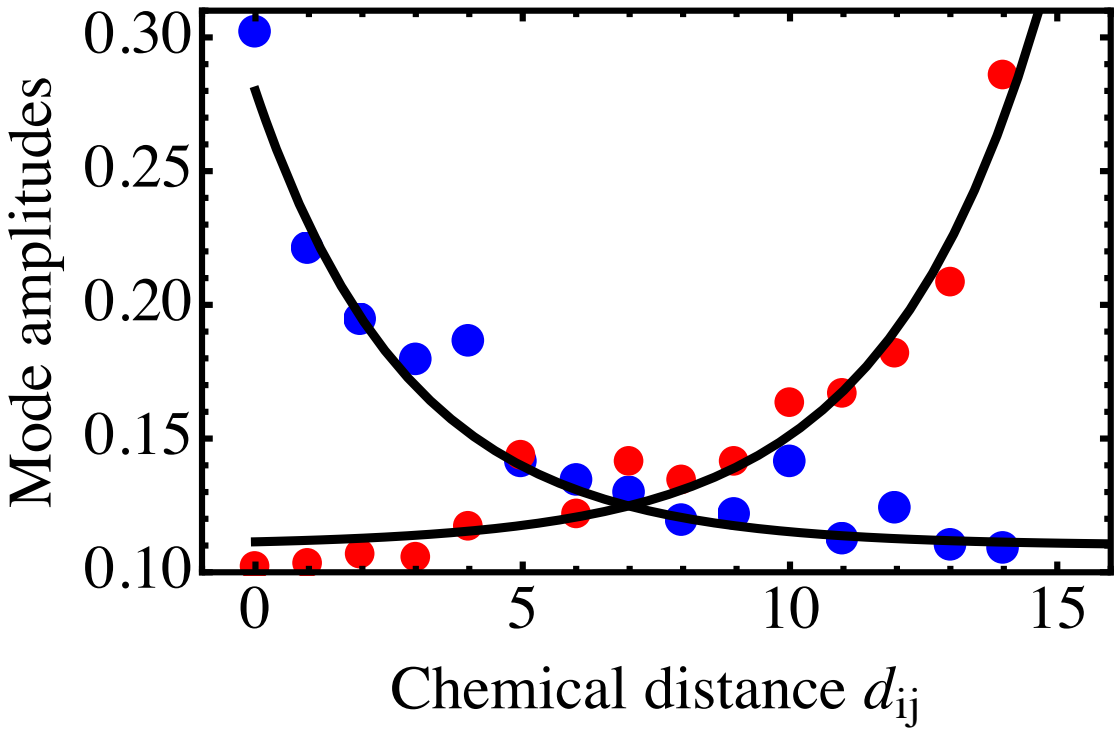

Figure 4.3: Spatial profile of the two lowest Schwinger boson modes for the 50 site cluster in Fig.4.2. The red and blue discs correspond to magnitude of mode amplitudes, at different separations, from the two dangling spins on the cluster. The spatial separation is called the 'chemical distance' and corresponds to the shortest length path between a site i, with mode amplitude ψ_i, and the dangling spin j on the cluster. The lines in black are exponential fits of the form (4.4) to the mode amplitudes. The best fit coefficients for the two modes are summarized in Table 4.1

spins[7]. Within SBMFT, effective interactions between emergent degrees of freedom arise out of spatial overlaps between their respective wave-functions. The decay constants of the single particle wave-functions should therefore be close to the decay scale of effective interactions between emergent spins. This is indeed found to be true. The disorder averaged decay length of single particle wave-functions of three lattice spacings is in agreement with the decay constant (~ 4.6) of effective mediated interactions[7].

We now turn our attention to the frequencies corresponding to the two low-

Modes	Frequency(J)	c_n	a_n	ξ_n
$n=0$	$\omega_0 = 1.17 \times 10^{-3}$	0.11	0.18	2.86
$n=1$	$\omega_1 = 3.81 \times 10^{-3}$	0.11	0.16	2.96

Table 4.1: Table showing the best fit parameters for exponential curve fits to the two lowest Schwinger boson mode amplitudes for the $N_s = 50$ site cluster shown in Fig.4.2.From left to right: the mode index number sorted from lowest to highest according to frequency, the frequency $\omega_{0,1}$ corresponding to the mode number $n = 0, 1$ in scales of $10^{-3}J$, the constants c_n, a_n and the decay constants ξ_n are defined in (4.4) and are in units of the lattice spacing. The frequency of the next higher energy SBMFT mode is $\sim 0.026J$

est single particle modes. Fig.4.4(1) shows the spectrum of single particle energies (in units of the Heisenberg coupling constant J). The energies span across three orders of magnitude with the two lowest energies an order of magnitude below the rest of the spectrum, as can be seen in Fig.4.4(2). Thus, each dangling spin on the cluster comes with a localized bosonic mode and an *anomalously* low single particle frequency. What do the modes corresponding to higher frequencies look like on the cluster?

Fig.4.5(b),(c) and (d) show some of the eigen-modes on the lattice corresponding to higher frequencies. These higher energy modes are different than the two lowest Schwinger boson modes in three important ways. Firstly, as is also seen from a comparison of Fig.4.5(a) with Fig.4.5(b),(c),(d), the higher energy modes are more localized. To make this statement more quantitative, we calculate the Inverse Participation Ratio (I.P.R.) [12] of the modes and find that generically, the lowest energy modes have the smallest I.P.R. Secondly, the higher energy modes, unlike the two lowest energy wave-functions, do not have a staggered sign pattern of the wave-function amplitudes. For example, the excited state mode in Fig.4.5(d) has opposite signs of the wave functions on sites belonging to the same sublattice. We will discuss these properties of the modes in greater detail in Section 4.5 . Finally, as is again seen in Figure 4.5(d), the

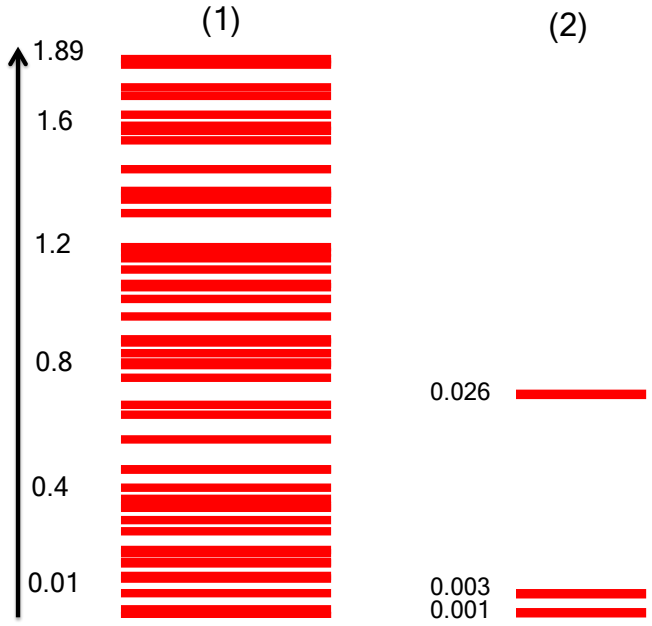

Figure 4.4: Single particle frequency spectrum of SBMFT frequencies for the 50 site cluster, shown in Fig. 4.2. Each frequency is shown by a horizontal red line. (1) The entire frequency spectra (2) three lowest frequencies, the scale for (2) is different than the scale for plotting frequencies in (1). Modes corresponding to the two lowest frequencies in (2), are shown in Fig,4.3. All frequencies are in units of the uniform Heisenberg exchange coupling J.

higher energy modes do not show high amplitudes on sites with dangling spins.

Diluted square lattices also have an *anomalously* low frequency localized mode for every dangling spin on the cluster. The association of a localized mode and a low frequency is generic to diluted square lattices as well. Fig.4.6(a) shows the distribution of mean field parameters on a diluted square lattice with two dangling spins shown by closed brown contours. A comparison with Fig.4.2(a) shows that the tip sites in each fork on the square lattice have small on-site potentials compared to the fork mid-points, very similar to the Bethe percolation cluster of Fig.4.2. The lowest eigen-mode shown in Fig.4.6(b) is again lowered an order of magnitude compared to the rest of the single particle spectrum. The mode has a staggered sign pattern and has maximal amplitude on the dangling

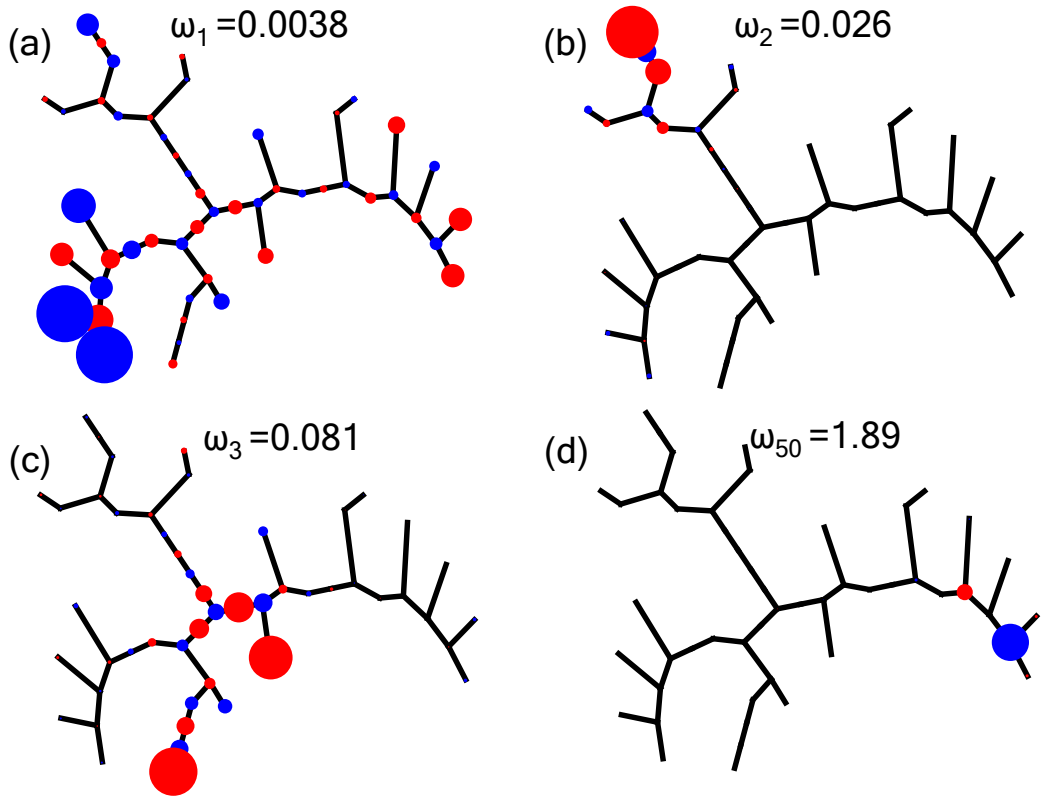

Figure 4.5: Eigen-modes corresponding to different frequencies on the Bethe lattice of Fig.4.2. In each case the radius of the discs is proportional to the amplitude of the modes and the color encodes the sign of the wave-function. (a) is the second lowest energy mode and has maximal amplitude on the dangling site, (b),(c): the next two higher (than (a)) energy modes. (d): The highest frequency mode on the lattice. The wave-function has opposite signs of the amplitudes on sites belonging to the same sub-lattice. This is in contrast to the low energy mode (a) where the sign pattern is staggered

sites similar to the low energy modes on the Bethe lattice in Fig.4.2(b).

Having established the correspondence between localized emergent moments on percolation clusters and their SBMFT characterization through localized modes and *anomalously* lowered frequencies, we now go on to provide, in greater detail, an interpretation of the mean field parameters and show how strong non-linearities in their (mean-field parameters) distribution creates localized single

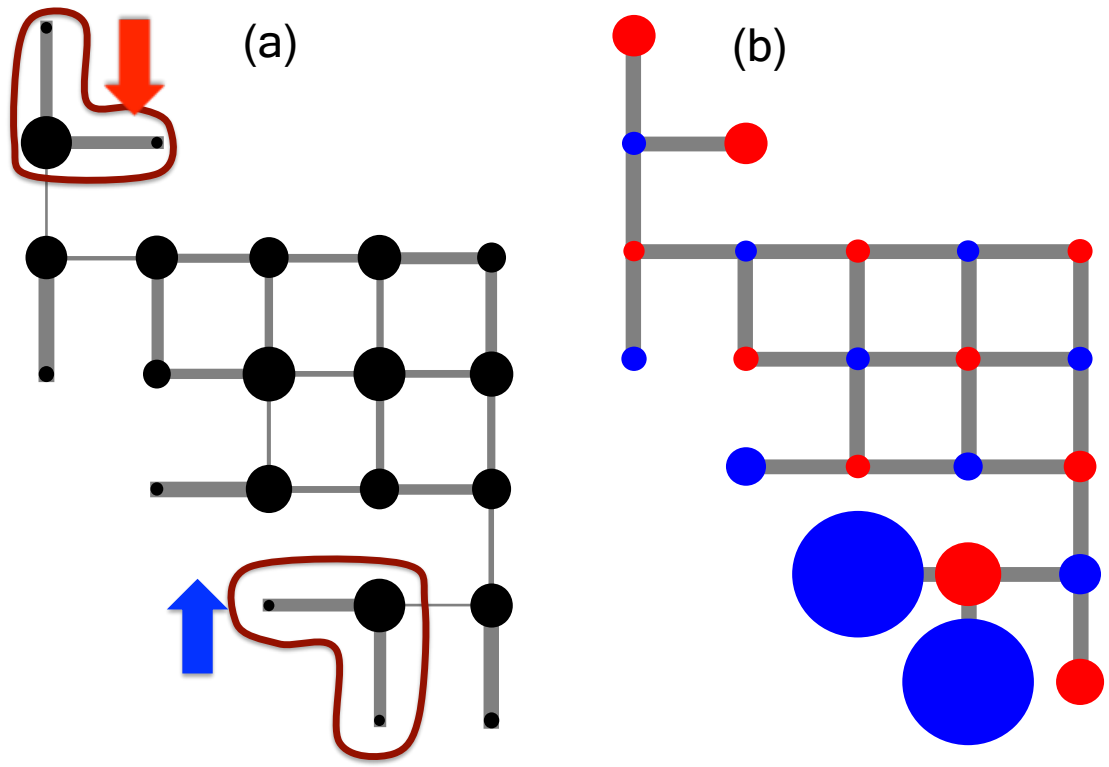

Figure 4.6: Distribution of SBMFT parameters $\{\lambda_i^*, Q_{ij}^*\}$ and the lowest eigen-mode on a 22 site diluted square lattice (a) Thickness of the bonds is proportional to the SBMFT bond variable: Q_{ij}^* and the radius of discs is proportional to the SBMFT Lagrange multiplier: λ_i^*. Brown contours enclose regions of three sites called 'forks'. Each fork contains a dangling spin. The sub-lattice type of the dangling spin is shown by small red and blue arrows beside the forks. (b) The lowest single particle eigen-mode. Area of discs is proportional to the mode amplitude on that site and the color encodes the sign

particle states.

4.4 A disordered potential landscape for the bosons

In this Section, we demonstrate how strong non-linearities in the mean field parameters leads to localized modes with *anomalously* low frequencies. Additionally, we also show that certain distributions of mean field parameters where

the difference between the bond amplitudes Q_{ij} on neighboring bonds is small, leading to a weakened dimerization, can lead to another kind of low energy excitation - a *delocalized* dangling spin. We also comment on the interactions between different dangling spins on the cluster and the effect of couplings between different emergent moments on the single particle spectrum.

The discussion in this Section is generic to both diluted Bethe and square lattices. Both of these lattices show a strong non-linearity in the distribution of optimal SBMFT mean field parameters. The single particle spectrum of SBMFT on both of these types of lattices shows almost zero frequencies with single particle modes that are exponentially localized around the dangling spin sites on the lattice.

Fig.4.2(a) and Fig.4.6(a) show strong non-linearities as a function of geometry, in the distribution of both mean field parameters λ_i^* and Q_{ij}^*, which is seen by the spread of large and small discs (with area proportional to λ_i^*) and the distribution of thick and thin bonds (thickness proportional to Q_{ij}^*) on the cluster. The geometry dependent variations in the mean field parameters are much stronger than on a regular lattice (like a uniform linear chain or square lattice) where all mean field parameters take uniform values. In the case of the Lagrange multipliers, presence of geometric disorder breaks equivalence between different sites on the lattice leading to strong non-uniformity in the λ_i^* field. In particular, as is evident from (3.5) the set of Lagrange multipliers $\{\lambda_i^*\}$ behave like an on-site potential for the bosons and therefore non-uniformity in the distribution of the Lagrange multipliers gives rise to a disordered potential for the bosons. We will now show that such a disordered landscape traps a localized eigen-mode.

Each of the two forks in Fig.4.2 and Fig.4.6 contains a dangling spin. As mentioned previously, the tip sites (coordination one) within the fork have $\lambda^*_{tip} \sim 0.5$ compared to the mid-point site, within the fork (coordination three), which has $\lambda^*_{mid} \sim 2.5$. Such a variation in the on-site potential, in moving from the tip site to the mid-point site within each fork, creates a local quantum barrier for a boson at the fork tip, leading to an evanescent eigen-mode as shown in Fig.4.2(b) and Fig.4.6(b). The localization length (or the decay constant) of such a mode can be expressed in terms of the height of the local quantum barrier and the frequency of the mode by solving the single particle Schrodinger's equation for the ground state wave-function of a particle in a quantum well[13]. The ground state wave-function decays exponentially in the classically forbidden region (outside the well) and has a decay constant $\xi \propto 1/\sqrt{V_0 - E_0}$, given in terms of the heigh of the barrier V_0 and the energy of the single particle mode E_0 ($E_0 < V_0$).

A similar analogy can be made for the single particle bosonic wave-function which has maximal amplitude at the fork tips and decays as we move away from the dangling spins. The barrier V_0 in this case is the difference in the on-site potentials at the fork mid-point λ_{mid} and the fork tip λ_{tip}, and the energy of the mode is just the single particle bosonic frequency ω_0. The decay length of the bosonic wave-function 4.3, analogous to a particle in quantum well, is given by $\xi_{\ell oc} \propto 1/\sqrt{(\lambda_{mid} - \lambda_{tip} - \omega_0)}$. Thus, localization increases with increase in the difference of the on-site potentials (Lagrange multipliers) at the fork tip and fork mid-point and also as the frequency of the mode is lowered. Thus a necessary, but by no means sufficient, condition for a site to have a non-zero density of dangling spins is to be a local minimum of the $\{\lambda^*_i\}$ field.

The set of bond amplitudes $\{Q^*_{ij}\}$, on the other hand, create a landscape for the bosons where local puddles of disorder coexist with locally ordered dangling regions. Since the strength of the bond amplitudes $\{Q^*_{ij}\}$ is directly proportional to the nearest neighbor spin-spin correlations: $\langle \mathbf{S}_i \cdot \mathbf{S}_j \rangle = 3Q^{*2}_{ij}/2$ (3.21), the presence of alternating strong and weak bonds in a local region of the cluster indicates strong nearest neighbor dimerization. Such regions are 'inert' and have an absence of dangling spins. Locally imbalanced regions on the other hand have a much weaker dimerization[6]. The bond amplitudes therefore present a picture where local emergent moments co-exist with dimerized regions. We will return to this picture in a later section when we discuss the propagation of long range order on the cluster.

Another kind of dangling spin excitation allowed by the distribution of the mean field parameters is a *delocalized* emergent moment. Delocalized moments occur in regions of the cluster where the gradient[7] in the on-site potentials is lower and differences between neighboring bond amplitudes smaller than in an inert locally balanced region. The local region over which the moment delocalizes has an overall net imbalance of sites belonging to one sublattice over sites belonging to the other sub-lattice.

The delocalization of the moment can be understood in a nearest neighbor dimerization picture. If a region of the cluster exists, where there are more than one maximal dimer coverings of the sites, then the emergent spin on an unpaired site can *hop* to another site belonging to the same sub-lattice, by a rearrangement of dimers. This rearrangement is possible when the dimerization is

[6]strong bond in inert regions of the cluster have a typical spin-spin correlation of $\sim 0.6J$ whereas bonds in the vicinity of an emergent spin have typical correlations of about $\sim 0.4J$

[7]gradient for the on-site potential is defined as the change in value of λ^*_i divided by the change in distance

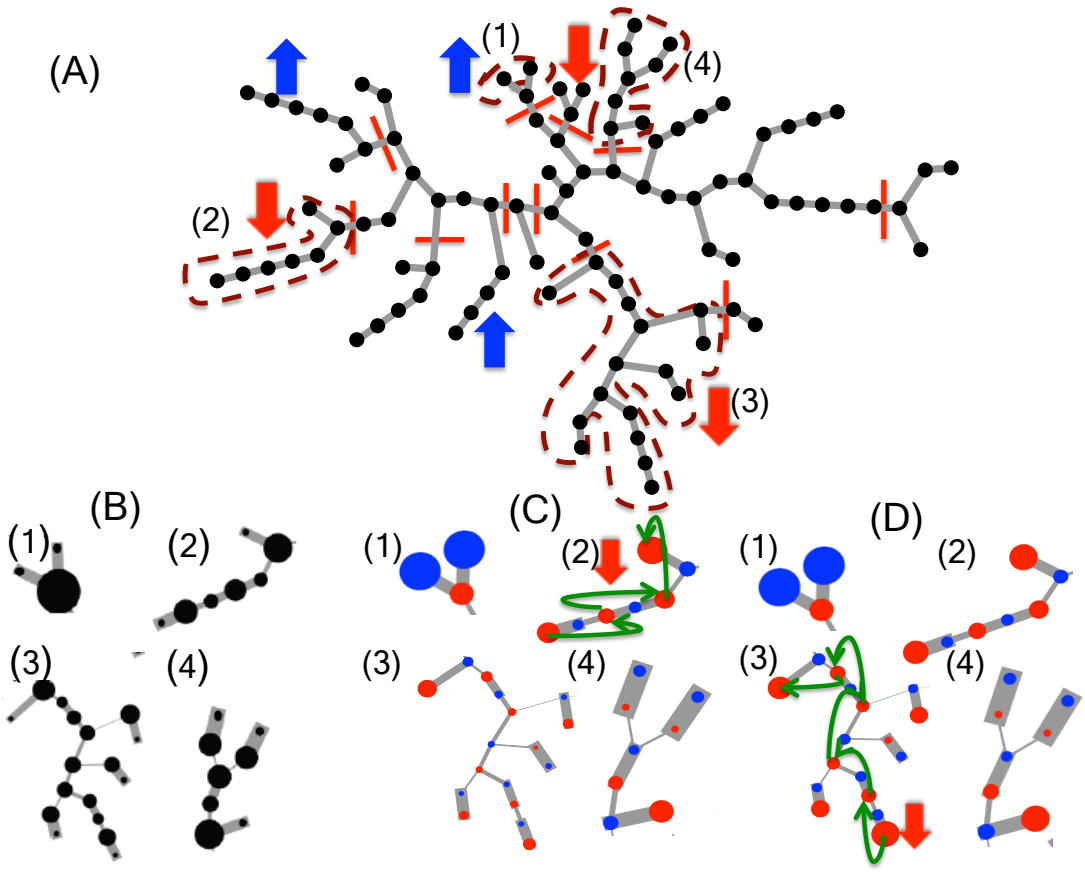

Figure 4.7: Schwinger Boson mean field parameters and lowest two eigen-modes on a $N_s = 100$ site Bethe lattice percolation cluster with six dangling spins. (A) Brown dashed contours encircling three dangling regions labeled (1)-(3). (4) is a locally balanced *inert* region. Red lines called 'prongs' break up the cluster in to smaller sub-clusters[7]. Red and blue arrows indicate the location and sub-lattice type of the dangling spin. (B) mean field parameters for the four regions in (A). The thickness of the bonds is proportional to Q^*_{ij} and the area of the discs is proportional to λ^*_i (C) Lowest eigen-mode on the four regions of (A). Region (2) in (C) shows a delocalized dangling spin with green arrows showing the sites it can *hop* to (D)Second lowest eigen-mode. Region (D)(3) shows another delocalized dangling spin. For both eigen-modes the amplitude of the discs is proportional to the wave-function and the color (red and blue) encode the sign of the wave-function

weak and there is no unique maximal dimer covering possible.

An easy way to visualize this is to consider a one dimensional open ended chain consisting of an odd number of sites, where the difference in the magnitude of nearest neighbor dimers is small and decreases as we go in to the bulk of the chain. This chain has an overall net imbalance of one and the weakened dimerization in the bulk allows a reshuffling of dimers, which makes the emergent moment *hop*. Such delocalized monomers were found to give rise to emergent spin one excitations by coupling strongly with another emergent moment residing on the same sub-lattice[7]. We now show a concrete example of a *delocalized* emergent moment.

Fig.4.7(A) shows a $N_s = 100$ site Bethe lattice percolation cluster at the percolation threshold. The cluster has six dangling spins located using the geometrical algorithm of Section 2.2. The red lines across bonds in (A) are *prongs*[7] which break up the cluster in to smaller sub-cluster. Each sub-cluster has a fixed monomer count i.e. the prongs divide up the cluster in to smaller regions which are independent with respect to monomer exchange. Three of the six regions containing a non-zero dangling spin count are encircled via brown dashed contours and labeled $(1) - (3)$. We will now tag the dangling spins in each of these three regions as *localized* or *delocalized*.

The dangling region (1) contains a dangling spin at the fork similar to the dangling spins seen earlier in Fig.4.2 and Fig.4.6. The dangling spin at the tips of the fork is completely localized due to a local quantum barrier formed by the mid-point of the fork as seen by the enhanced on-site potential at the fork mid-point in (B-1). Correspondingly, the bosons want to avoid sites with the largest on-site potentials and show large wave-function amplitudes at the fork tips and

small amplitudes at the fork mid-point in Fig.4.7 (C-1) and (D-1).

Regions Fig.4.7 (A-2) and Fig.4.7 (A-3), on the other hand, each contain a *de-localized* dangling spin. Within the sub-cluster Fig.4.7 (A-2) indicated by the dashed brown contour, the dangling spin is delocalized to effectively move along a one-dimensional chain with an odd number of sites. The bosonic wave-functions in Fig.4.7 (C-2) and (D-2) show alternating large and small amplitudes along the pathway. The high amplitudes are on the same sub-lattice (red) on which the dangling spin is delocalized to move. Fig.4.7 (C-2) shows the delocal-ization of the dangling spin through hopping arrows.

A similar delocalized dangling spin is found in region Fig.4.7(A-3) on the red sub-lattice. The mode amplitude for this delocalized dangling spin 'lights-up' in the second lowest eigen-mode on the lattice shown in Fig.4.7 (D-3). All sites belonging to the red sub-lattice over which the dangling spin can delocalize show high amplitudes compared to sites belonging to the other sub-lattice. One of the delocalization paths within the sub-cluster is shown by hopping arrows in Fig.4.7(D-3).

Both regions Fig.4.7 (A-2) and (A-3) show that dangling spins can delocal-ize over large parts of the cluster. Such delocalized dangling spins are more common than completely localized excitations (at the fork), as the cluster size increases. The presence of these delocalized excitations in the 'bulk'[8] of the per-colation cluster is contrary to earlier notions about quantum fluctuations being restricted to the 'edges' of the cluster[12].

Finally, region Fig.4.7 (A-4) is an example of a locally balanced inert sub-

[8]In a percolation cluster there is no sharp distinction between the bulk and the edge of the cluster. A typically rule of thumb is to label sites with coordination one as the edge and sites with coordination two and three as the bulk

cluster and does not have any dangling spins. The distribution of mean field parameters in Fig.4.7 (A-4) is as non-linear as other parts of the cluster with dangling spins, however, the lowest two bosonic modes Fig.4.7 (c4),(d4) do not show high amplitudes on sites within Fig.4.7 (A-4) compared to the regions Fig.4.7 (A-1)-(A-3) with dangling spins.

The presence of various kinds (both localized and delocalized) of dangling spin excitations on the cluster naturally brings up the question of the effect of interactions amongst emergent moments on the single particle frequencies and eigen-modes of the Schwinger boson spectrum. With this motivation in mind, we next discuss the correspondence between the number of dangling spins on the cluster and the number of low energy modes on the cluster.

4.5 Correspondence between dangling spins and low energy modes in SBMFT

In this Section, we show the correspondence between the number of dangling spins and the number of *anomalously* lowered SBMFT modes - modes with frequencies at least an order of magnitude below the rest of the spectrum. In Section 4.5.1 we devise a criterion for filtering the *anomalously* low energy frequencies from the SBMFT spectrum and show that there is a clear separation of energy scales between these *anomalously* low energy modes and the typical energies on the cluster. In Section 4.5.2 we show how interactions between dangling spins, and associated single particle modes, drives certain frequencies to *anomalously* low, almost zero values. These modes are identified as the finite size manifestation of Goldstone modes on the cluster. Furthermore, since these

Goldstone modes have maximal amplitudes only on the dangling spins, they also show the crucial role that emergent dangling degrees of freedom play in propagating long range order on the cluster.

4.5 .1 Filtering low energy modes from the SBMFT spectra

Starting from the simple example of two localized dangling spins on the clusters shown in Figs. 4.2 and 4.6, we observe that each dangling spin comes with a localized bosonic mode and an associated *anomalously* low frequency in the single particle SBMFT spectrum. This simple observation drives us to conjecture that the number of dangling spins must equal the number of low energy modes on the cluster. Indeed, we find a set of frequencies, typically in the range $10^{-2} - 10^{-3}J$ on clusters of size $N_s = 50$ sites Fig.4.4, which are lower than the typical range of frequencies $10^{-1} - 10^{0}J$ forming part of the continuum spectrum of single particle excitations on the cluster. We label this set of lowered frequencies $\{\omega_{\ell ow}\}$.

Fig.4.8 shows the spatial profiles of four modes belonging to the set $\{\omega_{\ell ow}\}$ for the $N_s = 100$ site Bethe percolation cluster of Fig.4.7. A comparison of the mode amplitudes in Fig.4.8 with the regions with a non-zero density of dangling spins in Fig.4.7 shows that all four modes have maximal amplitudes on the dangling sites. In addition, the mode corresponding to the lowest frequency ω_0 is staggered. We will return to this lowest energy mode later on in Section 4.5.2, when we discuss long range order on the cluster.

We outline a methodology for filtering $\{\omega_{\ell ow}\}$ set of frequencies from the single particle bosonic spectrum. In absence of a sharp distinction between the fre-

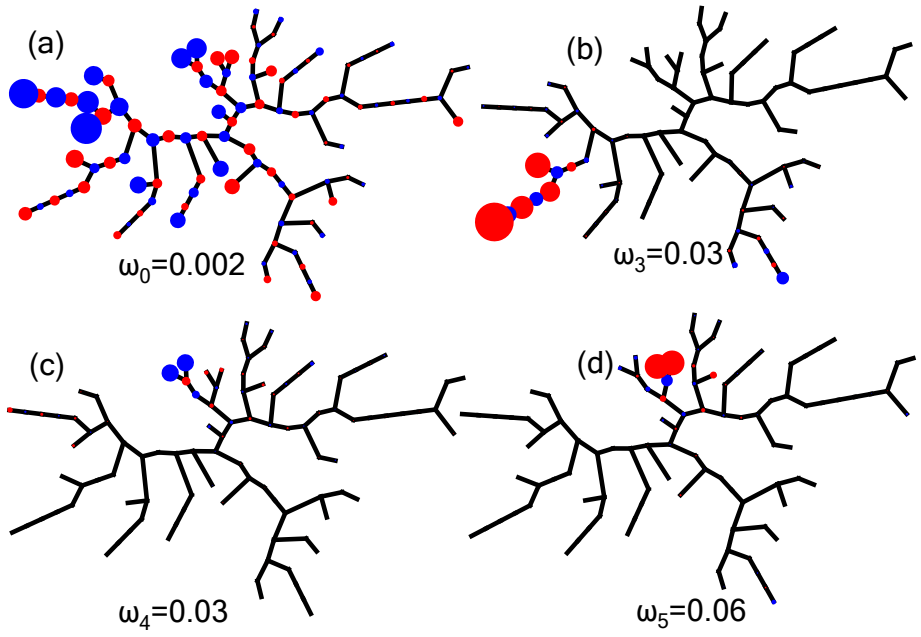

Figure 4.8: Single particle modes on a $N_s = 100$ site Bethe lattice cluster (same as in Fig.4.7). Four low energy modes are shown from the low frequency set $\{\omega_{low}\}$. For each mode the radius of the discs is proportional to the amplitude of the single particle mode and the color (red or blue) encodes the sign of the wave-function at that site. The frequencies of all four modes is given in units of the Heisenberg coupling constant J. All four modes show high amplitudes in regions with a non-zero density of dangling spins (compare with Fig.4.7(a) to find regions with a non-zero density of emergent moments). The lowest eigen-mode in (a) has a staggered sign pattern i.e. all sites belonging to sub-lattice A(B) have the same sign and opposite from all sites belonging to sub-lattice B(A)

quencies belonging to the set $\{\omega_{\ell ow}\}$ and the continuum spectrum, we devised the following criterion for filtering out $\{\omega_{\ell ow}\}$, i.e. determining a cluster dependent frequency cut-off such that frequencies below this cut-off form part of $\omega_{\ell ow}$ and frequencies above this cut-off are part of the typical frequency spectra on a locally balanced cluster. Given a frequency spectrum, we sort the frequencies in increasing order and compute successive single particle gaps between neighboring frequencies. The lowest frequency in the continuum set is the first frequency at which the gap is larger (typically by an *ad-hoc* factor of ten) than all previous gaps. This criterion is based on the observation from many-body calculations, where many-body gaps within the quasi-degenerate spectrum were smaller than the gap between the highest energy of the quasi-degenerate spectrum and the lowest energy of the Quantum rotor spectrum[7].

A good example of separation between $\{\omega_{\ell ow}\}$ and the continuum of frequencies is shown in Fig.4.4 where the two lowest frequencies belonging to $\{\omega_{\ell ow}\}$ have a gap of $\sim 2 \times 10^{-3} J$ and the separation between the highest frequency belonging to the set $\{\omega_{\ell ow}\}$ and the lowest frequency belonging to the continuum is $\sim 0.023 J$ - a factor of ten larger than the typical gap within $\{\omega_{\ell ow}\}$! Similar to many-body numerics, we can develop a measure to quantify the separation of the set of frequencies $\{\omega_{\ell ow}\}$ from the continuum higher energy spectrum.

Once we isolate the set $\{\omega_{\ell ow}\}$ from the SBMFT frequency spectrum, we can compute the mean frequency and the spread of the frequencies about the mean in $\{\omega_{\ell ow}\}$. The spread is quantified by the standard deviation $\sigma_{\ell ow}$ and we also compute a 'gap' $\triangle$ by taking the difference between the mean of frequencies belonging to the set $\{\omega_{\ell ow}\}$ and the lowest frequency outside the set $\{\omega_{\ell ow}\}$. This

gives us a measure:

$$r = \langle \sigma_{\ell ow} / \triangle \rangle_{dis} \tag{4.5}$$

The smaller the value of r (4.5), the sharper is the distinction between the set $\{\omega_{\ell ow}\}$ and the continuum frequencies.

For an ensemble of size 400 of $N_s = 50$ site clusters we find $r = 0.26 \pm 0.1$. As a comparison, the same quantity, calculated in many-body numerics gave a value of $r_{DMRG} \sim 0.17$. We therefore conclude that while the distinction between the set $\{\omega_{\ell ow}\}$ of frequencies, lowered due to the presence of emergent moments on the cluster and the interactions amongst them, is blurrier than in the many-body case, such a distinction does exist.

4.5 .2 Interactions between dangling spins and Goldstone modes

We now explain what kind of interactions between dangling spins can drive r (4.5) to a higher value, reducing the sharpness of the distinction between the set $\{\omega_{\ell ow}\}$ and the continuum of single particle frequencies. Interactions between dangling spins belonging to different sub-clusters drives certain frequencies from the set $\{\omega_{\ell ow}\}$ to higher values, closer to the continuum spectrum. A way of understanding this is to use the prescription given by the geometrical algorithm in Section 2.2 and [7] to break up a large cluster in to smaller sub-clusters at the bonds indicated by the red lines called *prongs* in Fig.4.7(a). Each sub-cluster, as mentioned in Section 2.2 and [7], has a fixed number of dangling spins as we re-arrange dimers within the sub-cluster i.e. a dangling spin

on the sub-cluster cannot leave the sub-cluster and hop to another sub-cluster. Neither can dangling spins from other sub-clusters enter the aforementioned sub-cluster.

We carry out an SBMFT optimization on each of the mutually 'disconnected' (with regard to dangling spin exchange) clusters by weakening (or turning off) the coupling link across the bond that cuts the prongs. The result of the optimization is going to give us a single lowered frequency and a corresponding mode that has higher amplitude on the sites with a non-zero density of dangling spins. In this artificial limit, the number of such *anomalously* low energy modes will (trivially) equal the number of dangling spins.

We now turn on the links between different sub-clusters by restoring the strength of the bonds cutting the prongs to their normal strengths (equal to the Heisenberg coupling J). Switching on these interactions is going to couple the emergent moments and drive certain frequencies from within the set $\{\omega_{\ell ow}\}$ to higher values. The strength of this interaction is going to decay as a function (roughly exponential) of the separation between the different moments. Thus the smaller the separation between two moments on the cluster, the larger the interaction and the greater the splitting. For this reason, clusters with delocalized dangling spins have a higher value of r and a blurrier distinction between $\{\omega_{\ell ow}\}$ and the continuum set of frequencies, because delocalization allows dangling spins to come closer together and interact. Similar pushing of energies out of the quasi-degenerate spectrum and in to the continuum Quantum rotor spectrum was seen in DMRG calculations[7].

Interactions between dangling spins not only drives certain single particle energies to higher frequencies but it also lowers the energy of certain modes.

In particular, the frequencies of two modes within the set $\{\omega_{low}\}$ are driven to *anomalously* low values (typically $\sim 10^{-3}J$ for $N_s = 50$ site clusters). The associated wave-functions are found to always have maximal amplitudes on the dangling spins and have a staggered magnetization pattern i.e. all sites belonging to sub-lattice A(B) have the same sign and opposite from the sign of sites belonging to the other sub-lattice B(A). We will now argue that these two *anomalously* low energy modes within SBMFT are the finite size manifestations of *Goldstone* modes on the cluster and signal the presence of long-range order on Bethe lattice percolation clusters[8].

As we argued in Chapter 3, long range order within SBMFT is associated with the closing of the single particle gap at particular places (usually high symmetry points in the zone) in the Brillouin zone. In the case of the one dimensional Heisenberg chain, we saw that when $\lambda = zQ$, the single particle frequencies became zero at the zone center $\mathbf{k} = 0$ and at the zone corner $\mathbf{k} = \pi$. These two wave-vectors are the polarization modes of gapless linearly dispersing excitations on the lattice called *Goldstone* modes. Goldstone modes are associated with the breaking of continuous SU(2) symmetry. Unlike ferromagnetic waves, the antiferromagnetic spin wave spectrum has two degenerate *Goldstone* modes corresponding to left and right circularly polarized light[10].

The two degenerate Goldstone modes signaling Neel order on a percolation cluster- a bipartite lattice, are defined by vectors $\boldsymbol{\eta}^{1,2}$ of length N_s (number of sites). The vector $\boldsymbol{\eta}^1$ has elements $\boldsymbol{\eta}^1_i = +1$ for $i \in$ sublattice A and $\boldsymbol{\eta}^1_i = -1$ for $i \in$ sub-lattice B. The vector $\boldsymbol{\eta}^2 = +1$ for all sites on the lattice. These two modes are orthogonal and on regular lattices (like the uniform one dimensional chain or the square lattice) they will have the sign pattern and the magnitudes

as defined by the vectors $\boldsymbol{\eta}^{1,2}$. However, on a non-uniform lattice, like a percolation cluster, we will find that the two lowest frequency modes, from within SBMFT, will have the same sign patterns as the vectors $\boldsymbol{\eta}^{1,2}$, but non-uniform amplitudes.

On finite clusters, the lowest frequency in single particle Schwinger boson spectrum has a finite size gap due to spin rotational invariance and is not zero. Long range order is therefore detected by studying the finite size scaling of the lowest frequency. If the lowest frequency ω_0 scales as $1/N_s$, it will vanish in the thermodynamic limit and bosons will condense in to the zero frequency mode. On the other hand, if the lowest frequency remains a constant as a function of increasing system size N_s, the single particle SBMFT spectrum is gapped and signals absence of long range magnetic order on the cluster.

On an ensemble of 400 clusters of size $N_s = 50$ sites, we verified the inverse scaling of the lowest SBMFT frequency ω_0 as a function of system size N_s. Thus, in the limit of infinite system size, the lowest SBMFT frequency will be driven to zero and bosons will condense in to this zero frequency mode. Presence of a Bose condensate signals long range order within SBMFT[9].

Once the two *anomalously* low frequencies from within SBMFT condense in the thermodynamic limit, we conjecture that the modes associated with these low frequencies must be the left and right circularly polarized Goldstone modes on the cluster. If this conjecture were to be true, then the two modes must correspond to a uniform and a staggered sign pattern - a signature of Goldstone modes on uniform lattices.

This is indeed found to be true and can be seen in Fig.4.8(a) which shows

the lowest frequency mode for a $N_s = 100$ site Bethe lattice percolation cluster. The mode is non-uniform with maximal amplitude on sites with dangling spins and has a staggered sign pattern. The other low frequency mode also has non-uniform amplitudes on different sites, but has a uniform sign on all sites. These two Goldstone modes are very different from the exactly zero energy *Goldstone* modes found within Spin Wave Theory, which have a uniform amplitude on all sites[12][9] within the cluster.

In *all* percolation clusters with a non-zero dangling spin count, the *two* lowest energy *Goldstone* modes always have maximal amplitudes on sites with a non-zero density of dangling spins. This is true even if the cluster has more than two dangling spins. In cases of more than two dangling spins, there will be a set of frequencies $\{\omega_{low}\}$ separated from the continuum of single particle frequencies on the cluster. Within this set $\{\omega_{low}\}$, the two lowest frequencies will be an order of magnitude lower than the rest of the frequencies in the set.

The presence of these twin *anomalously* low frequencies shows a crucial linkage between the presence of emergent dangling moments on the cluster and the propagation of long range order. More importantly, even within a dangling spin region, the wave-function amplitudes are maximal on sites belonging to the sub-lattice on which the dangling spin is confined to move. We will return to the propagation of long range order in the context of long distance spin-spin correlations, computed within SBMFT, in a later section.

The persistence of long-range order on percolation clusters up to the perco-

[9]Since the single particle spin wave spectrum vanishes at the zone center $\mathbf{k} = 0$ and the zone corner $\mathbf{k} = \pi$ the associated modes within Spin Wave Theory are given by $\psi_i \sim e^{i\mathbf{k}\cdot\mathbf{r}_i}$. The two modes have amplitudes $\psi_i = 1/\sqrt{N_s}$ (corresponding to the wave vector at the zone center) and $\psi_i = \eta_i/\sqrt{N_s}$ where $\eta_i = +1(-1)$ for $i \in$ sub-lattice $A(B)$ corresponding to the wave-vector at the zone corner

lation threshold[8] makes Linear Spin Wave Theory(LSWT) a natural (and much simpler than SBMFT) mean field framework to analyze low energy excitations on the cluster.

4.6 Failure of Spin Wave Theory

In this Section we use Spin Wave theory to probe the emergent spin excitations on percolation clusters and show that both Linear Spin Wave theory (LSWT) and Hartree Fock (LSWT + $1/S$ corrections) fail to capture the presence of emergent spins on the cluster. We first set the stage for Linear Spin Wave theory and discuss its implementation in detail. We next compare the single particle spectrum of LSWT with SBMFT and show that the LSWT spectrum fails to capture the *anomalous* lowering of single particle frequencies which in SBMFT was a smoking-gun signature of emergent spin excitations. We finally discuss the results of going beyond LSWT by addition of $1/S$ fluctuations and see a tendency of some high frequency modes being driven towards zero frequency.

4.6 .1 Linear Spin Wave Theory (LSWT)

In this section we develop implementation details of Linear Spin Wave Theory (LSWT) following the work of U.Hizi and C.L. Henley[14]. LSWT involves adding bosonic fluctuations about a classical ordered state in the form of spin waves. Unlike SBMFT, it requires *a priori* assumption of the ordered state about which the spin wave expansion is carried out. The LSWT formalism outline be-

low is applicable to any lattice, as long as we are expanding about a classical collinear state. In the case of the Bethe lattice percolation clusters, this ordered state is the up-down Neel antiferromagnet on the cluster. This classical state can be described by a vector $\boldsymbol{\eta}^T = (\eta_1, \eta_2, ..\eta_{N_s})$ where η_i are Ising variables taking values $\eta_i = +1$ for $i \in$ sub-lattice A and $\eta_i = -1$ for $i \in$ sub-lattice B.

The Heisenberg spin operators are mapped to Holstein-Primakoff[15] bosons via the transformation:

$$\begin{aligned} S_i^+ &\equiv \eta_i S_i^x + i S_i^y = \sqrt{2S - a_i^\dagger a_i} a_i \\ S_i^- &\equiv \eta_i S_i^x - i S_i^y = a_i^\dagger \sqrt{2S - a_i^\dagger a_i} \\ S_i^z &= \eta_i (S - a_i^\dagger a_i) \end{aligned} \tag{4.6}$$

The spin wave Hamiltonian is then obtained by expanding the square root under the assumption that the boson density per site $a_i^\dagger a_i \ll 2S$. To leading order it is convenient to express the spin wave Hamiltonian $\mathcal{H}_{SW}$ in terms of transverse (to the Neel order) spin deviation operators at every site: σ_i^x, σ_i^y. These transverse deviations are expressed in terms of the bosonic operators in the following way:

$$\begin{aligned} \sigma_i^x &= \eta_i \sqrt{\frac{S}{2}} (a_i + a_i^\dagger) \\ \sigma_i^y &= -i \sqrt{\frac{S}{2}} (a_i - a_i^\dagger) \end{aligned} \tag{4.7}$$

Finally, the spin wave Hamiltonian in terms of the transverse deviation operators can be expressed as:

$$\mathcal{H}_{SW} = -S \sum_{\langle i,j \rangle} \left[\eta_i \eta_j \sigma_i^x \sigma_j^x + \sigma_i^y \sigma_j^y + \eta_i \eta_j \left((\sigma_i^x)^2 + (\sigma_i^y)^2 \right) \right] \tag{4.8}$$

where we made us of the commutation relation $[\sigma_i^x, \sigma_j^y] = iS\eta_i \delta_{ij}$[14].

The spin wave Hamiltonian(4.8) can be more compactly expressed by defining vectors $\boldsymbol{\sigma}^T = (\sigma_1^x, \sigma_2^x, ..., \sigma_{N_s}^x, \sigma_1^y, \sigma_2^y, ..., \sigma_{N_s}^y)$ and the diagonal matrix $\boldsymbol{\eta}$ whose diagonal entries contain a $+1(-1)$ for sites belonging to sub-lattice A(B). The spin wave frequencies $\{\omega_{SW}^m\}$ and eigen-modes then satisfy the eigen-value equation:

$$\left(\frac{\omega_{SW}}{2S}\right)^2 \boldsymbol{\sigma} = \begin{pmatrix} (\boldsymbol{\eta}\mathbf{H})^2 & 0 \\ 0 & (\boldsymbol{\eta}\mathbf{H})^2 \end{pmatrix} \boldsymbol{\sigma} \tag{4.9}$$

where $\mathbf{H} = \mathbf{A} + \mathbf{Z}$. The matrix $\mathbf{A}$ is the adjacency matrix of the cluster with elements $\mathbf{A}_{ij} = 1$ for a connected bond and $\mathbf{A}_{ij} = 0$ for disconnected bonds. The matrix $\mathbf{Z}_{ij} = z_i \delta_{ij}$ is a diagonal matrix of the local coordinations z_i of every site on the lattice. Therefore, we need to diagonalize $\boldsymbol{\eta}\mathbf{H}$ to obtain the single particle spin wave frequencies and modes.

The matrix $\boldsymbol{\eta}\mathbf{H}$ is non-Hermitian and therefore the single particle modes obtained from diagonalizing it, will be non-orthogonal. To solve this problem of mode orthogonalization we note that if, $\mathbf{v}_m$ are the eigen-modes of $\boldsymbol{\eta}\mathbf{H}$ satisfying $\boldsymbol{\eta}\mathbf{H}\mathbf{v}_\mathbf{m} = \omega_\mathbf{SW}^\mathbf{m}\mathbf{v}_\mathbf{m}$, then the mode $\mathbf{H}^{1/2}\mathbf{v}_m$ is also an eigen-mode of the matrix $\mathbf{H}^{1/2}\boldsymbol{\eta}\mathbf{H}^{1/2}$. In addition, the matrix $\mathbf{H}^{1/2}\boldsymbol{\eta}\mathbf{H}^{1/2}$ is nicely Hermitian. We can use this property to orthogonalize the set of spin wave modes $\boldsymbol{v}_m$ by defining an inner product $(\mathbf{v}_m, \boldsymbol{\eta}\mathbf{v}_n)$ as follows:

$$(\mathbf{v}_m, \boldsymbol{\eta}\mathbf{v}_n) \equiv \mathbf{v}_m^\dagger \boldsymbol{\eta}\mathbf{v}_n = \frac{1}{|\omega_{SW}^m|}\mathbf{v}_m^\dagger \mathbf{H}\mathbf{v}_n = c_m \delta_{m,n} \tag{4.10}$$

Once we orthogonalize the modes following (4.10) we can proceed to diagonalize $\mathcal{H}_{SW}$ by introducing Bogoliubov quasi-particle operators $\alpha_m, \alpha_m^\dagger$ defined as:

$$\alpha_m = \frac{1}{2S|c_m|}\left[(\boldsymbol{\eta}\mathbf{v}_m)^\dagger \boldsymbol{\sigma}^x + i \text{ sgn } (c_m)(\boldsymbol{\eta}\mathbf{v}_m)^\dagger \boldsymbol{\sigma}^y\right] \tag{4.11}$$

where sgn(...) give the sign of the real number and the index m labels the spin wave modes. Substituting the Bogoliubov operators in to the Spin Wave Hamiltonian(4.8) gives us the diagonalized Hamiltonian in the quasiparticle basis:

$$\mathcal{H}_{SW} = \sum_m \omega_m \left(\alpha_m^\dagger \alpha_m + \frac{1}{2}\right) - SN_s \tag{4.12}$$

We can also compute various correlations like the boson density per site $\langle a_i^\dagger a_i \rangle$ and the spin-spin expectation $\langle \mathbf{S}_i \cdot \mathbf{S}_j \rangle$ in the ground state of the Spin Wave Hamiltonian at zero temperature. At zero temperature, the magnon occupation of the modes is zero and the only contribution arises from quantum zero point fluctuations. A crucial ingredient in computing spin-spin expectation value is the correlation matrix of transverse fluctuations $\mathbf{G}_{ij}$ given by $\mathbf{G}_{ij} = \langle \sigma_i^x \sigma_j^x \rangle = \langle \sigma_i^y \sigma_j^y \rangle$. We show below how to compute $\mathbf{G}$.

The correlation matrix of transverse fluctuations can be obtained by computing the expectation $\langle \boldsymbol{\sigma}^{x(y)} \boldsymbol{\sigma}^\dagger_{x(y)} \rangle$ by inverting the operator definitions in (4.11). In terms of the transverse fluctuations the Bogoliubov operators are given by:

$$
\begin{aligned}
\sigma_i^x &= \sum_m \sqrt{\frac{S}{2|c_m|}}(\alpha_m + \alpha_m^\dagger)\mathbf{v}_m \\
\sigma_i^y &= \sum_m \frac{1}{(i \text{ sgn } c_m)} * \sqrt{\frac{S}{2|c_m|}}(\alpha_m - \alpha_m^\dagger)\mathbf{v}_m
\end{aligned}
\tag{4.13}
$$

We can now proceed to compute the expectation $\langle \sigma_i^x \sigma_j^y \rangle$. The steps closely follow the evaluation of expectations in the vacuum of Schwinger bosons outlined previously(3.20). We express the transverse deviations in terms of the Bogoliubov quasi-particle operators using (4.13):

$$
\begin{aligned}
\mathbf{G}_{ij} &= \langle \sigma_i^x \sigma_j^x \rangle \\
&= \sum_{m,n} \sqrt{\frac{S}{2|c_m|}} \sqrt{\frac{S}{2|c_n|}} \langle (\alpha_m + \alpha_m^\dagger)(\alpha_n + \alpha_n^\dagger) \rangle \mathbf{v}_{mi} \mathbf{v}_{nj} \\
&= \sum_{m,n} \sqrt{\frac{S}{2|c_m|}} \sqrt{\frac{S}{2|c_n|}} \langle \alpha_n \alpha_m^\dagger \rangle \mathbf{v}_{mi} \mathbf{v}_{nj} \\
&= \sum_{m,n} \sqrt{\frac{S}{2|c_m|}} \sqrt{\frac{S}{2|c_n|}} \delta_{m,n} \mathbf{v}_{mi} \mathbf{v}_{nj} \\
&= \sum_n \frac{S}{2|c_n|} \mathbf{v}_{ni} \mathbf{v}_{nj}
\end{aligned}
\tag{4.14}
$$

where we again make use of the fact that the Spin Wave ground state is the vacuum of the Bogoliubov quasi-particles (magnons) and therefore the only non-zero operator expectation in (4.14) is $\langle \alpha_n \alpha_m^\dagger \rangle = \delta_{m,n}$. Having established the implementation details of Spin Wave theory we now proceed to compute the Spin wave spectrum numerically by building the adjacency and the local coordination matrices for a given percolation cluster and proceeding to diagonalize it to obtain the spin wave frequencies and modes. In the next sub-section we compare the spin wave spectrum and correlations with SBMFT results.

4.6 .2 Comparison of Linear Spin Wave results with SBMFT

Having established the framework for implementing Linear Spin Wave Theory on percolation clusters we now proceed to compare the spin wave spectrum with the Schwinger boson spectrum of excitations on the cluster. The main result of this sub-section will be to demonstrate the failure of Linear spin wave theory in capturing the *anomalous* lowering of energies that were characteristic of emergent spin excitations on the cluster.

Before comparing the spectra of single particle excitations within LSWT and SBMFT we first briefly comment on the LSWT Hamiltonian. The presence of quenched disorder enters the spin wave Hamiltonian at harmonic order through the site coordination matrix $\mathbf{Z}$, introduced in the previous sub-section. The matrix $\mathbf{Z}$ is completely analogous to the matrix $\mathbf{\Lambda}$ of on-site chemical potentials in the SBMFT Hamiltonian. In fact there is an exact mapping between the SBMFT and the LSWT Hamiltonians. The mappings $\mathbf{Z} \leftrightarrow \mathbf{\Lambda}$ and $\mathbf{A} \leftrightarrow \mathbf{Q}$ map the LSWT Hamiltonian to the SBMFT Hamiltonian and vice-versa. LSWT magnons therefore feel the presence of a disordered potential via the local coordination numbers of different sites.

We now proceed to do a direct comparison between the SBMFT and LSWT spectrum. A comparison of the single particle spectrum of excitations for the representative $N_s = 50$ site lattice of Fig.4.2 is shown in Fig.4.9. The SBMFT spectrum shows the presence of a couple of *anomalously* low energy frequencies with associated non-uniform single particle modes which are missing in the LSWT spectrum.

The LSWT spectrum has two *exactly* zero frequency uniform Goldstone modes

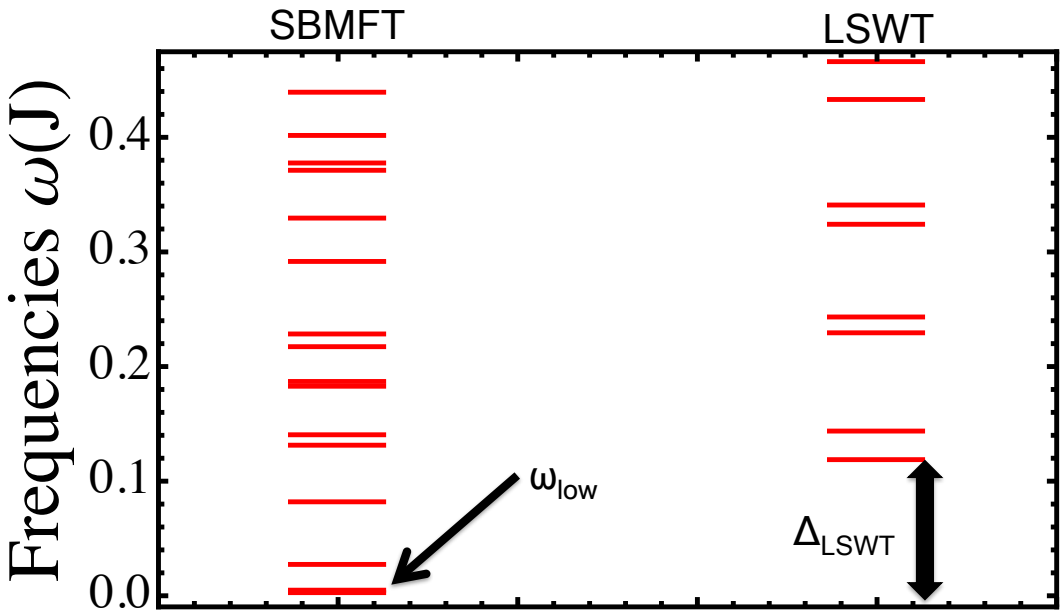

Figure 4.9: Comparison of single particle spectrum calculated within Linear Spin Wave Theory and SBMFT for the $N_s = 50$ site percolation cluster of Fig.4.2. Each single particle frequency is shown with a red horizontal line. A set of *anomalously* low frequencies in the SBMFT spectrum is marked $\omega_{\ell ow}$. The LSWT spectrum shows no such frequencies and lowest frequency is around $\sim 0.1J$. This gap in frequencies is indicated by $\triangle_{LSWT}$. All frequencies are in units of the Heisenberg exchange J. Also not shown in the figure are two exactly zero energy frequencies within LSWT(see text) corresponding to uniform modes

(corresponding to $\mathbf{k} = 0$ and $\mathbf{k} = \boldsymbol{\pi}$ polarizations) which are not shown in Fig. 4.9. These modes have a uniform amplitude on the cluster and treat all sites equivalently. These two Goldstone modes are therefore *opaque* to the presence of dangling spins on the cluster. The lowest energy mode in LSWT, shown in Fig.4.9, is of the order $\sim 10^{-1}J$ and shows maximal amplitude on sites belonging to an inert and locally balanced region of the cluster with no dangling spins.

This is in sharp contrast to the nature of low energy modes within SBMFT, which for the cluster of Fig.4.2, have two *anomalously* low energy modes with frequencies of the order $\sim 10^{-3}J$ and with associated wave-functions which are

non-uniform on the cluster and have maximal amplitudes within the dangling regions. The LSWT spectrum therefore seems to be *opaque* to the presence of emergent dangling moments on the cluster.

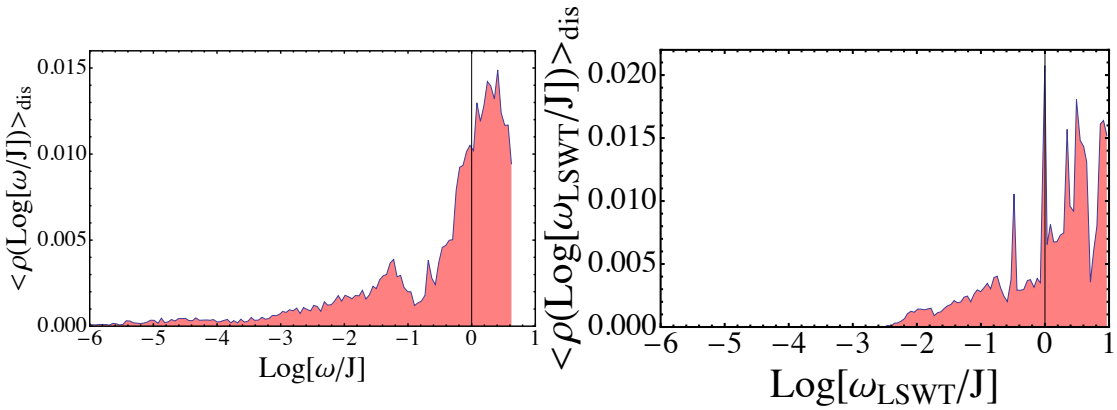

Figure 4.10: Comparison of disorder averaged single particle Density of States calculated from LSWT and SBMFT for an ensemble of 400 of size $N_s = 50$ percolation clusters. Left: The SBMFT density of states for frequencies ω plotted on a Log scale. The set of low energy frequencies coming from the presence of emergent spins on the cluster is seen in the low energy tail of the plot. Right: Density of States calculated within LSWT. For both panels, disorder averaging is done by aggregating frequencies from all clusters and binning them using a bin size. A simple arithmetic mean is then taken of frequencies in each bin to obtain the histograms. Histogram profiles are also ensured to have very low sensitivity to different bin sizes

The observation of the *anomalously* low energy modes, seen in SBMFT and missing from the LSWT spectrum, made for the single cluster in Fig.4.9, can be generalized to an ensemble of percolation clusters by calculating the disorder averaged single particle density of states. The single particle density of states $\rho(\omega)$ for a percolation cluster can be defined as:

$$\rho(\omega) = \sum_n \delta(\omega - \omega_n) \tag{4.15}$$

for a set of single particle frequencies $\{\omega_n\}$ obtained from within LSWT or SBMFT. For percolation clusters we also need to do a disorder averaging $\langle ... \rangle_{dis}$

of $\rho(\omega)$. This is carried out by taking an ensemble of 400 percolation clusters, each containing $N_s = 50$ sites, and calculating the single particle spectrum of excitations on each of the 400 clusters using LSWT or SBMFT. The list of all $400 \times N_s$ frequencies are aggregated[10], sorted and binned using a specific bin size ($0.008J$). Within each bin, we do a simple disorder averaging by taking the arithmetic mean of all frequencies within the bin. This procedure for disorder averaging gives rise to the histograms seen in Fig.4.10.

There are three critical observations to be made for the disorder averaged single particle density of states seen in Fig.4.10. Firstly, in the SBMFT spectrum there, very clearly, exists a low energy tail of frequencies missing from the LSWT spectrum. This tail of frequencies corresponds to the presence of emergent spin excitations on the cluster and it can be verified that all single particle wave-functions corresponding to the low energy tail of frequencies have maximal amplitudes on the dangling spins.

The second observation is about another property of the low energy tail of frequencies seen in the SBMFT spectrum in Fig.4.10. The tail is spread over low frequencies ranging across several orders of magnitude and indicates the absence of a missing length scale that can be associated with the spectrum of emergent spin excitations. In contrast, excitations on the cluster, with a well defined characteristic length scale, will have frequencies clustered around a characteristic frequency (roughly, the inverse of the length scale).

The absence of a missing characteristic length scale in the spread of the lowest frequencies, as we will now argue, is consistent with the presence of emer-

[10]We compute the Density of States for the Log of frequencies since for clusters with emergent spins, frequency spectrums have ranges spanning several orders of magnitude as can be seen from the low energy tail in Fig.4.10

gent modes on the cluster. A missing characteristic length scale indicates that the lowest energy modes are spread out across the entire cluster. These are precisely the Goldstone modes coming from interactions between emergent spins. At percolation, we expect the distribution of dangling regions to be more or less uniform and the lowest two single particle wave functions to spread out and 'light-up' in all such regions. Interactions between emergent spins prevents the Goldstone modes from being linked to specific dangling regions on the cluster and the Goldstone modes therefore do not have characteristic length scales (roughly of the size of the dangling regions). We also verify this prediction by calculating the Inverse Participation Ratio (I.P.R.)[12] for SBMFT modes on the cluster. The SBMFT Goldstone modes have the lowest I.P.R and are 'extended' on the cluster as opposed to the higher frequency SBMFT modes (typically $\sim 10^{-1} - 10^{0} J$) which have much higher I.P.R. and are localized.

Our final observation about Fig.4.10 is the sharp spike in the LSWT density of states at $\text{Log}(\omega_{SW}/J) = 0$ corresponding to $\omega_{SW}/J = 1$. This sharp feature in the LSWT density of state becomes sharper for larger system sizes. The modes corresponding to the unit frequencies are confined with amplitudes $\psi_i = \pm 1/\sqrt{2}$ on sites i that are the tips of forks on the cluster and strictly zero everywhere else. These modes arise out of an exact symmetry of the cluster under an interchanging of the two sites that are the tips of a fork. For example, for the $N_s = 50$ site cluster in Fig.4.2 the two unit frequency modes are each localized on one of the two forks and are antisymmetric with respect to amplitudes on the tips of the fork. These modes are a generic feature across percolation clusters with forks or dangling geometric features[12].

As we will see in the next sub-section, the frequency of these anti-symmetric

modes is lowered on adding $1/S$ fluctuations to LSWT. Based on this we conjecture that quantum fluctuations arising out of the presence of geometric disorder on the cluster drives the frequencies of precisely these anti-symmetric fork modes to *anomalously* low values. However, since these modes are anti-symmetric, the only way for them to be lowered to the symmetric Goldstone modes on the cluster, as in Fig.4.2(b), is for their frequencies to pass through zero. We see some evidence in support of this in the next sub-section.

Before ending this sub-section we make a technical observation about the validity of the Spin wave expansion(4.6) on the percolation cluster. Long range order has always been believed to be tenuous on the percolation cluster[16]. In other words, the order is barely able to survive on the cluster, especially close to the percolation threshold. The tenuous order has to do with strong quantum fluctuations on low coordination sites on the cluster. Within LSWT, a signature of these strong quantum fluctuations is the local boson number on every site. The larger the local boson occupancy, the smaller the local Neel moment, and the weaker is the order on the cluster. Typical values of the local boson occupation number are $\sim 0.7 - 0.8$ for $S = 1/2$ on coordination one and two sites for Bethe lattice percolation clusters. This value of the local boson occupancy barely meets the criterion of $\langle a_i^\dagger a_i \rangle \ll 2S$ valid for a spin wave expansion. It definitely suggests that we need to take in to account higher order finite spin size corrections to LSWT. These corrections are discussed in the next sub-section.

4.6 .3 $1/S$ corrections to Linear Spin Wave Theory

Presence of strong quantum fluctuations on low coordination sites requires corrections to the LSWT results of the previous sub-section. In this Section we take spin wave theory to the next higher order in the inverse spin size and find an Effective Hamiltonian quartic in the transverse fluctuation operators $\sigma_i^{x,y}$. We use Wick's theorem to decouple the quartic corrections and obtain a quadratic Hamiltonian at the mean field level. This Hamiltonian is called the Hartree Fock $\mathcal{H}_{HF}$ Hamiltonian. We discuss a methodology for self-consistently solving $\mathcal{H}_{HF}$ and compare the results obtained with exact DMRG and SBMFT calculations. We find that the Hartree-Fock Hamiltonian, like the LSWT Hamiltonian, fails to converge for $S = 0.5$. However, the self-consistent Hartree-Fock iterations significantly improve the spin-spin correlations (when benchmarked against exact DMRG numerics [7]). This confirms the presence of strong quantum fluctuations for $S = 0.5$ on a percolation cluster, and an improved (compared to LSWT) but failed attempt of Hartree-Fock theory to capture these fluctuations.

To obtain the quartic order Hamiltonian we take the mapping of the spin operators to the Holstein-Primakoff bosons to the next higher order in the bosonic operators by expanding the square-root(s) in (4.6). The resulting Hamiltonian, quartic in the bosonic operators $a_i, a_i^\dagger$, is expressed in terms of the transverse spin deviation operators $\sigma_i^{x,y}$ via the mapping (4.7). The resulting Hamiltonian $\mathcal{H}^{(4)}$ is given by,

$$
\begin{aligned}
\mathcal{H}^{(4)} &= \frac{1}{8S^2}\left(2\eta_i\eta_j\left(\left(\sigma_i^x\right)^2+\left(\sigma_i^y\right)^2\right)\left(\left(\sigma_j^x\right)^2+\left(\sigma_j^y\right)^2\right)\right) \\
&+\frac{1}{8S^2}\left(-\sigma_i^x\left(\left(\sigma_j^x\right)^3+\sigma_j^y\sigma_j^x\sigma_j^y\right)-\sigma_i^y\left(\left(\sigma_j^y\right)^3+\sigma_j^x\sigma_j^y\sigma_j^x\right)\right) \\
&+\frac{1}{8S^2}\left(-\sigma_j^x\left(\left(\sigma_i^x\right)^3+\sigma_i^y\sigma_i^x\sigma_i^y\right)-\sigma_j^y\left(\left(\sigma_i^y\right)^3+\sigma_i^x\sigma_i^y\sigma_i^x\right)\right) \qquad (4.16)
\end{aligned}
$$

Each term in the Hamiltonian $\mathcal{H}^{(4)}$ is quartic in the spin deviation operators and is therefore an interacting theory of magnons. A standard way to treat such Hamiltonians is to apply Wick's theorem to convert each four operator term in (4.16) in to a quadratic term. This results in two kinds of quadratic terms. The first kind re-normalizes the coefficients of the harmonic order spin wave Hamiltonian $\mathcal{H}_{SW}$(4.8) and the second kind of terms add new quadratic interactions to the spin wave Hamiltonian.

However, to carry out the following decoupling, we first need to compute expectations of the four spin operator terms in (4.16). The Wick's decoupling for (4.16) is similar to the analogous procedure carried out for computing spin-spin correlations in the Sp(N) phase of Schwinger bosons(3.21). Below, we give the Wick's decomposition results for the different quartic operators in $\mathcal{H}^{(4)}$, in terms of the correlation matrix of transverse deviation operators $\mathbf{G}_{ij} = \langle\sigma_i^x\sigma_j^x\rangle = \langle\sigma_i^y\sigma_j^y\rangle$:

$$
\begin{aligned}
\langle \sigma_i^x \sigma_i^x \sigma_j^x \sigma_j^x \rangle &= \mathbf{G}_{ii} \sigma_j^x \sigma_j^x + 4\mathbf{G}_{ij} \sigma_i^x \sigma_j^x + \mathbf{G}_{jj} \sigma_i^x \sigma_i^x \\
\langle \sigma_i^x \sigma_i^x \sigma_j^y \sigma_j^y \rangle &= \mathbf{G}_{ii} \sigma_j^y \sigma_j^y + \mathbf{G}_{jj} \sigma_i^x \sigma_i^x \\
\langle \sigma_i^y \sigma_i^y \sigma_j^x \sigma_j^x \rangle &= \mathbf{G}_{ii} \sigma_j^x \sigma_j^x + \mathbf{G}_{jj} \sigma_i^y \sigma_i^y \\
\langle \sigma_i^y \sigma_i^y \sigma_j^y \sigma_j^y \rangle &= \mathbf{G}_{ii} \sigma_j^y \sigma_j^y + 4\mathbf{G}_{ij} \sigma_i^y \sigma_j^y + \mathbf{G}_{jj} \sigma_i^y \sigma_i^y \\
\langle \sigma_i^x \sigma_j^x \sigma_j^x \sigma_j^x \rangle &= 3\mathbf{G}_{ij} \sigma_j^x \sigma_j^x + 3\mathbf{G}_{jj} \sigma_i^x \sigma_j^x \\
\langle \sigma_i^x \sigma_j^y \sigma_j^x \sigma_j^y \rangle &= \mathbf{G}_{ij} \sigma_j^y \sigma_j^y + \mathbf{G}_{jj} \sigma_i^x \sigma_j^x \\
\langle \sigma_i^y \sigma_j^y \sigma_j^y \sigma_j^y \rangle &= 3\mathbf{G}_{ij} \sigma_j^y \sigma_j^y + 3\mathbf{G}_{jj} \sigma_i^y \sigma_j^y \\
\langle \sigma_i^y \sigma_j^x \sigma_j^y \sigma_j^x \rangle &= \mathbf{G}_{jj} \sigma_i^y \sigma_j^y + \mathbf{G}_{ij} \sigma_j^x \sigma_j^x \\
\langle \sigma_j^x \sigma_i^x \sigma_i^x \sigma_i^x \rangle &= 3\mathbf{G}_{ji} \sigma_i^x \sigma_i^x + 3\mathbf{G}_{ii} \sigma_i^x \sigma_j^x \\
\langle \sigma_j^x \sigma_i^y \sigma_i^x \sigma_i^y \rangle &= \mathbf{G}_{ji} \sigma_i^y \sigma_i^y + \mathbf{G}_{ii} \sigma_i^x \sigma_j^x \\
\langle \sigma_j^y \sigma_i^y \sigma_i^y \sigma_i^y \rangle &= 3\mathbf{G}_{ji} \sigma_i^y \sigma_i^y + 3\mathbf{G}_{ii} \sigma_i^y \sigma_j^y \\
\langle \sigma_j^y \sigma_i^x \sigma_i^y \sigma_i^x \rangle &= \mathbf{G}_{ii} \sigma_i^y \sigma_j^y + \mathbf{G}_{ji} \sigma_i^x \sigma_i^x
\end{aligned} \tag{4.17}
$$

Using the expectations above we can now decouple (4.16) in to a quadratic theory. Plugging in (4.17) the above correlations in to (4.16) gives us:

$$
\begin{aligned}
\mathcal{H}^{(4)} = &\frac{1}{2S^2} \sum_{\langle i,j \rangle} \left((\eta_i \eta_j \mathbf{G}_{jj} - \mathbf{G}_{ij}) \left(\sigma_i^x\right)^2 + (2\eta_i \eta_j \mathbf{G}_{ij} - (\mathbf{G}_{ii} + \mathbf{G}_{jj})) \sigma_i^x \sigma_j^x \right) \\
&+ \frac{1}{2S^2} \sum_{\langle i,j \rangle} \left((\eta_i \eta_j \mathbf{G}_{ii} - \mathbf{G}_{ij}) \left(\sigma_j^x\right)^2 + (\eta_i \eta_j \mathbf{G}_{jj} - \mathbf{G}_{ij}) \left(\sigma_i^y\right)^2 \right) \\
&+ \frac{1}{2S^2} \sum_{\langle i,j \rangle} \left((2\eta_i \eta_j \mathbf{G}_{ij} - (\mathbf{G}_{ii} + \mathbf{G}_{jj})) \sigma_i^y \sigma_j^y + (\eta_i \eta_j \mathbf{G}_{ii} - \mathbf{G}_{ij}) \left(\sigma_j^y\right)^2 \right)
\end{aligned} \tag{4.18}
$$

The decoupled Hamiltonian $\mathcal{H}^{(4)}$ above is combined with the re-normalized quadratic Hamiltonian to give the Hartree-Fock mean field Hamiltonian $\mathcal{H}_{HF}$ which can be compactly expressed as:

$$\mathcal{H}_{HF} = \begin{pmatrix} (\boldsymbol{\sigma^x})^\dagger & (\boldsymbol{\sigma^y})^\dagger \end{pmatrix} \begin{pmatrix} \mathbf{H_{HF}} & \mathbf{0} \\ \mathbf{0} & \mathbf{H_{HF}} \end{pmatrix} \begin{pmatrix} \boldsymbol{\sigma^x} \\ \boldsymbol{\sigma^y} \end{pmatrix} \tag{4.19}$$

where the $N_s \times N_s$ matrix $\mathbf{H_{HF}}$ is given by:

$$(\mathbf{H_{HF}})_{ij} = \begin{cases} \mathbf{A}_{ij} \left(1 - \frac{1}{2S^2}(\mathbf{G}_{ii} + \mathbf{G}_{jj} - 2\eta_i\eta_j\mathbf{G}_{ij})\right) \text{ for } i \neq j \\ z_i + \frac{1}{S^2}\sum_j \mathbf{A}_{ij}(\eta_i\eta_j\mathbf{G}_{jj} - \mathbf{G}_{ij}) \text{ for } i = j \end{cases} \tag{4.20}$$

The Hartree Fock Hamiltonian above is quadratic in the transverse fluctuation operators and can be easily diagonalized once the matrices $\mathbf{Z}, \mathbf{A}, \mathbf{G}$ are known. The Hartree Fock frequencies and modes are the eigen-values and eigen-vectors, respectively, of the matrix $\boldsymbol{\eta}\mathbf{H}$.The Adjacency matrix $\mathbf{A}$ and the diagonal matrix of local coordination numbers $\mathbf{Z}$ are decided by the cluster geometry, therefore the only unknown is the matrix of transverse spin correlations $\mathbf{G}$. Furthermore, a self-consistent Hartree Fock solution will also satisfy the constraint $\langle \mathbf{G}_{ij} \rangle = \mathbf{G}_{ij}$. We therefore make an initial guess for $\mathbf{G}$ using linear Spin wave theory (or equivalently by taking the $S \to \infty$ limit in (4.20)). Once, an initial guess for $\mathbf{G}$ is obtained, we plug it in to (4.20), solve for the Hartree-Fock spectrum of frequencies and modes, re-evaluate $\mathbf{G}$ and plug in back in to (4.20). This iteration continues until we arrive at a self-consistent solution $\langle \mathbf{G}_{ij} \rangle = \mathbf{G}_{ij}$.

The Hartree Fock calculation does not converge to a self-consistent solution for $S = 0.5$. For an ensemble of size fifty clusters, we find several frequencies of the Hartree Fock Hamiltonian becoming imaginary for spin size equal to a half. We interpret this as an instability of the Hartree Fock Hamiltonian towards large spin fluctuations, which the Wick's decoupling is not able to capture.

In spite of the instability of the Hartree Fock calculation, we were able to measure spin-spin correlations in each cycle of the Hartree Fock calculation before the beginning of the instability. The agreement between Hartree-Fock computed spin correlations and exact numerical DMRG results is better than the agreement between the spin correlations from LSWT and DMRG.

The nearest neighbor spin-spin correlations are computed within Hartree Fock using the following expression:

$$\langle \mathbf{S}_i.\mathbf{S}_j \rangle = c + (2\mathbf{G}_{ij} + \mathbf{G}_{ii} + \mathbf{G}_{jj}) + \frac{2}{S^2}\left(\eta_i\eta_j\left(\mathbf{G}_{ii}\mathbf{G}_{jj} + \mathbf{G}_{ij}^2\right) - \left(\mathbf{G}_{ii} + \mathbf{G}_{jj}\right)\mathbf{G}_{ij}\right) \tag{4.21}$$

where c is a Spin length dependent constant given by $c = -S^2 - S + \eta_i\eta_j/4$. Fig. 4.11 shows nearest neighbor spin-spin correlations measured on the $N_s = 50$ site percolation cluster of Fig.4.2. The benchmark is the exact DMRG result[7]. The SBMFT result is able to replicate the qualitative behavior in most regions. The Hartree-Fock result is shown after a single self-consistent iteration. The iteration cycle was not able to proceed due to several frequencies, obtained from diagonalizing the Hartree-Fock Hamiltonian(4.20), becoming imaginary. We therefore show the correlations calculated using (4.21) after the first Hartree-Fock run. The Hartree-Fock calculation shows a significant improvement over LSWT in capturing the qualitative behavior of the correlations - in the figure we observe the DMRG troughs (crests), on most bonds, qualitatively agreeing with the Hartree-Fock troughs(crests).

Finally, we end this Section by highlighting the effect of Hartree-Fock calculation on the spectrum of single particle modes and frequencies, obtained

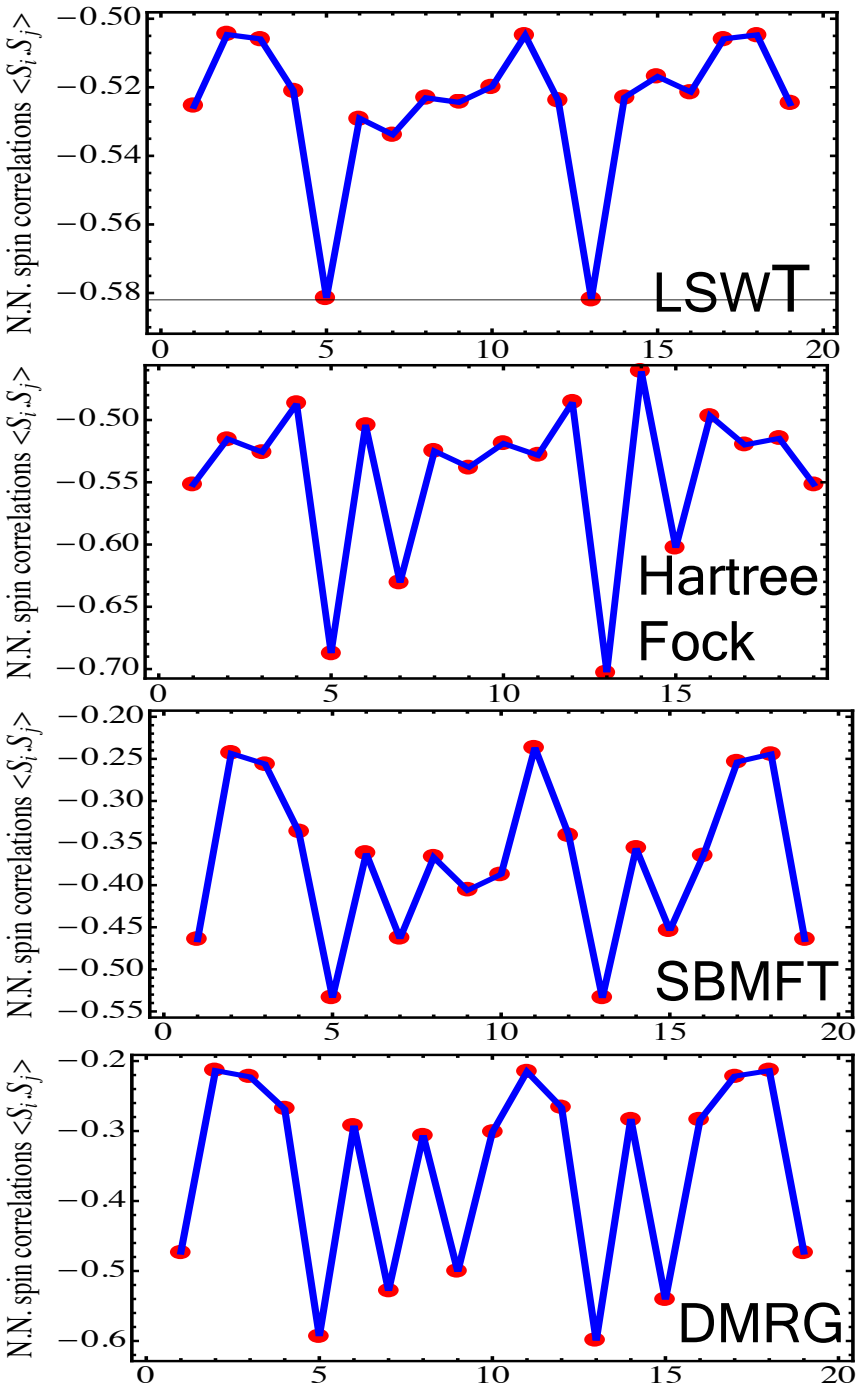

Figure 4.11: Comparison of nearest neighbor spin correlations computed within Linear Spin WaveTheory (LSWT), Hartree Fock, SBMFT and DMRG for the $N_s = 50$ site percolation cluster of 4.2. The bonds are along the shortest path connecting the two dangling spins. Hartree Fock calculation could only proceed until run one of the self-consistent iteration loop before frequencies went imaginary (see text). Hartree Fock is able to capture large fluctuations better than LSWT

within LSWT. The most drastic effect of Hartree-Fock is on the highly localized anti-symmetric fork modes with $\omega_{SW}/J = 1$. These were modes with unit frequency occurring in the LSWT spectrum. The modes had non-zero amplitudes only on the forks on the cluster. For this reason we will, from now on, refer to them as confined modes. For example, the LSWT spectrum for the cluster in Fig.4.2 has two unit frequency modes. Each mode is localized on one of the two forks or dangling spin regions on the cluster. Furthermore, each of the two modes is anti-symmetric, i.e. the mode has amplitudes $\psi_i = \pm 1/\sqrt{2}$ for sites i which are the tips of the fork on which the mode is localized.

Such confined anti-symmetric modes have a drastic lowering in single particle energies once the Hartree-Fock fluctuations are added to the LSWT calculation. Within a single Hartree-Fock iteration, the frequency of the two localized antisymmetric modes dropped from $\omega_{SW}/J = 1$ to $\omega_{SW}/J \sim 10^{-2}$. The modes, however, continued to be localized on the fork tips with anti-symmetric amplitudes. The Hartree-Fock calculation after a single iteration becomes unstable resulting in a large number of imaginary frequencies on diagonalizing (4.20) and we were unable to track any further lowering of these localized modes.

An important distinction between these confined Hartree Fock modes and the lowest single particle SBMFT modes are that the H-F modes have different signs of the mode amplitude on the two equivalent sites at the fork tips, whereas the SBMFT modes have same sign amplitudes. Therefore, for the H-F modes to connect smoothly to the symmetric SBMFT modes, their frequencies will have to be driven through zero due to the presence of strong quantum fluctuations.

The breakdown of LSWT and Hartree-Fock theory for capturing the quantum fluctuations of Heisenberg quantum magnets on percolation clusters, es-

tablishes SBMFT as the only mean field theory that can qualitatively describe the single particle frequencies and modes of bosons in the presence of geometric disorder. SBMFT is well known to be able to reproduce many qualitative features of the phases of quantum spins. However, not much attention has been given on the agreement of SBMFT with exact numerics. We next focus on the extent to which SBMFT can *quantitatively* capture the ground state spin correlations and energies of quantum Heisenberg magnets on percolation clusters.

4.7 Connection of SBMFT results to exact numerics

In spite of the widespread use of SBMFT for qualitatively mapping out the phases of quantum magnets, little attention has been given to its numerical accuracy in capturing ground state energies or spin-spin correlations. In this Section, in the context of quantum magnets on percolation clusters, we show that the use of non-uniform SBMFT, is able to *quantitatively* capture ground state spin-spin correlations (both short and long-ranged) to within $2-3\%$ with respect to exact DMRG numerics[7]. Also, for a large ensemble of percolation clusters, the ground state energy obtained from within SBMFT by summing over nearest neighbor spin-spin correlations, is found to agree to within 1% of DMRG numerics[7]. We therefore present non-uniform SBMFT as a powerful numerical tool to be used in conjunction with exact numerics to understand physical excitations of quantum spins at a mean field level.

The belief that SBMFT can only qualitatively(and not quantitatively) capture the phase diagrams of quantum magnets is due to two main reasons. Firstly, the theory is strictly non-variational due to the constraints(3.7) being satisfied

on average. As a result the SBMFT energy (3.11) is usually lower than the exact energy obtained from DMRG or Exact Diagonalization. Attempts to make the SBMFT energy variational have been made by using Gutzwiller projection operators that *exactly* constrain the Hilbert space of bosons on every site to agree with the space of states of the quantum magnets [17]. The Gutzwiller projection method, however, suffers from the drawback that it requires the computation of a permanent which has a computational complexity of N_s^3 (N_s is the number of sites on the lattice), and is therefore restricted to small system sizes.

The second reason for the inability of SBMFT to quantitatively reproduce correlations and energies from exact numerics is the assumption of spatial uniformity of mean field parameters which is *only* strictly valid for infinite system sizes. The *assumption* of uniform mean field parameters makes the theory analytically tractable, but it also prevents us from obtaining the numerically exact saddle point parameter values. Furthermore, for comparison with exact numerics, which are always done on finite lattices, we need to solve the self-consistent SBMFT equations with the constraints on finite system sizes. The non-uniform SBMFT procedure therefore circumvents the *assumption* of uniform values of the mean field parameters and allows calculation of numerically exact SBMFT saddle point solutions[18].

To demonstrate the accuracy of SBMFT spin-spin correlations, we show a comparison with exact DMRG correlations[19, 7] for the two percolation clusters in Fig.4.2 and Fig.4.6. Fig.4.12 shows the comparison between correlations of a single spin with all other spins along a path on the cluster. The path, shown in black, leads from one dangling region, where the tip spin is located, to the other dangling region. The single fixed tip spin is labeled 'tip' and shown on

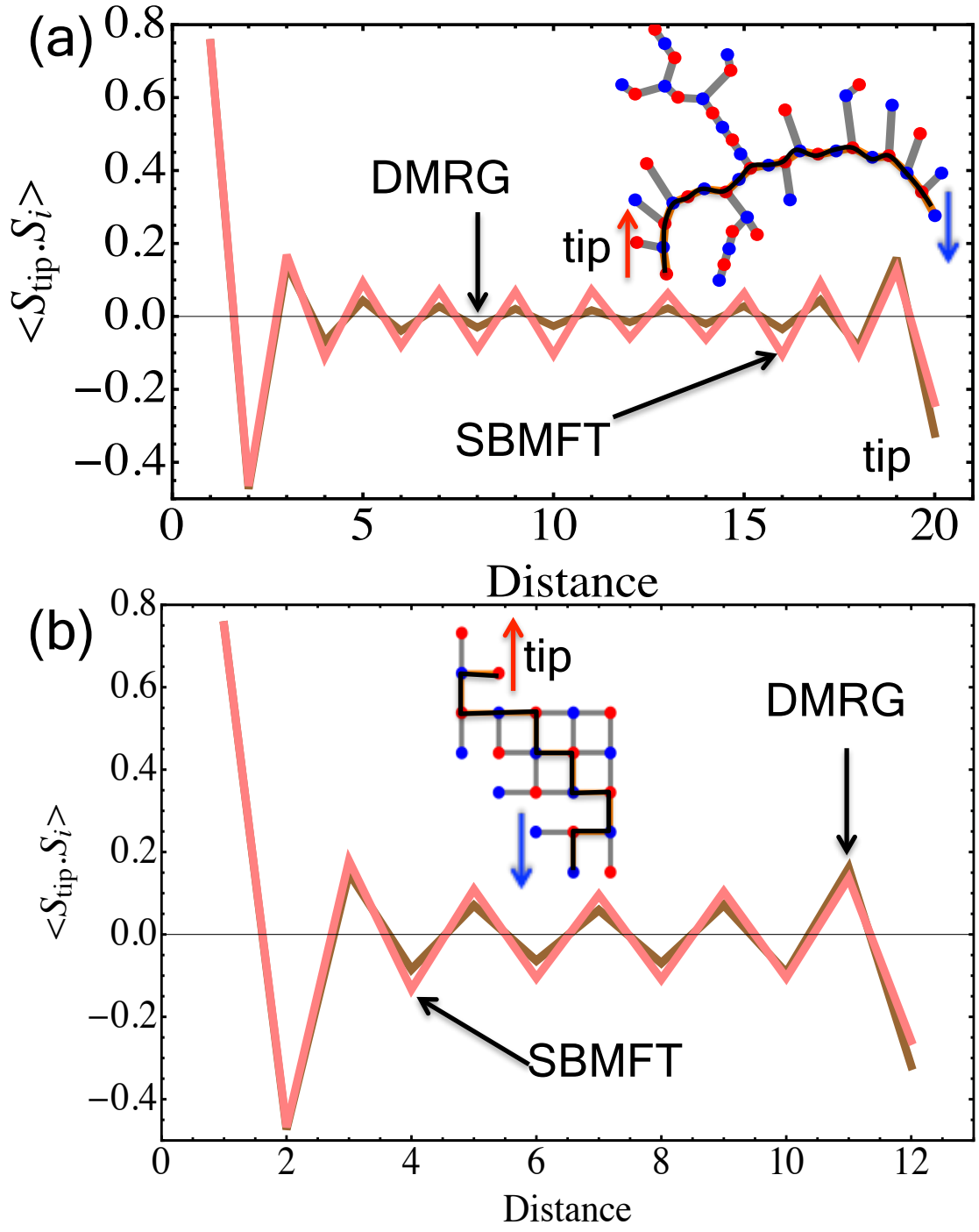

Figure 4.12: Comparison of spin-spin correlations between SBMFT and DMRG for the $N_s = 50$ site Bethe percolation cluster of Fig.4.2 and the $N_s = 22$ site square lattice percolation cluster of Fig.4.6. The spin-spin correlations shown in this Figure differ from the nearest neighbor correlations of Fig. 4.11. The correlations shown above are between a fixed 'tip' spin and all other spins along a path shown on the lattice. (a) Spin-spin correlations $\langle \mathbf{S}_{tip} \cdot \mathbf{S}_i \rangle$ between the 'tip' spin $\mathbf{S}_{tip}$ (labeled 'tip' and shown with a red arrow) and all spins $\mathbf{S}_i$ along the path on the lattice shown in black leading from one dangling spin to the other (shown with the blue down arrow). (b) Same comparison as in (a) for the square lattice

the cluster by a red, upward arrow.

Both short and long ranged correlations are captured well by SBMFT for both lattices. Furthermore, we observe a generic feature for both lattices. The spin-spin correlations decay in the middle of the path and are revived on entry in to the second dangling region. We will now argue that this is consistent with the picture of local emergent moments co-existing with locally balanced 'gapped' dimerized regions on the cluster.

The sites along the middle of the paths shown in the two clusters in Fig.4.12 belong to regions that are locally balanced and do not have any emergent dangling spins. This can also be seen from the distribution of the bond amplitudes in Fig.4.2 and Fig.4.6. All sites along the middle of the paths, shown in black, are paired up with neighboring sites in to strong nearest neighbor dimers. These locally balanced regions are therefore expected to have a local gap and exponentially decaying spin-spin correlations. This is indeed what is seen in Fig.4.12 where spin correlations are seen to decay on entry in to regions with no dangling spins along the middle of the path. Finally, towards the end of the paths, the spin correlations enter in to a region which is locally imbalanced and therefore has a non-zero density of dangling spins. These regions of local sub-lattice imbalance, are gapless, and the spin correlations experience a revival.

The decay and revival of spin correlations is the mechanism via which long range order propagates on the percolation cluster. The co-existence of locally gapped regions with locally gapless regions implies that spin correlations decay and are revived on encountering a region with an emergent spin. This revival is crucial for the long range propagation of the spin correlations. This, therefore, also directly implies that the presence of sub-lattice imbalance and

emergent dangling moments are *necessary* for the survival of long range order on the cluster.

We end this section by showing a comparison between the ground state energy computed within SBMFT and from exact DMRG numerics for an ensemble of 400 clusters with $N_s = 50$ sites each. Since, the nearest-neighbor SBMFT spin-spin correlations are accurate to within a 1%, the SBMFT estimate for the ground state energy is obtained by summing over the spin-spin correlation function of nearest neighbor bonds on the lattice. We therefore define the SBMFT energy per site, obtained from nearest neighbor SBMFT spin-spin correlations, as e_{corr}:

$$e_{corr} = \frac{1}{N_s} \sum_{\langle i,j \rangle} \langle \mathbf{S}_i \cdot \mathbf{S}_j \rangle_{SBMFT} \tag{4.22}$$

Fig.4.13 shows the comparison between DMRG and SBMFT energies for an ensemble of 400 Bethe lattice percolation clusters, each with $N_s = 50$ sites, at the percolation threshold. The SBMFT estimate for the ground state energy e_{corr} is obtained by summing over nearest neighbor spin-spin correlations(4.22). The maximum discrepancy between the DMRG ground state energies and the SBMFT estimate, at least for the clusters in the ensemble, is found to be less than 1%. Thus, e_{corr} is a more accurate method for comparing SBMFT numerics against exact DMRG calculations, as compared to the SBMFT energy e_{MF}(3.11).

The accuracy of the ground state spin-spin correlations also allows us to estimate the many-body singlet-triplet gap (for balanced clusters) using a Single-Mode approximation for the spin excitations. We also employ the SBMFT estimate for the many-body gap to extract effective spin-spin interactions between dangling spins on the cluster and show that they decay exponentially in the av-

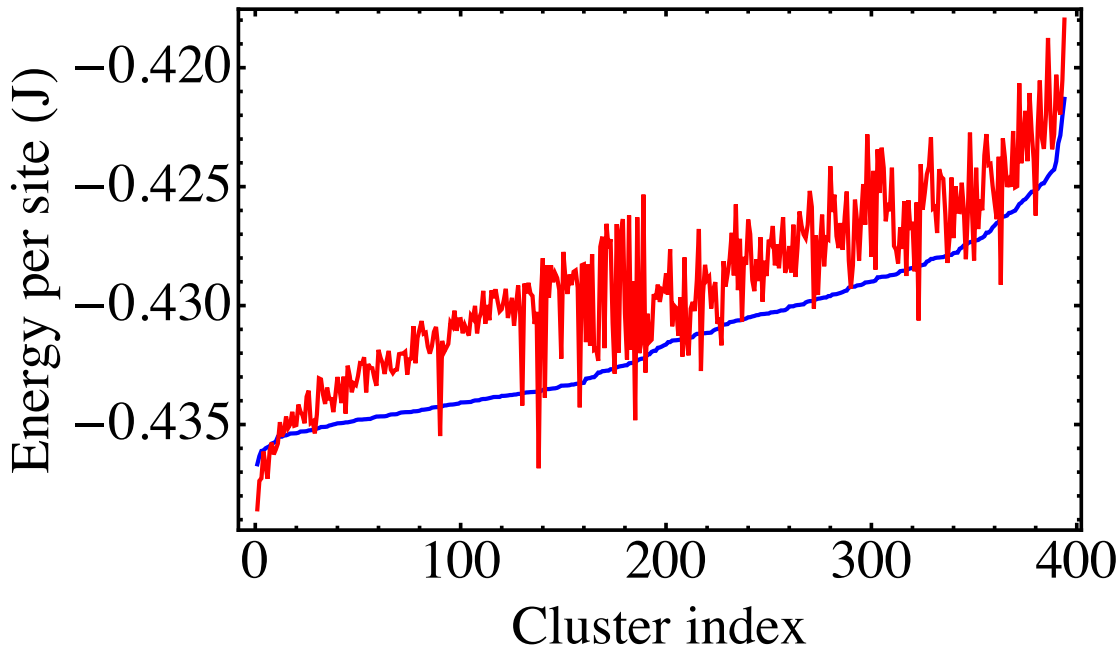

Figure 4.13: Comparison of ground state energies between SBMFT and DMRG for an ensemble of 400 Bethe lattice percolation clusters of size $N_s = 50$ sites each, at the percolation threshold. The Cluster Index corresponds to the index (1 to 400) of clusters sorted according to their DMRM energies. For every cluster, we make an ordered pair of energies from SBMFT and DMRG and then sort the list of ordered pairs in increasing strength of the DMRG energy. DMRG energies are shown by the blue line; SBMFT energies, obtained by summing over nearest neighbor spin-spin correlations, are shown by the jagged red line. The maximum percentage difference between the energies per site obtained via both methods is less than 1%, as seen near cluster index 120.

erage separation between the emergent moments, consistent with observations from exact numerics[7].

4.8 Excited states within SBMFT - *Single Mode Approximation*

In this Section, we show that it is possible to use SBMFT to make predictions beyond ground state properties using the *Single mode approximation*(SMA)[10]. We use the accurate ground state spin-spin correlations from SBMFT and SMA

to estimate the many-body singlet triplet gap for an ensemble of balanced Bethe lattice percolation clusters. We show that the gap prediction agrees well with DMRG numerics. In addition, the gap estimate is used to calculate effective mediated interactions between two dangling spins on balanced clusters. The mediate interactions are found to decay exponentially with the separation between the two dangling spins on the cluster, consistent with observations from exact DMRG numerics[7]. We finally show the dependence of the gap on the number of dangling spins on the cluster.

The Single Mode Approximation (SMA) is a variational technique for estimating the many-body gap of an interacting Hamiltonian by calculating the gap for single quasiparticle excitations above the many-body quantum ground state. Since, single particle excitations are only a subset of all possible excitations of any quantum system, the SMA gap is a variational upper bound on the exact many-body gap. The SMA spin wave function $|\Psi_{SMA}\rangle$ is an approximation to the triplet many-body state :$|\mathbf{S} = 1, \mathbf{S}^z = 1\rangle$ ($\mathbf{S}$ is the total spin angular momentum operator obtained by summing the spin half operators on all sites on the lattice and $\mathbf{S}^z$ is the z component of the total spin angular momentum operator) and is created by taking a weighted sum of single spin-flip excitations on all sites on the cluster:

$$|\Psi_{SMA}\rangle = \sum_{i=1}^{N_s} w_i \mathbf{S}_i^+ |\Psi_{MF}\rangle \tag{4.23}$$

where the set of weights $\{w_i\}$ need to be determined variationally, the operators $\mathbf{S}_i^+$ are Spin half raising operators and $|\Psi_{MF}\rangle$ is the SBMFT singlet ($|\mathbf{S} = 0, \mathbf{S}^z = 0\rangle$) ground state. The set of weights $\{w_i\}$ are determined by minimizing the SMA gap $\triangle_{SMA}$: the difference between the expectation of the Heisenberg

energy in the SMA variational state(4.23) and the ground state energy:

$$\triangle_{SMA} = \sum_{\langle i,j \rangle} (\langle \Psi_{SMA} | J\mathbf{S}_i \cdot \mathbf{S}_j | \Psi_{SMA} \rangle - \langle \Psi_{MF} | J\mathbf{S}_i \cdot \mathbf{S}_j | \Psi_{MF} \rangle) \tag{4.24}$$

The SMA gap is an approximation to the true numerically exact gap (as can be obtained from exact diagonalization or DMRG) and is a good approximation to the exact single-triplet gap for single-particle excitations. For collective spin excitations, like spin waves, the SMA gap is not a good representation of the true spin gap in the system. In the case of the diluted Bethe and square lattices, the lowest excitations above the ground state, are single spin flip excitations on the dangling spin sites. The SMA gap is therefore expected to be a good approximation to the true spin gap in this case.

The SMA gap $\triangle_{SMA}$ can be expressed in terms of the variational set of $\{w_i\}$ and is given by[19]:

$$\triangle_{SMA} = \frac{-J \sum_{\langle k,\ell \rangle} (w_k - w_\ell)^2 \mathbf{G}_{k\ell}}{2 \sum_{i=1,j=1}^{i=N_s, j=N_s} w_i w_j \mathbf{G}_{ij}} \tag{4.25}$$

where $\mathbf{G}$ is the matrix of spin correlations $\mathbf{G}_{ij} = \langle \mathbf{S}_i \cdot \mathbf{S}_j \rangle_{MF}$ computed within SBMFT(3.20),(3.21). The set of optimal weights $\{w_i^*\}$ will minimize $\triangle_{SMA}$ subject to the constraint that the SMA wave-function needs to be normalized: $\langle \Psi_{SMA} | \Psi_{SMA} \rangle = 1$. The normalization constraint is enforced using a site independent Lagrange multiplier Λ. The optimal set of weights are therefore obtained by defining a quadratic cost-function[19] $C_{SMA}(\{w_i\})$ given by:

$$C_{SMA} = \frac{-\sum_{\langle k,\ell \rangle}(w_k - w_\ell)^2 \mathbf{G}_{k\ell}}{2} - \Lambda \left(\sum_{i,j=1}^{N_s} w_i w_j \mathbf{G}_{ij} - 1 \right) \tag{4.26}$$

where Λ is a Lagrange multiplier and is exactly equal to the SMA gap $\triangle_{SMA}$. The quadratic cost-function can be minimized with respect to the set of weights by setting $\partial C_{SMA}/\partial w_i = 0$, for each weight w_i. This gives us a set of coupled linear differential equations. The optimal set of weights $\{w_i^*\}$ are the solution to the following generalized eigen-value problem:

$$\mathbf{M} \cdot \mathbf{w}^* = 2\Lambda \mathbf{G} \cdot \mathbf{w}^* \tag{4.27}$$

where the length N_s eigen-vectors $\mathbf{w}^*$ contain the optimal weights and the $N_s \times N_s$ matrix $\mathbf{G}$ is the matrix of spin spin correlations calculated in the SBMFT ground state: $\mathbf{G}_{ij} = \langle \Psi_{MF} | \mathbf{S}_i \cdot \mathbf{S}_j | \Psi_{MF} \rangle$. The matrix $\mathbf{M}$ is given by:

$$\mathbf{M}_{ij} = \begin{cases} 2 \sum_{\text{n.n. } j} \mathbf{G}_{ij} \text{ for } i = j \\ -2\mathbf{G}_{ij} * \mathbf{A}_{ij} \text{ for } i \neq j \end{cases} \tag{4.28}$$

Before discussing the results of the SMA calculation, we briefly comment on the validity (of approximating (4.25) as the true exact numerical DMRG gap) of the SMA approach. The SMA gap corresponds to single spin flip excitations - a subset of all possible spin excitations on the cluster. The gap is going to be a good approximation to the exact numerical DMRG gap, if the lowest excitations of the anti-ferromagnet on a percolation cluster are single spin flips or linear combinations of single spin excitations as in (4.23). However, since every dangling spin is a composite object with a dominant single flip excitation, but also sub-dominant non-linear (in the spin operators) multi-spin excitations [20], the

SMA gap is going to differ from the true gap by an amount proportional to the strength of these non-linear multi-spin excitations making up a dangling spin excitation.

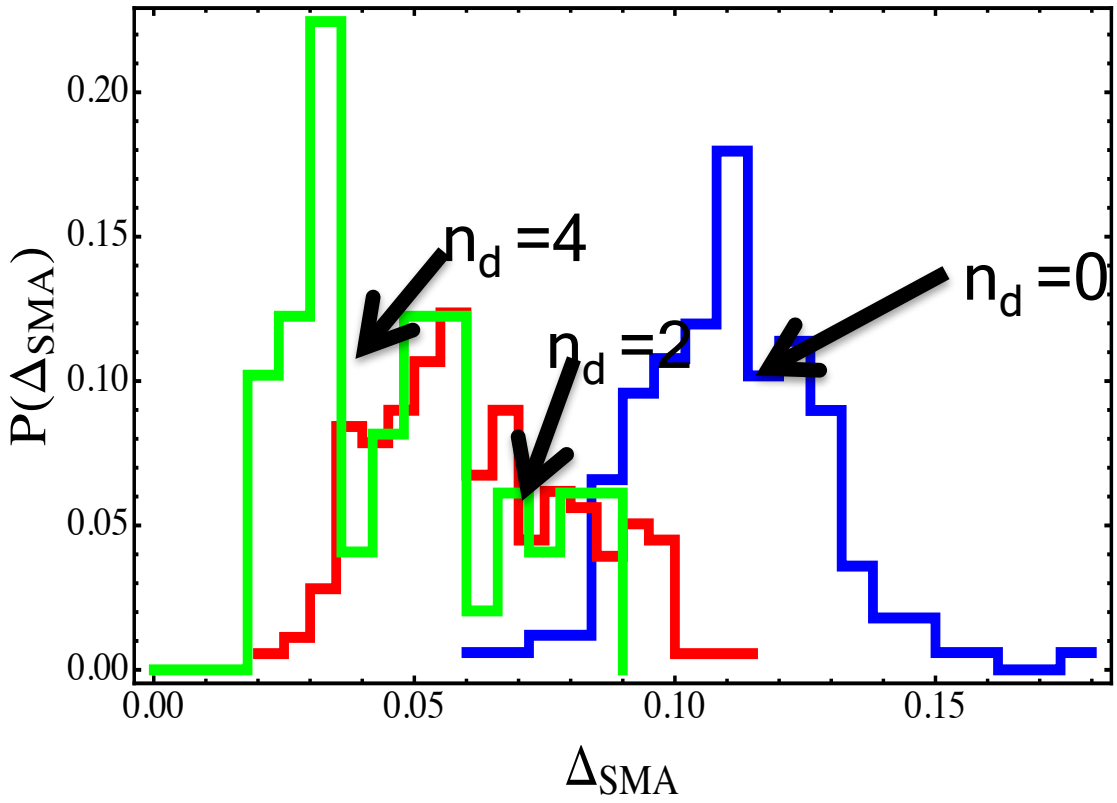

Figure 4.14: Histograms showing the SMA gap $\triangle_{SMA}$ for clusters with different number of dangling spins $n_d = 0, 2, 4$. An ensemble of size 400 clusters with $N_s = 50$ sites each is drawn from the percolation threshold. For each cluster, the SMA gap is calculated (see text (4.27)) and the number of dangling spins determined using the geometrical algorithm[7]. Histograms for each of the three groups of clusters (corresponding to zero, two or four dangling spins) are shown. For each group, SMA gaps are binned with a bin-size of $0.005J$. The fraction of clusters (within a dangling spin group) falling within a bin is denoted by P($\triangle_{SMA}$). The sum of the fraction of clusters in each bin is separately normalized to one for each group. Clusters with no dangling spins have a higher SMA gap compared to clusters with two or four dangling spins

The generalized eigen-value problem is solved for an ensemble of 400 size $N_s = 50$ clusters drawn at the percolation threshold. All clusters within the ensemble are sorted in to three groups according to their number of dangling spins

$n_d = 0, 2, 4$ (counted using a geometrical algorithm[7]). All clusters within a single dangling spin group are binned according to their SMA gaps with a bin size of $0.005J$. The probability of finding a cluster with a given SMA gap P($\triangle_{SMA}$) is calculated by dividing the number of clusters falling in a given bin by the total number of clusters belonging in that dangling spin group. This produces separate histograms for each of the three dangling spin groups containing clusters with zero, two and four dangling spins. These three histograms are shown in Fig.4.14.

Clusters with no dangling spins have a higher SMA gap compared to clusters with (two or four) dangling spins. This observation is consistent with the *anomalous* lowering of the exact numerical DMRG gap with the presence of dangling spins on the cluster[7]. Furthermore, the lowering of the gap is expected to scale as the inverse of the number of dangling spins, as was numerically observed in [7]. The more the number of dangling spins on the cluster (greater the sublattice imbalance), the lower will be the exact numerical DMRG singlet triplet gap. This is evident from Fig.4.14 where clusters with four dangling spins have a lower gap (on average) compared to clusters with two dangling spins. SMA gaps computed using SBMFT correlations therefore capture the many-body phenomenon of an *anomalously* lowered single-triplet gap due to the presence of sub-lattice imbalance, leading to emergent moments on the cluster.

Finally, using SMA, we calculate the effective antiferromagnetic interactions between dangling spins, residing on opposite sub-lattices, on Bethe lattice percolation clusters with two dangling spins. The effective interaction $J^{eff}_{\alpha\beta}$ between two dangling spins in regions α, β, on opposite sub-lattices, is (trivially) given by the single-triplet gap of the cluster. Within SBMFT, we estimate this gap

using $\triangle_{SMA}$. Therefore, for a balanced cluster with two anti-ferromagnetically interacting dangling spins, the effective mediated interaction is approximated by the SMA gap of the cluster. We also calculate an effective separation $\tilde{d}_{ij}$ between the dangling spins on sites i, j [11] on the cluster.

This effective separation is obtained by using a geometrical algorithm to calculate all possible pairs of separations between the two dangling spins. For each separation, we have a pair of sites (i, j) corresponding to the presence of a dangling spin on site $i \in$ sub-lattice A(B) and the second dangling spin on $j \in$ sub-lattice B(A). For this given separation, we compute the chemical distance d_{ij} - the shortest path on the lattice connecting sites i and j, from the cluster adjacency matrix. The effective separation $\tilde{d}_{ij}$ is a weighted sum (weighted by the two lowest Goldstone mode amplitudes indicating the probability of a boson or emergent moment on a given site on the cluster) of all possible pairs of separations between the two dangling spins and is given by:

$$\tilde{d}_{ij} = \frac{\sum_{n=1,2} \sum_{i,j} d_{ij} u_{in} v_{jn}}{\sum_{n=1,2} \sum_{i,j} u_{in} v_{jn}} \tag{4.29}$$

The SMA gap and the effective separation for an ensemble of $N_s = 50$ site clusters is shown in Fig.4.15. The (Log of) effective interactions J_{ij}^{eff} is plotted against the effective separation (4.29) for each cluster. The interactions are seen to decay exponentially with the effective separation between the dangling moments. An exponential fit of the form $J_{ij}^{eff} = J_0^* e^{-\tilde{d}_{ij}/\xi^*}$ gives best fit values $(J_0^*, \xi^* = (0.15(2), 10.1(1)))$. The decay length ξ^* is an upper bound on the decay constant of effective mediated interactions $\xi \sim 4 - 5$ obtained from exact numerics. Lastly, we note that the exponentially decaying interactions are also

[11] Since in general, a dangling spin may be delocalized over a certain region of the cluster

self-consistent with the localized SBMFT modes associated with each dangling spin region as seen in Fig.4.2,4.6.

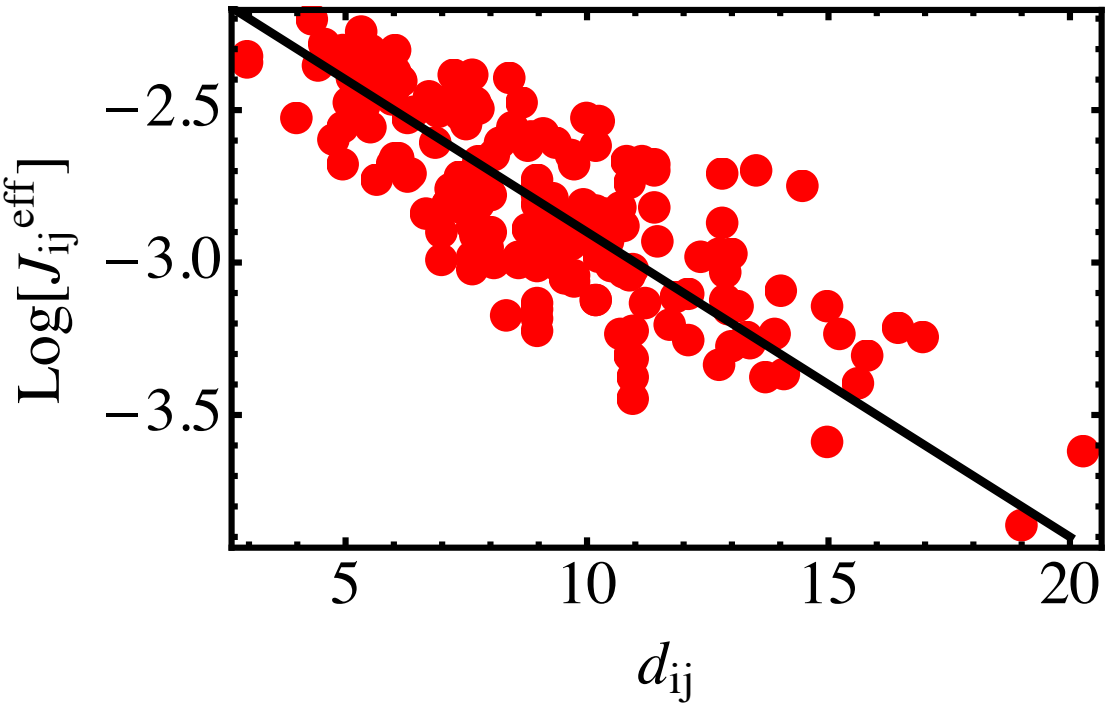

Figure 4.15: Decay of effective mediated anti-ferromagnetic interactions with effective separation (see text (4.29)) for an ensemble of $N_s = 50$ site Bethe lattice clusters. The interactions are shown to decay exponentially with the effective separation between dangling spins on the cluster. An exponential fit of the form $J_{ij}^{eff} = J_0^* e^{-\tilde{d}_{ij}/\xi^*}$ gives best fit values $(J_0^*, \xi^* = (0.15(2), 10.1(1)))$. The black like corresponds to the best-fit parameters. The same exponentially decaying profile of mediated interactions with separation between dangling spins was seen in exact numerics[7]

4.9 Conclusion

In summary, we have carried out Schwinger Boson mean field calculations for the case of non-uniform geometries, with specific emphasis on percolation clusters on the square and Bethe lattice. We also suggest why Linear Spin Wave Theory (and Hartree Fock) fail, and how SBMFT provides a way of understand-

ing the mechanism of formation of emergent spin degrees of freedom arising due to sublattice imbalance [5, 6, 7].

Particular to our approach was an understanding of the SBMFT mean field parameters: the λ_i and Q_{ij} were given the interpretation of an onsite potential and bond pairing amplitude respectively. We also showed that the low lying single particle wavefunctions turn out to have their largest amplitudes in regions associated with sublattice imbalance (i.e. the "dangling spins"). Thus, these modes provide a way of detecting emergent degrees of freedom on percolation clusters.

Our interpretations can be put on firmer ground, based on our observation that the number of low lying single particle frequencies to correspond to the number of dangling spins on the cluster. There are, of course, violations to this statement because the observed localized modes are not totally decoupled: interactions between them further split the single particle energies. In fact, a manifestation of the long range interactions is seen in the additional lowering of the lowest two frequencies from this set: we identified these as the equivalent of Goldstone modes. The fact that regions of sublattice imbalance are involved in this mode provides strong evidence for the link between the occurence of emergent degrees of freedom and long range order on the cluster, previously established numerically [8].

Finally we comment that SBMFT can provide reasonably accurate qualitative insights, complementing other highly accurate many body calculations such as DMRG. Being a mean field theory, we expect our implementation of SBMFT for non-uniform situations to perform equally well (and scale favorably) even in three dimensions where other methods are known to be limited.

BIBLIOGRAPHY

[1] S. Yan, D. A. Huse, and S. R. White, Science **332**, 1173 (2011).

[2] C. Castelnovo, R. Moessner, and S. L. Sondhi, Nature **451**, 42 (2008).

[3] S. T. Bramwell and M. J. P. Gingras, Science **294**, 1495 (2001).

[4] A. J. Willans, J. T. Chalker, and R. Moessner, Phys. Rev. Lett. **104**, 237203 (2010).

[5] L. Wang and A. W. Sandvik, Phys. Rev. B **81**, 054417 (2010).

[6] L. Wang and A. W. Sandvik, Phys. Rev. Lett. **97**, 117204 (2006).

[7] H. J. Changlani, S. Ghosh, S. Pujari, and C. L. Henley, Phys. Rev. Lett. **111**, 157201 (2013).

[8] A. W. Sandvik, Phys. Rev. Lett. **89**, 177201 (2002).

[9] S. Sachdev, Phys. Rev. B **45**, 12377 (1992).

[10] A. Auerbach, Interacting Electrons and Quantum Magnetism, Springer (1997).

[11] A. Auerbach and D. P. Arovas, Phys. Rev. Lett. **61**, 617 (1988).

[12] E. R. Mucciolo, A. H. Castro Neto, and C. Chamon, Phys. Rev. B **69**, 214424 (2004).

[13] G. R. Jenkins, lecture notes: http://www.physics.umd.edu/courses/Phys270/.

[14] U. Hizi and C. L. Henley, Phys. Rev. B **73**, 054403 (2006).

[15] T. Holstein and H. Primakoff, Phys. Rev. **58**, 1098 (1940).

[16] N. Bray-Ali and J. E. Moore, Phys. Rev. B **69**, 184505 (2004).

[17] T. Tay and O. I. Motrunich, Phys. Rev. B **84**, 020404 (2011).

[18] G. Misguich, Phys. Rev. B **86**, 245132 (2012).

[19] H. J. Changlani, S. Ghosh, C. L. Henley, and A. M. Läuchli, Phys. Rev. B **87**, 085107 (2013).

[20] Preprint: C. L. Henley and H. J. Changlani, arXiv:1407.4189.

CHAPTER 5

PHASE DIAGRAM OF THE KONDO LATTICE MODEL ON THE KAGOMÉ LATTICE

The text of this Chapter is a reproduction (with presentational changes for this thesis) of the paper written on the same subject in 2014[1]. In particular, Sections 5.3.1,5.3.2,5.4.3 and 5.5.3 are new additions, absent in the paper. This paper may also be accessed online at http://arxiv.org/pdf/1407.5354.pdf. I acknowledge the combined efforts that were involved in this project with Patrick O' Brien, Michael J. Lawler and Christopher L. Henley.

5.1 Non-coplanar orders on the Kagomé lattice

Two paths are known whereby local Hamiltonians in lattice models can stabilize complex spin order – meaning both that the spin configurations are complex in space, and that the phase diagram contains a zoo of different phases. One well-known path to such complexity is *state frustration*– meaning the ground states are massively degenerate. Any small perturbation, such as disorder [2], dipolar interactions [3], or simply the intrinsic quantum or thermal fluctuations [4, 5, 6], then suffice to select a particular state as the unique ground state.

A second path to complexity is through *frustrated interactions*, i.e. there are multiple kinds of Heisenberg spin couplings that cannot be satisfied simultaneously. Complexity may be realized with as few as *two* isotropic nearest neighbor interactions, but only when the spin sites form a *non-Bravais* lattice, such as Kagomé or Pyrochlore lattices or when the interactions are non quadratic [7, 8]: rigorously, on Bravais lattices with isotropic Heisenberg quadratic couplings–

at most simple coplanar spin spirals are realized [9].

Complex non-coplanar spin states are easily realized in the presence of non-isotropic interactions, such as due to spin-orbit coupling. However, stabilizing non-coplanar spin orders with isotropic spin space interactions is a harder problem.

The *noncoplanar* complex spin states are particularly intriguing for their unusual rigid-body-like order parameters. They are also motivated experimentally as they realize an Anomalous Hall effect due to Berry phases [10, 11, 12, 13], and theoretically since if such a phase loses long range order at sufficiently small spin-length, it is expected to become a *chiral spin liquid*, induced without any spin-orbit effects [14].

Even more complex behavior is possible when the frustrated spin-spin interactions decay slowly with distance. That is easily realized by coupling local moments to a band of *fermions*, which mediate oscillating couplings between the local Heisenberg moments – the so called Kondo Lattice Model (KLM)[10, 13, 15, 16].

In this Chapter, we construct the full phase diagram for a Kagomé lattice coupled to fermions, as a function of fermion filling and the fermion/local moment coupling strength. We used recipes to identity and classify states laid out previously [17, 18], which we have further extended here. The phase diagram so obtained includes many competing orders, with incommensurate wave vectors and non-coplanar spin arrangements. The complexity of the phase diagram motivates both a further theoretical examination of Kondo Lattice models and the experimental detection of novel spin orders found in this study.

The organization of the chapter is as follows. In Section 5.2 we introduce the Kondo Lattice model on the Kagome lattice. The model is studied in the 'weak coupling' or the 'RKKY limit' of the Kondo Lattice model in Section 5.3 . The Fourier content of the ground state spin orders of the RKKY Hamiltonian is discussed using the Luttinger-Tisza [19] method in Section 5.4 . Section 5.4 also shows the connection between the ordering wave-vectors of the spin orders (ground states of the RKKY Hamiltonian) and nesting vectors of the Fermi surface.

We do an explicit calculation of the ground state spin configurations of the RKKY Hamiltonian using a zero temperature Monte Carlo method in Section 5.6 . The various spin orders are classified in to different phases on the basis of their broken symmetries in Section 5.6 . We produce the first full picture of the phase diagram of the Kagomé Kondo lattice model in Section 5.7 . Section 5.8 summarizes the main results of this chapter and also mentions certain experimental materials where the Kagomé Kondo Lattice model might be realized.

5.2 Kondo Lattice model on Kagomé lattice

The Kondo lattice model(KLM) couples a single band of non-interacting electrons to localized classical moments via a spin exchange coupling. The local classical moments live on the Kagomé lattice, shown in Fig.5.1 - a *non-Bravais* lattice of corner sharing triangles. Every site has four nearest neighbor sites. The KLM model on the Kagomé lattice is given by the Hamiltonian:

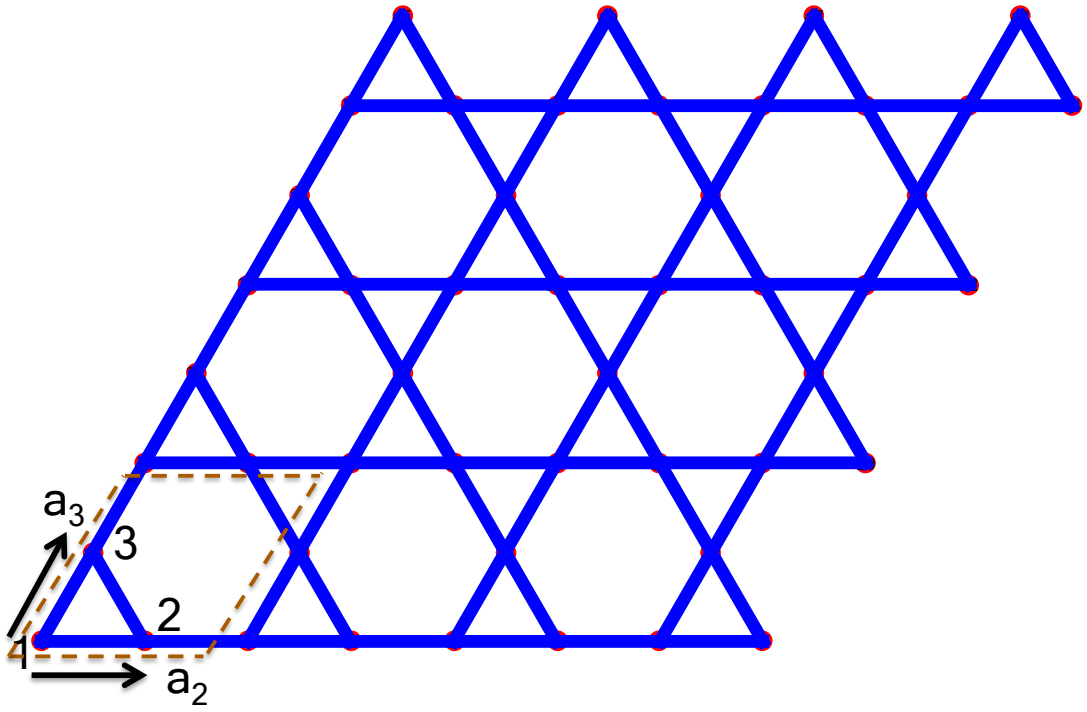

Figure 5.1: The Kagomé lattice of corner sharing triangles. The lattice is non-Bravais with three sites labeled $1, 2, 3$ within a unit cell shown by dashed brown lines. The three sites have basis vectors $\mathbf{a}_1 = (0, 0)$, $\mathbf{a}_2 = (1, 0)$ and $\mathbf{a}_3 = (1/2, \sqrt{3}/2)$. The basis vectors $\mathbf{a}_{2,3}$ are shown by arrows. The number of sites in the lattice are $N_s = 3 \times N_x N_y$ where $N_{x(y)}$ are the number of unit cells along the $x(y)$ directions

$$\mathcal{H}_{KLM} = -t \sum_{\langle i(\alpha) j(\beta) \rangle} c^{\dagger}_{i(\alpha)\sigma} c_{j(\beta)\sigma} - J_K \sum_{i=1,\alpha}^{N_s} \mathbf{S}_{i(\alpha)} \cdot \boldsymbol{s}_{i(\alpha)} \tag{5.1}$$

The first term is nearest-neighbor hopping with amplitude t of a single band of noninteracting electrons, with creation operator $c^{\dagger}_{i(\alpha)\sigma}$ at unit cell i and sublattice α [1]. The second term is the Kondo coupling, with $\boldsymbol{s}_{i(\alpha)}$ being the electron spin and $\mathbf{S}_{i(\alpha)}$ being classical Heisenberg spins representing the local moments. The number of sites on the lattice is denoted by N_s, and is related to the number of unit cells $N_x(N_y)$ along the $x(y)$ directions via: $N_s = 3 \times N_x N_y$. We seek to

[1] Realistic Kagomé materials have more complex band structures

find the optimal background-state configuration of the local moments $\{\mathbf{S}^{opt}_{i(\alpha)}\}$, for every fermion filling.

There are two existing methods to find the optimal ground state spin configuration $\{\mathbf{S}_{i(\alpha)}\}$ in (5.1) that minimizes the energy of $\mathcal{H}_{KLM}$(5.1) for a given set of Hamiltonian parameters. The two Kondo lattice model Hamiltonian(5.1) parameters are the electron filling n and the strength of the Kondo coupling J_K.

The first method is brute force finite temperature Monte Carlo by varying $\{\mathbf{S}_{i(\alpha)}\}$. The Monte Carlo method begins by generating many initial random spin configurations on the lattice. Each random spin configuration is then annealed using a single spin-flip Monte Carlo algorithm. The algorithm selects a spin on the lattice at random and makes a move where the spin direction is rotated by a small angle. The move is accepted(rejected) if the energy of the new spin configuration lowers(increases) in comparison to the spin configuration before the move. Such a procedure requires an exact diagonalization of the fermionic Hamiltonian(5.1) at every move of the Monte Carlo process and therefore scales as N_s^3, where N_s is the number of sites on the lattice. Such an algorithm is therefore computationally expensive and therefore limited to very small system sizes ($N_s \sim 100$ sites).

There have been recent improvements in the Monte Carlo algorithm for finding optimal spin configurations. One of these improvements involves the use of Chebyshev polynomials for approximating the single particle density of states [20, 21] and therefore the change in energy after every Monte Carlo move. Use of Chebyshev polynomials reduces the scaling exponent of the computation complexity of the Monte Carlo algorithm from 3 to 1. The second improvement has been to make the approximation where instead of diagonalizing the entire

Hamiltonian, containing all the sites in (5.1), we choose to diagonalize only a sub-set of the sites around the local spin that has been moved at a MC step[22]. This does not change the scaling exponent of the computational complexity of the algorithm (the scaling of the complexity with system size is still N_s^3), but reduces the complexity by a constant pre-factor.

Both these algorithms, especially the former, have allowed exploration of very large system sizes $N_s \sim 3 \times 100^2$ sites. In spite of this recent progress and new efficient algorithms, there are still big parts of the two dimensional (filling versus Kondo coupling strength) left unexplored. Also, both these methods do not provide any physical intuition in to the kind of states that are stabilized in different parts of the phase diagram.

The second most commonly used method for finding optimal spin states is to compile a database of ordered states on the lattice[13]. The true ground state of the KLM Hamiltonian, in any part of the phase diagram, is then approximated to be the lowest energy state from the trial data base. Such a procedure suffers from two severe short-comings. Firstly, the set of initial trial states put in to the data base is purely speculative and is restricted by our imagination to create ordered states on the lattice with small magnetic unit cells. The *true* ground state might not only be missing from the trial data base but might also be very different from the set of states in the data-base. Secondly, without a physical basis for selecting which states go in to the data base, it becomes difficult to explain the variational phase diagram and pin down the set of principles that govern the stability of spin orders in the phase diagram.

Faced with these restrictions we develop a methodology for producing the

full phase diagram of the Kondo Lattice model on the Kagomé lattice [2]. We look at a special limit of the Kondo Hamiltonian(5.1). This limit, which we call the 'RKKY' limit[23, 24], is when the Kondo coupling strength is a weak perturbation to the Fermi sea formed by the fermionic states. In this limit, as we will see in Section 5.3 , the KLM Hamiltonian is effectively given by a simple quadratic Heisenberg exchange Hamiltonian between classical spins with RKKY exchange couplings[23, 24]. Spin orders, in this simple limit, are dictated by the geometry of the Fermi surface and we uncover all such orders, many of which are complex non-coplanar spirals[1].

In the next Section we discuss the RKKY limit of the Kondo Hamiltonian and derive the effective quadratic Hamiltonian with long ranged oscillatory exchange RKKY interactions[23, 24].

5.3 RKKY Hamiltonian

In this Section, we show that in the limit of weak Kondo coupling $J_K \ll t$, the Kondo Hamiltonian (5.1) reduces to an effective quadratic Heisenberg Hamiltonian between classical spins on the lattice. We derive the effective RKKY interactions via two independent methods and show that both methods give consistent interactions in good agreement with one another. The fermion mediated RKKY interactions are found to be oscillate rapidly as the electronic filling is varied. In addition, there are fillings where the nearest neighbor RKKY coupling is not the dominant RKKY interaction. The rich and complex behavior of the RKKY interactions in both real space and as a function of electronic filling, will lead to

[2] the methodology is equally valid for other lattices as well

a variety of complex non-coplanar orders in Section 5.5.

5.3 .1 Deriving RKKY couplings in Fourier space

In the weak coupling limit, we treat the local Kondo coupling between the classical moments and the itinerant electron spin as a perturbation to the Fermi sea of electrons. To make this apparent, we re-write the Kondo Lattice Model Hamiltonian (5.1) as the sum of two independent terms as follows:

$$\mathcal{H}_0 = -\frac{t}{2} \sum_{\langle i(\alpha), j(\beta) \rangle} c^{\dagger}_{i(\alpha)} c_{j(\beta)} + \text{h.c.} \tag{5.2}$$

$$\mathcal{H}^{'} = -J_K \sum_{i=1}^{N_s/3} \sum_{\alpha=1}^{3} \mathbf{S}_{i(\alpha)} \cdot \boldsymbol{s}_{i(\alpha)} \tag{5.3}$$

where h.c. is the Hermitian conjugate of the first term in $\mathcal{H}_0$ and $\alpha = 1, 2, 3$ labels the three sub-lattices within each unit cell i. The electron spin $\boldsymbol{s}_{i(\alpha)}$ can be explicitly expressed in terms of the Pauli SU(2) matrices as follows:

$$\boldsymbol{s}_{i(\alpha)} = \frac{\hbar}{2} \sum_{\mu,\nu=\uparrow,\downarrow} c^{\dagger}_{i(\alpha),\mu} \boldsymbol{\sigma}_{\mu,\nu} c_{i(\alpha),\nu} \tag{5.4}$$

$\boldsymbol{\sigma}$ is a vector of Pauli matrices $\boldsymbol{\sigma} = (\sigma^x, \sigma^y, \sigma^z)$ and the $c^{\dagger}_{i(\alpha),\mu}(c_{i(\alpha),\nu})$ are fermionic creation (annihilation) operators which create(annihilate) an electron with spin μ, ν on sub-lattice α in unit cell i of the Kagomé lattice. In the limit, $J_K \ll t$, the Hamiltonian $\mathcal{H}^{'}$ is a perturbation to the hopping fermionic Hamiltonian $\mathcal{H}_0$. We first diagonalize $\mathcal{H}_0$ to find the spectrum of single particle energies

and eigen-modes and then treat the perturbative effect of $\mathcal{H}^{'}$ on them (single particle modes and energies).

To diagonalize $\mathcal{H}_0$ on the Kagomé lattice, we first define three lattice unit vectors. The Kagomé unit cell contains three non-equivalent sites related by $2\pi/3$ rotation in real space. The real space basis vectors of these three sites are given by:

$$\begin{aligned} \mathbf{a}_1 &= (0,0) \\ \mathbf{a}_2 &= (1,0) \\ \mathbf{a}_3 &= \left(\frac{1}{2}, \frac{\sqrt{3}}{2}\right) \end{aligned} \tag{5.5}$$

The Kagome unit cell contains three sites and has lattice vectors $2\mathbf{a}_2$ and $2\mathbf{a}_3$. The Hopping Hamiltonian $\mathcal{H}_0$ (5.2) can be expressed in Fourier space by defining momentum-resolved fermionic operators $c^{\alpha}_{\mathbf{k}}$ (Fourier transform of the fermion annihilation operator c^{α}_i in real space) for each sub-lattice α. Since the hopping Hamiltonian (5.2) treats both spin up and spin down fermions equivalently, we suppress the spin indices in the calculation of the free fermion band structure below.

$$c^{\alpha}_{\mathbf{k}} = \frac{1}{\sqrt{N_s/3}} \sum_{i=1}^{i=N_s/3} c^{\alpha}_i e^{-i\mathbf{k}\cdot(\mathbf{R}_i + \mathbf{a}_\alpha)} \tag{5.6}$$

where $\mathbf{R}_i = m(2\mathbf{a}_2) + n(2\mathbf{a}_3)$ (m, n are integers) is the position vector of unit cell i on the lattice and the vector $\mathbf{a}_\alpha$ ($\alpha = 1, 2, 3$), given in (5.5), labels sites within each unit cell. The spin indices have been suppressed in the definition of the momentum operator in (5.6) since the hopping Hamiltonian treats both

(up and down) spin states equivalently. As a consequence, the spectrum of frequencies and wave-functions of the fermion hopping Hamiltonian will (at least) have a twin degeneracy coming from the two spin eigen-states [3]. The hopping Hamiltonian can be expressed as a 3×3 matrix in the basis of momentum eigen-states $|\mathbf{k}^{\alpha}\rangle$ for every wave-vector $\mathbf{k}$ in the Kagomé first Brillouin zone (B.Z.) as follows:

$$\mathcal{H}_0(\mathbf{k}) = \begin{pmatrix} 0 & -2t\cos(\mathbf{k}\cdot\mathbf{a}_{12}) & -2t\cos(\mathbf{k}\cdot\mathbf{a}_{13}) \\ -2t\cos(\mathbf{k}\cdot\mathbf{a}_{12}) & 0 & -2t\cos(\mathbf{k}\cdot\mathbf{a}_{23}) \\ -2t\cos(\mathbf{k}\cdot\mathbf{a}_{13}) & -2t\cos(\mathbf{k}\cdot\mathbf{a}_{23}) & 0 \end{pmatrix} \tag{5.7}$$

where $\mathbf{a}_{\alpha\beta} \equiv \mathbf{a}_{\alpha} - \mathbf{a}_{\beta}$.

Diagonalizing (5.7) gives the single particle frequencies $\varepsilon^{\nu}_{\mathbf{k}}$ and 3×1 eigen-modes $u^{\nu}_{\mathbf{k}}$ for each of the three Kagomé bands $\nu = 1, 2, 3$. There is an additional double degeneracy coming from the spin up and spin down fermion indices, and we therefore have six modes for each wave-vector $\mathbf{k}$ (3 sub-lattices $\times 2$ spin components). The eigen-modes and frequencies satisfy the relationship:

$$\mathcal{H}_0(\mathbf{k})_{\alpha\beta} u^{\nu}_{\mathbf{k},\beta} = \varepsilon^{\nu}_{\mathbf{k}} u^{\nu}_{\mathbf{k},\beta} \tag{5.8}$$

where the α, β indices run over the three Kagomé sub-lattices. The energies in each of the three bands are given by:

[3] There will be additional degeneracies in the single particle fermionic spectrum coming from rotational and mirror symmetries int the Kagomé first Brillouin zone

$$\begin{aligned}
\varepsilon^1_{\mathbf{k}} &= -t\left[1-\sqrt{3+2\Lambda(\mathbf{k})}\right] \\
\varepsilon^2_{\mathbf{k}} &= -t\left[1+\sqrt{3+2\Lambda(\mathbf{k})}\right] \\
\varepsilon^1_{\mathbf{k}} &= 2t
\end{aligned} \tag{5.9}$$

where $\Lambda(\mathbf{k}) = \cos(\mathbf{k}\cdot\mathbf{a}_2)+\cos(\mathbf{k}\cdot\mathbf{a}_3)+\cos(\mathbf{k}\cdot(\mathbf{a}_3-\mathbf{a}_2))$. The eigen-modes of the matrix $\mathcal{H}_0(\mathbf{k})$ can be used to relate band resolved operators $c^{m\dagger}_{\mathbf{k}}$ to momentum space operators in the following way:

$$c^{\nu\dagger}_{\mathbf{k}} = \sum_{\alpha=1,2,3} u^{\nu}_{\mathbf{k},\alpha} c^{\alpha\dagger}_{\mathbf{k}} \tag{5.10}$$

Diagonalizing the free fermion hopping Hamiltonian in (5.2) therefore gives us three bands and fermionic eigen-states labeled by a wave-vector $\mathbf{k}$ in the first Brillouin zone, a band index $\nu = 1,2,3$ and a spin index $\mu =\uparrow,\downarrow$. To treat the perturbative effect of (5.3) on the free fermion bands, we carry out second-order perturbation theory in the ratio of the strength of the Kondo coupling to the hopping amplitude J_K/t. We denote the perturbative correction to the free fermion Kagomé dispersion due to the Kondo coupling $\mathcal{H}^{'}$ by $E_2(n)$ (n denotes the electronic filling). $E_2(n)$ is given by:

$$E_2(n) = J_K^2 \sum_{\mathbf{k}_{in},\mathbf{k}_{out},\nu,\nu'} \sum_{\mu,\mu^{'}=\uparrow,\downarrow} \frac{|\langle \mathbf{k}^{\nu}_{in,\mu}|\mathcal{H}^{'}|\mathbf{k}^{\nu'}_{out,\mu^{'}}\rangle|^2}{(\varepsilon^{\nu}_{\mathbf{k}_{in,\mu}} - \varepsilon^{\nu'}_{\mathbf{k}_{out,\mu^{'}}})} \tag{5.11}$$

where $|\mathbf{k}^{\nu(\nu^{'})}_{in(out)}\rangle$ are electronic states labeled by a wave-vector in the first Kagomé B.Z., a band index $\nu(\nu^{'}) = 1,2,3$ and a spin index $\mu(\mu^{'}) =\uparrow,\downarrow$. The subscripts in, out label momentum states below (in) and above(out) the Fermi surface. The second order correction $E_2(n)$ therefore arises from electron-hole

excitations where an electron(hole) at wave-vector $\mathbf{k}_{in}$ is destroyed (created), excited to a wave-vector $\mathbf{k}_{out}$, destroyed (created) at wave-vector $\mathbf{k}_{out}$ and re-created(re-destroyed) in the electronic state $\mathbf{k}_{in}$ below the Fermi surface.

Inserting $\mathcal{H}^{'}$ in to (5.11), calculating matrix elements corresponding to the electron-hole excitation process described above, and expressing the result in Fourier space gives us:

$$E_2(n) = \sum_{\mathbf{q}\in B.Z.} J_{\alpha\beta}(\mathbf{q})\mathbf{S}_\alpha(\mathbf{q}) \cdot \mathbf{S}_\beta(-\mathbf{q}) \tag{5.12}$$

where $\mathbf{S}_\alpha(\mathbf{q})$ is the Fourier transform of the local classical spins $\mathbf{S}_{i(\alpha)}$ (5.1) living on the sub-lattice α on the lattice and is given by:

$$\mathbf{S}_\alpha(\mathbf{q}) = \frac{1}{\sqrt{N_s/3}} \sum_i \mathbf{S}_i^\alpha e^{-i\mathbf{k}\cdot\mathbf{R}_i} \tag{5.13}$$

and the 3×3 matrix $J_{\alpha\beta}(\mathbf{q})$ is given by:

$$J_{\alpha\beta}(\mathbf{q}) = -\frac{J_K^2}{2} \sum_{\mathbf{k}_{in},\nu,\nu'} \frac{u^{\nu *}_{\mathbf{k}_{in},\alpha} u^{\nu'}_{\mathbf{k}_{in}+\mathbf{q},\alpha} u^{\nu' *}_{\mathbf{k}_{in}+\mathbf{q},\beta} u^{\nu}_{\mathbf{k}_{in},\beta}}{(\varepsilon^{\nu'}_{\mathbf{k}_{in}+\mathbf{q}} - \varepsilon^{\nu}_{\mathbf{k}_{in}})} e^{-i\mathbf{q}\cdot\mathbf{a}_{\alpha\beta}} \tag{5.14}$$

where $u^{\nu}_{\mathbf{q},\alpha}$ is an amplitude for destroying an electron with wave vector $\mathbf{q}$ in band ν and the summation is restricted to states $\mathbf{k}_{in}$ below the Fermi surface (F.S.). Note that in going from (5.11) to (5.14) we have switched dummy momentum indices from $(\mathbf{k}_{in}, \mathbf{k}_{out})$ to $\mathbf{k}_{in}, \mathbf{q}$ using the relation:

$$\mathbf{k}_{in} + \mathbf{q} = \mathbf{k}_{out} + \mathbf{G} \tag{5.15}$$

where $\mathbf{G}$ is a reciprocal lattice vector. The wave-vector $\mathbf{q}$ therefore connects excitations from below the Fermi surface (F.S.) to above the Fermi surface (F.S.). The matrix $J_{\alpha\beta}(\mathbf{q})$ is the non-bravais lattice analogue of the single particle electron Lindhard susceptibility $\chi_0(\mathbf{q})$ which has its most dominant contributions from wave-vectors $\{\mathbf{q}\}$ in the zone that connect states just within the Fermi surface to states just outside. Connections within this thin sliver[4] of the Fermi surface have the greatest contribution to $\chi_0(\mathbf{q})$ because of the energy denominator in second order perturbation theory. Similarly, as we will see in Section 5.3 , $J_{\alpha\beta}(\mathbf{q})$ also has its greatest (negative) contributions from wave-vectors that connect points just outside and just within the Fermi sea.

The real space couplings $\{J_{i(\alpha),j(\beta)}\}$ are obtained by Inverse Fourier transforming $J_{\alpha\beta}(\mathbf{q})$:

$$J_{i(\alpha)j(\beta)} = \sum_{\mathbf{q}} J_{\alpha\beta}(\mathbf{q}) e^{-i\mathbf{q}\cdot\mathbf{R}_{ij}} \tag{5.16}$$

and we obtain the RKKY Hamiltonian:

$$\mathcal{H}_{RKKY} = \frac{1}{2} \sum_{i(\alpha),j(\beta)} J_{i(\alpha)j(\beta)} \mathbf{S}_{i(\alpha)} \cdot \mathbf{S}_{j(\beta)} \tag{5.17}$$

Calculation of $J_{\alpha\beta}(\mathbf{q})$ is the most computationally expensive operation in the procedure for obtaining the real space couplings. For a lattice size N_s, calculation of $J_{\alpha\beta}(\mathbf{q})$ requires a double sum over states within the F.S. and states above the F.S. and therefore the worst case complexity is $\mathcal{O}(N_s^2)$. This, although better than the costs of fermionic diagonalization (which scale as N_s^3, see Section

[4]The thickness of the sliver increases with temperature. At zero temperature, on a discrete lattice, there are points within the zone which connect to points just outside the F.S.

5.2), is still expensive. We therefore, further reduce the computational cost by making use of the zone symmetries, as outlined below.

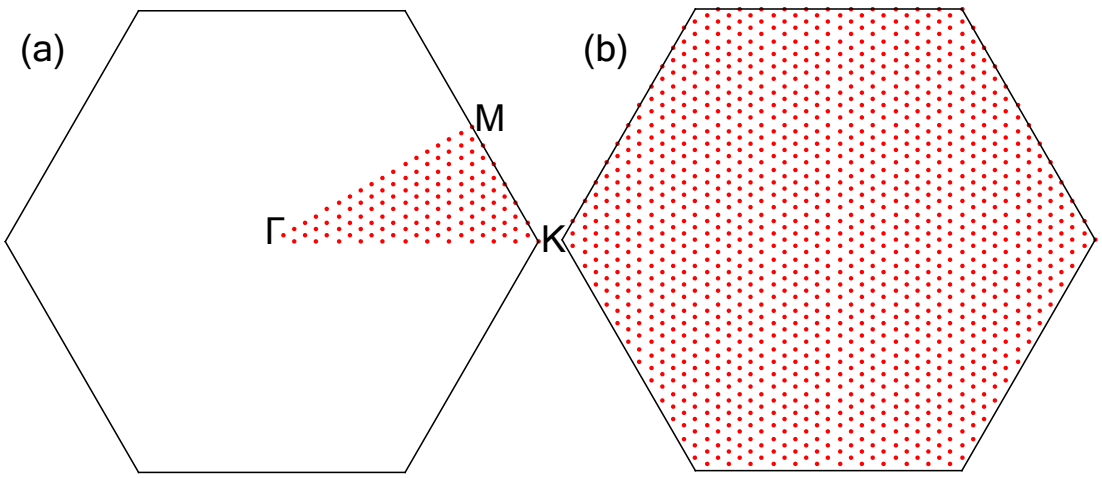

Figure 5.2: The Kagomé first Brillouin zone with wave-vectors shown by discrete points within the zone for a $N_s = 3 \times 36^2$ lattice. (a) The set of wave-vectors $\{\mathbf{q}\}$ within one-twelfth of the zone. For each of the wave-vectors, the matrix $J_{\alpha\beta}(\mathbf{q})$ is calculated by carrying out the double summation over all states within the Fermi sea and all states outside (see text). (b) The entire set of wave-vectors within the Kagomé first Brillouin zone generated from the subset of wave-vectors in (a) by the use of mirror and six-fold rotation symmetries in the zone. High-symmetry points in the zone are labeled: $\mathbf{\Gamma}$ corresponds to the zone center, $\mathbf{K}$ to the zone corner and $\mathbf{M}$ to the zone mid-point

The Kagomé Brillouin zone has a six fold C_6 symmetry in the zone (twelve-fold if we include reflection symmetries about high symmetry mirror planes in the zone) i.e. there are six equivalent wave-vectors related by a rotational symmetry in the zone. In addition to the six-fold symmetry there is an additional mirror symmetry in the zone which maps $\mathbf{q} \leftrightarrow -\mathbf{q}$. The presence of these symmetries requires computation of matrix elements of $J_{\alpha\beta}(\mathbf{q})$ *only* for wave-vectors

in *only* one-twelfth of the zone, as shown in Fig.5.2. The matrix $J_{\alpha\beta}(\mathbf{q})$ for the entire zone can then, by the use of symmetries, be created from the matrix elements of $J_{\alpha\beta}(\mathbf{q})$ for wave-vectors within one-twelfth of the zone. Finally, we only need to compute six entries of the complex 3×3 matrix $J_{\alpha\beta}(\mathbf{q})$ and use the Hermitian conjugate property of $J_{\alpha\beta}(\mathbf{q})$ to fill in the remaining three elements.

Calculation of $J_{\alpha\beta}(\mathbf{q})$ in Fourier space is an efficient and optimal method for calculating RKKY interactions between *all* pairs of sites within the lattice. Use of zone symmetries and a parallelized algorithm[5] allows us to go up to lattice sizes of $N_s = 3 \times 36^2$. There are, however, certain limitations to the Fourier space approach, which we discuss next.

There are two limitations of computing the set of $\{J_{i(\alpha)j(\beta)}\}$ via the method above. Firstly, symmetries in the zone at any filling lead to degeneracies in the single particle energies (typically six leading to twelve missing electronic states) requiring us to skip over or leave out fillings so as to avoid zero energy denominators in (5.14) [6]. The second limitation is a more severe form of the first constraint, where, for a window of fillings near Van Hove values [7], computation of (5.14) is restricted by large parallel parts of the F.S. with degenerate energies.

We resolve the first limitation by outlining a procedure for computing couplings in real space in Section 5.3.2. The second limitation will be circumvented by making *informed* guesses, based on the Luttinger-Tisza method (see Section 5.4), for the spin orders that are good candidate ground states of the RKKY

[5]Since $J_{\alpha\beta}(\mathbf{q})$ for each pair $(\mathbf{k}_{in}, \mathbf{k}_{out})$ of wave-vectors requires independent summations over the zone, the calculation is easily parallelized across several CPU cores using OpenMP

[6]The six fold (twelve if taking spin degeneracy in to account) comes precisely from the C_6 zone symmetry discussed before. So, while zone symmetries are a boon in the computation of $J_{\alpha\beta}(\mathbf{q})$, they are also a curse preventing us from calculating $J_{\alpha\beta}(\mathbf{q})$ at every filling

[7]Van Hove fillings are special fillings at which the F.S. becomes hexagonal with large parallel parts. The single particle density of states is divergent at a Van-Hove filling

Hamiltonian (5.17) at the Van-Hove fillings.

5.3 .2 Deriving RKKY couplings in real space

The second method for extracting the set of couplings is an approach in real space, cruder in spirit, but works as well (in terms of accuracy of the RKKY interactions) as the explicit calculation in Fourier space.The real space approach is computationally more expensive, scaling as $\sim N_s^3$, compared to the Fourier space approach which scales as $\sim N_s^2$. Using Exact Diagonalization (ED) of $\mathcal{H}_{KLM}$ (5.1), we evaluate the single particle energies of fermions in the background of a set of random spin configurations for a given J_K. These single particle energies $\{\varepsilon_m\}$ are summed up to the Fermi Surface (F.S.) to find the total energy $E_{ED}(n)$ as a function of filling:

$$E_{ED}(n) = \sum_{m=1}^{m=n} \varepsilon_m \tag{5.18}$$

The total energy $E_{ED}(n)$ can be expressed as a perturbative expansion in powers of J_K/t, in the limit of weak Kondo coupling, as follows:

$$E_{ED}(n) = E_0(n) + (J_K/t)^2 E_2(n) + (J_K/t)^4 E_4(n) + ... \tag{5.19}$$

where E_2 is the contribution to $E_{ED}(n)$from second order perturbation theory and $E_4(n)$ is a fourth order contribution to the exact energy from numerical diagonalization. $E_2(n)$ is just the RKKY energy computed in the previous subsection 5.3.1 and involves quadratic interactions between spins. Similarly, $E_4(n)$ is a quartic interaction between classical spins and involves contributions from

all four spin terms allowed by spin rotational invariance[8].

The second and fourth order contributions to the exact energy are then extracted by taking an ensemble of random spin configurations on the lattice. For each spin configuration taken from the list of random spin configurations, $\mathcal{H}_{KLM}$ is numerically diagonalized to obtain the single particle energies, which are summed up to the Fermi surface, for different Kondo coupling strengths. The set of total energies (up to the Fermi surface) at different coupling strengths, for all random spin configurations in the ensemble, is fit to a functional form:

$$E_{ED}(n) = E_0^{fit}(n) + (J_K/t)^2 E_2^{fit}(n) + (J_K/t)^4 E_4^{fit}(n) + ... \tag{5.20}$$

with fit parameters $\{E_0^{fit}, E_2^{fit}, E_4^{fit}\}$, using linear least squares fitting. $E_2^{fit}(n)$ is therefore a best-fit estimator for the RKKY energy $E_2(n)$ and the RKKY couplings can be extracted from $E_2^{fit}(n)$. Once we recover the set of $\{E_2^{fit}(n)\}$ for all spin configurations in the fitting data base (typically containing ~ 1000 spin configurations), we fit it to the following functional form

$$E_2^{fit}(n) = \varepsilon_0(n) + J_1^{fit}(n) \sum_{\langle ij \rangle} \mathbf{S}_i \cdot \mathbf{S}_j + J_2^{fit}(n) \sum_{\langle\langle ij \rangle\rangle} \mathbf{S}_i \cdot \mathbf{S}_j \tag{5.21}$$

by minimizing the norm of the following matrix equation

$$\underset{J_1^{fit}(n), J_2^{fit}(n), ...}{\text{Min}} |\mathbf{M}(n) \cdot \mathbf{x}(n) - \mathbf{b}(n)| \tag{5.22}$$

with $\{J_1^{fit}(n), J_2^{fit}(n), ...\}$ as fit parameters. $\mathbf{M}$ is a $N \times (n_J+1)$, where n_J is the

[8]All odd spin terms vanish in the perturbative expansion (5.20) because of time reversal symmetry and spin rotational invariance

number of couplings to be fit along with an additional constant $\varepsilon_0(n)$ in (5.21). The matrix $\mathbf{M}$ contains the classical energies corresponding to the couplings $J_{1,2,...}(n)$ for each random spin configuration, arranged along the rows. $\mathbf{x}$ is a vector of length $n_J + 1$ given by $\mathbf{x}^T = (\varepsilon_0(n), J_1(n), J_2(n), ...)$ and the vector $\mathbf{b}$ contains the extracted $E_2^{fit}(n)$ from (5.20) for each of the N spin configurations.

5.3 .3 RKKY couplings

In this sub-section, we present a comparison between the RKKY interactions calculated from both the Fourier and real space approaches and also comment on the nature of the RKKY interactions on the Kagomé lattice.

The RKKY couplings for a Bravais lattice, in d dimensional space, between sites i, j, asymptotically decay as $J_{ij} \sim \cos(2k_F r_{ij} + \varphi)/r_{ij}^d$ [23, 24], where $k_F(n)$ is the filling n dependent Fermi wave-vector, r_{ij} is the real space separation between sites i, j on the lattice and φ is a phase-shift. The couplings are oscillatory and decay with a power law envelope $\sim r_{ij}^{-d}$. On a frustrated lattice, like the Kagomé, the RKKY interactions for small fillings $n < 0.1$, when the F.S. is circular, are given by:

$$J_{i(\alpha)j(\beta)} = J_0 \frac{\cos(2k_F r_{i(\alpha)j(\beta)} + \varphi_{\alpha\beta})}{r^2_{i(\alpha)j(\beta)}} \tag{5.23}$$

where J_0 is a constant amplitude (depending on J_K^2/t), the indices i, j label unit cells on the Kagome lattice, the indices $\alpha, \beta = 1, 2, 3$ label sub-lattices within the unit cell and $\varphi_{\alpha\beta}$ is a sub-lattice dependent phase shift. The RKKY interac-

tions, on atleast the Kagome lattice, are frustrated[9] and can favor a variety of complex spin orders.

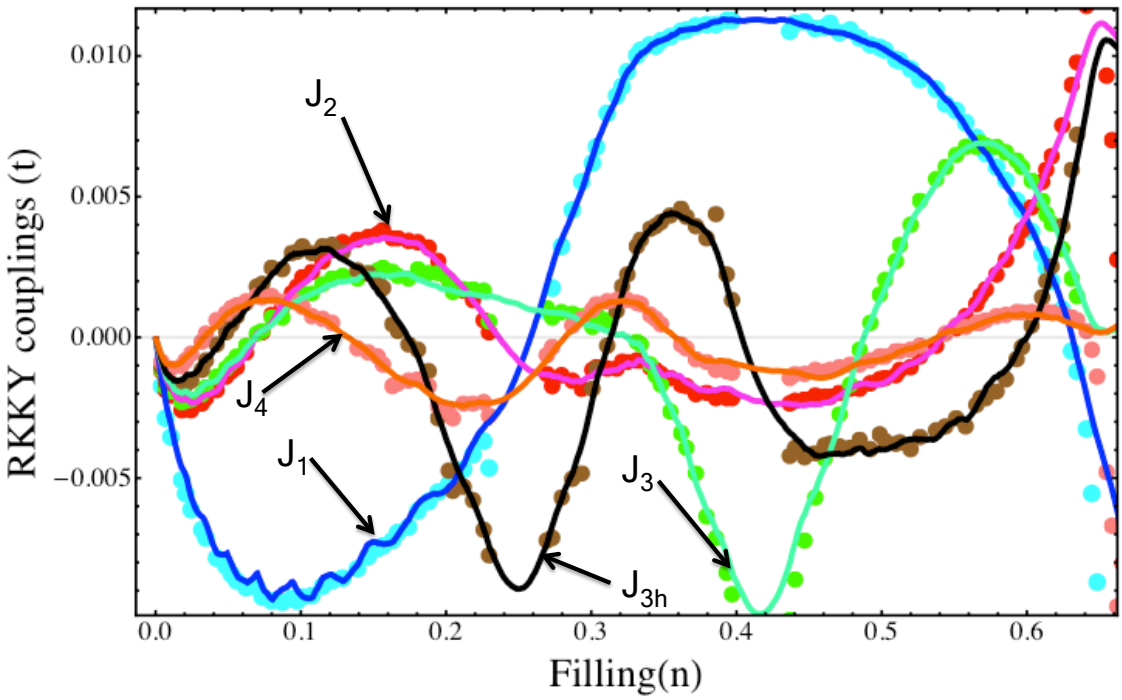

Figure 5.3: Variation of couplings with different displacements as a function of electronic filling. All couplings are plotted in units of J_K^2/t. The continuous curves are obtained via the real space fitting procedure (see text). The discrete set of points along each curve are calculation results from second order perturbation theory. Both independent methods of computing RKKY interactions gives consistent results. The different couplings correspond to J_1 (nearest neighbor separation), J_2 (second nearest neighbor), the two kinds of third nearest neighbor interactions: J_3 and J_{3h} (between diagonally opposites in a hexagon) and fourth nearest neighbor coupling J_4. Only fillings in the bottom two bands are considered. The second order perturbation theory calculation is missing data-points near Van-Hove fillings $n = 1/4, 5/12$ where the calculation is singular due to a divergent density of fermionic states

The first five couplings are plotted in Figure 5.3. as a function of filling. Negative (positive) couplings correspond to ferromagnetic (antiferromagnetic)

[9]Frustration means that there is no single spin order that can satisfy all RKKY interactions on the Kagomé lattice

interactions. The continuous curves indicate the interactions calculated in real space by the fitting procedure and the discrete set of points along each curve are the Fourier space calculation results for the RKKY interactions. Both methods agree well and are consistent.

The plot in Fig.5.3 also highlight a drawback of the Fourier space calculation. There are two intervals of fillings where the Fourier space calculation is missing data-points. These are around the filling intervals $n = 1/4$ and $n = 5/12$, both of which correspond to Van-Hove singularities in the first and second Kagomé bands. Presence of such singularities leads to a divergent density of single particle fermionic states. Fillings corresponding to the Fermi surface falling in these degenerate states invalidates the second order perturbation theory calculation(5.14) due to zero energy denominators arising from the presence of degenerate energy levels above and below the Fermi sea.

The first few RKKY interactions on the Kagomé lattice Fig.5.3 show a rich dependence on the electronic filling. Observe that the farther the interaction, the more oscillations are seen; and there are some fillings at which both J_1 and J_2 are dominated by more distant couplings. It should also be noted that (at $T = 0$) the magnitude of RKKY couplings decays (in two dimensions) as $1/|r_{ij}|^2$, a long-range coupling, so it may be dangerous to truncate couplings to the first few neighbors [25].

A final thing to note is that the fillings extend only up to the second Kagomé band, i.e. $n = 2/3$. Beyond this filling, the Fermi sea enters in to the third Kagomé band, which is flat - meaning that the energy spectrum is dispersionless and all $N_s/3$ states are degenerate and have the same energy $2t$(5.9). For fillings corresponding to the presence of the Fermi surface in the flat Kagomé band, the

interactions are expected to be linear in J_K, arising from degenerate first order perturbation theory. This calculation will not form a part of the present chapter and will be left to future work.

The optimal set of background spin configurations that minimize the RKKY energy and best satisfy the rich set of RKKY interactions Fig.5.3 will be found in two steps. In the first step, in Section 5.4, we use a method called Luttinger-Tisza[19] to determine the wave-vector content of the optimal spin configurations. This method is exact on Bravais lattices, however for non-Bravais lattices like the Kagomé, it serves as a guide for constructing a normalizable spin configuration from the optimal Luttinger-Tisza wave-vectors.

In the second step, detailed in Section 5.5, we carry out an iterative minimization to find the optimal spin configuration and show that the dominant wave-vectors making up the optimal spin orders are *always* a sub-set of the optimal Luttinger-Tisza wave-vectors. In addition, we also uncover a variety of complex non-coplanar spin orders on the Kagomé lattice. We next discuss the Luttinger-Tisza method.

5.4 Orders from Luttinger-Tisza analysis

In this Section we make an *informed* guess, based on a theorem strictly valid only for Bravais lattices, of the wave-vector content of the optimal spin orders that minimize the RKKY energy(5.17) using the Luttinger-Tisza method[19, 17, 18]. We first introduce the method and compare its applicability on Bravais lattices as compared to non-Bravais lattice. We then determine the optimal Luttinger-Tisza ordering wave-vectors and show its remarkable connection to

the geometry of the Fermi surface. We end this Section by constructing a few classical spin orders from the optimal Luttinger-Tisza ordering wave-vectors on the Kagomé lattice.

5.4 .1 Luttinger-Tisza (L.T.) method

The Luttinger-Tisza (L.T.) method is an approach to obtain the ordering wave-vectors of spin configuration(s) that minimizes the energy of a Spin Hamiltonian, in this case the RKKY Heisenberg exchange Hamiltonian (5.17), subject to the constraint of unit spin normalization at every site. The Luttinger-Tisza method takes as input a spin-spin bilinear Hamiltonian and determines the optimal spin arrangement that is the ground state of the spin Hamiltonian. Our starting point for this Section is the RKKY Hamiltonian(5.17).

The Luttinger-Tisza method diagonalizes the matrix of interactions in Fourier space $J_{\alpha\beta}(\mathbf{q})$(5.14) for every $\mathbf{q}$ in the zone and picks up the wave-vector corresponding to the lowest eigen-value as the *optimal* Luttinger-Tisza wave-vector $\mathbf{Q}_{L.T.}$. If it is possible to construct a normalizable spin configuration from the optimal L.T. wave-vector, it is guaranteed to be the lowest energy state on a Bravais lattice. For a non-Bravais lattice, like the Kagomé, it is usually not possible to construct a normalizable spin configuration using *only* the dominant L.T. wave-vectors and we need to also mix in sub-dominant L.T. modes.

The L.T. framework gives a star of C_6 symmetry related L.T. wave vectors $\{\mathbf{Q}_{L.T.}\}$ which have the most dominant (negative) contribution to $J_{\alpha\beta}(\mathbf{q})$. Each such contribution, coming from a wave vector in the zone, is obtained by diagonalizing $J_{\alpha\beta}(\mathbf{q})$:

$$J_{\alpha\beta}(\mathbf{q})u^{\nu}(\mathbf{q}) = \lambda^{\nu}(\mathbf{q})u^{\nu}(\mathbf{q}) \tag{5.24}$$

where the ν index labels the three bands, $\lambda^{\nu}(\mathbf{q})$ is the eigenvalue corresponding to the mode $u^{\nu}(\mathbf{q})$[10] and band ν. The wave vector that goes along with the smallest eigenvalue of $J_{\alpha\beta}(\mathbf{q})$ is identified to be L.T. ordering vector $\{\mathbf{Q}_{L.T.}\}$. The optimal $L.T.$ eigenvalue $\lambda_{L.T.}$ sets a strict lower bound on the energy of the spin order: $\langle \mathcal{H}_{RKKY} \rangle \geq -N|\lambda^{opt}(\mathbf{Q}_{L.T.})|$ and the L.T. mode $u^{\nu=1}(\mathbf{Q}_{L.T.})$ ($\nu = 1$ labels the band in which all the lowest L.T. eigen-values lie) tells us how the Fourier weight at a given $\mathbf{Q}_{L.T.}$ spreads across the three sublattices.

On a Bravais lattice, for example the triangular lattice, it is *always* possible to construct a spin configuration, from the optimal L.T. wave-vectors $\mathbf{Q}_{L.T.}$, that satisfies the constraint of unit spin normalization at every site. A simple example of a two dimensional spin configuration constructed from the optimal L.T. wave vector $\mathbf{Q}_{L.T.}$is a coplanar spiral given by $\mathbf{S}_i = (\cos(\mathbf{Q}_{L.T.} \cdot \mathbf{R}_i), \sin(\mathbf{Q}_{L.T.} \cdot \mathbf{R}_i), 0)$. This also implies that if there are more than one, distinct spin configurations, that can be constructed from $\mathbf{Q}_{L.T.}$and satisfy unit spin normalization on every site on the Bravais lattice, then they must be degenerate.

Such a degeneracy may be broken on a non-Bravais lattice where the different sub-lattices might choose to go along with different optimal L.T. wave-vectors, thereby breaking sub-lattice symmetry. This happens when the star of Luttinger-Tisza wave-vectors are insufficient to construct a normalizable optimal spin configuration. The spin order might also break the symmetry between different spin-components on a given sub-lattice, for example, each component might choose to go along with a different $\mathbf{Q}_{L.T.}$. The Luttinger-Tisza method

[10]These modes of the $J_{\alpha\beta}(\mathbf{q})$matrix should not be confused with the modes of $\mathcal{H}_0(\mathbf{k})$(5.7)

gives no prescription[11] for how the spin-order might choose to break the O(3) spin rotational symmetry on the lattice.

It is therefore always important to compare the optimal Luttinger-Tisza wave-vectors $\mathbf{Q}_{L.T.}$with the Fourier content of the optimal spin configurations obtained from a brute force procedure like Monte Carlo or iterative minimization[17, 18]. The many ways of breaking the degeneracy between competing spin orders, all using the dominant L.T. wave-vectors, adds to the richness of the phase diagram of symmetry broken spin orders on the Kagomé lattice. Next, we put the L.T. method to use and obtain the optimal wave-vectors at several different fillings and show their ($\mathbf{Q}_{L.T.}$) connection to nesting Fermi surface wave-vectors in the Kagomé first B.Z.

5.4 .2 Connecting optimal Luttinger-Tisza wave-vectors to Fermi surface geometry

In the weak Kondo coupling or the RKKY limit, the Kondo term in (5.1) is a weak perturbation to the single band of itinerant electrons and therefore the matrix of RKKY interactions $\{J_{i(\alpha)j(\beta)}\}$ and its dominant instabilities is determined by the shape and geometry of the Fermi surface. In this Section, we show how the filling n dependent wave-vector $\mathbf{Q}_{L.T.}(n)$ of the optimal Luttinger-Tisza mode $u^{\nu}(\mathbf{Q}_{L.T.})$ evolves with filling.

At any given filling, $\mathbf{Q}_{L.T.}$is found to connect points just within the Fermi sea,

[11] An exception is in the case where a normalizable spin configuration on the lattice can be constructed using *only* the L.T. wave-vectors. In such a case the mode vectors $u^{\nu}(\mathbf{Q}_{L.T.})$ indicate what linear combinations of the L.T. wave-vectors need to be taken to construct a normalizable optimal spin configuration

to electronic states just outside the Fermi surface. Such electron-hole excitations, created with the L.T. vector $\mathbf{Q}_{L.T.}$, are gapless and cause the dominant instability in the matrix of interactions in Fourier space $J_{\alpha\beta}(\mathbf{q})$.

Because the wave-vector $\mathbf{Q}_{L.T.}$connects points near the Fermi surface, its shape and evolution with filling is intricately tied to the shape and geometry of the Fermi surface, at any given filling. $\mathbf{Q}_{L.T.}$, at any filling, is therefore a nesting vector of the Fermi surface. This vector however is not always the conventional nesting vector connecting flat and parallel parts of the Fermi surface[10, 16], as we discuss next.

The evolution of the Fermi surface for fillings in the lowest Kagomé band $\nu = 1$ is shown in Fig.5.4. For fillings n very close to zero, the Fermi surface is circular and does not have the six-fold symmetry of the zone. As a result, there is no sharp nesting vector $\mathbf{Q}_{L.T.}$and electron-hole excitations are created with wave-vectors near $\mathbf{Q}_{L.T.}$=0 which leads to ferromagnetic RKKY interactions. This is also seen in the RKKY couplings in Fig.5.3, where for filling intervals close to zero, all five interactions are ferromagnetic.

For $n \lesssim 0.05$, some distant interactions become antiferromagnetic: we conjecture the L.T. wave vector steadily evolves towards the zone M point, so the spin states are ferromagnetic with some incommensurate twist added [12].

The $\mathbf{Q}_{L.T.}(n)$ vector hits the zone edge at $n = 0.105$ (see Fig.5.5), and continues to move (or, equivalently, to move back) *smoothly* along a mirror symmetry line in the zone, passing through the zone M points, and shown by dashed black lines in Fig.5.4. Throughout this trajectory, the $\mathbf{Q}_{L.T.}(n)$ vector

[12]this cannot be proven numerically: in a finite interval $n = [0, 0.05]$, $\mathbf{Q}_{L.T.}(n)$ locks at the ferromagnetic value

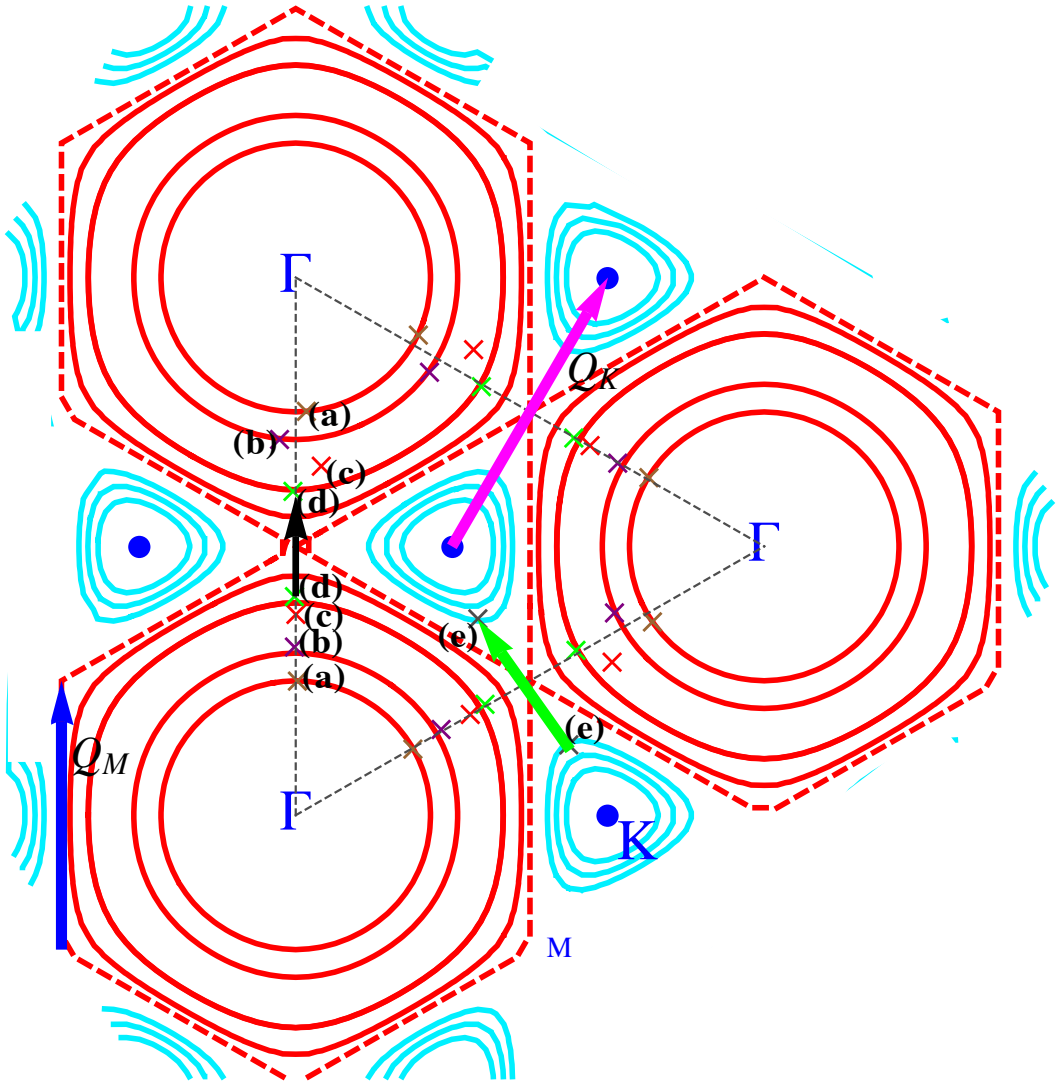

Figure 5.4: Evolution of the Fermi surface and the optimal Luttinger-Tisza vectors $\mathbf{Q}_{L.T.}$with filling. The Kagomé first Brillouin zone and its two copies, translated by reciprocal lattice vectors, is shown. The zone center, mid-point and corner are labeled $\boldsymbol{\Gamma}, \boldsymbol{M}, \boldsymbol{K}$, respectively. The red-contours show constant energy Fermi-surfaces at different fillings for $0 < n < 1/4$. Blue contours show Fermi surfaces for fillings in the range $1/4 < n < 1/3$. The dashed Hexagonal Fermi-surface occurs at the Van-hove filling $n = 1/4$. The set of points (a)-(e) label electronic states just below and above the Fermi sea at different fillings. Vectors in black and green are shown to connect states labeled (d) and (e) and are the nesting vectors causing the dominant instability in $J_{\alpha\beta}(\mathbf{q})$. Nesting vectors lying at special high symmetry points in the zone are shown by arrows and labeled $\mathbf{Q}_M$ (at $n = 1/4$) and $\mathbf{Q}_K$ (at $n = 1/3$)

arises from connections between points on the Fermi surface. Points on the Fermi surface labeled (a)-(d) indicate electronic states just below, and just above (the same points in the copy of the zone translated by the reciprocal lattice vector $\mathbf{b}_2 = (0, 2\pi/\sqrt{3})$) the Fermi surface. The wave-vector connecting each state ((a)-(d)) below the Fermi surface to the state just outside (labeled by the same letters in the translated copy of the zone) is the nesting or the optimal L.T. vector $\mathbf{Q}_{L.T.}$. $\mathbf{Q}_{L.T.}$therefore evolves along a mirror symmetry line connecting the zone mid-points and approaches the zone center at $\mathbf{\Gamma}$. $\mathbf{Q}_{L.T.}$, therefore, connects parts of the Fermi surface with the maximum curvature – an observation also noted in a recent study of KLM on Bravais lattices [26].

As $n \to 0.25$, the dominant Fermi surface wave-vector approaches the zone-boundary where the F.S. kisses itself, and $\mathbf{Q}_{L.T.}(n)$ approaches the $\mathbf{\Gamma}$ point again, as shown in Fig.5.5. However, exactly at $n = 1/4$, and probably for a small interval on either side of it, a different nesting vector beats out the one we described: this comes from a conventional nesting between flat segments of Fermi surface. and includes a brief detour of $\mathbf{Q}_{L.T.}(n)$ to the $\mathbf{M}$ point – a first order transition, shown by a large blue arrow in Fig.5.5. This conventional nesting instability, at the Van-Hove singularity $n = 1/4$, is caused by the nesting vector connecting the zone mid-points and shown by the label $\mathbf{Q}_M$ in Fig.5.4. $\mathbf{Q}_M$ connects a very large number (divergent in the thermodynamic limit) of degenerate electronic states on both sides of the Fermi sea causing a logarithmic singularity in the Fourier transformed matrix of interactions $J_{\alpha\beta}(\mathbf{q})$(5.14).

For $1/4 < n < 1/3$, the Fermi surface again shrinks to small circles with C_3 symmetry, centered at the zone corner $\mathbf{K}$. Correspondingly, $\mathbf{Q}_{L.T.}(n)$ again connects points of maximum curvature on the F.S., as shown by the green ar-

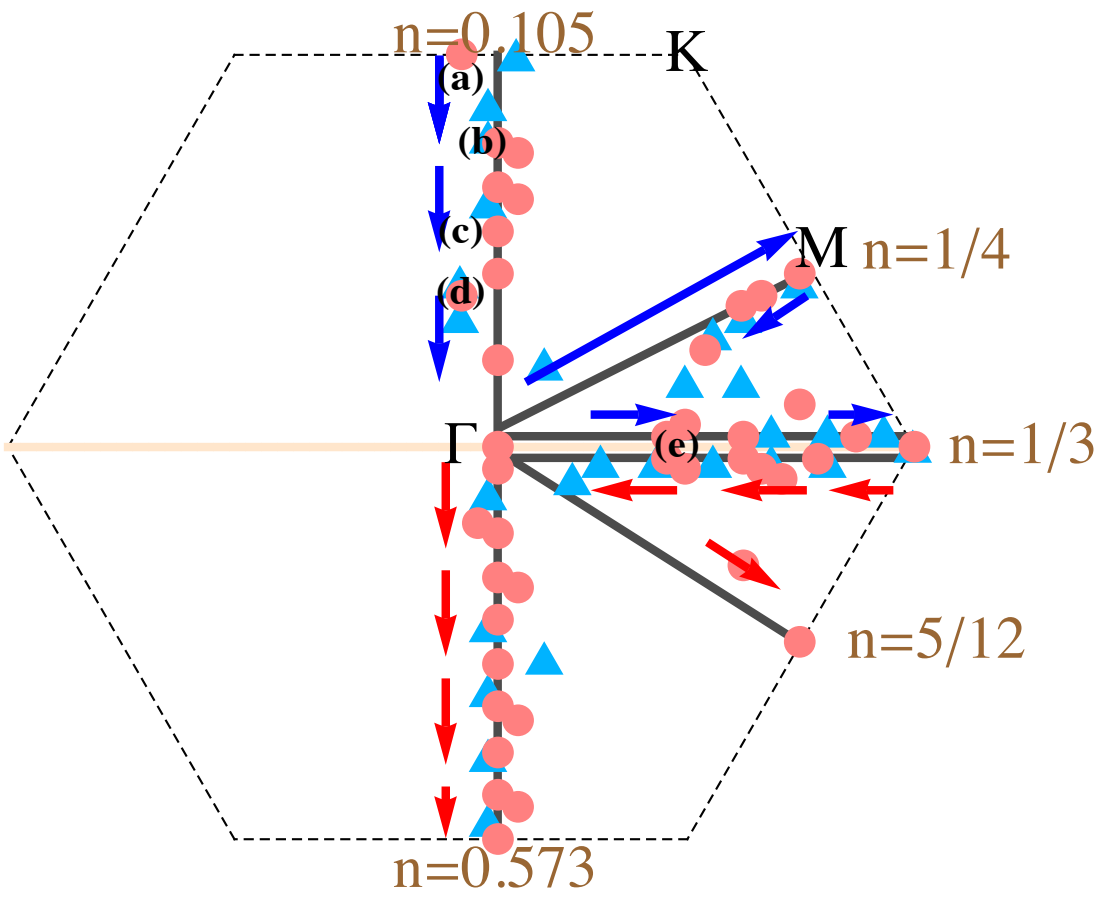

Figure 5.5: Trajectory of the optimal Luttinger-Tisza wave-vector $\mathbf{Q}_{L.T.}$ in the first Kagomé Brillouin zone as the filling is varied, for two different system sizes $N_s = 3 \times 24^2$ and $N_s = 3 \times 36^2$. The 3×3 interaction matrix $J_{\alpha\beta}(\mathbf{q})$ (5.24) is diagonalized for every $\mathbf{q}$ in the zone and the lowest eigen-value is chosen. From this list of $N_s/3$ eigen-values, the wave-vector at which the smallest eigen value occurs is chosen to be $\mathbf{Q}_{L.T.}$. The location of $\mathbf{Q}_{L.T.}$ at every filling is shown by blue triangles (for the $N_s = 3 \times 24^2$) and by pink circles (for $N_s = 3 \times 36^2$). Small blue and red arrows guide the trajectory of $\mathbf{Q}_{L.T.}$. Starting from $n = 0.105$, $\mathbf{Q}_{L.T.}$ evolves to move from the zone M point, towards the zone center. Close to $n = 1/4$, there is a discontinuous jump from close to $\mathbf{\Gamma}$ to the M point. At exactly $n = 1/4$, $\mathbf{Q}_{L.T.}$ lies at the zone mid-point. Slightly above $n = 1/4$, $\mathbf{Q}_{L.T.}$ moves back close to $\mathbf{\Gamma}$ and gradually moves towards the zone corner, reaching it at exactly $n = 1/3$. The trajectory in the Kagomé second band is shown by red arrows. Trajectories of $\mathbf{Q}_{L.T.}$ in both bands are related by $\mathbf{Q}_{L.T.}(n) = \mathbf{Q}_{L.T.}(2/3 - n)$

row in Fig.5.4, connecting states labeled (e). $\mathbf{Q}_{L.T.}$now moves along a different symmetry axis of the zone, connecting the zone corners (see Fig.5.5). At exactly $n = 1/3$ filling the Fermi surface shrinks to a point at the zone corner and the nesting vector $\mathbf{Q}_{L.T.}$is exactly at the zone corner, shown by the vector labeled $\mathbf{Q}_K$ in Fig.5.4.

For $n > 1/3$, the first band is filled and the F.S. falls in the second band. Due to a symmetry relating these two bands, the evolution from $n = 1/3$ to $n = 2/3$, as shown in Fig. 5.5, is the same as the first band, so that n and $2/3 - n$ always have the same $\mathbf{Q}_{L.T.}$. This is also seen in Fig.5.5.

The distribution of Luttinger-Tisza eigenvalues $\lambda^{\nu}_{L.T.}(\mathbf{q})$ across different $\{\mathbf{q}\}$ in the zone, for the range of fillings $0.333 < n < 0.381$ is shown in Fig.5.6. In this range of fillings, the Fermi sea, starting at $n = 1/3$ grows as circles, centered at the zone corner. The Fermi surface slowly acquires a C_3 symmetry, with increasing filling, and approaches the Van-Hove singularity at $n = 5/12$ in the Kagomé second band. The nesting vector, similar to the one shown connecting the (e) electronic states in Fig.5.4, moves from close to the zone corner, along an axis connecting the zone corners, to the zone center $\mathbf{\Gamma}$, as shown in Fig.5.5. For the fillings in Fig.5.6, the dominant (negative) Luttinger-Tisza eigen-value is seen to move from the zone corners, at a filling of one-third, towards the zone center. Also evident from the figure is the six fold symmetry in the L.T. vectors $\{\mathbf{Q}_{L.T.}\}$, as seen by the six red peaks in Fig.5.6(k).

The optimal Luttinger-Tisza wave-vectors therefore evolve in the zone, as the Fermi surface changes with filling. $\mathbf{Q}_{L.T.}$always move along special symmetry axis in the zone, connecting either the zone mid-points or the zone corners. The L.T. method presents us with a set of optimal L.T. wave-vectors at every

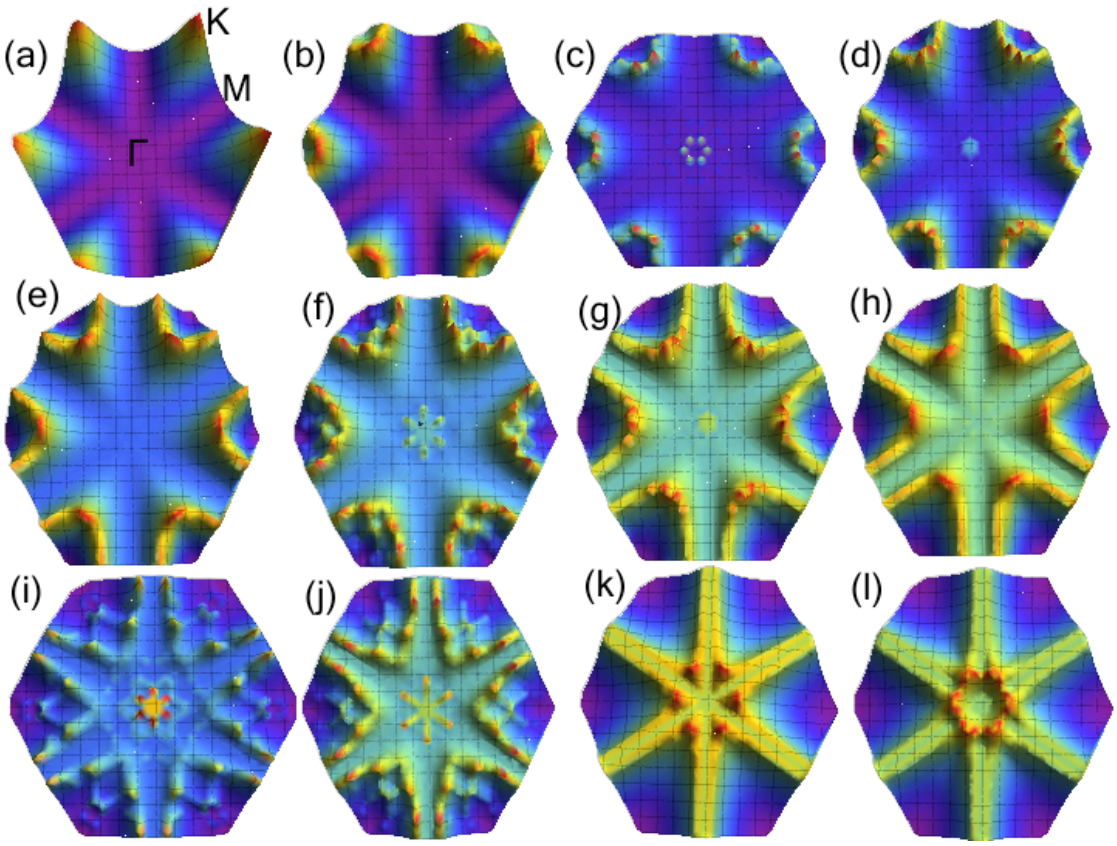

Figure 5.6: Eigenvalues $\lambda^{\nu}(\mathbf{q}, \mathbf{n})$ of the $J_{\alpha\beta}(\mathbf{q})$ in the lowest band $\nu = 1$(see (5.24)) in the Kagomé first B.Z. The eigenvalues $\lambda^{\nu}(\mathbf{q})$ of $J_{\alpha\beta}(\mathbf{q})$ matrix (5.24) in the lowest band evolve with filling n: (a) 0.333 (b)0.343 (c) 0.352 (d) 0.354 (e) 0.364 (f) 0.372 (g) 0.375 (h) 0.381 (i) 0.41. Data for $N = 3{\times}36^2$ lattice and color scheme is red(high), blue (low). The optimal Luttinger-Tisza wave-vector is seen to move from the zone corner to the zone center.This happens in the range of fillings $1/3 < n < 5/12$, and is also seen from the locus of $\mathbf{Q}_{L.T.}(n)$ in Fig.5.5

filling (except for filling corresponding to the Van-Hove points) to construct a normalizable spin configuration from.

Unfortunately, except for a few commensurate fillings where $\mathbf{Q}_{L.T.}$ lies at special symmetry points in the zone, it is not possible to find a spin configuration made entirely out of the optimal L.T. wave-vectors and which also satisfies the constraint of unit spin normalization at every site. For such general cases, we need to carry out an iterative minimization procedure for finding the op-

timal spin configuration. We next discuss some special fillings at which it is indeed possible to construct normalizable spin configurations from the set of $\mathbf{Q}_{L.T.}$wave-vectors.

5.5 Commensurate orders at special fillings

We look at special fillings where it is possible to construct normalizable spin configurations from the set of optimal Luttinger-Tisza wave-vectors $\{\mathbf{Q}_{L.T.}\}$. It is important to use both the optimal L.T. wave-vector and the corresponding L.T. mode $u^{\nu}(\mathbf{Q}_{L.T.})$ to construct a normalizable spin configuration on the lattice. The L.T. wave-vector, by itself, is not sufficient to determine a guess for the optimal spin configurations minimizing the RKKY energy (5.17), for a given set of RKKY couplings $\{J_{i(\alpha),j(\beta)}\}$.

A simple example of this can be observed near fillings close to zero, where $\mathbf{Q}_{L.T.} = 0$, and the two simplest states which can be constructed with unit spin normalization is the simple ferromagnetic state and the anti-ferromagnetic 120 deg. $\mathbf{q} = 0$ state [1]. Both these states have $\mathbf{Q}_{L.T.} = 0$ as their ordering wave-vectors and both states are normalizable. However, *only* the ferromagnetic state is stabilized at fillings near zero because all RKKY interactions are ferromagnetic as seen in Fig.5.3. Therefore, it is important to look at the Luttinger-Tisza modes $u^{\nu}(\mathbf{Q}_{L.T.})$ at the optimal wave-vectors $\{\mathbf{Q}_{L.T.}\}$ to determine the optimal spin configurations.

There are three advantages of constructing normalized spin configurations from Luttinger-Tisza modes $u^{\nu}(\mathbf{Q}_{L.T.})$ at special fillings where it is possible to do so using only the optimal L.T. modes without any contributions from modes

located at other wave-vectors in the zone. The first is that the constructed states will have commensurate ordering vectors- i.e. the ordering wave-vector of the spin configuration will lie at a special symmetry point in the zone. This would lead us to construct some well known states on the Kagomé lattice which are also stabilized in various other models[13][27].

Secondly, these commensurate states will form part of a trial data-base for the variational calculation described in Section 5.7 . It is important to include such commensurate states in the trial-data base because, although some of them might not be stabilized in the RKKY limit of the model, they might be stable at large strengths of the Kondo coupling.

Finally, for special fillings at Van-Hove points in the zone, where $J_{\alpha\beta}(\mathbf{q})$is singular, and it is not possible to obtain RKKY couplings, construction of such commensurate orders with ordering wave-vectors that nest the Fermi surface, is our best guess for states that are expected to be stable in such parts of the phase diagram. With these motivations in mind, we next outline the construction of some simple commensurate orders on the Kagomé lattice.

5.5 .1 Ferromagnetic order at $n = 0$

The simplest commensurate order is the (collinear) Ferromagnetic order where all spins on the lattice point in the same direction in spin space. The state is expected to be stable near $n = 0$[14], where all RKKY interactions are ferromagnetic.

[13]For example, we can construct the well known coplanar $\sqrt{3} \times \sqrt{3}$ state which is also the ground state on addition of quantum or thermal fluctuations to the nearest neighbor Heisenberg model

[14]Ferromagnetic state is also the lowest energy state for all fillings in the flat Kagomé band, as found from the variational calculation of Section 5.7

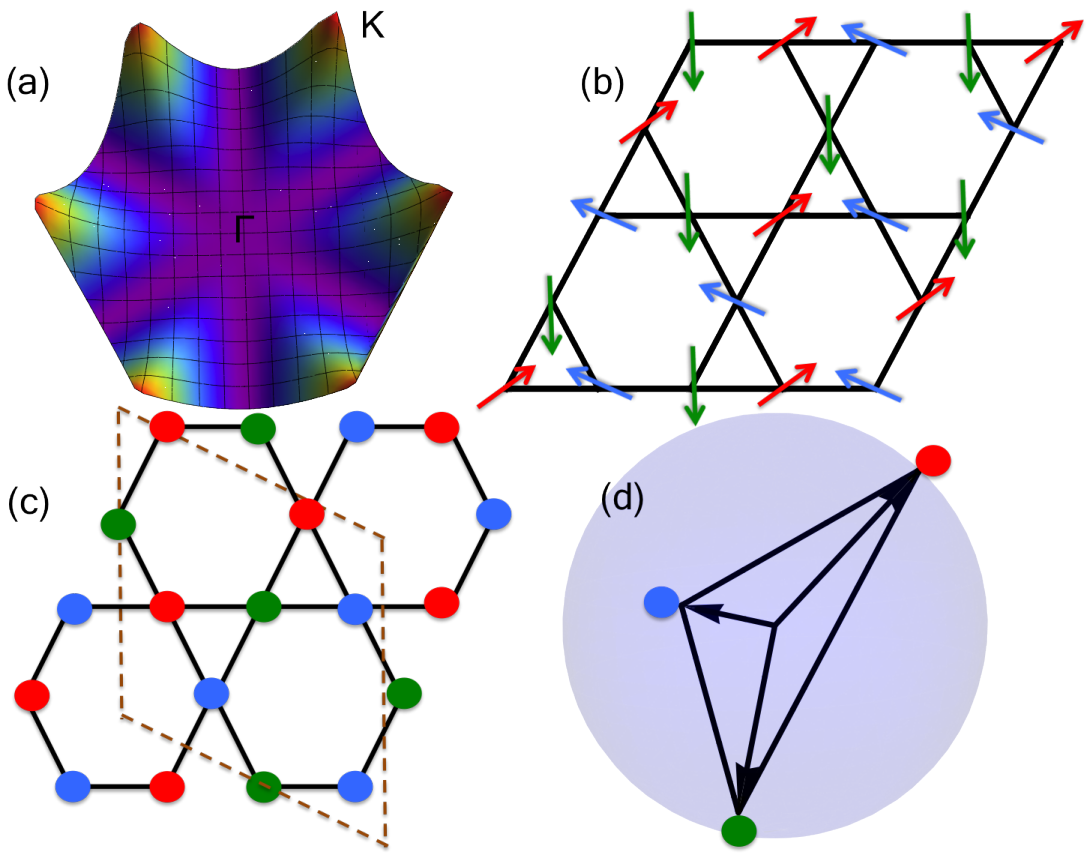

Figure 5.7: Stabilization of $\sqrt{3} \times \sqrt{3}$ in the RKKY limit of the Kondo Lattice Model at one-third filling. (a) Distribution of Luttinger-Tisza eigen-values $\lambda^{\nu}(\mathbf{q})$ in the lowest band $\nu = 1$ in the first Brillouin zone $\{\mathbf{q}\}$. The magnitude of the eigen-values are shown on a color scale with red corresponding to the highest values and blue to the minimum values. The most dominant negative eigen-value of the Luttinger-Tisza matrix $J_{\alpha\beta}(\mathbf{q})$occurs at the zone corner, labeled by K. (b) The $\sqrt{3} \times \sqrt{3}$ order on the Kagomé lattice. The three distinct spin directions are shown in different colors - red, green and blue. (c) $\sqrt{3} \times \sqrt{3}$ order on the lattice, the different colored discs indicate different spin directions. Dashed brown lines enclose the magnetic unit cell for the $\sqrt{3} \times \sqrt{3}$ order. The magnetic unit cell contains nine sites. (d) A 'common-origin plot' constructed by plotting all spins on the lattice, for the $\sqrt{3} \times \sqrt{3}$ order, as vectors with a common origin. The plot shows only three distinct directions in spin space. The tips of the vectors form an equilateral triangle

The wave vector $\mathbf{Q}_{L.T.}$ of the L.T. mode $u^{\nu}(\mathbf{Q}_{L.T.})$ lies near $n = 0$ lies at the zone center, $\mathbf{Q}_{L.T.} = 0$ and the spins on the lattice are given by: $\mathbf{S}_i^{\alpha} = (1, 0, 0)$ (this spin order is one from an infinite family of degenerate spin configurations obtained by global O(3) rotations of the state $\mathbf{S}_i^{\alpha} = (1, 0, 0)$). The magnetic unit cell of the Ferromagnetic state contains a single site. We next move on to more complex coplanar orders.

5.5 .2 $\mathbf{q} = 0$ order at $n = 0$ and $n = 2/3$

The simplest coplanar antiferromagnetic order on the Kagomé lattice is the $\mathbf{q} = 0$ order. The order has a magnetic unit cell of three sites, same as the Kagomé lattice sites. Spin on the three sublattices are coplanar and make a relative angle of $2\pi/3$ rad.. The state therefore belongs to a family of three coloring states on the Kagome lattice [28]. The 3 coloring states are an extensive (in the system size) family of degenerate ground states of the nearest neighbor classical Heisenberg anti-ferromagnet on the Kagomé lattice. All 3 coloring states are ground states of the nearest neighbor classical Heisenberg anti-ferromagnet on the Kagome lattice.

The $\mathbf{q} = 0$ state has an ordering wave-vector $\mathbf{Q}_{L.T.} = 0$, which occurs at two fillings: $n = 0$ and $n = 2/3$. However, at both these fillings, the dominant RKKY interactions are ferromagnetic Fig.5.3, and therefore we do not expect the $\mathbf{q} = 0$ to be the ground state of the RKKY Hamiltonian (5.17) at these two fillings. We however, construct this state, and put it in the variational data-base of trial ground states of the Kondo Hamiltonian in the later section.

The $\mathbf{q} = 0$ state on the Kagomé lattice is parametrized as:

$$\mathbf{S}_{i(\alpha)} = \mathbf{Re}[e^{i(\mathbf{Q}_{L.T.}\cdot\mathbf{R}_i+\varphi_\alpha)}(\mathbf{e}_1 - i\mathbf{e}_2)] \tag{5.25}$$

where $\mathbf{Q}_{L.T.} = 0$, $\mathbf{R}_i$ is the position vector of the unit cell i, $\varphi_\alpha = 2\pi(\alpha-1)/3$ and $\mathbf{e}_{1,2}$ are two orthonormal unit vectors.

5.5 .3 $\sqrt{3}\times\sqrt{3}$ order at $n = 1/3$

The $\sqrt{3}\times\sqrt{3}$ order, shown in Fig5.7(b), is a coplanar order with nine sites in the magnetic unit cell. Nearest neighbor spins, similar to the $\mathbf{q} = 0$ state, are at a relative angle of $2\pi/3$. In spin space there are only three different directions in which all spins point. The tips of the three different spins on the lattice form an equilateral triangle in spin space as shown in Fig.5.7(d).

The magnetic unit cell of the $\sqrt{3}\times\sqrt{3}$ order, as shown by a dashed brown line in Fig.5.7(c), has nine sites (instead of three as in the $\mathbf{q} = 0$ order). The order has a wave-vector $\mathbf{Q}_K$ lying at the zone corner as shown in Fig.5.4. This ordering wave-vector is the optimal Luttinger-Tisza wave-vector of an optimal spin configuration at exactly $n = 1/3$ filling (see Fig. 5.7(a)). The matrix $J_{\alpha\beta}(\mathbf{q})$has its most dominant negative eigen-value at the zone corners as shown by the distribution of $\lambda^\nu(\mathbf{q})$ in the zone in Fig.5.7(a). We conjecture, based on the agreement between the ordering wave vector of the $\sqrt{3}\times\sqrt{3}$ order and the optimal wave-vector of the L.T. mode at one-third filling, that the ground state of the RKKY Hamiltonian (5.17) at one-third filling is the $\sqrt{3}\times\sqrt{3}$ order.

An independent line of reasoning for the stability of the $\sqrt{3}\times\sqrt{3}$ order at one-third filling is obtained by observing the dominant RKKY interactions shown in

Fig.5.3. At a filling of $n = 1/3$, the dominant nearest neighbor J_1 interaction is anti-ferromagnetic (positive). There are an extensive number of ground states favored by just the J_1 interaction. These are all states with nearest neighbor spins making a relative angle of $2\pi/3$ rad. with respect to each other. Since there are an extensive number of such classical states on the lattice (the $\mathbf{q} = 0$ state, in the previous section, being another example of such a state) the J_1 interaction does not select from within this extensive space of degenerate states. The nest dominant interaction J_2 is ferromagnetic (negative) in Fig.5.3 and this favors the $\sqrt{3} \times \sqrt{3}$ state over the $\mathbf{q} = 0$ order, since second nearest neighbor spins are perfectly aligned and parallel in the $\sqrt{3} \times \sqrt{3}$ state, whereas they are at $2\pi/3$ rad. in the $\mathbf{q} = 0$ order.

The $\sqrt{3} \times \sqrt{3}$ order, similar to the $\mathbf{q} = 0$ order, can be parametrized as

$$\mathbf{S}_{i(\alpha)} = \mathbf{Re}[e^{i(\mathbf{Q}_K \cdot \mathbf{R}_i + \varphi_\alpha)}(\mathbf{e}_1 - i\mathbf{e}_2)] \tag{5.26}$$

where $\mathbf{Q}_K$ lies at the zone corner and $\varphi_\alpha = 2\pi(\alpha - 1)/3$ for sub-lattices $\alpha = 1, 2, 3$.

We next move on to more complicated non-coplanar commensurate orders on the Kagomé lattice. There are two such orders with wave-vectors lying at the zone mid-points and these orders are expected to be stable at the Van-Hove fillings of $n = 1/4$ and $n = 5/12$.

5.5 .4 The non-coplanar *Cuboc2* state at $n = 1/4$ and $n = 5/12$

At the Van-Hove fillings of $n = 1/4$ and $n = 5/12$ the Luttinger-Tisza wave-vector is expected[15] to lie at the zone mid-points. One such vector is shown in Fig.5.4 and labeled $\mathbf{Q}_M$. Two non-coplanar states can be constructed from the three inequivalent (but related by C_3 symmetry) wave-vectors lying at the zone-mid points. Both these states have twelve sites in the magnetic unit cell with spins pointing at the vertices of a *cuboctahedron*, hence the nomenclature *Cuboc1*[14] and *Cuboc2*[29]. We discuss the *Cuboc2*[29] state first.

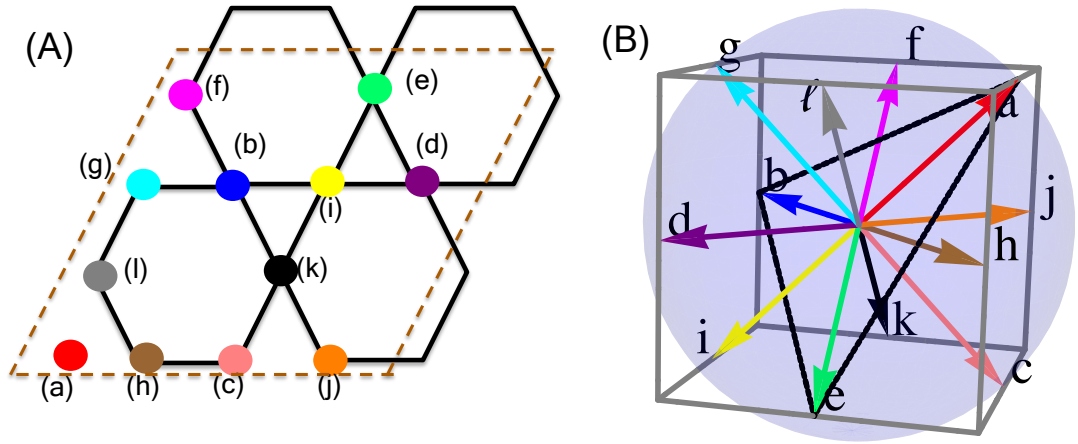

Figure 5.8: *Cuboc2* state on the Kagomé lattice. (A) The twelve site magnetic unit cell of the *Cuboc2* state is shown with each of the twelve spins shown by a differently colored disc. The coloring of the discs corresponds to the color of the spins in (B) pointing at the mid-points of the twelve edges of a unit cube. The *Cuboc2* state is non-coplanar with nearest neighbor spins making an angle of $\pi/3$ rad. and is therefore expected to be stable for fillings where the nearest neighbor RKKY interaction J_1 in Fig.5.3 is ferromagnetic (negative)

The twelve spins in the magnetic unit cell of the *Cuboc2* state are shown

[15]Since the Luttinger-Tisza matrix $J_{\alpha\beta}(\mathbf{q})$is singular at both these fillings, it is not possible to find the optimal eigen-vector corresponding to the lowest eigen-value. However, wave-vecttors lying at the zone-mid points perfectly nest the hexagonal Fermi surface (shown in Fig.5.4)

by the differently colored discs in Fig.5.8(A). Each colored disc corresponds to a spin direction in Fig.5.8(B). The nearest neighbor spins in the *Cuboc2* state make a relative angle of $\pi/3$ radians. The state will therefore be favored for fillings where the nearest neighbor RKKY interaction J_1 is the most dominantly negative interaction. The nearest neighbor RKKY J_1 interaction is not the most dominant of the set of RKKY interactions $\{J_{i(\alpha)j(\beta)}\}$ at fillings $n = 1/4, 5/12$. However, as for the $\mathbf{q} = 0$ state, the *Cuboc2* state can still form part of the trial data base and can appear in parts of the phase diagram away from the RKKY limit [16].

The *Cuboc2* state, due to its non-coplanar structure, has a non-vanishing scalar spin chirality defined by $\chi_{i,j,k} = \mathbf{S}_i \cdot \mathbf{S}_j \times \mathbf{S}_k$. There are two degenerate classes of states related by an improper rotation in spin space (or real space). The value of χ_{ijk} is $+1/\sqrt{2}$ on all the up triangles and $-1/\sqrt{2}$ in all the down triangles in one of the two states. In the other degenerate state,χ_{ijk} has a value $-1/\sqrt{2}$ on all the up triangles and $+1/\sqrt{2}$ on all the down triangles on the Kagomé lattice. The equal and opposite scalar chiralities lead to zero overall flux and no Anomalous Hall response[11]. Because of this scalar spin chirality, an additional property of the *Cuboc2* state is its Z_2 symmetry. The *Cuboc2* state has a Z_2 symmetry i.e. there are two degenerate states related by a Z_2 symmetry. One of these states has a chirality $+1(-1)$ on all the up (down) triangles and the other partner state has a chirality $-1(+1)$ on all the up (down) triangles.

In two spatial dimensions, gapless spin waves destroy long range order at any finite temperature, due to the Mermin-Wagner theorem[30]. However, in spite of the destruction of long range order in the spins at any finite temperature,

[16] *Cuboc2* state is found to be stable at the commensurate filling $n = 2/3$ in the variational phase diagram Fig.5.15

an emergent chiral order, like the the Z_2 order of the *Cuboc2* state, can exist up to finite temperatures[29, 31]. This Z_2 symmetry is absent in all other ground state spin orders of the RKKY Hamiltonian (5.17) on the Kagomé lattice, all of which possess a *continuous* $O(3)$ symmetry which remains unbroken in two spatial dimensions at finite temperatures. These states (with continuous symmetries) can therefore only be realized at zero temperature in two dimensions.

Finally, the *Cuboc2* state can be parameterized as follows:

$$\begin{aligned}
\mathbf{S}_{i(1)} &= \frac{1}{\sqrt{2}}[\cos(\mathbf{Q}_2 \cdot \mathbf{R}_i)\mathbf{e}_2 + \cos(\mathbf{Q}_3 \cdot \mathbf{R}_i)\mathbf{e}_3] \\
\mathbf{S}_{i(2)} &= \frac{1}{\sqrt{2}}[-\cos(\mathbf{Q}_1 \cdot \mathbf{R}_i)\mathbf{e}_1 + \cos(\mathbf{Q}_3 \cdot \mathbf{R}_i)\mathbf{e}_3] \\
\mathbf{S}_{i(3)} &= \frac{1}{\sqrt{2}}[-\cos(\mathbf{Q}_1 \cdot \mathbf{R}_i)\mathbf{e}_1 + \cos(\mathbf{Q}_2 \cdot \mathbf{R}_i)\mathbf{e}_2]
\end{aligned} \tag{5.27}$$

where $\mathbf{Q}_2 = 2\pi(1/4, -1/(4\sqrt{3}))$, $\mathbf{Q}_3 = \mathcal{R}_{\pi/3}\mathbf{Q}_2$ and $\mathbf{Q}_1 = \mathcal{R}_{2\pi/3}\mathbf{Q}_2$. $\mathcal{R}_\theta$ is the 2×2 rotation matrix.

We next move on to the anti-ferromagnetic cousin of the *Cuboc2* state, called the *Cuboc1* order.

5.5 .5 The non-coplanar *Cuboc1* state at $n = 1/4$ and $n = 5/12$

Within the manifold of the 120 degree or three coloring[28] classical states on the Kagome lattice, the *Cuboc1* state, shown in Fig.5.9, is a *maximally* non-coplanar 120 deg. state. Spins in each of the up and down triangles are coplanar and form relative angles of $2\pi/3$ as seen from the triangle in Fig.5.9(B),

however the planes of two corner sharing triangles are at a relative angle of $\cos^{-1}(-1/3)$rad. (thereby implying that normals to the triangular planes point along the vertices of a regular tetrahedron[32]). The state is one from amongst the extensive degenerate manifold of ground states of the nearest neighbor classical Heisenberg model on the Kagomé lattice (in the presence of only a nearest neighbor anti-ferromagnetic interaction, the *Cuboc1* is degenerate in energy with the $\mathbf{q} = 0$ and the $\sqrt{3} \times \sqrt{3}$ orders).

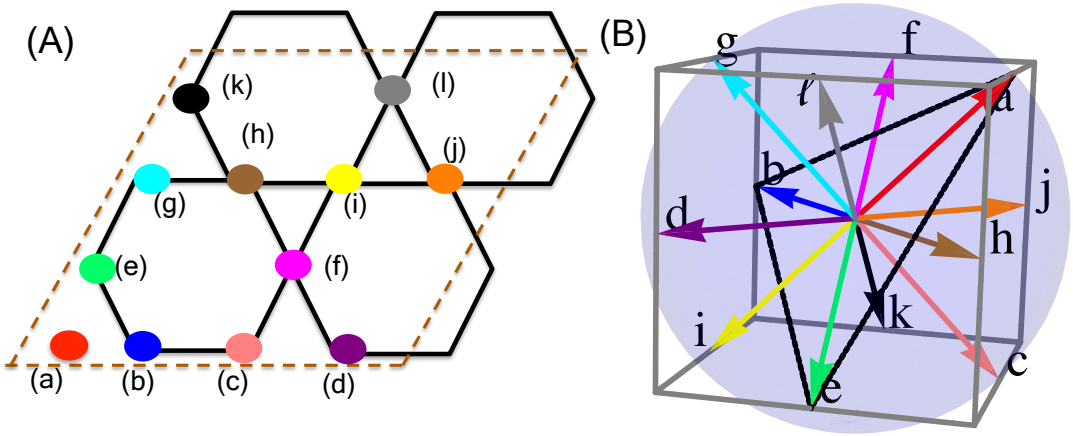

Figure 5.9: *Cuboc1* state on the Kagomé lattice. (A) The twelve site magnetic unit cell of the *Cuboc1* state is shown with each of the twelve spins shown by a differently colored disc. The coloring of the discs corresponds to the color of the spins in (B) pointing at the mid-points of the twelve edges of a unit cube. Spins in each triangle are coplanar and point along the vertices of an equilateral triangle, as shown by the triangle in (B), similar to the $\mathbf{q} = \mathbf{0}$ and $\sqrt{3} \times \sqrt{3}$ orders (see Fig.5.7(D)). The *Cuboc1* state is non-coplanar with nearest neighbor spins making an angle of $2\pi/3$ rad. and is therefore expected to be stable for filling $n = 5/12$ where the nearest neighbor RKKY interaction J_1 in Fig.5.3 is anti-ferromagnetic (positive)

The *Cuboc1* is a good candidate state for the ground state of the RKKY Hamiltonian at $n = 5/12$ because the Fermi surface at this filling is perfectly nested by three inequivalent wave-vectors lying at the zone mid-points (see Section 5.4.2

and Fig.5.4). These wave-vectors also happen to be the ordering vectors of the *Cuboc1* state. The state, parametrized in terms of these ordering wave-vectors, is given by:

$$\begin{aligned}
\mathbf{S}_{i(1)} &= \frac{1}{\sqrt{2}}[\cos(\mathbf{Q}_2 \cdot \mathbf{R}_i)\mathbf{e}_2 + \cos(\mathbf{Q}_3 \cdot \mathbf{R}_i)\mathbf{e}_3] \\
\mathbf{S}_{i(2)} &= \frac{1}{\sqrt{2}}[\cos(\mathbf{Q}_1 \cdot \mathbf{R}_i)\mathbf{e}_1 - \cos(\mathbf{Q}_3 \cdot \mathbf{R}_i)\mathbf{e}_3] \\
\mathbf{S}_{i(3)} &= -\frac{1}{\sqrt{2}}[\cos(\mathbf{Q}_1 \cdot \mathbf{R}_i)\mathbf{e}_1 + \cos(\mathbf{Q}_2 \cdot \mathbf{R}_i)\mathbf{e}_2]
\end{aligned} \tag{5.28}$$

where $\mathbf{Q}_2 = 2\pi(1/4, -1/(4\sqrt{3}))$, $\mathbf{Q}_3 = \mathcal{R}_{\pi/3}\mathbf{Q}_2$ and $\mathbf{Q}_1 = \mathcal{R}_{2\pi/3}\mathbf{Q}_2$, similar to the *Cuboc2* state. In addition, the nearest neighbor RKKY coupling at $n = 5/12$ (see Fig.5.3) is the most dominant interaction and is antiferromagnetic (positive), favoring the $2\pi/3$ alignment of nearest neighbor spins in the *Cuboc1* state.

We end this Section by summarizing the major results. Using the Luttinger-Tisza[19] method we track the evolution of the optimal Luttinger-Tisza wave-vector (which is expected to be the ordering wave-vector of the different ground state spin configurations of the RKKY Hamiltonian (5.17)) as a function of filling and show that for *all* fillings, L.T. wave-vector comes from nesting wave-vectors of the Fermi surface. We uncovered two different kinds of nesting mechanisms. For a generic filling, the Fermi surface is circular (with a three or six fold symmetry) and in the absence of any parallel edges, the nesting wave-vectors connect points with the maximum curvature on the Fermi surface (Fig.5.4). This kind of nesting is different from the nesting behavior at special Van-Hove fillings in the zone, where the nesting wave-vector connects straight and parallel edges of the perfectly hexagonal Fermi surfaces.

Using the optimal Luttinger-Tisza wave-vectors we construct five commensurate spin orders on the Kagomé lattice and indicate regions of the phase diagram where they are expected to be stable, consistent with the behavior of the dominant RKKY interactions in Fig.5.3. In the next section, using brute force minimization of the RKKY Hamiltonian (5.17), we calculate the optimal spin orders on the Kagomé lattice at several different fillings.

5.6 Symmetry broken orders

In most generic cases the L.T. modes are insufficient for creating a normalizable spin configuration. In such cases, the L.T. wavevector is insufficient to define a spin order, because the L.T. star usually includes several symmetry-related wavevectors, and there are many different ways these could be distributed on the three sublattices of the Kagomé lattice, or even across the different spin components on a given Kagomé sub-lattice.

To find the optimal ground state spin configurations of the RKKY Hamiltonian (5.17) we develop an approach complementary to the Luttinger-Tisza method. The approach is variational in spirit and is called 'iterative minimization'. We carry out iterative minimization of the Hamiltonian at several fillings in the lowest two Kagomé bands. The resultant optimized spin configurations are parametrized using both real and Fourier space diagnostics. A rich set of symmetry broken orders, as ground states of the RKKY Hamiltonian, are found on the Kagomé lattice and we classify them in to eight phases depending on the nature of their broken symmetries. We begin by discussing the iterative minimization procedure and diagnostics for detecting the nature of symmetry

breaking for the different optimal spin orders.

5.6 .1 Numerical minimization of the RKKY Hamiltonian and diagnostics for spin configurations

We describe below the procedure for obtaining the optimal spin configuration $\{\mathbf{S}^{opt}_{i(\alpha)}\}$, at several different electronic fillings, by minimizing the energy of the RKKY Hamiltonian (5.17). We also develop a set of diagnostics for parametrizing the optimal spin orders.

Iterative minmization

The iterative minimization procedure is a zero temperature algorithm where spins on the lattice are chosen at random and aligned with their local fields. The local field $\mathbf{h}_{i(\alpha)}$ at a site belonging to unit cell i and sub-lattice α on the lattice is given by:

$$\mathbf{h}_{i(\alpha)} = \sum_{j(\beta)\neq i(\alpha)} J_{i(\alpha)j(\beta)}\mathbf{S}_{j(\beta)} \tag{5.29}$$

where $\{J_{i(\alpha)j(\beta)}(n)\}$ is the set of RKKY interactions at filling n and the sum runs over all spins, except the spin at site $i(\alpha)$, on the lattice. At every step of the iteration, we choose a set of $N < N_s$ spins (N is $\mathcal{O}(N_s)$) on the lattice at random and orient each of their directions along the local fields at their sites. The configuration of local fields corresponds to the spin configuration in the previous iteration and is the same for all N spin updates.

This algorithm is different than the minimization methods for short ranged Heisenberg interactions[17, 18] where only a single (instead of N) spin is updated at every iteration. Updating N spins makes the move non-local in configuration space and leads to faster convergence[33].The iterations continue until the RKKY energies in successive iterations have converged and energy differences are below a tolerance, which is typically set to be around $\sim 10^{-10}$.

The iterative minimization procedure is a 'steepest descent' algorithm and is susceptible to getting stuck in local minimums. We therefore start with several initial random spin configurations and ensure that the same lowest minimum is achieved. All iterations are done using periodic boundary conditions for the spin orders. The optimal spin configuration $\{\mathbf{S}^{opt}_{i(\alpha)}\}$is then diagnosed for the nature of its symmetry breaking using the methods outlined next.

Diagnostic: Common origin plot

An insight into the nature of the spin configuration $\{\mathbf{S}^{opt}_{i(\alpha)}\}$; obtained from the iterative minimization; can be obtained by plotting all spins on the lattice as unit vectors with a common origin[17, 18]. Such a plot reveals the symmetry of the spin order in spin space. Examples of common origin plots for some of the commensurate orders constructed in the previous Section can be seen in Figures: 5.7(D), 5.8(B) and 5.9(B). A useful technique for displaying the order in spin space is to display spins belonging to the three different sub-lattices in three different colors. This reveals the sub-lattice symmetry of the spin order.

A drawback of the common origin plot is that it completely obscures the symmetry of the spin order in real space. To reveal this symmetry we directly

plot the optimal spin configuration on the Kagomé lattice and attempt to identify the symmetry properties of the spin order. This is particularly illuminating and easier to do in the case of two dimensional lattices like the Kagomé.

However, since most of the optimal spin orders are incommensurate and non-coplanar, and therefore difficult to visualize in real space, our most effective diagnostic is to detect orders in Fourier space, which we discuss next.

Diagnostic: Fourier composition of optimal spin orders

The Fourier space diagnostic involves obtaining the Fourier composition of all three spin components on each of the three Kagomé sub-lattices. The Fourier compositions allows us to identify the dominant wave-vectors making up the optimal spin configurations on each of the sub-lattices. This is particularly helpful in the case of incommensurate orders, whose symmetry might be difficult to infer in real space, but will have a sharp distribution in Fourier space centered at the incommensurate ordering wave-vector of the spin configuration.

To obtain the Fourier composition of each sub-lattice we define the Fourier transform of the optimal spin distribution, on each of the three Kagomé sub-lattices, in the following way:

$$\mathbf{S}_{\alpha}^{opt}(\mathbf{q}) = \frac{1}{\sqrt{N_s/3}} \sum_{i} \mathbf{S}_{i(\alpha)}^{opt} e^{-i\mathbf{q}\cdot\mathbf{R}_i} \tag{5.30}$$

where $\mathbf{R}_i$ is the position vector of unit cell i on the lattice. $\mathbf{S}_{\alpha}^{opt}(\mathbf{q})$ is a 3×1 complex vector. The Fourier weights of the wave-vector $\mathbf{q}$ in the optimal spin configuration $\{\mathbf{S}_{i(\alpha)}^{opt}\}$can then be mapped out by defining, for each $\{\mathbf{q}\}$ in the

first Brillouin zone, $\eta_\alpha(\mathbf{q})$[17]:

$$\eta_\alpha(\mathbf{q}) = \frac{\sum_{\mu=x,y,z} \left(S_\alpha^{opt,\mu}(\mathbf{q})\right)^* S_\alpha^{opt,\mu}(\mathbf{q})}{\sum_{\mathbf{q}\in 1stB.Z.} \sum_{\mu=x,y,z} \left(S_\alpha^{opt,\mu}(\mathbf{q})\right)^* S_\alpha^{opt,\mu}(\mathbf{q})} \tag{5.31}$$

where the index μ runs over the three spin components x, y, z.

The set of wave-vectors from the zone, with the largest $\eta_\alpha(\mathbf{q})$ across all α, will be called the dominant star of wave-vectors making up the spin configuration. For commensurate orders, the sum of $\eta_\alpha(\mathbf{q})$, across all $\{\mathbf{q}\}$ belonging to the dominant star, equals one i.e. the spin configuration uses up *only* wave-vectors from the dominant star and furthermore these vectors lie at special commensurate positions in the zone. An incommensurate spin order, on the other hand, will have most of its weight (typically greater than 90%) within the dominant star of wave-vectors, and the remainder of its weight will be distributed across a tail of sub-dominant modes which are required for unit spin normalization at every site on the lattice.

As an example of the distribution of $\eta_\alpha(\mathbf{q})$ across the different sub-lattices, we can consider some of the commensurate orders discussed before. The coplanar $\sqrt{3} \times \sqrt{3}$ order is an example where all three sub-lattices are composed of a single wave-vector $\mathbf{Q}_K$(5.26) lying at the zone corner. Hence, the Fourier composition of the three sub-lattices is one for the wave-vector at the zone-corner: $\eta_1(\mathbf{Q}_K) = \eta_2(\mathbf{Q}_K) = \eta_3(\mathbf{Q}_K) = 1$ and zero for all other wave-vectors.

Similarly, the non-coplanar *Cuboc1* and *Cuboc2* states are examples where each sub-lattice has contributions from two of the three inequivalent wave-vectors at the zone mid-points (5.28),(5.27). Correspondingly, two of the three

[17] $\{|\mathbf{S}_\alpha(\mathbf{q})|^2\}$ satisfy the normalization condition: $\sum_{\mathbf{q}\in 1stB.Z.} |\mathbf{S}_\alpha^{opt}(\mathbf{q})|^2 = N_s/3$

wave-vectors will share equal $\eta_\alpha(\mathbf{q})$ on each of the three sub-lattices: $\eta_1(\mathbf{Q}_1) = \eta_1(\mathbf{Q_2}) = 1/2$, where $\mathbf{Q}_1$ and $\mathbf{Q}_2$ are two of the three inequivalent wave-vectors and the other two sub-lattices have the contribution from wave-vectors $\{\mathbf{Q}_2, \mathbf{Q}_3\}$ and $\{\mathbf{Q}_3, \mathbf{Q}_1\}$.

Our primary tool for classifying symmetry broken orders will be the measure $\eta_\alpha(\mathbf{q})$(5.31), which tells us the Fourier weights at different points $\mathbf{q}$ in the zone, that the optimal spin order $\{\mathbf{S}^{opt}_{i(\alpha)}\}$is composed of. However, a drawback of using $\eta_\alpha(\mathbf{q})$ is that we lose information about the sub-lattice locking angles, which might be another way in which spin orders might break symmetries across the three sub-lattices. This phase angle $\varphi_{\alpha\beta}(\mathbf{q})$ between sub-lattices α, β, at wave-vector $\mathbf{q}$, can be defined by taking the overlap between the Fourier transformed vectors on each of the two sub-lattices $\varphi_{\alpha\beta}(\mathbf{q}) =$ arg. $((\mathbf{S}^{opt}_{\alpha}(\mathbf{q}))^\dagger \cdot \mathbf{S}^{opt}_{\beta}(\mathbf{q}))$. Two phases where the different sub-lattices lock with respect to each other with different angles should correspond to different symmetry broken phases. This additional level of phase classification based on sub-lattice locking angles will not be considered in this study for the sake of keeping the phase diagram simple.

We next discuss the nomenclature, based on the metric $\eta_\alpha(\mathbf{q})$, for classifying the different symmetry broken orders occurring in the RKKY phase diagram.

5.6 .2 Nomenclature for classification of symmetry broken orders

The optimal spin configurations from iterative minimization is our starting point for the classification of symmetry broken orders of the RKKY hamiltonian (5.17).

Let us imagine Fourier transforming the actual ground state $\{\mathbf{S}_{i(\alpha)}^{opt}\}$ from iterative minimization. The first step is to identify the dominant mode (which, virtually always, is closely similar to the dominant L.T. mode). This is done using $\eta_\alpha(\mathbf{q})$ (5.31) which maps out the Fourier weights of different wave vectors $\mathbf{q}$ in the optimal spin configuration. The combined set of wave vectors with the highest $\eta_\alpha(\mathbf{q})$ across all sublattices is defined as the star of dominant modes. We zero out the wave vectors except those from that dominant star, and reassemble the configuration in real space: this state will be called the "purified" configuration. The purified configuration $\{\mathbf{S}_{i(\alpha)}^{pure}\}$ is therefore given by[18]:

$$\mathbf{S}_{i(\alpha)}^{pure} = \sum_{\mathbf{q}\in \text{ dom. } \{\mathbf{q}\}} \mathbf{S}_\alpha(\mathbf{q}) e^{i\mathbf{q}\cdot\mathbf{R}_i} \tag{5.32}$$

This is the key starting point, for both our nomenclature to classify orders, and also in the practical processing of configurations from simulation results.

The second part of our label is to specify the way in which different ordering vectors go with the three Kagomé sublattices. The m different ordering

[18]The purified spin configuration constructed from the dominant wave-vectors will *not* be normalized. This is because if the dominant wave-vectors lie at incommensurate zone - points, there will be small but non-zero contributions from sub-dominant modes. Zeroing their contribution in the construction of the purified spin state will violate unit spin normalization at every site. We therefore re-normalize the purified configuration by hand.

wavevectors in use (from that same star) are labeled $a, b, ...$ (As illustrated in Fig. 5.5, it turns out the L.T. vectors and correspondingly the dominant modes, always fall on mirror axes of the zone, which implies the star has at most 3 inequivalent wave vectors hence $m \leq 3$.) Then the label, e.g. (a, b, c), has three entries referring to sublattices 1, 2, and 3 respectively, each listing which wave vectors are used on that sublattice [19] (For short, it is conventional to use the term "mQ" order, distinguishing the number of wave vectors but not their relation to the sublattices.)

As the filling varies, the L.T. wavevectors and the ordering wavevectors found from simulations vary continuously. We classify these phases as being in the same "phase family", if they share the same broken symmetries and evolve smoothly with n. Spin orders which share the same Fourier composition on each of the three sub-lattices are classified as a single phase. For example, all coplanar spirals, where each sub-lattice is dominantly made up of the same incommensurate wave-vector from the zone, will be classified as a single (a, a, a) phase. The label "a" is representative of the wave-vector and the notation (a, a, a) shows that all three sub-lattices are made up of the same wave-vector.

Now it is important to note that there might be several *distinct* coplanar spiral spin-orders with different incommensurate wave-vectors, all being labeled as belonging to (a, a, a) type phase. Each spin order within this set is a *continuously varying second order phase*. To keep the phase diagram simple, we club all such spin orders in to a single (a, a, a) type phase and call it a $1\mathbf{Q}$ order.

Such a classification is incomplete and a bit too crude for our purposes. For

[19] This notation is incomplete, in that it does not specify whether the coefficients of the different wavevectors are equal or unequal, nor does it specific particular phase relationships between the amplitudes of the same wavevector appearing in different sub-lattices. Hence, two qualitatively distinct phases may have the same label.)

example, within the (a, a, a) type phase there might be further types of symmetry breaking and therefore a more detailed need for phase classification. The Fourier weight of the wave-vector "a" in the optimal spin order might be the same on all three sub-lattices, i.e. $\eta_1(a) = \eta_2(a) = \eta_3(a)$ or it might be different. In our more detailed phase classification procedure, described next, we have different notations for whether a dominant wave-vector treats all sub-lattices symmetrically (meaning whether it has the same Fourier weight, as measured by $\eta_\alpha(\mathbf{q})$, on all sub-lattices) and in the case when it breaks symmetry between the sub-lattices.

This detailed classification is done by assigning a numeric subscript to dominant modes on a sublattice based on the symmetry of $\eta_\alpha(\mathbf{q})$ across α [20]. A phase label (a_1, b_1, c_1) indicates that the order is of type "$3\mathbf{Q}$". A "$3\mathbf{Q}$" mode therefore is mode up of three different wave-vectors from the zone and the dominant modes (corresponding to the dominant wave-vectors) have the same Fourier weight on all three sub-lattices. For convenience, we skip writing numerical indices for phases which have no symmetry in the distribution of $\eta_\alpha(\mathbf{q})$. All spin orders recovered in the RKKY limit are classified in to eight competing phases. Most of these phases consist of non-coplanar incommensurate spins: such states dominate the RKKY phase diagram for small J_K. We describe each of these eight phases next, beginning with the simplest coplanar spirals.

[20] We can also look at the locking angles between the different sublattices. For simplicity of classification and due to a limited resolution in fillings, we choose $\eta_\alpha(\mathbf{q})$ as the sole criterion

5.6 .3 The $1\mathbf{Q}$ (a, a, a) and (a_1, a_1, a_1) phases

The simplest spin orders are those belonging to the $1\mathbf{Q}$ type phase, where all sub-lattices are made out of the same L.T. wave-vector (a member of the dominant star of L.T. wave-vectors from the zone). The two dimensional (in spin space) spin orders trace out coplanar spirals on the lattice.

A coplanar spiral is parametrized by its ordering wave vector $\mathbf{q}$ and two phases dependent on the locking between the sublattices. For two orthonormal unit vectors $\mathbf{e}_{1,2}$, a coplanar spiral can be parametrized as

$$\mathbf{S}_{i(\alpha)} = \mathbf{Re}[e^{i(\mathbf{q}\cdot\mathbf{R}_i+\varphi_\alpha)}(\mathbf{e}_1 - i\mathbf{e}_2)] \tag{5.33}$$

Depending on the location of $\mathbf{q}$ in the zone, the spiral can further be classified as commensurate - if $\mathbf{q}$ lies at a special symmetry point in the zone) or incommensurate - if $\mathbf{q}$ lies at an arbitrary wave vector. Examples of special commensurate coplanar spirals are the two well known $\mathbf{q} = 0$ and the $\sqrt{3} \times \sqrt{3}$ Fig.5.7 orders with ordering wave vectors $\mathbf{q} = \mathbf{\Gamma}$ and $\mathbf{q} = \mathbf{K}$ lying at the zone center and zone corner, respectively. For both orders, $\varphi_\alpha = 2\pi(\alpha - 1)/3$ which makes an angle of $2\pi/3$ between spins, locally, on every triangle.

An incommensurate order, on the other hand, has a special direction in real space defined by $\mathbf{q}$ and a set of points $\{\mathbf{R}_{i(\alpha)}\}$, such that $\mathbf{q}\cdot\mathbf{R}_{i(\alpha)} = 2\pi m(\sqrt{N_s/3})^{-1}$ for an integer m. As we move along $\{\mathbf{R}_{i(\alpha)}\}$, we trace out $(\sqrt{N_s/3})^{-1}$ equally spaced coplanar directions in spin space as shown in Fig.5.10. As discussed in the previous section, the two kinds of spiral orders can belong to an (a, a, a) phase or a more symmetric (a_1, a_1, a_1) phase. States from these phases are shown in Fig.5.10 below.

$Filling(n)$	$\mathbf{q}(2\pi)$	η_1	η_2	η_3
0.321	$\begin{pmatrix} 0.27 \\ 0.04 \end{pmatrix}$	0.47	0.47	0.45
0.325	$\begin{pmatrix} 0.14 \\ 0.29 \end{pmatrix}$	0.497	0.497	0.497
$1/3$	$\begin{pmatrix} 2\pi/3 \\ 0 \end{pmatrix}$	0.5	0.5	0.5

Table 5.1: Dominant wave vectors and their Fourier weights on the sublattices. Left to right: Filling at which the spin order originates in the RKKY limit, dominant wave vector in the first B.Z., weight of the dominant wave vectors on each of the three sub-lattices. The ordering wave-vector $\mathbf{q}$ is a vector in the two dimensional Kagome B.Z. and has two components corresponding to the x, y coordinates of the vector. The $\mathbf{S}_\alpha(\mathbf{q})$ are 3×1 column vectors with each entry of the column corresponding to the Fourier transformed spin component (x, y, z). Spin order at filling 0.321 corresponds to (a, a, a) phase. The more symmetric spin orders found at 0.325 (coplanar spiral Fig.5.10 (2A)-(2C)) and at $n = 1/3$ ($\sqrt{3} \times \sqrt{3}$ order Fig.5.7) form part of the (a_1, a_1, a_1) phase

Most of the coplanar spiral spin orders are found near a filling $n = 1/3$ and have wave-vectors lying close to the zone corner. At a filling $n = 0.321$, the states are of the (a, a, a) type and the dominant wave-vector has different weights on the three sub-lattices (or same weights on two of the three sub-lattices and a different weight on the third). As we approach $n = 1/3$, we transition in to the highly symmetrical (a_1, a_1, a_1) type phase where the dominant wave-vector has the same weight on all three sub-lattices. An incommensurate spiral order within this phase occurs at $n = 0.325$, and a commensurate order is the well known $\sqrt{3} \times \sqrt{3}$ which is stabilized at exactly $n = 1/3$.

We next discuss phases where each of the three sub-lattices have two dominant wave-vectors. Depending on the distribution of the weights of the dominant wave-vectors across the three sub-lattices, the spin orders can be classified in to (ab, bc, ca), (a_1b_2, c_1a_2, b_1c_2) or the highly symmetrical (a_1b_1, b_1c_1, c_1a_1) phases.

$\mathbf{q}(2\pi)$	$\mathbf{S}_1(\mathbf{q})$	$\mathbf{S}_2(\mathbf{q})$	$\mathbf{S}_3(\mathbf{q})$
$\begin{pmatrix} 0.12 \\ -0.19 \end{pmatrix}$	$\begin{pmatrix} 0.32e^{-i2.9} \\ 0.4e^{i1.55} \\ 0.26e^{i2.8} \end{pmatrix}$	$\begin{pmatrix} 0.37e^{i0.9} \\ 0.45e^{-i0.8} \\ 0.3e^{i0.4} \end{pmatrix}$	$\begin{pmatrix} 0.36e^{-i0.5} \\ 0.43e^{-i2.2} \\ 0.29e^{-i} \end{pmatrix}$

Table 5.2: Ordering wave vectors and spin Fourier transform for reconstructing purified spin order at $n = 0.311$ Fig.5.10(1A)-(1C). From left to right: Ordering wave vector $\mathbf{q}$ for the $1\mathbf{Q}(a, a, a)$ state, spin F.T. at each wave vector.The spin order Fig.5.10(1A)-(1C) has an additional significant contribution ($\sim 30\%$) on sublattice $\alpha = 1$ from an additional wave vector $\mathbf{q}_2 = 2\pi(0.12, 0.19)$ with Fourier weight $\mathbf{S}_{\alpha=1}(\mathbf{q}_2) = (0.25e^{i1.93}, 0.1e^{i1.96}, 0.3e^{-i1.19})$

$Filling(n)$	$\eta_1(\mathbf{q}_1)$	$\eta_1(\mathbf{q}_2)$	$\eta_2(\mathbf{q}_2)$	$\eta_2(\mathbf{q}_3)$	$\eta_3(\mathbf{q}_1)$	$\eta_3(\mathbf{q}_3)$
0.115	0.22	0.22	0.28	0.19	0.29	0.19
0.146	0.21	0.21	0.27	0.19	0.28	0.19
0.181	0.22	0.22	0.22	0.22	0.22	0.22

Table 5.3: Fourier weights of dominant wave-vectors on the sublattices for the (ab, bc, ca) type phases. Left to right: Filling at which the spin order originates in the RKKY limit., weights of the dominant wave vectors on each of the three sublattices. Fillings 0.115 and 0.146 correspond to (ab, bc, ca) phase, while the more symmetric spin order at 0.181 is a spin set from the (a_1b_2, c_1a_2, b_1c_2) phase. Spin configurations are shown in Fig. 5.11. The dominant wave-vectors are: $\mathbf{q}_1 = 2\pi(0.19, -0.13), \mathbf{q}_2 = 2\pi(0.02, -0.22), \mathbf{q}_3 = 2\pi(0.20, 0.09)$ for $n = 0.115$. $\mathbf{q}_1 = 2\pi(0.15, 0.1), \mathbf{q}_2 = 2\pi(0.02, -0.18), \mathbf{q}_3 = 2\pi(0.15, -0.1)$ for $n = 0.146$ and $\mathbf{q}_1 = 2\pi(0.02, -0.13), \mathbf{q}_2 = 2\pi(0.1, 0.08), \mathbf{q}_3 = 2\pi(-0.13, 0.05)$ for $n = 0.181$.

5.6 .4 The (ab, bc, ca) type phases

The (ab, bc, ca) type of phases belong to the "$3\mathbf{Q}$" family of orders since each spin configuration in the family is made out of three wave-vectors:a, b, c from the zone. The dominant modes on each sublattice are made out of two of the six fold Luttinger-Tisza star of wave-vectors. The first kind of order has different weights of the modes on the three sublattices– indicated as a (ab, bc, ca) phase and shown in Table 5.3 and 5.4 where each sub-lattice is composed of two wave-vectors from the star of dominant L.T. wave-vectors. However, the Fourier weight of a wave-vector on two different sub-lattices is different. The

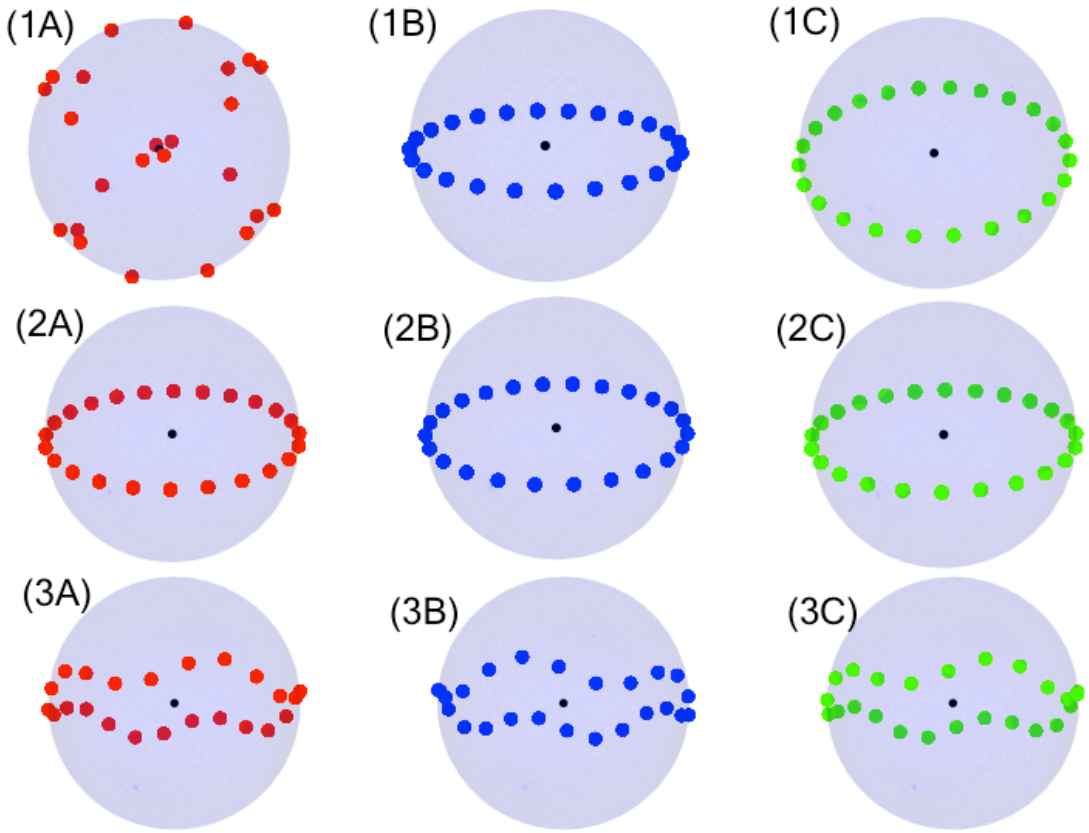

Figure 5.10: Common origin plot of incommensurate coplanar spiral orders belonging to (a, a, a) and (a_1, a_1, a_1) phases. 1(A)-(C): spins on each of the three sublattices for a spin order recovered from MC at $n = 0.311$,2(A)-(C): at $n = 0.321$,3(A)-(C): at $n = 0.325$. The ordering wave vectors for the three states in Table 5.1 and Table 5.2 along with Eq.5.33 can be used to construct $\{\mathbf{S}^{pure}_{i(\alpha)}\}$ (5.32)

second phase is more symmetric as can be seen in Table 5.3 and is labeled $(a_1 b_2, c_1 a_2, b_1 c_2)$. Here, there are three wave-vectors: a, b, c making up the spin configuration and the subscripts $1, 2$ refer to the distinct Fourier weights that these wave-vectors have on different sub-lattices. For example, the Fourier weight of wave-vector a on sub-lattice 2, denoted by a_2, is the same as the Fourier weight of wave-vector b on sub-lattice 1, denoted by b_2.

The commensurate *Cuboc1* Fig.5.9 and *Cuboc2* Fig.5.8 are also examples of spin orders belonging to the $3\mathbf{Q}$ phase where each sub-lattice is composed of

two of the three inequivalent wave-vectors at the zone mid-points (5.28),(5.27). Both states are highly symmetrical and are classified as belonging to the (a_1b_1, b_1c_1, c_1a_1) phase. Both the *Cuboc1* and *Cuboc2* states have twelve spins in the magnetic unit cell pointing towards the mid-points of the edges of a unit cube. The symmetry in spin space is therefore of a cuboctahedron - a polygon with twelve identical vertices, hence the name *Cuboc1* and *Cuboc2*. In real space,both states have 2×2 unit cell as shown in Fig.5.8.

Parametrization of constituent states of the (ab, bc, ca) type phase, such as the spin configurations shown in Fig 5.11 is done using the Fourier transform of the spin orders $\{\mathbf{S}_\alpha(\mathbf{q}_\mu)\}$ from iterative minimization. The "purified" order is obtained by simply inverse F.T. the vectors $\{\mathbf{S}_\alpha(\mathbf{q}_\mu)\}$, given in Table 5.4, using Eq. 5.32

$\mathbf{S}_1(\mathbf{q}_1)$	$\mathbf{S}_1(\mathbf{q}_2)$	$\mathbf{S}_2(\mathbf{q}_2)$	$\mathbf{S}_2(\mathbf{q}_3)$	$\mathbf{S}_3(\mathbf{q}_1)$	$\mathbf{S}_3(\mathbf{q}_3)$
$\begin{pmatrix} 0.33e^{i1.4} \\ 0.3e^{-i0.3} \\ 0.16e^{i3.1} \end{pmatrix}$	$\begin{pmatrix} 0.32e^{-i0.8} \\ 0.33e^{-i2.4} \\ 0.11e^{i1.6} \end{pmatrix}$	$\begin{pmatrix} 0.36e^{-i0.6} \\ 0.37e^{-i2.3} \\ 0.13e^{i1.7} \end{pmatrix}$	$\begin{pmatrix} 0.09e^{-i2.8} \\ 0.15e^{-i3.1} \\ 0.4e^{-i3} \end{pmatrix}$	$\begin{pmatrix} 0.37e^{i1.2} \\ 0.34e^{-i0.4} \\ 0.18e^{i3} \end{pmatrix}$	$\begin{pmatrix} 0.09e^{i2.7} \\ 0.15e^{i3} \\ 0.4e^{-i3.1} \end{pmatrix}$
$\begin{pmatrix} 0.29e^{i1.1} \\ 0.15e^{-i2.3} \\ 0.33e^{-i0.5} \end{pmatrix}$	$\begin{pmatrix} 0.29e^{i1.9} \\ 0.15e^{-i1.5} \\ 0.32e^{i0.3} \end{pmatrix}$	$\begin{pmatrix} 0.33e^{i2} \\ 0.17e^{-i1.4} \\ 0.37e^{i0.4} \end{pmatrix}$	$\begin{pmatrix} 0.19e^{i2} \\ 0.39e^{2i} \\ 0.04e^{i2} \end{pmatrix}$	$\begin{pmatrix} 0.33e^{i} \\ 0.16e^{-i2.4} \\ 0.37e^{-i0.6} \end{pmatrix}$	$\begin{pmatrix} 0.19e^{i1.9} \\ 0.39e^{i1.9} \\ 0.04e^{i1.9} \end{pmatrix}$
$\begin{pmatrix} 0.06e^{-i0.6} \\ 0.03e^{-i0.6} \\ 0.47e^{i2.5} \end{pmatrix}$	$\begin{pmatrix} 0.29e^{i2.6} \\ 0.36e^{-i0.5} \\ 0.01e^{i2.6} \end{pmatrix}$	$\begin{pmatrix} 0.36e^{-i3} \\ 0.29e^{-i3} \\ 0.06e^{-i3} \end{pmatrix}$	$\begin{pmatrix} 0.06e^{-i0.5} \\ 0.03e^{-i0.5} \\ 0.46e^{i2.6} \end{pmatrix}$	$\begin{pmatrix} 0.3e^{i2.5} \\ 0.37e^{-i0.6} \\ 0.01e^{i2.5} \end{pmatrix}$	$\begin{pmatrix} 0.36e^{-i2.9} \\ 0.29e^{-i2.9} \\ 0.06e^{-i2.9} \end{pmatrix}$

Table 5.4: Spin Fourier transform $\mathbf{S}_\alpha(\mathbf{q})$ for reconstructing orders belonging to the $3\mathbf{Q}$ (ab, bc, ca) type phases. The three rows correspond to fillings (1) at $n = 0.115$, (2) at $n = 0.146$ and (3) at $n = 0.181$. The dominant wave-vectors are: $\mathbf{q}_1 = 2\pi(0.19, -0.13), \mathbf{q}_2 = 2\pi(0.02, -0.22), \mathbf{q}_3 = 2\pi(0.20, 0.09)$ for $n = 0.115$. $\mathbf{q}_1 = 2\pi(0.15, 0.1), \mathbf{q}_2 = 2\pi(0.02, -0.18), \mathbf{q}_3 = 2\pi(0.15, -0.1)$ for $n = 0.146$ and $\mathbf{q}_1 = 2\pi(0.02, -0.13), \mathbf{q}_2 = 2\pi(0.1, 0.08), \mathbf{q}_3 = 2\pi(-0.13, 0.05)$ for $n = 0.181$. An approximate and un-normalized spin order can be constructed using the information provided above using the recipe provided in text (see Eq.5.32)

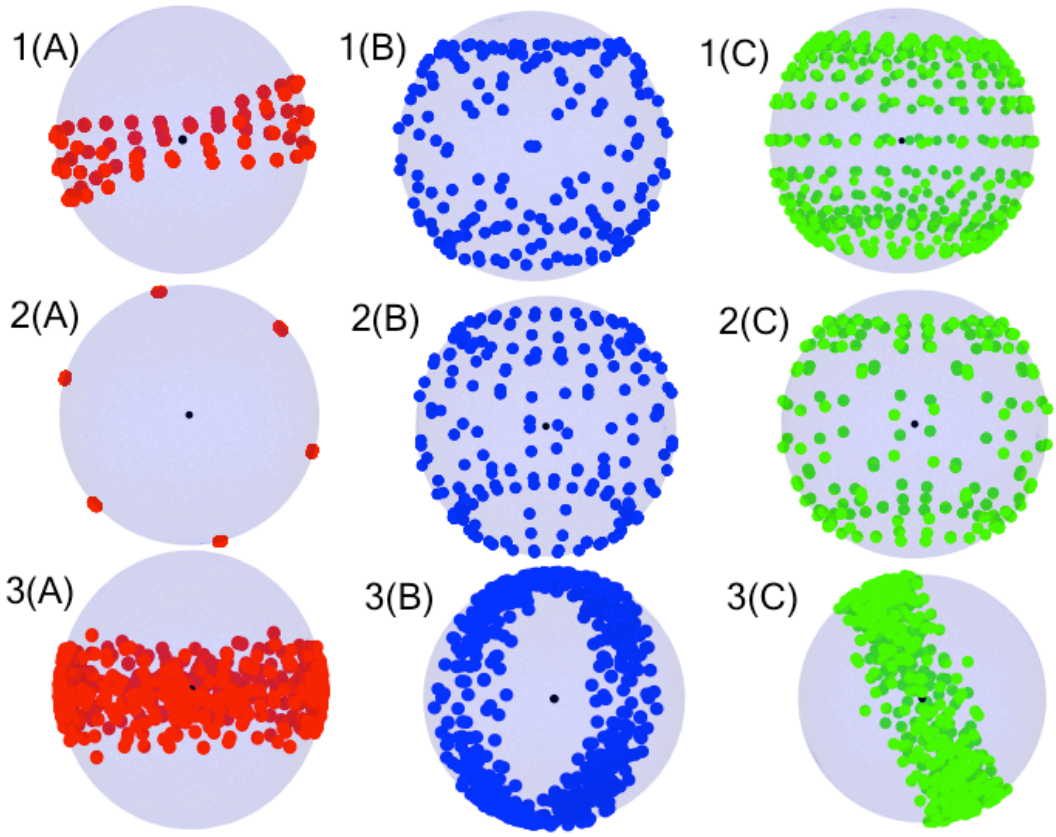

Figure 5.11: Common origin plot of spin orders from the (ab, bc, ca) and (a_1b_2, c_1a_2, b_1c_2) phases. 1(A)-(C): spins on each of the three sublattices for a spin order recovered from MC at $n = 0.115$,2(A)-(C): at $n = 0.146$,3(A)-(C): at $n = 0.181$. The ordering wave vectors for the three states in Table 5.3 and $\mathbf{S}_\alpha(\mathbf{q})$ along with 5.32 can be used to construct $\{\mathbf{S}_i^{pure}\}$

5.6 .5 The (a, b, c) and (a_1, b_1, c_1) type phases

Spin orders belonging to these phases have three dominant wave-vectors- one going with each sub-lattice. Since all orders forming part of these phases are composed of three dominant wave-vectors from the zone, they are referred to as "$3\mathbf{Q}$" orders. The $3\mathbf{Q}$ nomenclature was first introduced in the context of a chiral order on the triangular lattice[10]. The most general orders are of the type (a, b, c) where the weight of each of the three wave-vectors is different on the three sub-lattices. Because each sub-lattice is described by a single domi-

nant wave-vector, spins on each of the three sub-lattices trace out spirals in spin space. The spirals are not co-planar due to contributions from the sub-dominant modes [21]. The planes of the spirals on the different sub-lattices can, in general, lock at any angle with respect to each other.

However, for most spin orders belonging to the (a, b, c) or (a_1, b_1, c_1) type phases, we find the inter sub-lattice locking angles of the spirals to be $\pi/2$ radians. This is specifically true for orders belonging to the highly symmetric (a_1, b_1, c_1) phase, where the weights of the three different wave-vectors (a, b, c), from the dominant star of Luttinger-Tisza optimal vectors, is the same on all the three sub-lattices.

Spin configurations from the (a, b, c) phase at different fillings is shown in Fig.5.12. For each spin order, separate common origin plots of spins belonging to the different sub-lattices is shown in (A)-(C). Figure in sub-panel (D) for every filling, shows the purified normalized spin configuration obtained by filtering out the three dominant modes, making up the spin order, across the three sub-lattices. The purified spin orders, for almost all fillings, clearly show three coplanar spirals. For most orders, the planes of the spirals are mutually orthogonal. Exceptions to this observation are the spin orders at $n = 0.226, 0.228$ and at $n = 0.527$ where spins on two of the three sub-lattices lie in the same plane perpendicular to the plane in which spins on the third sub-lattice lie. The dominant wave-vectors, the vector $\mathbf{S}_\alpha(\mathbf{q})$ in Fourier space, and the weights $\eta_\alpha(\mathbf{q})$ of the dominant wave-vectors for various spin orders belonging to the $3\mathbf{Q}$ (a, b, c), and (a_1, b_1, c_1) phases is summarized in Table 5.5.

States where the planes of the three coplanar spirals are mutually orthogo-

[21] If the dominant wave-vector has weight one on the sub-lattice, then the resulting spin configuration on that sub-lattice will be a perfect coplanar spiral

nal, can be parametrized as:

$$\begin{aligned}
\mathbf{S}^{recons}_{i(\alpha=1)} &= \mathbf{Re}[e^{(\mathbf{q}_1.\mathbf{R}_i+\varphi_1)}(\mathbf{e}_1 - i\mathbf{e}_2)] \\
\mathbf{S}^{recons}_{i(\alpha=2)} &= \mathbf{Re}[e^{(\mathbf{q}_2.\mathbf{R}_i+\varphi_2)}(\mathbf{e}_2 - i\mathbf{e}_3)] \\
\mathbf{S}^{recons}_{i(\alpha=3)} &= \mathbf{Re}[e^{\mathbf{q}_3.\mathbf{R}_i+\varphi_3)}(\mathbf{e}_1 - i\mathbf{e}_3)]
\end{aligned} \tag{5.34}$$

where $\mathbf{e}_{1,2,3}$ forms a triad of orthonormal vectors (see Table 5.5). The wave-vectors $\mathbf{q}_{1,2,3}$ and the phase parameters $\varphi_{1,2,3}$ is summarized in Table 5.6

Before ending the Section on symmetry broken orders we make two important points. Firstly, all spin orders stabilized at various fillings in the RKKY limit of the Kondo Lattice Model are generically incommensurate. This was mathematically expected from the Fermi surface nesting arguments of Section 5.4.2 and was empirically shown in Section 5.5. The dominant ordering wave-vectors of these orders lies at incommensurate positions in the zone and was empirically, *always* found to agree with the optimal Luttinger-Tisza modes found by diagonalizing the matrix of interactions $J_{\alpha\beta}(\mathbf{q})$in Fourier space at different fillings. The incommensurate-ness of the orders comes from the Fermi surface geometry, which for a generic filling, is nested by incommensurate wave-vectors. These wave-vectors which cause the dominant instability in the Luttinger-Tisza matrix $J_{\alpha\beta}(\mathbf{q})$are also the ordering wave-vectors of the spin orders.

A second consequence concerns the method by which neutron diffraction might experimentally distinguish these complex orders. Spin structure factor obtained from Neutron scattering on itinerant Kagomé compounds will show sharp peaks at incommensurate positions in the zone, very similar to the profile

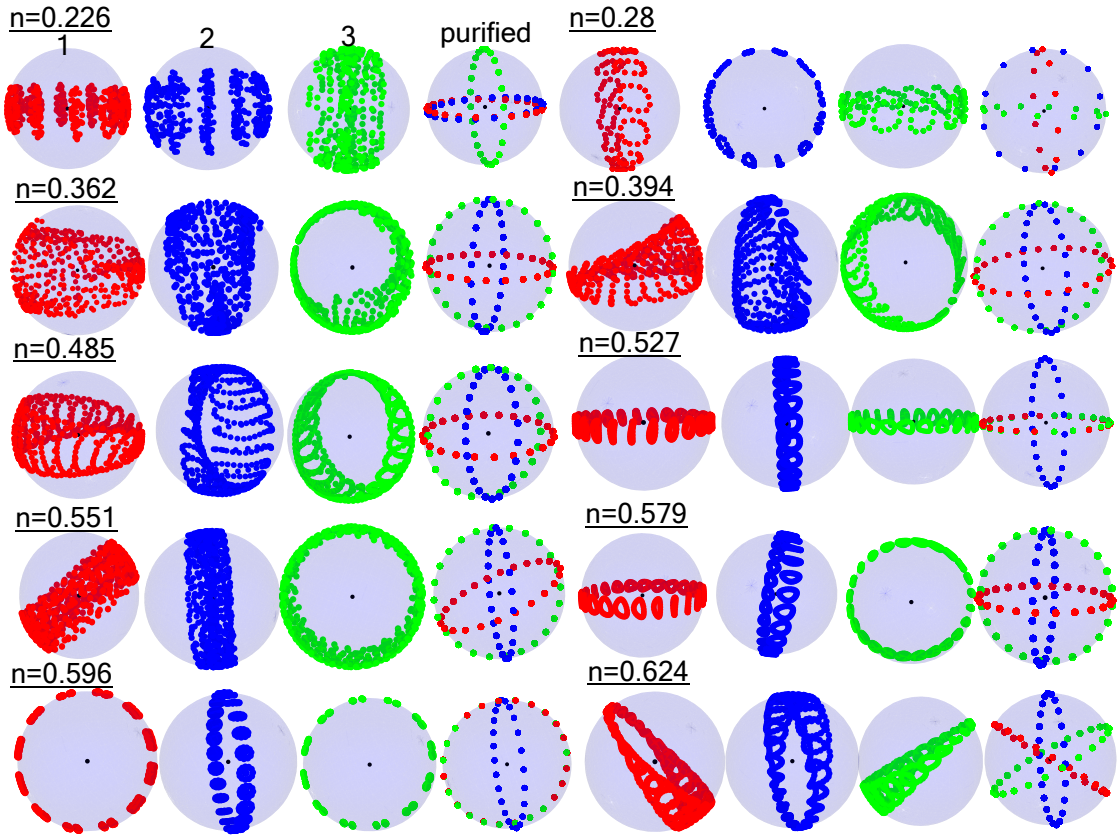

Figure 5.12: Common origin plots of the spin configurations from the (a, b, c) and the (a_1, b_1, c_1) phases. The figure is divided in to 10 panels based on fillings which are indicated at the beginning of each panel. Each panel contains four figures. The four figures are labeled in the first panel corresponding to filling $n = 0.228$. Labels 1,2,3 show common origin plots of spins (recovered from iterative minimization) on each of the three sub-lattices. The fourth figure labeled "purified" shows the spins in the "purified" configuration obtained by filtering out the dominant modes making up the spins on each of the three sub-lattices and normalizing the purified configuration according to the prescription in (5.32). The labels repeat in all the following panels. The dominant wave-vectors making up the spin configurations are summarized in Table5.5. Spin orders where the three coplanar spirals lie in mutually orthogonal planes are parametrized according to (5.34) with parameters tabulated in Table 5.6

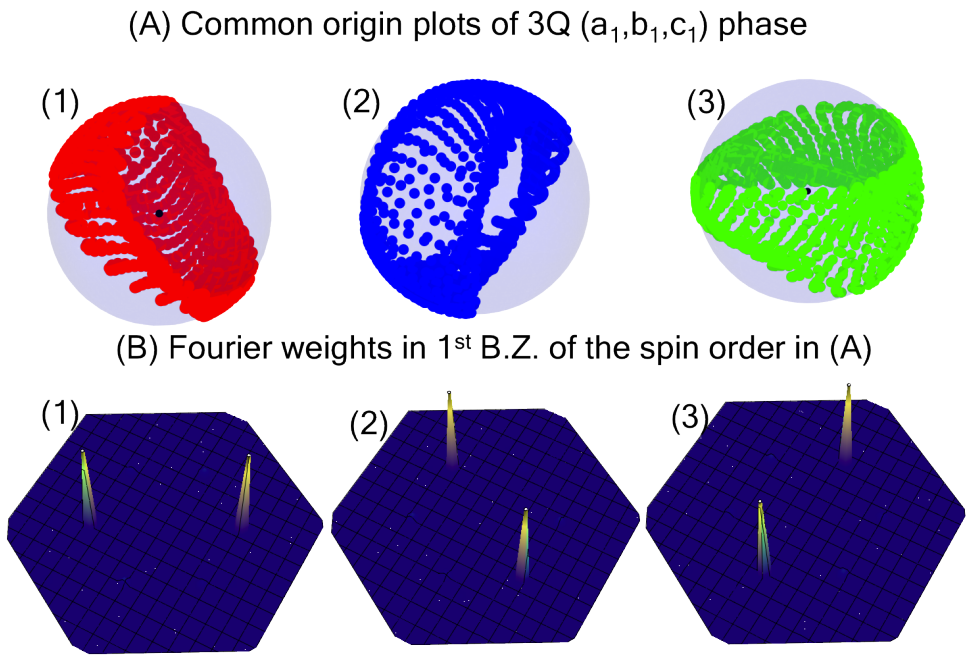

Figure 5.13: Common origin plots for a representative spin configuration from the $3\mathbf{Q}$ (a_1, b_1, c_1) phase and the profile of $\eta_\alpha(\mathbf{q})$ for each of the three sub-lattices $\alpha = 1, 2, 3$ for wave-vectors $\{\mathbf{q}\} \in$ 1st. Brillouin zone. (A): The common origin plots of spin in each of the three sub-lattices is shown in (1),(2) and (3) in red, blue and green colors, respectively. (B)The Fourier composition of the spin pattern in (A). The peaks in the zone seen in (B) - (1),(2),(3) are at incommensurate zone points and are at locations corresponding to the dominant ordering wave-vectors of spin lying on the three sub-lattices. Similar profiles of the spin structure factor are expected from Neutron Scattering studies of the complex spin orders discussed in this study

of $\eta_\alpha(\mathbf{q})$ in the first Brillouin zone. An example of the profile of $\eta_\alpha(\mathbf{q})$ for a representative spin configuration from the $3\mathbf{Q}$ (a_1, b_1, c_1) phase, at a filling $n = 0.375$, is shown in Fig.5.13. The profile shows sharp peaks at incommensurate wave-vectors in the zone which are the dominant ordering wave-vectors of spins on each of the three sub-lattices.

The iterative minimization and subsequent diagnosis of spin orders shows the abundance of non-coplanar orders in the weak coupling limit of the Kondo

Hamiltonian on the Kagomé lattice. It is important to emphasize that the non-coplanarity of the orders primarily arises due to the non-Bravais nature of the Kagomé lattice. In comparison, on a triangular lattice, over a wide range of fillings where the dominant nearest neighbor RKKY interaction is anti-ferromagnetic, no non-coplanar order is stable and the coplanar 120 degree state dominates the filling versus Kondo coupling strength phase diagram. RKKY interactions therefore offer a route for realizing complex non-coplanar orders on the Kagomé.

Such orders are abundant in the weak coupling limit but do they survive for larger strengths of the Kondo coupling where the RKKY Hamiltonian is no longer valid? We answer this question in the next Section by building a variational phase diagram and testing the robustness of non-coplanar orders, found in the RKKY limit, at larger Kondo coupling strengths.

5.7 Variational Phase Diagram

In this Section we study the phase diagram of the Kondo Lattice Model (5.1) as a function of two parameters: the electronic filling n and the ratio of the Kondo coupling strength to the hopping parameter J_K/t. The two dimensional phase diagram is constructed by compiling a trial data base of orders obtained in the RKKY limit of the model, and also including the five commensurate orders discussed previously. The ground state of the Kondo Lattice model at any filling and coupling strength is *approximated* to be the lowest energy state from the variational data base.

We find large regions of the phase space dominated by non-coplanar orders of both commensurate and incommensurate kinds. We identify a new region of

intermediate Kondo couplings where commensurate orders are dominant, but some highly symmetrical incommensurate orders are reentrant and make new appearances.

Construction of the variational phase diagram has a two fold motivation. Firstly, we want to test the robustness, at finite and larger values of the Kondo coupling strength, of the vast variety of complex non-coplanar orders that were ground states of the Kondo Lattice model in the weak coupling limit. Secondly, the intermediate coupling regime ($1 < J_K/t < 100$) is analytically inaccessible because an effective Hamiltonian (like the RKKY model and the Double Exchange Hamiltonian for the weak and infinite Kondo coupling limits, respectively) in this part of the phase diagram, does not exist. We therefore resort to a numerical variational approach to predict the spin orders dominating the phase diagram in the intermediate Kondo coupling regime.

The first step to creating a variational phase diagram is to build a compilation of classical spin orders. We do this by solving the Kondo Lattice Model exactly in the weak coupling limit at several fillings and obtaining the optimal ground state spin orders. All these spin orders, many examples of which were shown in the previous Section, become part of the trial data base. We also add five commensurate and well known orders in the data base. These are the ferromagnetic, $\mathbf{q} = 0$, $\sqrt{3} \times \sqrt{3}$ and the *Cuboc1* and *Cuboc2* orders discussed in Section 5.4 .

The second step is an exact fermionic diagonalization of all the classical spin orders in the variational data base for every filling and several Kondo coupling strengths. The Kondo Hamiltonian (5.1) is diagonalized by adding two non-local boundary phases $\varphi_{1,2}$ to the hopping fermions. The fermionic energies are

averaged over several values (typically 100) of the boundary phases to eliminate finite size effects which become increasingly important at small J_K/t.

To benchmark the diagonalization routine, we confirm that the ground state spin orders of the RKKY Hamiltonian are also the lowest energy spin configurations of the Kondo Lattice model for all fillings, and for small enough couplings J_K, where the RKKY Hamiltonian(5.17) is a good approximation to the Kondo Lattice Model Hamiltonian (5.1). We next discuss the variational phase diagram.

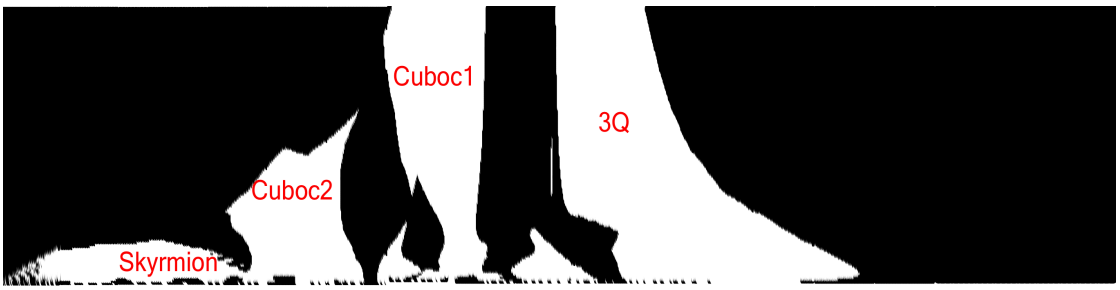

Figure 5.14: Variational phase diagram showing different competing phases of the KLM Hamiltonian (5.1) in the (n, J_K) plane. The range along the filling axis is $n = (0, 1)$ at unit intervals and along coupling axis is $J_K = [0, 8]$ at $0.05t$ separation. Smoothly evolving phases with the same broken symmetries are indicated by numerals (1)-(8). Energies at every point are averaged over 100 values of the boundary phases. The strip shown at the bottom is the RKKY phase diagram (function of n) with the same color convention as the phases above (Data for N=3×24^2). The border line at very small Kondo coupling has a complex jitter which in some cases is a numerical artifact (see text)

The variational phase diagram shows large regions where non-coplanar orders are stable. Fig.5.14 shows the variational phase diagram in the (n, J_K) plane. All collinear and coplanar orders are shaded in black. Regions left in white are places in the phase diagram where different non-coplanar orders are expected to be the ground states of the Kondo Lattice model. Some of the non-coplanar orders are labeled in red. The *Cuboc1*(Fig.5.9)[27] and *Cuboc2* (Fig.5.8) [29] are non-coplanar commensurate spin orders, whereas the region labeled "$3Q$", consists of spin orders from the $3\mathbf{Q}$ (a, b, c) phase discussed in Section

5.6 . The phase diagram confirms the robustness of these non-coplanar orders, which were ground states of the Kondo lattice model in the weak coupling limit, at larger values of the Kondo coupling.

The black and white phase diagram in Fig.5.14 distinguishing coplanar from non-coplanar orders has some numerical artifacts in the very small Kondo coupling limit. For the range of fillings where the dominant J_1interaction is ferromagnetic, there are black jitters where the ferromagnetic state is the is the approximate lowest energy state for fillings at which states from the RKKY limit were not included in the variational calculation. There are also similar black jitters corresponding to the Ferromagnetic state even for fillings where the dominant RKKY interaction is the nearest neighbor interaction and is antiferromagnetic. The stability of the Ferromagnetic state for such filling ranges is an artifact and is expected to go away with better averaging or with larger system sizes.

The interplay between different orders in Fig.5.15 is interpreted by dividing the phase diagram, across all fillings, in to a small, intermediate and high J_K/t regime.

In the small $J_K/t \ll 1$ regime (RKKY limit), the spin orders stabilized in the variational phase diagram are completely consistent with the predictions from the RKKY limit using RKKY approaches of Luttinger-Tisza (see Section 5.4.1) and iterative minimization (see Section 5.5.1). This regime is dominated by non-coplanar orders. Most of these orders are incommensurate (as in Fig.5.10, Fig.5.11,Fig. 5.12) and their phase boundaries typically fan out from a filling point where they were exact ground states of Eq.(5.17). On entry in to the intermediate J_K regime (typically around one) these orders lose out to commen-

surate states, with a few exceptions where incommensurate orders, originally found from the RKKY calculation, persist and are re-entrant.

Large regions of the intermediate J_K/t regime of the phase diagram also stabilizes non-coplanar orders. Of these, the non-coplanar *Cuboc1*(found at $n = 5/12$ [22]), and *Cuboc2* (at $n = 2/3$) orders are commensurate, while the orders making up the (a_1, b_1, c_1) phase shown in red in Fig.5.15 are incommensurate and belong to the $3\mathbf{Q}$ (a, b, c) phase of Section 5.6 . Commensurate orders evolve smoothly from the low to the intermediate regime, the incommensurate orders are reentrant and cannot be continuously evolved (without crossing another state) from the small J_K regime.

Finally, the large J_K regime (also the Double Exchange limit of (5.1)) favors the trivial ferromagnetic order.

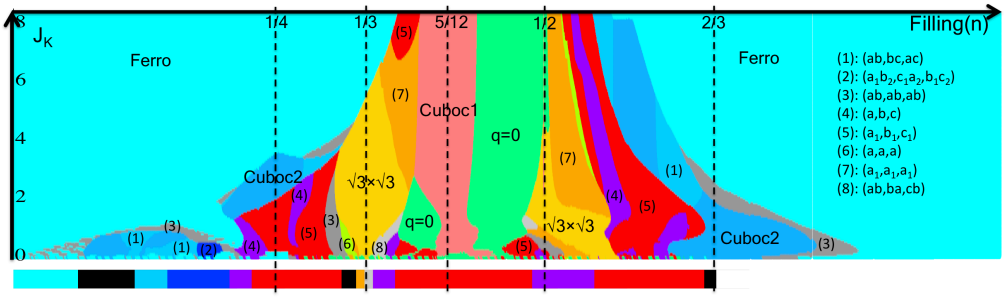

Figure 5.15: Variational phase diagram showing different competing phases of the KLM Hamiltonian (5.1) in the (n, J_K) plane. The range along the filling axis is $n = (0, 1)$ at unit intervals and along coupling axis is $J_K = [0, 8]$ at $0.05t$ separation. Smoothly evolving phases with the same broken symmetries are indicated by numerals (1)-(8). Energies at every point are averaged over 100 values of the boundary phases. The strip shown at the bottom is the RKKY phase diagram (function of n) with the same color convention as the phases above (Data for N=3×24^2)

[22] At $n = 1/4$ for small J_K in Fig.5.15 the coplanar $\mathbf{q} = 0$ order is stable instead of *Cuboc1*. This is a finite size effect, *Cuboc1* wins for larger lattice sizes

5.8 Conclusion

In this chapter, we have shown that, on a Kagomé lattice,a Kondo-lattice coupling local moments and electrons with the simplest possible electron band structure, yields a host of generically non-coplanar and incommensurate spin states. We computed the RKKY spin-spin couplings induced by fermions, and verified that the "Luttinger-Tisza" framework (dominant eigenmodes of the interaction matrix) is a reliable guide to the orders we found by Monte Carlo simulations. This framework explains the overall evolution of the spin order with filling in terms of Fermi surface nesting (Fig.5.4, Fig.5.5). There are additional dimensions to spin orders than the L-T vectors, in particular the possibility of non-coplanar states based on multiple ordering vectors, examples of which are shown in Fig.5.11, Fig.5.12.

Finally, we used a different, "variational" method to obtain the approximate phase diagram for larger Kondo couplings (Fig. 5.15). We discovered an intermediate regime (before the ferromagnetic state sweeps the phase diagram in the Double Exchange limit): commensurate states are more prominent here, as expected, but (empirically) we found "reentrant" incommensurate orders also appear at different fillings than they were found in the limit of small J_K. Such orders were neglected in previous studies[13] of KLM phase diagram. The intermediate regime could be more systematically studied using improved MC algorithm[20, 21] or with an effective spin Hamiltonian including multi-spin interactions[15].

Non-coplanar orders appear rarely in Kagomé systems. Our results suggest that, in Kondo-coupled systems without spin-orbit effects, non-coplanar orders

are abundant. Candidate materials for realizing such orders are the layered itinerant Kagomé ferromagnet Fe_3Sn_2[34] and doped FeCrAs[35].

n	$\mathbf{q}_1(2\pi)$	$\mathbf{q}_2(2\pi)$	$\mathbf{q}_3(2\pi)$	$\mathbf{S}_1(\mathbf{q}_1)$	$\mathbf{S}_2(\mathbf{q}_2)$	$\mathbf{S}_3(\mathbf{q}_3)$	η_1	η_2	η_3
0.226	0.25 0.12	−0.25 0.12	0.02 −0.27	$0.29e^{i1.38}$ $0.38e^{i1.48}$ $0.48e^{-i0.18}$	$0.26e^{-i1.82}$ $0.38e^{-i1.61}$ $0.46e^{i2.95}$	$0.45e^{i1.48}$ $0.39e^{-i0.48}$ $0.30e^{i0.29}$	0.92	0.86	0.90
0.341	0.12 −0.24	0.12 0.24	−0.27 0.01	$0.2e^{-i2.1}$ $0.41e^{-i1.36}$ $0.2e^{i1.87}$	$0.49e^{i1.54}$ $0.18e^{-i2.5}$ $0.14e^{i0.97}$	$0.06e^{-i1.7}$ $0.24e^{i1.44}$ $0.47e^{i1.44}$	0.5	0.58	0.57
0.355	0.1 −0.2	0.1 0.2	−0.23 0.01	$0.18e^{i2.04}$ $0.46e^{i1.76}$ $0.22e^{-i2.28}$	$0.42e^{-i0.21}$ $0.19e^{-i2.6}$ $0.42e^{-i1.7}$	$0.43e^{-i0.48}$ $0.21e^{-i2.88}$ $0.44e^{-i1.94}$	0.6	0.8	0.84
0.492	0.1 0.13	0.1 −0.13	0.06 0.16	$0.27e^{i0.94}$ $0.43e^{i1.48}$ $0.47e^{-i0.26}$	$0.45e^{-i3.02}$ $0.28e^{i}$ $0.43e^{i1.84}$	$0.27e^{-i2.05}$ $0.41e^{-i2.55}$ $0.46e^{-i0.81}$	0.96	0.92	0.92
0.527	0.23 0.16	0.23 −0.15	0.02 0.27	$0.47e^{i1.98}$ $0.48e^{i0.3}$ $0.2e^{i1.23}$	$0.47e^{-i1.87}$ $0.17e^{-i2.55}$ $0.49e^{-i0.34}$	$0.46e^{-i1.98}$ $0.47e^{-i0.3}$ $0.21e^{-i1.19}$	0.98	0.98	0.96
0.551	0.21 0.1	−0.2 0.1	0.02 −0.22	$0.01e^{-i2.17}$ $0.49e^{i1.15}$ $0.47e^{i2.7}$	$0.45e^{-i2.86}$ $0.49e^{-i1.35}$ $0.19e^{i3.10}$	$0.48e^{i0.39}$ $0.03e^{-i2.91}$ $0.47e^{i1.98}$	0.92	0.94	0.9
0.28	0.125 0.12	−0.17 0.04	0.04 −0.17	$0.25e^{-i1.69}$ $0.49e^{i3.02}$ $0.43e^{-i1.69}$	$0.41e^{i0.43}$ $0.44e^{-i1.47}$ $0.35e^{i2.68}$	$0.48e^{i1.2}$ $0.28e^{i2.5}$ $0.41e^{i2.9}$	0.96	0.96	0.96
0.362	0.1 −0.15	0.08 0.16	0.18 0.01	$0.43e^{i0.16}$ $0.4e^{-i1.51}$ $0.22e^{-i1.06}$	$0.36e^{-i2.31}$ $0.29e^{-i1.76}$ $0.42e^{i2.6}$	$0.27e^{-i2.48}$ $0.4e^{i1.55}$ $0.4e^{-i0.27}$	0.8	0.8	0.8
0.394	0.06 −0.08	0.04 0.09	0.1 0.01	$0.47e^{i2.78}$ $0.1e^{i2.34}$ $0.47e^{i1.2}$	$0.38e^{i0.74}$ $0.47e^{i2.44}$ $0.29e^{i1.1}$	$0.36e^{-i1.01}$ $0.44e^{i0.85}$ $0.34e^{i2.75}$	0.9	0.9	0.9
0.485	0.1 0.08	−0.12 0.04	0.02 −0.13	$0.44e^{i1.71}$ $0.46e^{i0.24}$ $0.22e^{i2.38}$	$0.33e^{i1.45}$ $0.44e^{i2.54}$ $0.4e^{-i2.5}$	$0.45e^{-i1.5}$ $0.17e^{i1.6}$ $0.48e^{-i3.06}$	0.92	0.92	0.92
0.579	0.25 0.1	0.22 −0.15	0.02 0.27	$0.44e^{-i2.12}$ $0.28e^{i1.76}$ $0.47e^{-i0.36}$	$0.38e^{-i1.88}$ $0.41e^{-i0.91}$ $0.42e^{i0.21}$	$0.39e^{-i0.62}$ $0.49e^{i0.94}$ $0.31e^{-i0.65}$	0.98	0.98	0.98
0.596	0.23 0.15	0.25 −0.12	0.02 0.27	$0.48e^{-i2.78}$ $0.19e^{i2.6}$ $0.47e^{i1.85}$	$0.48e^{-i2.53}$ $0.47e^{i2.08}$ $0.21e^{i-0.44}$	$0.48e^{i2.77}$ $0.2e^{-i2.55}$ $0.47e^{-i1.85}$	0.98	0.98	0.98
0.624	0.17 0.12	−0.18 0.08	0.02 −0.2	$0.48e^{-i1.46}$ $0.32e^{-i0.1}$ $0.38e^{-i2.87}$	$0.35e^{-i0.31}$ $0.37e^{i2.2}$ $0.47e^{-i2.21}$	$0.17e^{i2.2}$ $0.49e^{-i2.8}$ $0.46e^{i1.86}$	0.96	0.96	0.9

Table 5.5: Dominant wave-vectors and their Fourier weights on the sub-lattices for representative spin orders from the phases –(a, b, c) and (a_1, b_1, c_1). Corresponding spin configurations are shown in Fig. 5.12

n	$\mathbf{q}_1(2\pi)$	$\mathbf{q}_2(2\pi)$	$\mathbf{q}_3(2\pi)$	$\varphi_1(2\pi)$	$\varphi_2(2\pi)$	$\varphi_3(2(\pi)$
0.28	$\begin{pmatrix} 0.125 \\ 0.12 \end{pmatrix}$	$\begin{pmatrix} -0.17 \\ 0.05 \end{pmatrix}$	$\begin{pmatrix} 0.05 \\ -0.17 \end{pmatrix}$	-0.91	-1.36	-0.86
0.362	$\begin{pmatrix} 0.1 \\ -0.15 \end{pmatrix}$	$\begin{pmatrix} 0.08 \\ 0.17 \end{pmatrix}$	$\begin{pmatrix} 0.19 \\ 0.01 \end{pmatrix}$	-2.04	-0.58	0.99
0.394	$\begin{pmatrix} 0.06 \\ -0.08 \end{pmatrix}$	$\begin{pmatrix} -0.04 \\ -0.09 \end{pmatrix}$	$\begin{pmatrix} 0.1 \\ 0.01 \end{pmatrix}$	0.39	1.9	1
0.485	$\begin{pmatrix} 0.1 \\ 0.08 \end{pmatrix}$	$\begin{pmatrix} -0.12 \\ -0.05 \end{pmatrix}$	$\begin{pmatrix} 0.02 \\ -0.13 \end{pmatrix}$	0.91	2.26	1.1
0.527	$\begin{pmatrix} 0.22 \\ 0.15 \end{pmatrix}$	$\begin{pmatrix} 0.22 \\ -0.15 \end{pmatrix}$	$\begin{pmatrix} 0.02 \\ 0.27 \end{pmatrix}$	-0.12	-1.53	-3.02
0.551	$\begin{pmatrix} 0.21 \\ 0.1 \end{pmatrix}$	$\begin{pmatrix} -0.2 \\ -0.1 \end{pmatrix}$	$\begin{pmatrix} 0.02 \\ -0.23 \end{pmatrix}$	-0.48	1.79	-0.97
0.579	$\begin{pmatrix} 0.25 \\ 0.12 \end{pmatrix}$	$\begin{pmatrix} 0.23 \\ -0.16 \end{pmatrix}$	$\begin{pmatrix} -0.02 \\ -0.28 \end{pmatrix}$	1.8	0.64	-0.37
0.596	$\begin{pmatrix} 0.22 \\ 0.15 \end{pmatrix}$	$\begin{pmatrix} -0.25 \\ 0.12 \end{pmatrix}$	$\begin{pmatrix} 0.02 \\ 0.27 \end{pmatrix}$	0.97	-0.35	0.96

Table 5.6: Set of parameters for constructing the purified spin configurations from the (a, b, c) and (a_1, b_1, c_1) phases according to the ansatz outlined in Eq. 5.34 for spin configurations shown in Fig. 5.12

BIBLIOGRAPHY

[1] S. Ghosh, P. O' Brien, M. J. Lawler and C. L. Henley, arXiv:1407.5354.

[2] E. F. Shender, V. B. Cherepanov, P. C. W. Holdsworth, and A. J. Berlinsky, Phys. Rev. Lett. **70**, 3812 (1993).

[3] S. E. Palmer and J. T. Chalker, Phys. Rev. B **62**, 488 (2000).

[4] C. L. Henley, Phys. Rev. B **80**, 180401 (2009).

[5] G.-W. Chern and R. Moessner, Phys. Rev. Lett. **110**, 077201 (2013).

[6] U. Hizi and C. L. Henley, Phys. Rev. B **73**, 054403 (2006).

[7] D. Solenov, D. Mozyrsky, and I. Martin, Phys. Rev. Lett. **108**, 096403 (2012).

[8] S. Hayami, T. Misawa, Y. Yamaji, and Y. Motome, Phys. Rev. B **89**, 085124 (2014).

[9] T. A. Kaplan and N. Menyuk, Phil. Mag. **87**, 085124 (2006).

[10] I. Martin and C. D. Batista, Phys. Rev. Lett. **101**, 156402 (2008).

[11] K. Ohgushi, S. Murakami, and N. Nagaosa, Phys. Rev. B **62**, R6065 (2000).

[12] M. Taillefumier, B. Canals, C. Lacroix, V. K. Dugaev, and P. Bruno, Phys. Rev. B **74**, 085105 (2006).

[13] Y. Akagi and Y. Motome, J. Phys. Soc. Jpn. **79**, (2012).

[14] L. Messio, C. Lhuillier, and G. Misguich, Phys. Rev. B **87**, 125127 (2013).

[15] Y. Akagi, M. Udagawa, and Y. Motome, Phys. Rev. Lett. **108**, 096401 (2012).

[16] G.-W. Chern, Phys. Rev. Lett. **105**, 226403 (2010).

[17] S. R. Sklan and C. L. Henley, Phys. Rev. B **88**, 024407 (2013).

[18] M. Lapa and C. L. Henley, Preprint: arXiv:1210.6810 .

[19] J. M. Luttinger and L. Tisza, Phys. Rev. **70**, 954 (1946).

[20] Y. Kato, I. Martin, and C. D. Batista, Phys. Rev. Lett. **105**, 266405 (2010).

[21] K. Barros and Y. Kato, Phys. Rev. B **88**, 235101 (2013).

[22] S. Kumar and J. van den Brink, Phys. Rev. Lett. **105**, 216405 (2010).

[23] M. A. Ruderman and C. Kittel, Phys. Rev. **96**, 99 (1954).

[24] K. Yosida, Phys. Rev. **106**, 893 (1957).

[25] T. Yavors'kii, M. J. P. Gingras, and M. Enjalran, J. Phys. Condens. Matter 19, 145274 (2007).

[26] S. Hayami and Y. Motome, arXiv:1406.3119 **70**, 954 (2014).

[27] L. Messio, C. Lhuillier, and G. Misguich, Phys. Rev. B **83**, 184401 (2011).

[28] C. L. Henley, Phys. Rev. B **80**, 180401 (2009).

[29] J.-C. Domenge, P. Sindzingre, C. Lhuillier, and L. Pierre, Phys. Rev. B **72**, 024433 (2005).

[30] N. D. Mermin and H. Wagner, Phys. Rev. Lett. **17**, 1133 (1966).

[31] J.-C. Domenge, C. Lhuillier, L. Messio, L. Pierre, and P. Viot, Phys. Rev. B **77**, 172413 (2008).

[32] K. Barros, J. Venderbose, G-W. Chern and C. D. Batista, arXiv:1407.5369.

[33] U. Wolff, Phys. Rev. Lett. **62**, 361 (1989).

[34] L. A. Fenner, A. A. Dee, and A. S. Wills, J. Phys. Condens. Matter 21 (2009).

[35] W.Wu, A. McCollam, I. Swainson, P. M. C. Rourke, D. G. Rancourt and S. R. Julian, Europhysics Lett. 85 17009 (2009).

CHAPTER 6

STATE-SELECTION IN THE DOUBLE EXCHANGE MODEL ON THE KAGOMÉ LATTICE

The text and main results of this Chapter have not been published. Help from Benjamin Sung in verifying several results in this chapter is acknowledged.

6.1 Introduction

The Double Exchange model is a model of spin-less fermions hopping on a lattice with complex (in general) amplitudes. It is a special limit of the Kondo Lattice Model (6.1), discussed in Chapter 5, where the strength of the on-site Kondo coupling between the itinerant electron and the classical local moment is taken (theoretically) to infinity. The resultant model is call the Double Exchange Hamiltonian[1, 2].

The Double Exchange Hamiltonian was used to explain the origin of the colossal magneto-resistance in the Manganites[3]. The Manganites are transition metal oxides whose resistivity, at low enough temperatures and doping concentrations, was seen to drop drastically compared to the resistivity value at higher temperatures. This drop in resistivity was shown to be related to the development of magnetic order in the Manganites. Most Manganites were experimentally shown to be ferromagnetic metals at low enough temperatures, and underwent a phase transition to antiferromagnetic insulators at higher temperatures[3, 4].

The hopping amplitude of spin-less fermions, within the Double Exchange model, is dependent on the relative angles between classical spins on the lattice[1,

2]. The hopping amplitude is maximal when the spins are all aligned in the same direction (ferromagnetic configuration) and it is zero when the spins are perfectly anti-parallel (anti-ferromagnet). The Manganites undergo a magnetic phase transition in to a ferromagnetic phase (below a critical temperature) and the conductivity of therefore sharply increases in comparison to its value in the higher temperature paramagnetic or anti-ferromagnetic phase.

Although the Double-Exchange model always favors the collinear Ferromagnetic order, more complex non-coplanar anti-ferromagnetic orders can be realized if a super-exchange interaction is added to the Double Exchange Hamiltonian, strong enough to destabilize the ferromagnetic order[5]. Addition of a super-exchange interaction has been the route to stabilizing complex non-coplanar orders on frustrated lattices and for the realization of exotic quantum phases of matter[6, 7, 8, 9]. Electrons moving through a non-coplanar classical spin texture acquire non-trivial Berry phases[10, 8], similar to the Aharanov-Bohm phase acquired by electrons moving in a magnetic field. Non-coplanar configurations can therefore induce chirality (handedness) in the fermionic states leading to an *Anomalous* Hall response[6, 7] and non-zero Chern numbers in the absence of any magnetic field or spin-orbit coupling.

Techniques for searching non-coplanar orders, which can give rise to *chiral* fluxes, are however very limited. In this Chapter, we propose an Effective Hamiltonian as an efficient and systematic method for mapping out phase diagrams of the Double-Exchange model as a function of the electronic filling. Although the technique is general enough to be applicable to any lattice, we take the specific example of the frustrated Kagomé lattice and derive an Effective Hamiltonian in terms of fermionic fluxes though the lattice. The Effective

Hamiltonian is then used to study state-selection within the manifold of 120deg states on the lattice. Finally, we look at a special filling in the Double Exchange limit where all states are degenerate and we show how leading order corrections to the Hamiltonian, arising from charge flucuations, favors anti-ferromagnetic orders.

The organization of this chapter is as follows: in Section 6.2 we mathematically introduce the Double-Exchange Hamiltonian and point out the conventional Monte-Carlo techniques existing in the literature for finding ground states of the Double Exchange Hamiltonian, and the drawbacks of the existing techniques.

In Section 6.3, we derive an Effective classical Hamiltonian for the Double-Exchange model as a loop expansion in terms of fluxes through plaquettes on the lattice. We highlight how the employment of such a classical Effective Hamiltonian can eliminate most of the short comings of existing Mont-Carlo approaches for searching classical spin ground states of the Double Exchange model. The Effective Hamiltonian is generic to all fillings, lattices and spin configurations.

The classical Effective Hamiltonian is used to explain state selection within the manifold of classical 3 coloring[11] states on the Kagome lattice and we show how for certain filling ranges, the complex non-coplanar *Cuboc1* state is the ground state of the Double Exchange Hamiltonian (in the presence of a super-exchange) interaction.

Finally, in Section 6.5, we point out that at half filling *all* classical spin states are exactly degenerate. We show how this degeneracy is lifted at finite large strengths of the Kondo coupling (compared to the electron hopping band width)

in favor of the *Cuboc1* state. We present conclusions in Section 6.6 and comment on future work.

6.2 Double Exchange Hamiltonian

In this Section, we introduce the Double-Exchange Hamiltonian and show that it is the infinite Kondo coupling limit of the Kondo Lattice model (6.1). We derive the complex hopping amplitudes of the spin-less fermions on the lattice and show that they give rise to $U(1)$ fluxes through loops on the lattice. We also argue how the Double-Exchange Hamiltonian favors the trivial ferromagnetic order for all electronic fillings. We end the Section by motivating the need for addition of a classical super-exchange interaction between spins on the lattice to the Double Exchange Hamiltonian to stabilize more complex anti-ferromagnetic non-coplanar orders on the lattice.

The Double-Exchange model is the infinite Kondo coupling limit of the Kondo Lattice model(KLM) (5.1) For the sake of completeness, we re-write the Kondo Hamiltonian from (5.1):

$$\mathcal{H}_{KLM} = -t \sum_{\langle i(\alpha) j(\beta) \rangle} c^{\dagger}_{i(\alpha)\sigma} c_{j(\beta)\sigma} - J_K \sum_{i=1,\alpha}^{N_s} \mathbf{S}_{i(\alpha)} \cdot \boldsymbol{s}_{i(\alpha)} \tag{6.1}$$

The first term is nearest-neighbor hopping with amplitude t of a single band of non-interacting electrons, with creation operator $c^{\dagger}_{i(\alpha)\sigma}$ at unit cell i and sub-lattice α. The second term is the Kondo coupling, with $\boldsymbol{s}_{i(\alpha)}$ being the electron spin and $\mathbf{S}_{i(\alpha)}$ being classical Heisenberg spins representing the local moments living on the Kagomé lattice5.1.

The KLM Hamiltonian (6.1) describes the hopping of fermions on the lattice with amplitude t and a local Kondo coupling to classical spins on the lattice. In the limit $J_K/t \to \infty$, the low energy fermionic band has spins perfectly aligned with the direction of the local classical moment. The other higher energy band has fermionic spins anti-aligned with the local classical moments and is $2J_K$ higher in energy than the lower energy band. The higher energy band is completely projected out in the (theoretical) limit of $J_K/t \to \infty$. Removal of this anti-aligned spin band, reduces the number of fermionic states on the lattice to be exactly equal to the number of sites N_s on the lattice and the hopping fermions are also effectively spin-less.

In this limit of spin-less fermions, the hopping from one site i to another site j on the lattice is dependent on the difference θ_{ij} between the direction of classical spins on the lattice. This hopping amplitude is complex in general. The Double-Exchange Hamiltonian therefore describes the hopping of spin-less fermions on the lattice with complex hopping amplitudes t_{ij} and is given by:

$$\mathcal{H}_{DE} = \sum_{\langle ij \rangle} t_{ij} c_i^\dagger c_j + \text{h.c.} \tag{6.2}$$

where the complex hopping amplitude t_{ij} is a function of the angle between classical spins θ_{ij} on the lattice and a non-trivial Berry phase (arising out of the non-coplanarity of classical spins):

$$t_{ij} = e^{ia_{ij}} \cos(\theta_{ij}/2) \tag{6.3}$$

where the Berry phase a_{ij} is the vector gauge potential created by the background spin configuration[7]. The accumulated phase $\sum_{\langle ij \rangle} a_{ij}$ around a loop on

the lattice can be related to the solid angle subtended by the spins on the loop, on a unit sphere. The tip of the classical spin vectors around the loop defines a set of discrete points on the unit sphere. We connect the dots with spherical "straight" lines. The area enclosed by the curve on the unit sphere subtends an angle at the center of the sphere - called the solid angle. The accumulated Berry phase around a loop is equal to a half of this solid angle.

The phase or the flux through the loop is therefore 0 or π for coplanar spins[1] and is a non-zero (or non π) value for non-coplanar spins. A non-zero and non π value of the flux through a loop on the lattice indicates the breaking of time reversal symmetry and the origin of chiral fermionic eigenstates.

The complex hopping amplitude t_{ij}(6.3) arises from the overlap between the fermionic spin bi-linears on the two sites i, j on the lattice. Since the spin of an electron has an SU(2) symmetry, a spin state of the fermion can be expressed as 2×1 column vector or a bilinear. Let us represent the spin state of an electron, with its spin perfectly aligned with the local classical spin vectors $(\theta_{i(j)}, \varphi_{i(j)})$ on sites i, j, by the bilinears $|\chi_i\rangle$ and $|\chi_j\rangle$, respectively. A state $|\chi_{i(j)}\rangle$ can be obtained from a reference state $|\chi_{ref}\rangle^\dagger = (1, 0)$ aligned along the z direction in spin space, by an SU(2) rotation operator $\mathcal{R}(\theta_{i(j)}, \varphi_i(j))$, in the following way:

$$|\chi_{i(j)}\rangle = \mathcal{R}(\theta_{i(j)}, \varphi_{i(j)})|\chi_{ref}\rangle \tag{6.4}$$

where the $\mathbf{SU}(2)$ rotation operator is given by:

[1]For a coplanar state the discrete set of points on a unit sphere are all contained in a spherical great circle, irrespective of the angles between neighboring spins

$$\mathcal{R}_{\theta_{i(j)},\varphi_{i(j)}} = e^{i\varphi_{i(j)}\boldsymbol{\sigma}_z/2} e^{i\theta_{i(j)}\boldsymbol{\sigma}_y/2} \tag{6.5}$$

where $\boldsymbol{\sigma}_{y(z)}$ are the Pauli spin operators. The rotation operator (6.5) can be expressed as a 2×2 matrix (acting on the bilinears $|\chi_{i(j)}\rangle$) using the following relation:

$$e^{i\boldsymbol{\sigma}\cdot\mathbf{n}} = \cos(\theta/2) + i\sin(\theta/2)\boldsymbol{\sigma}\cdot\mathbf{n} \tag{6.6}$$

where $\boldsymbol{\sigma}$ is the vector of Pauli matrices and $\mathbf{n}$ is a unit vector along the axis of rotation, θ is the rotation angle. Using (6.4), it is straight-forward to compute both bilinears $|\chi_{i(j)}\rangle$ and the hopping amplitude t_{ij} is then given by the overlap:

$$t_{ij} = \langle\chi_i|\chi_j\rangle \tag{6.7}$$

The (norm of) hopping amplitude(6.3) is maximal when $\theta_{ij} = 0$. This favors the ferromagnetic order because the electrons can reduce their kinetic energy by hopping on the lattice. The standard technique to destabilize the ferromagnetic order and to favor more complex anti-ferromagnetic orders within the Double Exchange model is to add a nearest neighbor classical super-exchange interaction of the following form:

$$\mathcal{H}_{AF} = \sum_{\langle i,j\rangle} J_{AF}\mathbf{S}_i \cdot \mathbf{S}_j \tag{6.8}$$

where J_{AF} is positive (anti-ferromagnetic) and taken to be uniform across all bonds. There are two ways in which a super-exchange interaction can arise in

the model. First, it can arise out of a second itinerant band of electrons which are half-filled on the lattice. The exchange interaction (6.8) then naturally arises from energetically forbidden second order hopping processes which generate an effective anti-ferromagnetic exchange between classical spins[12]. Since such a mechanism requires the presence of a second band, which we will not consider in this study, the term (6.8), will be considered as a phenomenological interaction added to the Double-Exchange Hamiltonian.

The second mechanism, for generating a super-exchange interaction of the form in (6.8), is more organic to the Double-Exchange model, but arises only at a very special filling. At a filling $n = 1$ (corresponding to $n = 1/2$ of the spin-full Kondo Lattice Hamiltonian (6.1)) in the Double-Exchange Hamiltonian, all spin configurations are exactly degenerate. This is because, $n = 1$ fills up all the available states within the Double -Exchange limit. At $n = 1$, all sites are singly occupied by fermions, with the fermion spin aligned along the direction of the local classical spin. The state therefore has an energy per site of $-J_K$.

However, $1/J_K$ corrections to the Double-Exchange Hamiltonian at $n = 1$, makes the second projected out spin band available to electrons for virtual transitions (as in processes at the level of second-order perturbation theory), and this generates a super-exchange term of the form (6.8) with $J_{AF} = t^2./J_K$. We will comment more on this in Section 6.5.

The Double-Exchange Hamiltonian with the addition of the super-exchange term in (6.8) can favor a host of anti-ferromagnetic orders. The methods to uncover these spin orders are very similar to the Monte Carlo methods discussed in Section 5.2 in the context of the Kondo Lattice Model 6.1. The forbidding $\mathcal{O}(N_s^3)$ cost of diagonalizing the Double-Exchange Hamiltonian has made

Monte-Carlo methods based on exact fermionic diagonalization difficult and expensive. As a result, most calculations of the Double-Exchange model have been done with Monte Carlo methods based on exact diagonalization, using Ising spins[13]. To obviate the need for fermionic diagonalizationa at every step of the Monte Carlo process we nexr propose an effective Hamiltonian for estimating (to a high degree of accuracy), the ground state energies of the Double-Exchange Hamiltonian, for *any* generic spin configuration, and at *all* fermionic fillings. The Effective Hamiltonian method replaces the cost of exact fermionic diagonalization from $\mathcal{O}(N_s) \rightarrow \mathcal{O}(1)$ and therefore is highly attractive for faster and more efficient Monte Carlo simulations.

6.3 Deriving an Effective Flux Hamiltonian

In this Section we derive an Effective flux Hamiltonian from the Double-Exchange Hamiltonian(6.2) by integrating out the fermionic degrees of freedom. The Effective flux Hamiltonian is in terms of $U(1)$ fermionic fluxes through loops on the lattice. The Effective Hamiltonian is obtained by fitting a functional form for the Double- Exchange energy, dependent on fluxes through loops on the lattice, to an ensemble of energies corresponding to random spin configurations on the lattice. The Effective Hamiltonian is shown to be of high accuracy (with energy differences from exact diagonalization calculations being to within 1%) and also provides an insight in to what kinds of spin orders might be stable on the Kagomé lattice. We begin by describing the procedure for constructing the Effective Hamiltonian.

The central ingredients of the Effective Hamiltonian are going to be the loop

fluxes. A flux φ_ℓ through loop ℓ on the lattice is obtained by summing over the arguments of the complex hopping amplitudes on bonds making up the loop. The flux φ_ℓ is therefore given by:

$$\varphi_\ell = \sum_{\langle i,j\rangle \in \ell} \text{arg. } \langle \chi_i | \chi_j \rangle \tag{6.9}$$

where $|\chi_i\rangle$ is a bilinear representing the electron spin at site i on the lattice. Using, (6.3) and (6.7) it is easy to see that:

$$\varphi_\ell = \sum_{\langle i,j\rangle \in \ell} a_{ij} \tag{6.10}$$

where a_{ij} is the Berry phase across the directed bond $i \to j$ on the lattice. The fluxes φ_ℓ are gauge invariant up to a global $U(1)$ transformation which keeps the Double-Exchange ground state energy unchanged.

The ground state energy is a function of the fluxes through loops on the lattice. With no prior justification, and validated only *a posteriori* by the agreement between energies from Effective Hamiltonian and exact diagonalization, we present the following functional form for the Effective Hamiltonian:

$$\mathcal{H}_{eff}(n, \{\mathbf{S}_i\}) = \sum_{\mathcal{G}_a \in \mathcal{G}} t^\ell \left(\prod_{\langle i,j\rangle \in \mathcal{G}_a} \cos(\theta_{ij}/2) \right) h_{\mathcal{G}_a}(n) \cos(\varphi_{\mathcal{G}_a}(\{\mathbf{S}_i\})) \tag{6.11}$$

Each term in the Effective Hamiltonian in (6.11) depends on a loop on the lattice. Let us define $\mathcal{G}$ to be the set of all (even or odd length) loops on the lattice. An element $\mathcal{G}_a$ specifies an element of the set $\mathcal{G}$, with the arbitrary integer

a labeling the distinct kinds of loops on the lattice. The length of each loop $\mathcal{G}_a$ is given by ℓ and equals the number of bonds making up the loop.

The length of the loop ℓ also determines the number of hoppings t^ℓ required for the fermion to traverse once around the loop. Each hopping is attenuated by a factor $\cos(\theta_{ij}/2)$ which depends on the spin configuration on the loop ℓ. The flux φ_ℓ is the flux through the loop and the set of loop coefficients or "couplings" $\{h_\ell(n)\}$ are the fit parameters of the Effective Hamiltonian, and depend only on the geometry of the loop ℓ and the filling. The Effective Hamiltonian (6.11) can therefore be considered a series expansion in the (cosine of)fluxes through loops on the lattice, with the terms organized in increasing length of the loops on the lattice. Such flux Hamiltonians are common in Bosonic mean field theories where an expansion of the form (6.11) for the mean field energy can be shown to be analytically exact[14, 15].

The exponential attenuation of hoppings (t^ℓ in (6.11)) with increasing length ℓ of the loops, ensures the convergence of the series(6.11) for a general background configuration of classical spins $\{\mathbf{S}_i\}$ on the lattice. This can be seen in the simple case of a background classical spin configuration where all nearest neighbor classical spin angles are the same and equal to a constant $|\theta|$. In this case, the flux term in (6.11) for a loop of length ℓ is preceded by an amplitude $(t\cos\theta/2)^\ell$ and successive terms in (6.11) correspondingly to larger and larger loops on the lattice have diminishing contributions, vanishing in the limit $\ell \to \infty$. The Effective Hamiltonian is therefore a controlled series expansion in the length of the loops on the lattice.

The only unknowns in the flux expansion expression are the set of loop coefficients or "couplings" $\{h_{\mathcal{G}_a}(n)\}$. These are extracted using a real space fitting

procedure similar to the calculation for finding the RKKY interactions (see Section 5.3), where instead of fitting the RKKY Hamiltonian (5.17) to numerical energies obtained from exact diagonalization of Kondo Lattice Model Hamiltonian (6.1) for a data base of randomly generated spin configurations, we fit the functional form in (6.11) to the data base of exact numerical Double Exchange energies obtained by diagonalizing (6.2). A data-base of random spin configurations is built and exact fermionic diagonalization done for all spin configuration in the data base, by diagonalizing the Double-Exchange Hamiltonian (6.2) in real space. The energies of each spin configuration, at every filling, is then fit to the functional form of the Effective Hamiltonian (6.11) by doing linear least squares fitting with fit parameters $\{h_{\mathcal{G}_a}(n)\}$.

More specifically, we find the optimal set of parameters $\{h_{\mathcal{G}_a}(n)\}$ that minimize the norm ϵ_{DE} of the following scalar equation:

$$\epsilon_{DE} = |\mathbf{M}(n) \cdot \mathbf{h}(n) - \boldsymbol{\varepsilon}(n)| \tag{6.12}$$

where, $\mathbf{M}$ is a $N \times n_h$ matrix (N is the number of random spin configurations in the fitting data base and n_h is the number of fit parameters), $\mathbf{h}$ is a $n_h \times 1$ column vector containing the fitting parameters and $\boldsymbol{\varepsilon}$ is a $N \times 1$ vector of Double-Exchange enrgies for each of the N random spin configurations, obtained by filling the single particle fermionic energies up to the filling n. Also, as is evident from the explicit filling n dependence shown in (6.12), this fitting procedure is carried out for every filling.

Before presenting the results of the fitting procedure, we write out the Effective Hamiltonian for the first few dominant loops on the Kagomé lattice of

length three and six, for the specific case of spin configurations where all nearest neighbor angles are the same and equal to θ:

$$\begin{aligned}\mathcal{H}_{eff} = h_0(n) + h_{\Delta}(n)\tilde{t}^3(\theta) \sum_{\Delta_i=1}^{\Delta_i=2N_s/3} \cos(\varphi_{\Delta_i}) + h_{2\Delta}(n)\tilde{t}^6(\theta) \sum_{\Delta_i=1}^{\Delta_i=2N_s/3} \cos(2\varphi_{\Delta_i}) \\ + h_{hex}(n)\tilde{t}^6(\theta) \sum_{i=1}^{i=N_s/3} \cos(\varphi_{hex_i}) + h_{bowtie1}(n)\tilde{t}^6(\theta) \sum_{i=1}^{i=N_s/3} \cos(\varphi_{bowtie1_i}) \\ + h_{bowtie2}(n)\tilde{t}^6(\theta) \sum_{i=1}^{i=N_s/3} \cos(\varphi_{bowtie2_i}) + \mathcal{O}(\tilde{t}^7(\theta))\end{aligned} \tag{6.13}$$

where the summations Δ_i are taken over all $2N_s/3$ triangles on the lattice, $h_0(n)$ is a filling dependent and flux independent constant [2], $h_{\triangle}(n)$ is the coefficient of the expansion corresponding to the flux through the triangle (the smallest non-trivial loop on the lattice) and $h_{2\triangle}(n), h_{hex}(n), h_{bowtie1}(n), h_{bowtie2}(n)$ are the coefficients of loops of length six on the lattice corresponding to the fermion hopping twice around the triangle, around a hexagon and the two different ways of traversing a bow-tie loop, respectively. The exponent of $\tilde{t}(\theta) \equiv t\cos\theta/2$, indicates the order of the loop expansion (6.11), and is equal to the length ℓ of the loops.

Couplings for loops of length three and six are shown in Fig.6.1. Also shown is a triangular loop of length three and 3 loop of length six on the Kagome lattice, with the most dominant contributions to the Effective flux Hamiltonian and corresponding to the terms in (6.13). The small arrows around the loops indicate the directions for traversing the loop for computation of the fluxes in (6.13).

[2]Such a term arises from self-retracing loops. The simplest such loop is of length two and corresponds to a fermion hopping across a bond and back again. These loops have zero flux for any spin configuration

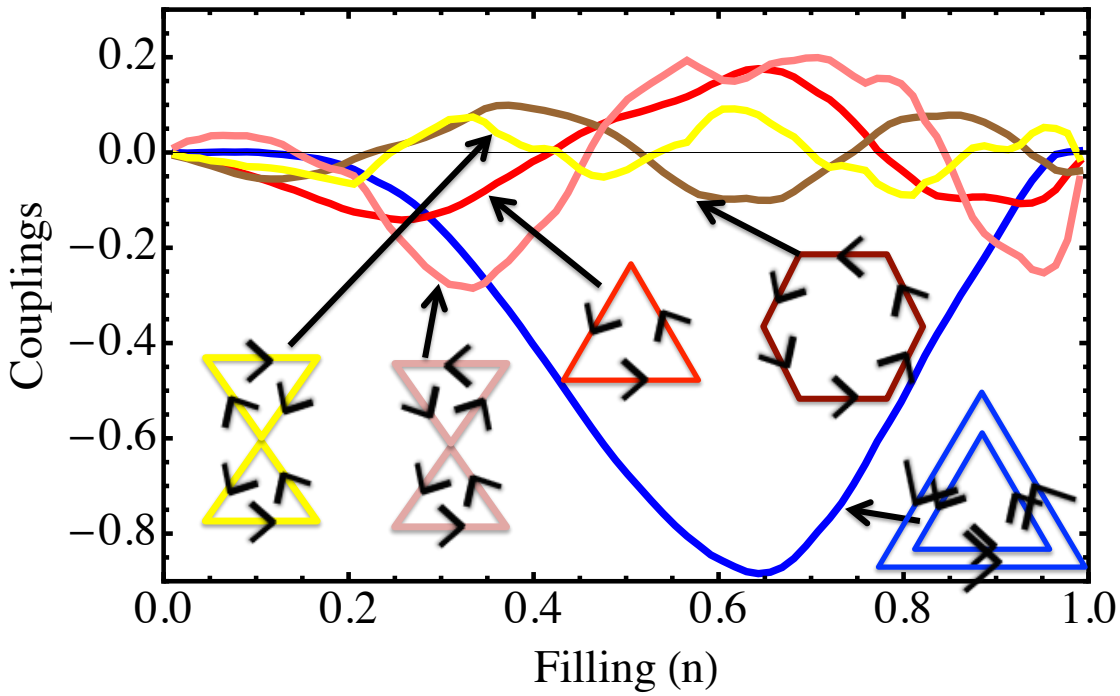

Figure 6.1: Couplings corresponding to loop fluxes in the Effective Hamiltonian (6.11),(6.13) as a function of electronic filling n. Each curve corresponds to the coupling coefficient of a loop on the lattice, indicated by arrows going from the loop to a specific curve in the plot. Coefficients for five different dominant flux loops are shown. The curve in blue is for length three triangular loops on the lattice. Curve in red is for a loop where a fermion traverses a triangular loop twice. Curve in brown is the coefficient of hexagonal flux loops on the lattice and the curves in pink and yellow correspond to coefficients of two different types of bow-tie flux loops on the lattice. In every loop show, the arrows indicate the direction in which to traverse the loop for flux computation. All data is for $N_s = 3 \times 36^2$ lattice with a fitting data-base of $N = 400$ random spin configurations

The Effective-Hamiltonian favors spin configurations which give rise to zero flux through all triangles on the lattice. The coefficient $h_\Delta(n)$ is the most dominantly negative coupling and favors the ferromagnetic order which has zero flux through the triangles (and all other loops on the lattice). The Effective Hamiltonian therefore predicts the Ferromagnetic state to be the ground state of the Double-Exchange Hamiltonian for *all* fillings, consistent with previous predictions[1, 2].

We now comment on how degeneracy between states can be systematically resolved by fluxes through loops on the lattice. Imagine a set of states, all of which have the same fluxes though the triangular loops of length three on the lattice. This implies that all such spin states are degenerate in energy up to order $\tilde{t}^3$ in the loop expansion(6.11). Now, if the same set of states have different fluxes through the next higher loops of length six on the lattice, state selection will occur at order $\tilde{t}^6$ and break the energy degeneracy between states. An example of this resolution of degeneracy will be demonstrated in the next Section, in the case of the degenerate 120 degree states on the Kagome lattice, all of which have the same flux through triangular loops on the lattice, but have different exact Double-Exchange energies, arising from differences in flux distributions through loops of length six on the lattice. The Effective flux Hamiltonian is therefore a systematic way of studying the lifting of degeneracy between energetically competing states.

The couplings corresponding to loops of different lengths on the lattice, shown in Fig.6.1, have been obtained numerically in the case of the Double Exchange Hamiltonian. However, there exist analytical resummation methods to compute these coupling coefficients by enumerating all possible loops on the lattice, as was done for spin-wave fluctuations about a collinear spin state on the Pyrochlore lattice by Uzi and Henley[16]. A similar computation (left for future work) for the Effective Double Exchange Hamiltonian on the Kagome lattice will be a check for the numerically computed coefficients in Fig.6.1.

Fig.6.1 also shows that the magnitude of the couplings $\{h_{\mathcal{G}_a}(n)\}$ decays with increasing length ℓ of the loops. It is important to note that there are filling regions where some of the loop length six couplings are greater (in magnitude)

than the single triangle coupling $h_\Delta(n)$. This, however, does not necessarily imply[3] that the sixth order (in $\tilde{t}$ (6.13)) terms are greater than the third order terms in (6.13), since each coupling coefficient also needs to be weighted by the amplitude factor $\tilde{t}$, which goes as $\tilde{t}^6$ for loops of length six and $\tilde{t}^3$ for loops of length three, suppressing the sixth order corrections (in comparison to the third order term) to the energy in (6.13).

Couplings corresponding to loops of length three and six, for special commensurate fillings, are shown in Table 6.1. For a generic filling the couplings $h_\ell(n)$ are expected to decay as a power law in the length ℓ of the loop. This is because, the fermionic excitations are gapless for a generic filling. For ordered states, presence of a magnetic unit cell will give rise to bands, and for special fillings at which the system is a band insulator, the couplings $h_\ell(n)$ will decay exponentially. In both cases, atleast for practical purposes, the decay of couplings with increasing length of the loops is fast enough for us to retain only couplings corresponding to the first few dominant loops on the lattice, to get energies from the Effective Hamiltonian to within 1% agreement with exact diagonalization values.

We next use the Effective Hamiltonian (6.11) to study state-selection within the manifold of 120 degree states on the Kagomé lattice, which become competitive with the Ferromagnetic state in the presence of a super-exchange interaction (6.8)

[3]For very small fillings, $n \to 0$, $h_\Delta(n)$ goes almost to zero, so that other couplings will dominate even when multiplicities are accounted for

Filling (n)	h_Δ	$h_{2\Delta}$	h_{hex}	$h_{bowtie1}$	$h_{bowtie2}$
$n = 1/4$	-0.08	-0.141	0.013	-0.171	0.006
$n = 1/3$	-0.233	-0.097	0.077	-0.285	0.075
$n = 5/12$	-0.449	-0.001	0.086	-0.139	0.008
$n = 1/2$	-0.672	0.077	0.022	0.108	-0.037
$n = 2/3$	-0.873	0.17	-0.097	0.19	0.048

Table 6.1: Table enumerating the couplings $h_\ell(n)$ in the Effective flux Hamiltonian (6.11) at several commensurate fillings n. h_Δ is the coefficient of the term corresponding to the flux through triangular loops of length three on the lattice. $h_{2\Delta}$ corresponds to the flux acquired by the fermion on traversing a triangular loop twice. h_{hex} is the coupling coefficient of flux around hexagons. $h_{bowtie1,bowtie2}$ loops are shown in Fig.6.1 and correspond to the coefficients of the two different ways for a fermion to encircle a bow-tie loop. All couplings are in units of the electron hopping t and all data is for a Kagomé lattice of size $N_s = 3 \times 36^2$. Size of the fitting database is $N = 400$.

6.4 State-Selection within the manifold of 120deg. states on the Kagomé lattice

In this Section, we explore fermion induced state-selection on the Kagomé lattice within the manifold of 120 degree., 3 coloring[11] states, all of which are ground states of the nearest neighbor classical Heisenberg model. Since the Double Exchange Hamiltonian (6.2) always favors the Ferromagnetic order to be the ground state, we engineer a non-trivial problem of state selection by adding a super-exchange (6.8) interaction to the Double Exchange Hamiltonian.

The strength of the super exchange interaction is taken to be strong enough (compared to the Double Exchange interaction) such that the Ferromagnetic order is no longer the ground state. For sufficiently large super-exchange interaction, the ground states of the combined Double Exchange and Super Exchange Hamiltonian lie within the manifold of the three coloring 120 degree [11] states and the Double Exchange interaction selects from within this manifold, break-

ing the degeneracy between the 120 degree states.

We find that the two coplanar $\mathbf{q} = 0$ and $\sqrt{3}\times\sqrt{3}$ states remain degenerate for all fillings even after addition of Double Exchange coupled fermions to the system. However, there is a lifting of degeneracy between the coplanar states and the non-coplanar *Cuboc1* state. The non-coplanar *Cuboc1* order Fig.6.2 is found to be the lowest energy state for a wide range of fillings. We show that the Effective Hamiltonian predicts the lifting of this degeneracy due to fluxes through hexagonal loops on the lattice. We end this Section by making a comparison of energies obtained from the Effective Hamiltonian and from exact fermionic diagonalization, thereby commenting on the accuracy of the Effective Hamiltonian.

The Hamiltonian for studying state-selection is given by:

$$\begin{aligned} \mathcal{H} &= \mathcal{H}_{DE} + \mathcal{H}_{AF} \\ &= \sum_{\langle i,j \rangle} t_{ij} c_i^\dagger c_j + J_{AF} \sum_{\langle i,j \rangle} \mathbf{S}_i \cdot \mathbf{S}_j \end{aligned} \tag{6.14}$$

where we take the limit $J_{AF} \gg t$ to ensure that the ferromagnetic state is destabilized and we are within the manifold of the ground states of $\mathcal{H}_{AF}$. Ground states of $\mathcal{H}_{AF}$ for anti-ferromagnetic ($J_{AF} > 0$) belong to the family of extensively degenerate 120 degree states all of which have nearest neighbor spins making an angle of $2\pi/3$ radians. Three well known states from this family: $\mathbf{q} = 0, \sqrt{3} \times \sqrt{3}$ and *Cuboc1* were discussed in 5.4 . We now discuss state-selection within the manifold of these three states by switching on the coupling to fermions.

Fig.6.2 shows the one-dimensional phase diagram of the Hamiltonian (6.14),

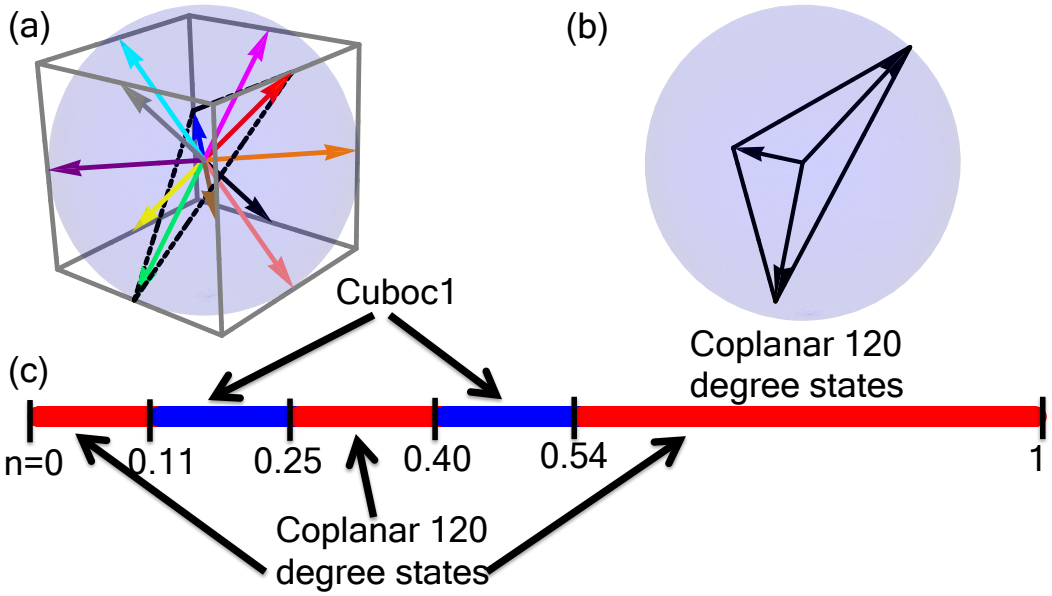

Figure 6.2: State selection within the Double Exchange model in the presence of a super-exchange interaction between classical spins on the lattice (6.14). (a) The common origin plot (see Section 5.5.1) of the non-coplanar *Cuboc1* state shown with twelve spins, forming the magnetic unit cell, pointing towards the mid-points of the edges of a unit cube. Spins in each triangle are coplanar, as shown by the three spins lying in a triangular plane shown with black dashed lines. (b) Common origin plot of the coplanar 120 degree or 3 coloring [11] states (c) The phase diagram is shown as a function of a single parameter, the electron filling n. Regions in red correspond to the coplanar $\mathbf{q} = 0$ and $\sqrt{3} \times \sqrt{3}$ states which are *exactly* degenerate at all fillings. Regions in blue show filling intervals where there is a unique state selection favoring the non-coplanar *Cuboc1* state. Data for making the phase diagram is obtained from exact fermionic diagonalization for a lattice size of $N_s = 3 \times 36^2$

in the limit $J_{AF} \gg t$, as a function of the electronic filling n. The red regions in Fig.6.2 correspond to the degenerate coplanar states shown by the common origin plot of spins on the lattice in the Figure. The coplanar states are therefore lower in energy that the non-coplanar *Cuboc1* state in three disjoint filling intervals of $n \in [0, 0.11], [0.25, 0.40]$ and $n \in [0.54, 1]$. However for these aforementioned filling ranges, there is no unique state selection from within the manifold of coplanar 120 degree states on the Kagomé lattice. Unique state se-

States	φ_{Δ}	$\varphi_{2\Delta}$	φ_{hex}	$\varphi_{bowtie1}$	$\varphi_{bowtie2}$
Ferro.	0	0	0	0	0
$\mathbf{q}=0$	π	0	0	0	0
$\sqrt{3}\times\sqrt{3}$	π	0	0	0	0
$Cuboc1$	π	0	π	0	0
$Cuboc2$	0.27	0.55	π	0	0.55

Table 6.2: Fluxes through loops of length three and six for five different ordered states on the Kagomé lattice. The six loops are shown in Fig.6.1. All fluxes are in radians.

lection, however, does take place for fillings in the range $n \in [0.11, 0.25]$ and $n \in [0.40, 0.54]$ where the lowest energy state is the non-coplanar *Cuboc1* state, with a magnetic unit cell containing twelve spins pointing to the mid-points of the edges of a unit cube, as shown in Fig.6.2. Thus, the Hamiltonian (6.14) lifts the degeneracy between 120 degree states on the Kagome lattice and favors the complex non-coplanar *Cuboc1* state in certain filling intervals.

The lower energy of the *Cuboc1* state in comparison to the coplanar states is easily seen from the distribution of fluxes through different loops on the lattice, tabulated in Table6.2. The coplanar and the *Cuboc1* states are degenerate (in fluxes and energy) up to the triangular loop of length three, meaning that all three states have the same flux through all triangular loops on the lattice and therefore have the same energy via the Effective Hamiltonian. All states have the same π flux. However, the fluxes for the states differ at the level of hexagonal loops of length six, where the coplanar states have zero flux and the *Cuboc1* state has π flux. The *Cuboc1* state is therefore favored for fillings where the coefficient of the hexagonal flux term in (6.13) is positive and the coplanar states are favored when the coefficient is negative. Thus state-selection between the coplanar and non-coplanar 120 degree states on the Kagomé lattice happens through hexagonal loops on the lattice with the splitting between states of the

order $\mathcal{O}(\tilde{t}^6) = \mathcal{O}(t\cos(\theta/2))^6 = \mathcal{O}(1/2^6)$, where $\theta = 2\pi/3$ for all the 120 degree states in Fig.6.2.

The competition as a function of filling between 0 and π hexagonal flux states brings up the question whether it is possible to stabilize states with chiral (neither 0 nor π) time reversal symmetry breaking fluxes. While such states can definitely be stabilized by the Double Exchange part of the Hamiltonian (6.14), the presence of a non zero or non π flux will imply a state outside the manifold of the 3 coloring 120 degree states and will therefore not be a ground state of the dominant super-exchange part of the interaction in (6.14). Stabilizing chiral states is however possible in regimes where the strength of the super-exchange interaction is comparable or weaker compared to the strength of the Double-Exchange interaction. A possible stable candidate state for this regime of interactions is the non-coplanar *Cuboc2* state of Fig. 5.8.

We end this Section by benchmarking the accuracy of the Effective Hamiltonian in reproducing energies from exact diagonalization of the Double-Exchange Hamiltonian (6.2). A comparison of the energies, at several commensurate fillings and for five ordered states, between exact diagonalization and the Effective Hamiltonian is shown in Table 6.3. For several fillings, although relative percentage differences between exact and effective energies might be as large as 5%, difference in energies of competing states from exact diagonalization and from the Effective Hamiltonian are mostly to within 1%. The Effective Hamiltonian can be systematically made more accurate by increasing the loop flux terms (beyond the dominant first few loops on the lattice) in the Effective Hamiltonian (6.13) and also by increasing the size of the fitting data-base.

We next move on to study state-selection at a very special limit of the Double

States	n=1/4		n=1/3		n=5/12		n=1/2		n=2/3	
	E.D.	$\mathcal{H}_{eff}$	ED	$\mathcal{H}_{eff}$	ED	$\mathcal{H}_{eff}$	ED	$\mathcal{H}_{eff}$	ED	$\mathcal{H}_{eff}$
Ferro.	0.5	0.572	0.667	0.717	0.797	0.82	0.864	0.883	0.858	0.869
$\mathbf{q}=0$	0.357	0.377	0.429	0.436	0.441	0.457	0.432	0.451	0.333	0.381
$\sqrt{3}\times\sqrt{3}$	0.357	0.377	0.429	0.436	0.441	0.457	0.432	0.451	0.333	0.381
Cuboc1	0.359	0.376	0.418	0.436	0.443	0.458	0.443	0.452	0.333	0.380
Cuboc2	0.451	0.463	0.581	0.602	0.684	0.711	0.766	0.772	0.722	0.73

Table 6.3: Comparison of energies of the Double-Exchange Hamiltonian from the Effective Hamiltonian approach (6.11) at several commensurate fillings $n = 1/4, 1/3, 5/12, 1/2, 2/3$ and for five ordered states on the Kagomé lattice. Energies from the Effective Hamiltonian, labeled $\mathcal{H}_{eff}$, are computed using couplings (fit parameters) for a lattice size $N_s = 3\times 36^2$ and using a fitting data-base with $N = 400$ random spin configurations. Energies from exact diagonalization labeled E.D. are calculated using a lattice size $N_s = 3 \times 36^2$ sites. **All Double-Exchange energies are negative (only magnitudes of the energy are shown). All energies from the Effective Hamiltonian have errors bars in their third decimal place**

Exchange model: a filling of one corresponding to a single fermion occupancy at every site, where *all* spin states are exactly degenerate and $1/J_K$ corrections to the energy favors anti-ferromagnetic orders.

6.5 Double Exchange model at a filling one (half-filling of spin-full model)

In this Section we explore state-selection within the Double-Exchange model at a special filling of $n = 1$, where all spin configurations are exactly degenerate on the lattice. We derive an Effective Hamiltonian to different orders in $1/J_K$ and show that state-selection occurs at order $\sim t^6/J_K^5$ and selects the complex non-coplanar *Cuboc1* state.

The Double-Exchange model at a filling of one corresponds to a single fermion

occupancy at every site. This filling corresponds to complete occupancy of the lower fermionic spin band of the Kondo model and any increase in filling corresponds to creating particles in the upper spin band, which is energetically forbidden with a cost of $\sim 2J_K$, and is completely projected out in the limit $J_K \to \infty$. Therefore, at a filling of one, each fermion is stationary and has its spin aligned with the direction of the local spin at every site. All hoppings are forbidden and all spin configurations are exactly degenerate with an energy per site of $-J_K$.

What happens if we now consider the leading order $1/J_K$ corrections at a filling one? At a unit filling and in the limit $J_K \to \infty$, every electron occupies a single site on the lattice and any hopping process corresponds to a double occupancy of a site and comes with an energy cost of $2J_K$ and is therefore energetically forbidden in the infinite J_K limit. Finite J_K corrections to the energy of the singly occupied, infinite J_K state, come from electronic processes where an electron can hop to a neighboring site, pay an energy cost $2J_K$ and then hop back to its original site. This process which is allowed by second order perturbation theory is called "virtual" since there is no net transport of electrons from one site to another. These virtual hopping processes generate an effective exchange Hamiltonian between classical spins on the lattice, much like the super-exchange mechanism[12]. To calculate this exchange, we write down the Hamiltonian $\mathcal{H}(n=1)$ at unit filling:

$$\mathcal{H}(n=1) = -J_K - \sum_{\langle i,j \rangle} t c_i^\dagger c_j + \text{ h.c.} \tag{6.15}$$

and treat the hopping Hamiltonian as a perturbation to the energy of the degenerate spin states at $-J_K$. Thus, in the limit $J_K \gg t$, an electron on site i,

with spin aligned with the local classical moment along the z direction (without loss of generality), can hop via the hopping term in (6.15), to a neighboring site which is occupied by another fermion with its spin aligned along θ_j [4],. Since site j already has a single electron occupancy, the only available state for the electron hopping from site i, is to occupy the state anti-parallel to the direction of the local classical moment at site j. This corresponds to a hopping element given by $t\langle\chi_i|\chi_j\rangle$, where $|\chi_j\rangle$ is given by:

$$|\chi_j\rangle = \mathcal{R}(\pi + \theta_j)|\chi_i\rangle \tag{6.16}$$

where $\mathcal{R}$ is the rotation matrix defined in (6.5). The effective hopping is therefore given by $t \sin\theta_{ij}/2$ (obtained by letting $\theta_{ij} \to \theta_{ij} + \pi$ in (6.3)) and the leading order $1/J_K$second order correction to the energy of all states at unit filling is given by:

$$E^{(2)}(n=1) = -J_K - \frac{t^2}{J_K}\sum_{\langle i,j\rangle}\sin^2(\theta_{ij}/2) = -J_K - 2\frac{t^2}{J_K} + \frac{t^2}{J_K}\sum_{\langle i,j\rangle}\mathbf{S}_i\cdot\mathbf{S}_j \tag{6.17}$$

where we use the identity $\sin^2(\theta_{ij}/2) = 1 - \mathbf{S}_i\cdot\mathbf{S}_j$. The exchange Hamiltonian (6.17) favors anti-ferromagnetic states which maximize the angle θ_{ij} between neighboring classical spins on the lattice. Thus the leading $1/J_K$ correction to the Double-Exchange energy at $n = 1$, favors anti-ferromagnetic orders. On the Kagomé lattice, this correction favors the well known 120degree classical states, and selects them from the entire space of classical states on the Kagomé lattice, at unit filling. However degeneracy within the manifold of 120 degree states

[4]For simplicity of calculation, we ignore the azimuthal angles and consider co-planar configurations, however the final result (6.17) is valid for any generic spin configuration

remains unbroken.

Predictions from the second order correction (6.17) to the Double-Exchange energy at unit filling are numerically verified in Figure 6.3 where energy corrections for the three 120degree states $\mathbf{q} = 0, \sqrt{3} \times \sqrt{3}$ and *Cuboc1* and the *Cuboc2* state is plotted as a function of $1/J_K$. The energy corrections are obtained for these states by calculation their exact energies at several (large) values of the Kondo coupling strength using exact fermionic diagonalization of the Kondo Hamiltonian (6.1) at half-filling[5] and subtracting $-J_K$ from the energies. This allows us to calculate the coefficient of the t^2/J_K term in (6.17). For ordered states with uniform nearest neighbor angles θ, the coefficient is simply $-2\sin^2(\theta/2)$. This predicts a value of $-3/2$ for the 120 degree states ($\theta = 2\pi/3$ for the 120 degree states) and a value of $-1/2$ for the *Cuboc2* state, consistent with the slopes of the lines shown in Fig.6.3

Before ending this Section we comment on the lifting of the remnant degeneracy between the 120 degree states on the Kagomĺattice, at higher orders in perturbation theory. Higher orders (in t^2/J_K) in perturbation theory will lead to virtual second order hopping processes along longer paths on the lattice. For example, to order t^3/J_K^2 the virtual second order hopping can go once around a triangular loop on the lattice. A non-trivial effect of such longer virtual hopping paths, is the Berry phase acquired by the fermions through virtual hoppings around closed loops. These Berry phases, along with the more trivial $\sim t\sin(\theta_{ij}/2)$ exchange amplitudes will contribute to higher order corrections to the Double-Exchange energy at unit filling.

On the Kagomé lattice, the exchange amplitudes $\sim t\sin(\theta_{ij}/2)$ for a hopping

[5]A filling of half in the Kondo Hamiltonian corresponds to unit filling in the Double-Exchange model

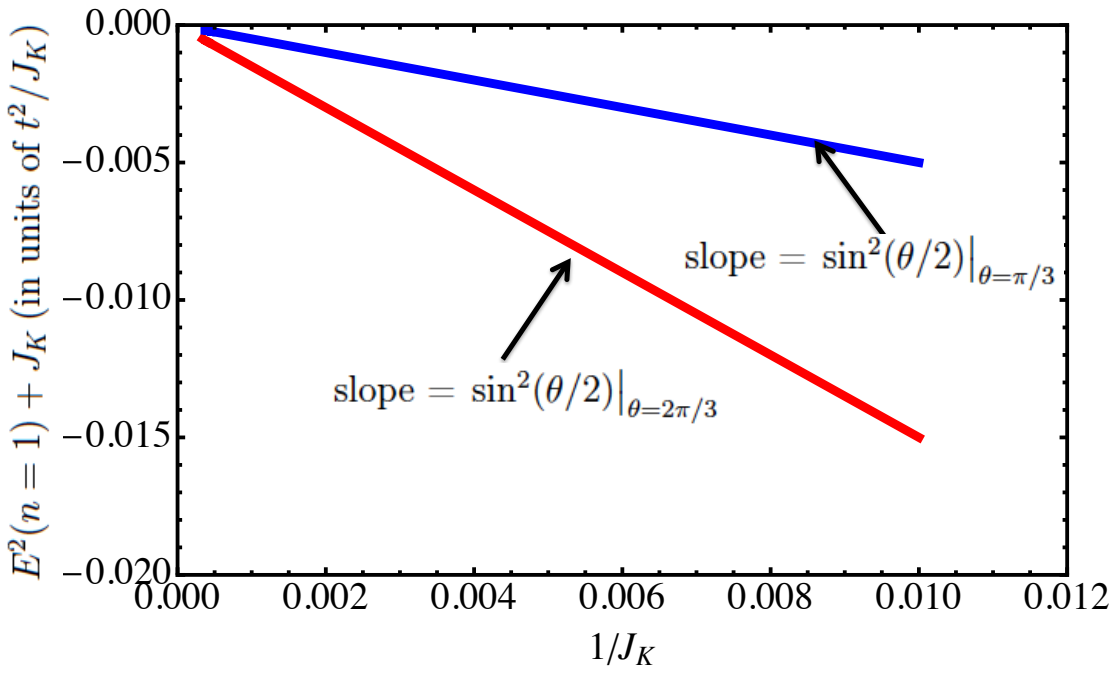

Figure 6.3: $1/J_K$ corrections to the Double-Exchange energy at unit filling (see (6.17)) for the three 120 degree states ($\mathbf{q} = 0, \sqrt{3} \times \sqrt{3}$ and *Cuboc1*) and the *Cuboc2* state. The two lines correspond to the best fit curves to the numerically computed $E^{(2)} + J_K$ energies for the four states by exactly diagonalizing the Kondo Lattice Model Hamiltonian (6.1) for several different values of J_K. All three 120 degree states are degenerate and have a slope of $-3/2$, in good agreement with the analytical slope from (6.17). The *Cuboc2* state has a slope $-1/2$, again in excellent agreement with the analytical slope in (6.17). The three 120 degree states are lower in energy and are favored by the Effective Hamiltonian in (6.17)

process, at *any* order in perturbation theory do not resolve the degeneracy between the 120 degree states. This is because all higher orders in perturbation theory are amplitude dependent - containing functions of $f(\cos(\theta_{ij}/2), \sin\theta_{ij}/2)$ sines and cosines of nearest neighbor angles, which are the same for all 120 degree states. Degeneracy is therefore broken via Berry phases which are different for the coplanar and the *Cuboc1* states for hexagonal loops as shown in Table6.2. Degeneracy is therefore broken at order t^6/J_K^5 in perturbation theory via loops of length six on the lattice. Length six virtual hoppings select the non-coplanar *Cuboc1* state as the lowest energy state and also break the degeneracy between

coplanar states on the Kagomé lattice.

6.6 Conclusion

The biggest achievement of this Chapter has been the discovery of an Effective Hamiltonian (6.11) for the Double Exchange model, expressed as a loop expansion in terms of fluxes through plaquettes on the lattice. Before the Effective Hamiltonian (6.11), there existed no computationally cheap methodology for calculating the fermionic energies within the Double Exchange Hamiltonian. All calculations to find the optimal classical spin ground state of the Double Exchange Hamiltonian involved doing an explicit brute force diagonalization[5] of the hopping Double Exchange Hamiltonian(6.2). The Effective Hamiltonian (6.11) is valid for all fillings, for any classical background spin configuration (of both Heisenberg and Ising spins) and explicitly takes in to account both the amplitudes and the Berry phases of the hopping fermions. The procedure outlined in Section 6.3 for deriving the Effective Hamiltonian can be carried out on *any* lattice.

The incorporation of the non trivial Berry phases through loop fluxes in (6.11) is a significant improvement over past attempts [17] to find Effective spin Hamiltonians for estimating the Double Exchange energies. All past attempts have failed to take in to account the Berry phases acquired by the fermions as they hop in a non-coplanar background spin environment.

The success of the Effective Hamiltonian is diluted by the fact that we have not been able to use it explicitly in a Monte Carlo simulation to find new classical spin ground states of the Double Exchange model. This is an important and

immediate direction for future work. It is important to reiterate that because of the simple functional form of the Effective Hamiltonian, standard Monte-Carlo searches for spin ground states should become very efficient by replacing the $\mathcal{O}(N_s^3)$ cost of exact diagonalization at every Monte Carlo update step by a cheaper $\mathcal{O}(1)$ functional evaluation.

We have also discovered a corner of the parameter space of the Double Exchange Hamiltonian where a charming, previously overlooked, problem of state-selection resides. This corner in parameter space is at a unit filling in the infinite J_K limit. Due to the large energy cost of double occupancy of sites, no hopping processes are allowed and *all* classical spin states are *exactly degenerate* at this filling. We show that the leading order $1/J_K$ corrections gives rise to an Effective anti-ferromagnetic Hamiltonian (6.17) and favors maximally anti-ferromagnetic states.

The Effective anti-ferromagnetic exchange Hamiltonian (6.17) has a simple Heisenberg form and on Bravais lattices, like the square or triangular lattice, will break the degeneracy and select the conventional Neel up-down anti-ferromagnet and the coplanar 120 degree order, respectively. However, on frustrated lattices, like the Kagome and the Pyrochlore, there will be a remnant degeneracy within the manifold of maximally anti-ferromagnetic states and state-selection will occur at a higher order in the inverse of the Kondo coupling strength. This non-trivial state-selection arises out of the delicate interplay between the Double Exchange Hamiltonian and geometric frustration.

Specifically on the Kagome lattice, we find (in Section 6.5) that this state-selection occurs at a higher order in the inverse strength of the Kondo coupling and is induced by the effect of non-trivial Berry phases. The selection occurs

in favor of the non-coplanar *Cuboc1* state and selects this state from within the manifold of classical 120 degree three coloring [11] states on the Kagome lattice. It will be of great interest to explore the effects of such state-selection on the Pyrochlore lattice - an interesting opportunity for future study.

BIBLIOGRAPHY

[1] P. Anderson and H. Hasegawa, Phys. Rev. **100**, 675 (1955).

[2] P. de Gennes, Phys. Rev. **118**, 141 (1960).

[3] Yurii A Izyumov and Yu N Skryabin, Phys. -Usp. 44 109 (2001).

[4] J M D Coey, M Viret and S. V. Molmar, Adv. Phys. 48 167 (1999).

[5] S. Kumar and J. van den Brink, Phys. Rev. Lett. **105**, 216405 (2010).

[6] N. Nagaosa, J. Sinova, S. Onoda, A. MacDonald, and N. Ong, Rev. Mod. Phys. **82**, 1539 (2010).

[7] K. Ohgushi, S. Murakami, and N. Nagaosa, Phys. Rev. B **62**, R6065 (2000).

[8] I. Martin and C. D. Batista, Phys. Rev. Lett. **101**, 156402 (2008).

[9] H. Ishizuka and Y. Motome, Phys. Rev. B **87**, 081105 (2013).

[10] K. Ohgushi, S. Murakami, and N. Nagaosa, Phys. Rev. B **62**, R6065 (2000).

[11] C. L. Henley, Phys. Rev. B **80**, 180401 (2009).

[12] A. Auerbach, Interacting Electrons and Quantum Magnetism, Springer (1997).

[13] H. Ishizuka and Y. Motome, Phys. Rev. Lett. **108**, 257205 (2012).

[14] O. Tchernyshyov, R. Moessner and S. L. Sondhi, Europhys. Lett. 73, 278 (2006).

[15] U. Hizi, P. Sharma, and C. Henley, Phys. Rev. Lett. **95**, 167203 (2005).

[16] U. Hizi and C. L. Henley, Phys. Rev. B **73**, 054403 (2006).

[17] O. Erten, O. N. Meetei, A. Mukherjee, M. Randeria, N. Trivedi, and P. Woodward, Phys. Rev. B **87**, 165105 (2013).

CHAPTER 7

NON-UNIFORM SADDLE POINTS AND Z_2 EXCITATIONS ON THE KAGOMÉ LATTICE

The text and main results of this Chapter have not been published. Discussions with Michael Lawler, Gil Young Cho and Junping Sheng are acknowledged.

7.1 Introduction

Quantum spin liquids (QSL's)[1] are quantum phases of matter with no long range magnetic order. In recent years, QSL's have been the playground for realizing complex forms of matter and quantum states with exotic properties. These quantum states of matter arise due to strong quantum fluctuations which also inhibit magnetic ordering down to zero temperature. The resulting quantum state has no classical analogue, is highly entangled and has emergent *fractionalized* excitations and gauge fields[1].

Quantum fluctuations are therefore the most important ingredient for realizing a QSL. Quantum fluctuations are naturally enhanced at low spatial dimensions and when the spin size is small. Because of these reasons,spin half Heisenberg antiferromagnetic models in two dimensional lattices with frustrated geometries can realize QSL.

QSL's can be divided into two groups on the basis of whether they break any symmetries. The first group corresponds to QSL's which do not break any spatial, time reversal or rotational symmetries and lack long range magnetic order. For these reasons they are also sometimes called *Symmetric Spin Liq-*

uids(SSL's). We will use this nomenclature from now onwards. For a given lattice, the number of such quantum states and therefore *distinct* QSL's is severely constrained and can be enumerated using a mathematical technique called the Projective Symmetry Group (P.S.G.)[2]. P.S.G. has since been used to enumerate QSL's which preserve all lattice symmetries on a variety of lattices in both two [3, 4, 5, 6] and three dimensions[7].

The second group of quantum spin liquids are states that break some or all spatial and time reversal symmetries of the lattice, but are magnetically disordered similar to their symmetric cousins. Examples of such symmetry breaking spin liquid states are time reversal symmetry breaking chiral states on the Kagome lattice[8, 9] and the spatial symmetry breaking states reported by Misguich[10] and Clark et al[11].

Finding and cataloguing spin liquid states on the basis of the different ways in which they might break some or all symmetries is a harder problem compared to using P.S.G. for finding symmetry preserving SSL's. This is so because there are many more spin liquids which might spontaneously break some or all symmetries. However, there are very few spin liquids which preserve all symmetries[12, 3].

Recent progress to find spin liquids which break some or all symmetries has been made both theoretically [13] and numerically[10] for the Kagomé lattice. In particular, numerical work by Misguich[10] provides an unbiased exploration of the space of symmetry breaking QSL states on the Kagomé lattice. Such an exploration is in the spirit of other works[11] using variational wave-functions, which allow the mean field ground state of a mean field theory of the Heisenberg spin half model on the lattice, to *spontaneously* break symmetries.

In this Chapter we adapt the non-uniform Schwinger Boson Mean Field theory (non-uniform SBMFT) for an unbiased exploration of the low energy mean field solutions on the Kagome lattice. We also use the theory to develop concrete numerical realizations of non-trivial topological excitations in the background of Z_2 spin liquid states on the Kagomé lattice. The organization of the chapter is as follows: In Section 7.2 we do a brief recap of the Sp(N) formulation of Schwinger Boson Mean field theory to numerically explore mean field ground states on the Kagomé lattice. We then enumerate a few Symmetric Spin liquid states on the Kagomé lattice, which have been discovered within SBMFT[12] and also by using PSG[3], in Section 7.3 .

Section 7.3 shows that the constraints of spatial and time reversal symmetries on the mean field ground state, severely restricts the number of Symmetric Spin Liquid solutions within SBMFT. We therefore, relax these symmetry constraints on the ground state, and carry out an unbiased search for symmetry breaking SBMFT solutions on the Kagomé lattice in 7.4 . We report several symmetry breaking solutions in 7.4 in the low energy manifold of SBMFT solutions on a 48 site lattice. Finally, in Section 7.5 we develop concrete numerical realizations of topological particle excitations in a Z_2 gapped spin liquid on the Kagomé lattice. We summarize the main results of this chapter and provide future research directions in Section 7.6 .

7.2 Sp(N) Schwinger Boson Mean Field theory - Recap

In this Section, for the purposes of the present Chapter, we provide a brief recap of the Sp(N) Schwinger boson formalism developed in Section 3.4 .2. We

study the spin-half Heisenberg Hamiltonian on the Kagomé lattice (a Kagomé lattice is illustrated in Fig.5.1 of an earlier chapter),

$$\mathcal{H}_{heis} = J \sum_{\langle i,j \rangle} \mathbf{S}_i \cdot \mathbf{S}_j \tag{7.1}$$

where $J > 0$ is a uniform nearest-neighbor antiferromagnetic coupling and $\mathbf{S}_i$ and $\mathbf{S}_j$ are spin half operators on sites i and j, respectively. Schwinger boson mean field theory is a mapping of the spin half operators to N flavors of bosons via the mapping described in (3.22). In the limit $N \to \infty$, also called the "large N" limit, the bosonic Hamiltonian is given by:

$$\mathcal{H}_{Sp} = \boldsymbol{\beta}^\dagger \mathbf{M}_{Sp} \boldsymbol{\beta} + \sum_{\langle ij \rangle} J|Q_{ij}|^2 + (1+\kappa) \sum_{i=1}^{N_s} \lambda_i \tag{7.2}$$

where $\boldsymbol{\beta}^T = (b_{1\uparrow}, .., b_{N_s\uparrow}, b^\dagger_{1\downarrow}, .., b^\dagger_{N_s\downarrow})$ and the Hamiltonian matrix is given by

$$\mathbf{M}_{Sp} = \begin{pmatrix} -\mathbf{\Lambda} & J\mathbf{Q} \\ -J\mathbf{Q}^* & -\mathbf{\Lambda} \end{pmatrix} \tag{7.3}$$

where $\mathbf{\Lambda}_{ij} = \delta_{ij}\lambda_i$ and $\mathbf{Q}$ is an anti-symmetric matrix of bond variables. The set of Lagrange multipliers $\{\lambda_i\}$ enforce the constraint of a fixed number of bosons at every site $\langle b^\dagger_{i\uparrow} b_{i\uparrow} + b^\dagger_{i\downarrow} b_{i\downarrow} \rangle = \kappa = 2S$ (see Eq.(3.7), S is the spin size) and the bond variables Q_{ij} need to be determined self-consistently $\langle Q_{ij} \rangle = 0.5 \langle b_{i\uparrow} b_{j\downarrow} - b_{i\downarrow} b_{j\uparrow} \rangle = Q_{ij}$, where the average $\langle ... \rangle$ is taken in the Schwinger boson mean field ground state.

The set of mean field parameters which satisfy the constraint of a fixed number of bosons per site and the self-consistency condition of the bond variables

(3.7) is called an **Ansatz**. Each **Ansatz** corresponds to a spin liquid state within SBMFT (for a small enough κ). Thus, low κ SBMFT solutions with uniform bond amplitudes and Lagrange multipliers give rise to symmetric spin liquid states.

In addition to characterizing a spin liquid state using an **Ansatz** of mean field parameters: $\{\lambda_i^*, Q_{ij}^*\}$ ($*$ indicates the optimal values of mean field parameters satisfying constraints (3.7)), spin liquid states can also be labeled by specifying the distribution of fluxes through loops on the lattice. Within SBMFT, a gauge invariant way of defining fluxes is to compute the following phase for even length loops on the lattice[14]:

$$\Phi_\ell = Q_{ij} * (-Q_{jk}^*) * Q_{kl} * (-Q_{lm}^*)....(-Q_{ai}^*) \tag{7.4}$$

where letters i, j, k, l, m, a label sites around the loop ℓ and $*$ is the complex conjugation operator.

We now briefly discuss how spin rotational, spatial and time reversal symmetries are encoded in to the values of the mean field parameters. The spin rotational invariance of the original SU(2) invariant Heisenberg Hamiltonian (7.1) is implicitly preserved in the mapping to the Schwinger bosons. Symmetries in addition to spin rotational invariance, such as the space group and time reversal symmetries, can be broken by the mean field parameters. A non-uniform distribution of the mean field parameters will break spatial symmetries. Similarly, distributions of mean field parameters which give rise to fluxes Φ_ℓ around loops that are not zero or π, break time-reversal symmetries and will give rise to *Chiral spin liquids*[13].

Before ending this Section we make an important note about the presence

of an *emergent* symmetry in the mean field **Ansatz** that is absent in the original SU(2) invariant Heisenberg Hamiltonian(7.1). Notice that the global transformation $b_{i\sigma} \rightarrow -b_{i\sigma}$ (for $\forall i$ and $\sigma =\uparrow, \downarrow$) leaves the mean field **Ansatz** invariant. This Z_2 symmetry does not correspond to any of the *physical* (spin rotational, lattice space group, time reversal) symmetries and arises as a consequence of the decoupling of the mean field Hamiltonian in the large N limit. As a result of this symmetry, all spin liquids found within SBMFT will be called Z_2 spin liquids. We next discuss some symmetric Z_2 spin liquids on the Kagomé lattice[12, 3].

7.3 Symmetric Spin Liquids in the Large N limit on Kagomé

In this Section, we review Symmetric Spin Liquids[2, 3] - Schwinger Boson mean field states that do not break any lattice or time reversal symmetries. These states have uniform mean field parameters and have fluxes (7.4) of either 0 or π through loops on the lattice. Discussion of Symmetric Spin Liquids will set the stage for talking about symmetry breaking QSL's in Section 7.4 .

Wen[2] proposed a concept for enumerating all the symmetry preserving quantum spin liquids on any given lattice. The concept called the "Projective Symmetry Group", imposes constrains on the distribution of the Schwinger Boson mean field parameters so that the mean field state is invariant under all symmetries. For example, the condition of translational invariance on a spin liquid mean field state would imply uniformity of all the bond amplitudes Q_{ij} and the Lagrange multipliers λ_i in (7.2). Imposing the further constraint of time reversal invariance would imply that the mean field states can only have 0 or π fluxes (7.4) through all even length loops on the lattice.

Wang and Vishwanath[3] found that enforcing all the constraints imposed by symmetries on a mean field state, severely restricts the number of allowed (by symmetries) symmetric spin liquid states on a given lattice. For example, keeping only the nearest neighbor bond amplitudes $\{Q_{ij}^*\}$ in the Schwinger boson equations (7.2), gives *four* SSL's on the Kagome lattice.

Fig7.1 shows two of the four symmetric Z_2 spin liquids on the Kagomé lattice[3, 12]. The symmetric spin liquids are labeled as the $Q_1 = Q_2$ state and the $Q_1 = -Q_2$ state[12]. Since the matrix $\mathbf{Q}$ in Eq. (7.3) is anti-symmetric in the spatial indices, the direction of the arrows in each state in Fig.7.1 indicates positive bond amplitudes $Q_{ij}^* = Q$. All bond amplitudes are uniform and so are all the Lagrange multipliers on the lattice. The direction of positive bond amplitudes, indicated by the arrows, can be used to compute the fluxes(7.4) through even length loops on the lattice. The smallest non-trivial even length loops are the hexagon and the rhombus. The $Q_1 = Q_2$ state has a flux of π through the hexagonal loops and a zero flux through the rhombus, whereas the $Q_1 = -Q_2$ state has zero flux through both the hexagonal and the rhombus loops. Based on this distribution of fluxes, the $Q_1 = Q_2$ state is also referred to as the $[\pi, 0]$ state (where the ordered pair enclosed within square brackets refer to the fluxes through the hexagon and the rhombus) and the $Q_1 = -Q_2$ state is called the $[0, 0]$ state[3].

Both the symmetric spin liquid states survive for small enough values of the spin size, characterized by the measure $\kappa = 2S$. For κ above a certain threshold value, called κ_c, the two symmetric spin liquid states "condense" to classical states with long range order on the lattice. Within SBMFT, "condensation" of bosons corresponds to the closing of the single particle gap in the SBMFT fre-

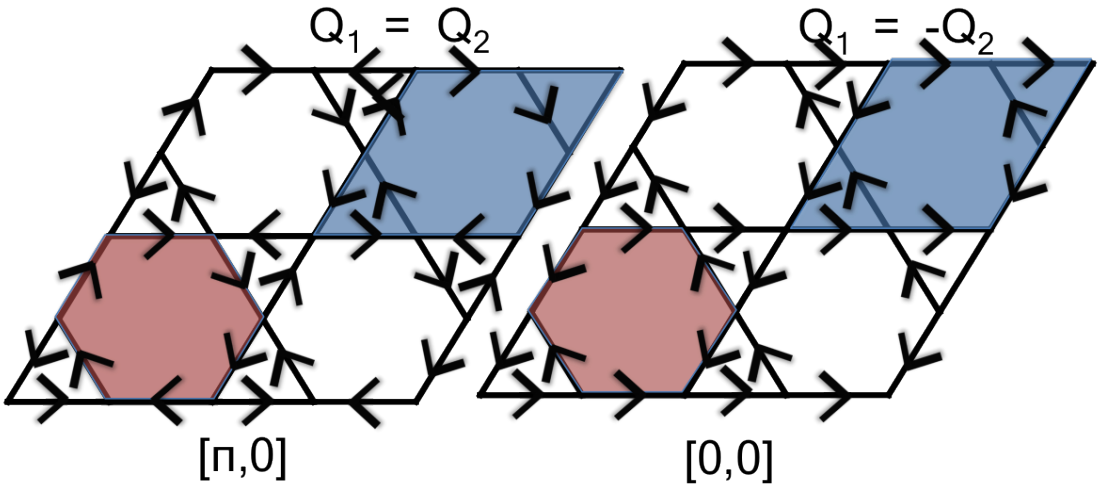

Figure 7.1: Symmetric spin liquid states within SBMFT on the Kagomé lattice. The states are labeled as the $Q_1 = Q_2$ and the $Q_1 = -Q_2$ state[12]. The direction of arrows in each state indicates the direction of positive bond amplitudes. The two smallest non-trivial even length loops on the lattice - hexagon and the rhombus are shaded in pink and blue. The gauge invariant fluxes (7.4) through these loops are $[\pi, 0]$ for the $Q_1 = Q_2$ state and $[0, 0]$ for the $Q_1 = -Q_2$ state

quency spectrum. Once the gap closes, all bosons condense into the lowest frequency mode, and the resulting state has magnetic long range order with an ordering wave-vector determined by the location in the zone where the single particle frequency goes to zero. For the two Symmetric Spin Liquid states $Q_1 = Q_2$ and $Q_1 = -Q_2$ in Fig.7.1, critical values of the spin size are $\kappa_c(Q_1 = Q_2) = 0.50$ and $\kappa_c(Q_1 = -Q_2) = 0.53$[12]. On condensation, the $Q_1 = Q_2$ state gives rise to the $\mathbf{q} = 0$ long range order with a unit cell containing three sites and the $Q_1 = -Q_2$ state gives rise to the $\sqrt{3} \times \sqrt{3}$ magnetic order with a nine site magnetic unit cell[12].

We now turn to the SBMFT energies of the two states in Fig.7.1. For all values of $\kappa < \kappa_c$, the zero flux $Q_1 = -Q_2$ state is the lowest energy state on the lattice[12]. The energetics can be understood within an analytic framework introduced by Tchernyshyov et al.[14], who write down the Schwinger Boson

mean field energy as a loop expansion in terms of fluxes through even length loops on the lattice. Such an expansion, valid *only* for uniform mean field parameters and therefore for Symmetric Spin Liquids, predicts that the lowest energy states wants to expel fluxes through all loops on the lattice. This theorem, called the 'Greedy Boson' theorem, therefore predicts the $[0,0]$ $Q_1 = -Q_2$ state to be the lowest energy state on the lattice, consistent with numerical findings in [12].

We end this Section by discussing a few more symmetric spin liquid states found by Wang and Vishwanath[3] using the Projective Symmetry Group (P.S.G.). Using P.S.G., keeping only nearest neighbor uniform bond amplitudes Q_{ij}, two additional (to the states in Fig.7.1) states with flux distributions $[\pi,\pi]$ and $[0,\pi]$ were found. The ordering of the energies of these four states, according to the Greedy Boson theorem, will be: $E([0,0]) < E[(0,\pi)] < E(\pi,0) < E(\pi,\pi)$.

Thus the number of spin liquid states on the Kagomé lattice are severely restricted by the constraints of lattice space group and time reversal symmetries on the mean field **Ansatz**. In the next Section, we relax these symmetry constraints and provide a methodology for an unbiased search (within SBMFT) of Z_2 spin liquid states on the Kagomé lattice.

7.4 Symmetry breaking SBMFT solutions on Kagomé

In this Section we use the non-uniform SBMFT technique, discussed in Section 3.4 of an earlier chapter, to search for symmetry breaking spin liquid states on the Kagomé lattice. We briefly discuss the numerical search for SBMFT saddle points starting from several random initial distributions of the mean field

parameters on the lattice. We find a multitude of low energy symmetry breaking SBMFT solutions on a $N_s = 3 \times 4^2$ Kagomé lattice and discuss some of the symmetry breaking spin liquid states in greater detail.

The numerical algorithm takes an ensemble of initial configurations of bond amplitudes on the lattice. Each initial configuration from the ensemble, corresponds to a random distribution of complex bond amplitudes $\{Q_{ij}^{init}\}$ on nearest neighbor bonds on the lattice. For each such configuration, we follow the self-consistent iteration steps outlined in Section 3.4 of an earlier chapter, to find a saddle point solution $\{\lambda_i^*, Q_{ij}^*\}$. Each self-consistent iteration steps comprises of finding the optimal set of Lagrange multipliers that fixes the number of bosons per site to κ and of updating the matrix $\mathbf{Q}$ of bond amplitudes. At the end of the self-consistent iterations, once the tolerances (see Section 3.4) have been met, we verify that the saddle point solution is indeed a minimum of the bond amplitudes and a maximum of the Lagrange multipliers [1].

The Kagome lattice has an exponentially (in the system size) large number of low energy saddle point solutions [10, 14]. To identify local minima with positive Hessians (stable minimas) corresponding to distinct and symmetry unrelated solutions, we start the optimizer with very many initial random starting points and study the final optimized solutions. Typically, about 15-20 lowest energy solutions at the end of the optimization cycle are analyzed where we look at the fluxes through the loops on the lattice and the bond amplitudes. Solutions which differ in the flux distributions or the variations in the bond amplitudes are classified as distinct.

[1] This is done by computing the matrix of second derivatives of the SBMFT energy with respect to the mean field parameters. This matrix, called the Hessian, is then diagonalized and the sign of the smallest eigen-value tells us the curvature of the surface in parameter space

Furthermore, we make sure that the optimizer lands in the minima corresponding to each distinct solution several (at least 10% of the total number of initial starts with random mean field parameters) times to make sure that it is not a meta-stable solution which might further relax into one of the already catalogued lower energy solutions.

After the entire ensemble of random initial spin configurations is optimized, we catalogue distinct spin liquid states on the basis of their optimal mean field parameters and the distribution of fluxes through loops on the lattice. We next discuss the results of our search for low energy SBMFT solutions on Kagomé.

Fig.7.2 shows the energy differences with respect to the lowest energy $Q_1 = -Q_2$ Symmetric Spin Liquid state, at every self-consistent iteration step of the SBMFT search algorithm. The different curves correspond to several different spin liquid states, on a $N_s = 3 \times 4^2$ lattice, at a value of $\kappa = 0.24$ (deep in the spin liquid regime of SBMFT). The SBMFT self-consistent iterations converge, once the energy of the state plateaus. Only curves corresponding to distinct spin liquid saddle point solutions are shown. Some of the curves stop at an earlier number of self-consistent bond iterations compared to others because they meet the tolerance criterion for fluctuations in bond amplitudes, in successive iteration cycles, to be below a certain pre-set threshold value (typically 10^{-10}see Section 3.4.1).

All spin liquid states shown have a large basin of attraction with respect to the SBMFT search algorithm[2]. Some of the lowest energy spin liquid states are

[2]The basin of attraction for a given spin liquid state can be quantified by starting with very many different initial random bond amplitudes on the lattice, and counting the number of times that the algorithm converges to the minimum corresponding to the spin liquid state. The ratio of this count to the size of the initial random starting ensemble gives a measure of the basin of attraction of a given spin liquid state

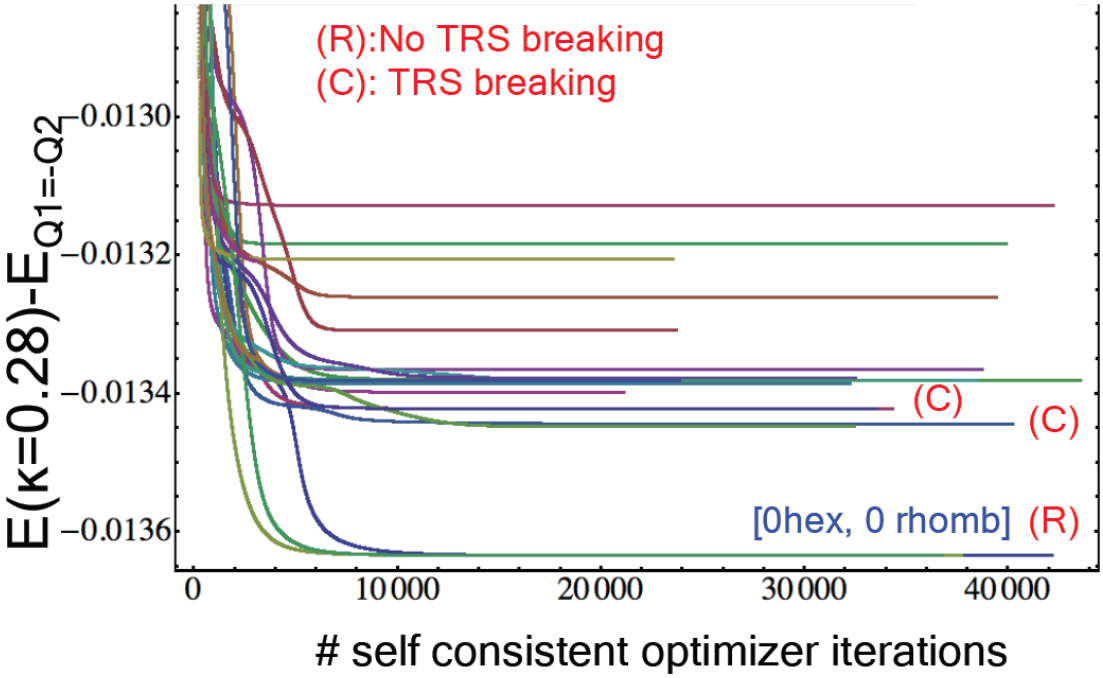

Figure 7.2: Energy difference between non-uniform low energy SBMFT solutions and the Symmetric $Q_1 = -Q_2$ Spin Liquid state as a function of the self-consistent iteration steps of the search algorithm. The energy of the Symmetric state is at zero and is shown by a blue thick line and labeled $Q_1 = -Q_2$. Each curve corresponds to a minima with a distinct symmetry breaking mean field solution of the SBMFT equations. Some of the low energy curves are labeled "C" ("R") to indicate whether the solution breaks (preserves) time reversal symmetry. The lowest energy state is triply degenerate and has zero flux (see Eq. (7.4)) through the hexagonal and rhombus loops on the lattice. The zero fluxes through hexagonal and rhombus loops on the lattice is indicated by the label $[0hex, 0rhomb]$ beside the lowest energy solutions. All data is for a lattice size of 48 sites with a value of $\kappa = 0.28$, chosen so that all solutions are in the spin liquid regime of SBMFT

also labeled with "C" for chiral ("R" for real) depending on whether the state breaks (preserves) time reversal symmetry. The higher energy lines are not labeled "C" or "R" because they have not been analyzed for the distribution of fluxes. Fig. 7.2 shows a large number of symmetry breaking spin liquid solutions to the SBMFT Hamiltonian, lower in energy than the Symmetric $Q_1 = -Q_2$ state. We next discuss the lowest energy solutions in greater detail.

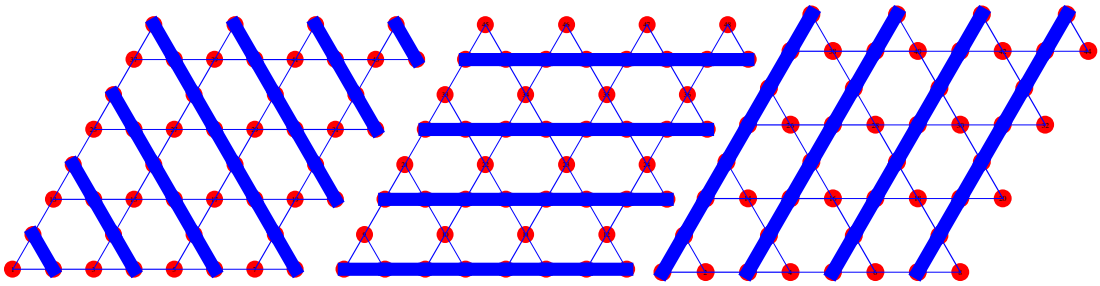

Figure 7.3: Bond amplitudes of the three degenerate lowest energy symmetry breaking spin liquid states on a 48 site lattice. The thickness of the bonds is proportional to $Q^*_{ij} -$ min. $\{|Q_{ij}|^*\}$ and the area of the red discs is proportional to the Lagrange multipliers. Variation in bond amplitudes (difference between the strongest and weakest bonds on the lattice) is $\sim 5\%$ and in the Lagrange multipliers is $\sim 0.1\%$.The state has zero flux through the hexagonal and rhombus loops on the lattice

The lowest energy solution found by the search algorithm has a large basin of attraction (approximately $\sim 40\%$ of random initial bond configurations fall in to the minima corresponding to this lowest energy solution) and has a triple degeneracy, as can be seen by the three lowest energy curves merging in to a single plateau in Fig.7.2. The triple degeneracy is inferred from the observation that several independent runs with different initial conditions converged to one of the three states above. While, it is possible that the algorithm might have missed local minima corresponding to other, possiblly degenerate mean field solutions, this seems unlikely, at least within the basin of attraction of our current search algorithm. In Fig.7.2 we show only three curves from a set of it-

erations, with different bond relaxation histories, relaxing to the three different striped orientations of the lowest energy state, as shown in Fig.7.3.

The lowest energy solution in Fig.7.2 is about 1% lower in the energy per site compared to the uniform $Q_1 = -Q_2$ solution[12][3]. The pattern of the bond amplitudes $\{Q^*_{ij}\}$ in the lowest energy solution is shown in Fig.7.3 where the thickness of the bond amplitudes are proportional (except for the weakest bond on the lattice whose magnitude of the bond variable is zero) to the difference between the magnitudes of each bond and the weakest bond on the lattice. This is done to enhance the contrast between the strong and weak bonds on the lattice. The percentage difference between the magnitudes of the strongest and weakest bonds on the lattice is about 5% and the modulation is therefore small. Each of the three Kagomé lattices in Fig.7.3 corresponds to one of the triply degenerate lowest energy solution. The pattern of the bond amplitudes shows that the three low energy states break the three-fold orientational symmetry of the Kagomé lattice. A similar state was found on a 36 site Kagomé lattice and was called a "stripe state"[10]. We will adopt this name to refer to the lowest energy state in Fig.7.3.

The lowest energy stripe state continues to be the lowest energy state on the $N_s = 48$ site lattice for values of κ in the range $\kappa \in [0, 0.4]$. The amplitude modulations in the bonds are much stronger (with the strongest bonds being $\sim 5\%$ higher in amplitude compared to the weakest bonds on the lattice) compared to the modulations of the Lagrange multipliers $\{\lambda^*_i\}$ which are around 0.1%. The very small variation in the magnitudes of the on-site Lagrange multipliers, seen

[3]The uniform $Q_1 = -Q_2$ solution was not obtained starting from random initial bond configurations. It was obtained by starting with a uniform bond amplitude configuration with directed bond amplitudes corresponding to the flux pattern of the uniform state. This specific starting configuration immediately led to a uniform optimized $Q_1 = -Q_2$ solution

in Fig. 7.3, is due to incomplete relaxation, this small difference will become zero in the thermodynamic limit. The stripe state also does not break time reversal symmetry and is a $[0\text{hex}, 0\text{rhomb}]$ state, implying that it has zero fluxes through hexagonal and rhombus loops on the lattice[3].

The zero fluxes through the hexagonal and rhombus loops in the lowest energy state is in agreement with the predictions of the Greedy boson theorem which states that the lowest energy state wants (if possible) to expel all fluxes through the loops[14]. The consistency of the zero flux lowest energy solution found from the optimizer and the Greedy Boson theorem is surprising since the theorem holds only for translationally invariant states with uniform mean field parameters, unlike the lowest energy solution from the optimizer which breaks three-fold orientational symmetry as shown in Fig.7.3.

We next look at the first (excited) Chiral saddle point solution which breaks time reversal symmetry and has chiral fluxes through loops on the lattice. The lowest (in energy) such chiral saddle point solution is labeled "C" in Fig.7.2 and is shown in Fig.7.4. The chiral solution has a non-uniform distribution of fluxes through hexagonal plaquettes with the average flux being ~ 0.14 rad. .

The large number of low energy symmetry breaking spin liquid solutions of the SBMFT equations shown in Fig.7.2 need to be checked for robustness to finite size effects. A robustness check would mean to show(numerically or analytically) that the symmetry breaking mean field states obtained on finite sized Kagome lattices in this Section, continue to be lower in energy than uniform saddle point solutions.

It is also very important to find whether any of the low energy solutions

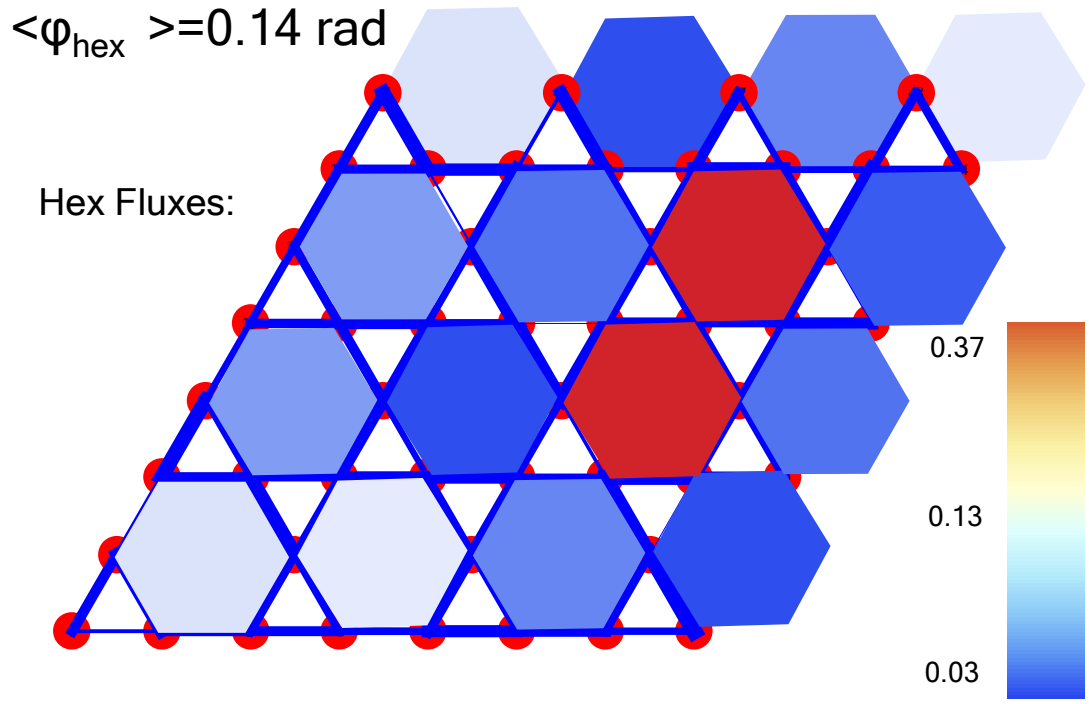

Figure 7.4: An excited chiral saddle point solution obtained from the search algorithm. The state breaks breaks time reversal symmetry and has a non uniform distribution of fluxes. The label "Hex Fluxes:" is to indicate the color coded magnitude of fluxes (7.4) through hexagonal loops on the lattice. The correspondence between the color coding and the flux values is shown by the color scale in the bottom right. The average hexagonal flux is 0.14 rad.

in Fig.7.2 survive Gutzwiller projection and yield an actual spin state of the Heisenberg Hamiltonian. The presence of an exponentially large number of symmetry breaking solutions that we found on the Kagomé lattice, many of which are lower in energy than the lowest Symmetric spin liquid state, indicates the strong competition between states on the lattice. Some of the symmetry breaking solutions may also point towards the dominant instabilities of the Symmetric Spin liquid solutions in the presence of disorder, or additional spin-spin interaction corrections to the dominant nearest neighbor Heisenberg Hamiltonian(7.1).

Finally, the saddle point solutions corresponding to the lowest excitations in Fig.7.2 are mean field states with smooth modulations of the mean field parameters. These excited states with smoothly modulated mean field parameters are lower in energy than the mean field states with defect excitations like visons [15] as was also found in the numerical study by Misguich[10].

A possible reason for why the vison state is a higher energy excitation than a smoothly modulated zero flux state is given by the Greedy Boson theorem. A 2 vison state changes the flux through the two hexagons containing the visons from 0 to π. This energy cost is cubic in the length of the spin size: κ^3[14, 3] and for large enough κ (still in the spin-liquid regime) can be higher than the cost of smooth modulations which scale as κ^2[16].

We next move on to realizing topological quasi-particle excitations in Z_2 spin liquids in a numerical experiment using the methodology of non-uniform SBMFT 3.4 .

7.5 Realizing topological quasi-particle excitations within SBMFT

In this Section we perform a numerical experiment to realize particle excitations of a Z_2 spin liquid state. We first introduce the three kinds of topological excitations in a Z_2 spin liquid and show that all of them can be realized within SBMFT. We then numerically create these excitations and show that they correspond to stable non-uniform saddle point solutions of the SBMFT Hamiltonian. The Section highlights the richness of the non-uniform SBMFT numerical technique in creating non-trivial topological excitations on discrete lattices.

Within the SBMFT framework, a Z_2 spin liquid has three kinds of topological particle excitations. The first kind of particle excitation is an "e"(electric) particle and within the SBMFT representations, is a bosonic spinon carrying the charge(hence the nomenclature electric and notation "e"), but not the spin of an electron. The "e" particles or the bosonic spinons are present at the mean field level, due to the mapping of the spin half operators to Schwinger bosons.

The second type of excitation is called a "Vison"- a flux excitation where loops on the Kagome lattice, due to the presence of a defect bond (with the direction of the bond flipped in comparison to the direction that would have corresponded to a zero flux configuration on the lattice) threads a flux of π through the loops containing the defect bond. Because of the flux nature of the excitation, a Vison excitation is called a "m" (for magnetic) type of excitation. Both the electric: "e" and the magnetic "Vison" excitations have a duality, analogous to the duality between electric and magnetic fields in classical electromagnetism.

The third and last excitation is a bound state of the "e" (bosonic spinon) and the "m" magnetic vison excitations and is called a "ε" excitation. The "ε" excitation is a particle-like excitation with fermionic statistics [15]. Fig7.5 shows a cartoon of the three topological particles.

All three particles can be created at the mean field level using the SBMFT parameters. The "e" particles or the bosonic spinons are present at the mean field level due to the mapping of the spin half operators to Schwinger bosons. In the absence of any visons, the "e" particles are completely delocalized and are just the Schwinger bosons of SBMFT with well defined momentum quantum numbers labeling single particle states. The spectrum of the "e" particle is gapped for a small enough value of κ.

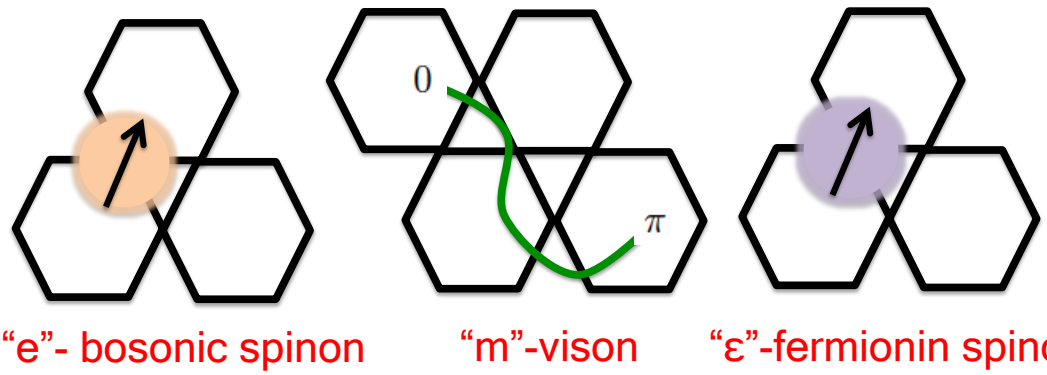

Figure 7.5: Three kinds of topological particles in a Z_2 spin liquid. The "e" particle is shown by the orange blob and is a bosonic spinon carrying the spin, but not the charge of an electron. The spin of the boson is indicated by the black arrow in the center of the orange blob. The "m" type of particle is a magnetic excitation called a vison and corresponds to two hexagons on the lattice containing a π flux in the background of zero flux loops. Visons can only be created in pairs. The two visons are connected by a string, shown by the green line, which intersects all bonds on the lattice that are flipped in sign (with respect to the all zero flux state) to create the vison excitation. The last topological particle is the most non-trivial and corresponds to a bound state of the bosonic spinon and a vison, is shown by a purple blob and is called an ε particle. The ε particle has fermionic statistics

Visons can be created in the background of any spin liquid state specified by an **Ansatz** $\{\lambda_i^*, Q_{ij}^*\}$. The vison can be created by flipping the direction of Q_{ij} on a bond on the lattice, which threads a flux(7.4) of π through the hexagon containing the flipped bond. Visons are *always* created in pairs, flipping the sign of Q_{ij} on a bond on the lattice, changes the flux to π in the hexagon containing the bond, but also in the bow-tie loop that shares the flipped bond with the hexagon. The two visons can be separated by flipping another bond on the lattice which changes the flux through the bow-tie back to zero and transfers the π phase to the next hexagon. A series of flipped bonds on the lattice can therefore separate two vison excitations. The line cutting the flipped bonds is called a 'string'. The string is completely classical in nature and has no dynamics of its own. Also, it is important to emphasize that the string is not a physical

object, meaning that there exists a set of gauge transformations that will allow the string to cut through a set of new bonds. The only physical constraint for the string is that it needs to begin at one of the defect loops containing a π flux, cut through a series of flipped (in sign) bonds and end at another defect loop containing a π flux.

The string(s) connecting the visons in a SBMFT saddle point solution is very similar to the strings separating monopole excitations within defect tetrahedra in spin ice[1, 17]. Just like different spin configurations in spin ice correspond to different physical states, different string positions connecting equidistant defect loops gives rise to distinct mean field spin liquid solutions. A pair of visons is shown by the two green blurbs in Fig.7.6. Also shown are a series of bonds in red corresponding to the flipped Q_{ij} amplitudes. The contour cutting the flipped bonds in red, is shown by a dashed green line and is the string connecting the pair of "m" excitations or visons.

The pair of visons in the background of the spin liquid state is a stable excitation within SBMFT, *only* if there exists a stable saddle-point solution of the SBMFT equations which contains the two vison configuration of Fig.7.6. Inserting a pair of visons in to a spin liquid state, by simply flipping the arrows on a series of bonds, does not mean that the Schwinger Boson mean field states realize such a topological excitation.

We find such a saddle point solution by beginning the non-uniform SBMFT optimizer from a configuration that corresponds to the two visons inserted in to the background of a zero flux $Q_1 = -Q_2$ spin liquid state. The optimizer is then run through a series of self-consistent iterations, where it adjusts the bond amplitudes and the Lagrange multipliers on the lattice, to find the closest *stable*

saddle-point solution which retains the two visons of the initial starting configuration. The existence of such a stable saddle-point solution then corresponds to a valid mean field state and a stable vison configuration.

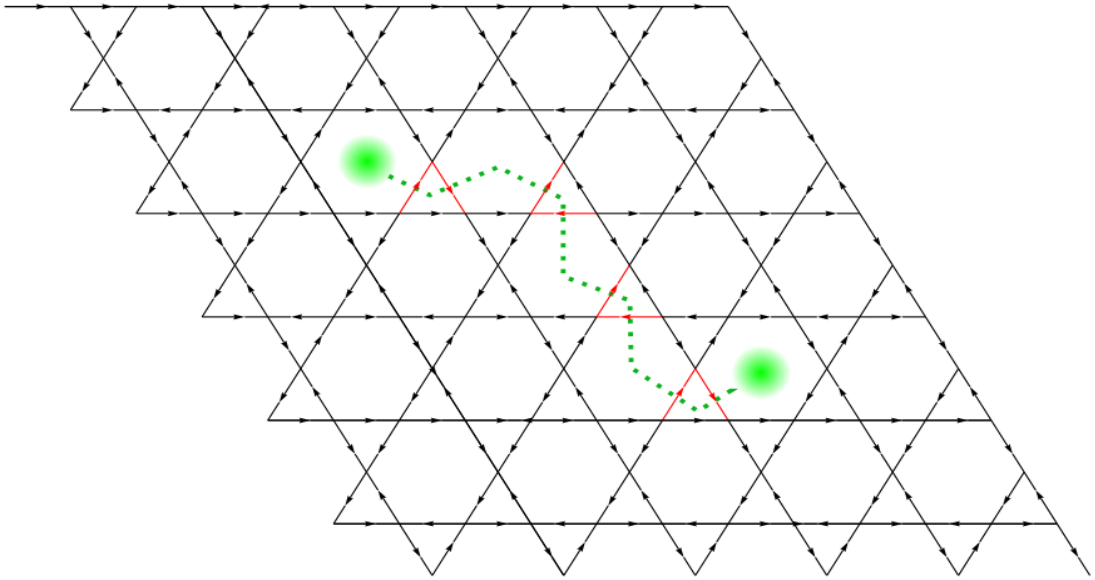

Figure 7.6: A pair of vison excitations in the background of a Z_2 spin liquid state on the Kagomé lattice. The two hexagons containing the visons are shown by the green blurbs. The direction of arrows on each bond on the lattice, creates an **Ansatz** for a background spin liquid, on top of which the two vison excitations are created. The visons are created by flipping the sign (reversing the arrows) on a series of bonds shown in red. The line cutting these series of bonds is called a 'string', shown by the dashed green contour, and connects the two vison excitations.

We are left with the realization of the third kind of topological particle in Fig.7.5 - the "ε" excitation which is a fermionic spinon. The fermionic spinon should naturally emerge as a bound spin wave-function, localized around the visons, in a mean field Schwinger boson state which stabilizes a two vison configuration. The smoking gun signature of the fermionic spinon will be a bound state in the single particle SBMFT spectrum since the "ϵ" particle is a bound state of the "e" and "m" particles. The bound state should correspond to a low energy (compared to the rest of the spectrum) and an eigen-mode that is localized on

the visons.

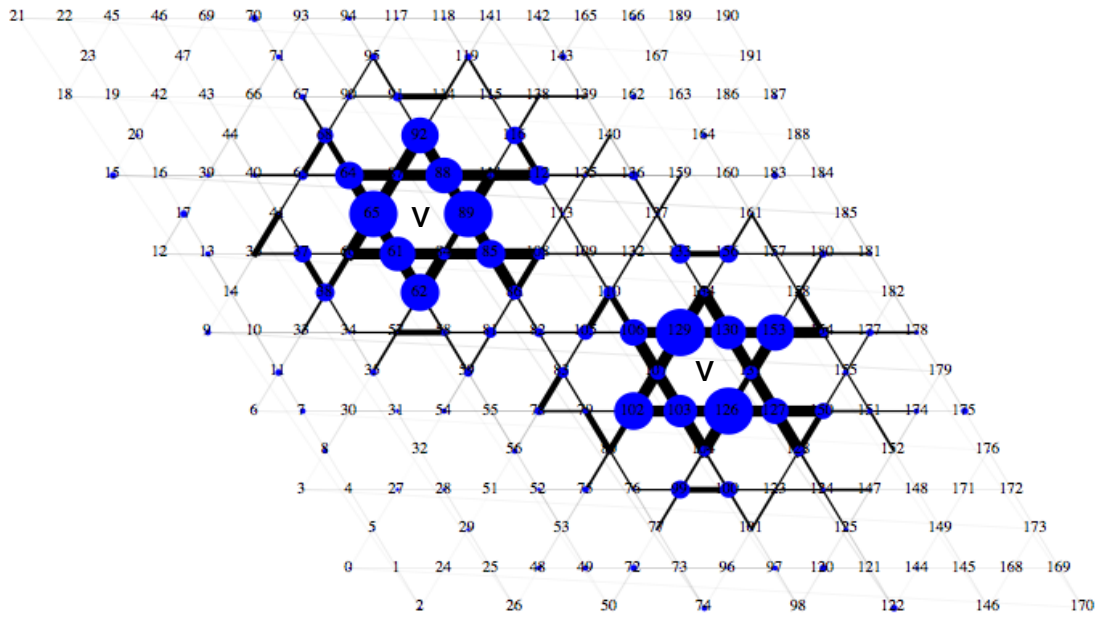

Figure 7.7: SBMFT saddle point solution containing a pair of vison excitations. The pair of hexagons containing a π flux vison excitation is marked with a 'v' in the Figure. The thickness of the bonds is proportional to the optimal bond amplitudes at the end of the self-consistent iteration cycle. The area of the blue discs at every site is proportional to the probability of finding a spinon (square of the amplitude of the eigen-mode) in the lowest single particle frequency of the SBMFT spectrum. The lowest eigen-mode is doubly degenerate with amplitudes of both degenerate modes localized around the visons. This single particle state is conjectured to be a bound vison-spinon state and therefore is a numerical realization of an "ε" topological particle excitation

Fig.7.7 shows the optimal bond amplitudes and the lowest eigen-mode profile of a stable saddle point solution of the Schwinger boson mean field equations that contains two visons - π flux hexagons marked with a 'v' in the Figure. The lowest eigen-mode has an energy $\omega_0 = 0.47J$, for a $\kappa = 0.4$ and is doubly degenerate. The next higher energy in the spectrum is $1.2J$. The "ϵ" particle is therefore very weakly bound since the gap between the lowest and the first excited frequency is small[4]. The eigen-modes corresponding to one of the two

[4]Typically the gap should be compared to an energy scale related to the inverse of the lo-

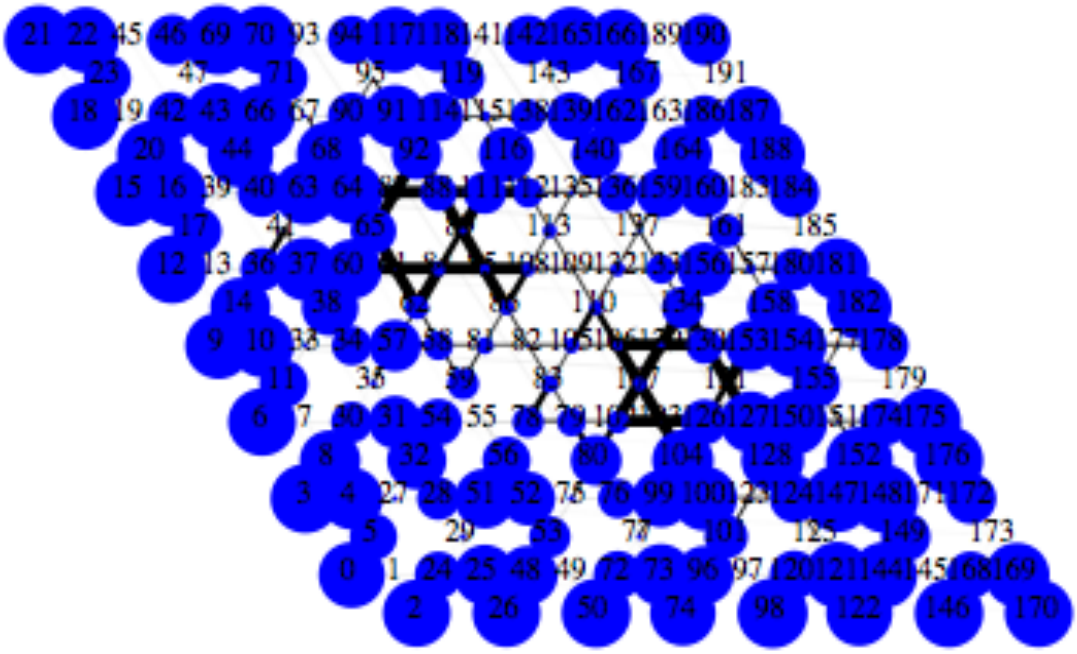

Figure 7.8: A higher frequency SBMFT eigen-mode corresponding to a delocalized spinon on the lattice. Similar to Fig7.7, the areas of the discs at every site is proportional to the probability of finding a spinon at that site. The thickness of the bonds is proportional to the optimal bond amplitudes. The calculation is done for a Kagomé lattice containing 108 sites, at $\kappa = 0.4$

degenerate modes is shown by the blue colored discs at every site in Fig.7.7. The area of the discs, at every site, is proportional to the probability of finding a spinon at that site. The eigen-mode has maximal amplitudes around the two visons. We conjecture that the localized (at the visons) eigen-mode in Fig.7.7 corresponds to the wave-function of a bound state of the bosonic "e" and the magnetic vison "m" particles in Fig.7.5. This feature in addition to the stability of the π flux vison state in the mean field solution, indicates that the bound state is a fermionic spinon and is therefore a numerical realization of the ε topological particle.

calization length of the "ϵ" particle. The smaller the localization length, the lower will be the energy of the bound state and greater will be the difference between the ground and first excited state energy. The small difference $1.2 - 0.47 \sum 0.7J$ indicates that the "ϵ" particle has a large localization length and is only weakly bound

A point to be made here is that I (with collaborators) attempted to find a set of lowest energy wave-functions that would be perfectly localized around the two visons. Several attempts to find such a linear combination failed and this exercise will therefore be left for future work.

The state shown in Fig.7.7 has the bososnic spinon "e" particle weakly bound (the mean-field energy of the bound state is only lowered by about 10% with respect to the energy of the zero flux state with no visons), since the mode energy is not drastically lowered compared to the rest of the spectrum, which contains frequencies corresponding to delocalized modes on the lattice. An example of such a mode is shown in Fig.7.8, at a energy $\omega_1 = 0.6J$, and corresponds to an eigen-mode that is spread out all over the lattice, in sharp contrast to the localized modes seen in Fig.7.7. The mode in Fig.7.8 is similar in spatial modulation and energy to the higher frequency single particle bosonic modes found for a zero flux $Q_1 = -Q_2$[12] solution in the absence of the vison pair.

Table7.1 summarizes the energies of the three topological quasiparticles. The energies of the "e" and "ε" particle are equal to the smallest single particle frequencies in the bosonic spectrum of the optimized spin liquid solution corresponding to the $Q_1 = -Q_2$ state[12] (zero flux through loops and absence of visons) and the $Q_1 = -Q_2$ state with a vison pair inserted, respectively. The energy of the magnetic vison excitation is calculated in a similar manner by taking the difference between the zero point energies of the mean field state in the absence and in the presence of the vison pair.

A negative energy for the vison configuration does not imply that the system favors a spontaneous creation of visons. For every vison configuration, there are also bosonic spinons which come with an energy cost of creation and a sponta-

Excitation	Energy(J)	Stability
"e" bosonic spinon	0.31	Stable
"m" magnetic vison	-0.29	Stable
"ε" fermionic spinon	0.27	Unstable

Table 7.1: Energies of the three topological quasiparticle excitations in a Z_2 spin liquid shown in Fig.7.5 for $\kappa = 0.4$ (κ is twice the spin length). The energy of the "e" bosonic spinon and "ε" fermionic spinon is equal to the lowest single particle frequencies in the single particle spectrum of the mean field saddle point solution found by the optimizer in the zero flux $Q_1 = -Q_2$ state[12] and the $Q_1 = -Q_2$ state with the two-vison configuration, respectively. The energy of the vison is calculated by taking the difference between the zero point energies of the zero flux $Q_1 = -Q_2$ state[12] and the $Q_1 = -Q_2$ state with the two-vison configuration. There are two ways to compare the stability of the particles. The first is calculated from the sign of the lowest eigenvalue of the Hessian matrix: the matrix of second order derivatives of the mean field energy with respect to the mean field parameters [10]. The second criterion is to add the energies of two particles from the table above, and compare with the energy of the third particle. All calculations are done on a $N_s = 3 \times 4^2$ Kagome lattice with periodic boundary conditions, for a value of $\kappa = 0.4$ in the quantum disordered regime of the SBMFT equations. For more information about creating the quasiparticles and calculating their energies, see text on pages 242 and 243

neous creation of visons is only possible if the total mean field energy(sum of "e" and "m" particles) is negative.

The magnetic vison excitation is the most stable amongst the three kinds of excitations and has a mean field energy lower than the uniform zero flux $Q_1 = -Q_2$ state[5]. Also, the fermionic spinon "ϵ" has a lower energy compared to the free bosonic spinon "e" state due to the additional lowering of energy coming from being in a bound state with the magnetic vison.

We also note in Table 7.1the stabilities of the three types of quasiparticles by observing the sign of the lowest eigenvalue of the Hessian matrix[10]. The matrix of second derivatives of the mean field energy with respect to the mean field

[5]The spin liquid state with the two visons is however higher in energy than the modulated zero flux state shown in Fig. 7.3 and Fig.7.2

parameters is constructed numerically[10]. The matrix is then diagonalized and the sign of the smallest eigenvalue reveals the local curvature of the landscape in mean field parameter space. A negative (positive) sign corresponds to stable (unstable) mean field saddle point solutions. Based on the sign of the smallest eigenvalue of the Hessian Matrix, we see in Table7.1 that the bound "ε" particle is unstable and is likely to decay in to the constituent vison and spinon excitations.

What is the physical origin of the weakly bound spinon state seen in Fig.7.7? The profile of the Lagrange multipliers creates a local one body quantum well around each of the two visons. This one body potential is seen by the bosonic spinons "e" and to minimize the energy of the mean field state, the spinon wavefunction has maximal amplitude on sites that correspond to the minima of the two wells. The suppression of the Lagrange multipliers, at the minima of the quantum wells, is very weak compare to the value of the Lagrange multiplier at other places on the lattice and therefore the spinon state is only very weakly bound (the energy of the bound fermion is only lower by about 10% compared to the free spinon as seen by comparing the energies of the bosonic spinon and the fermionic spinon in Table 7.1). We cannot rule out the possibility of the existence of another stable saddle point solution of SBMFT which retains the twin vison configuration, but has a larger variation in the profile of Lagrange multipliers around the visons, leading to spinon states with stronger localization and lower frequencies compared to the state seen in Fig.7.7. We leave the search of such solutions to future work.

7.6 Conclusion

In this Chapter we have carried out an unbiased search for symmetry breaking spin liquid solutions, within Schwinger Boson Mean Field Theory, on the Kagomé lattice. We find that mean field ground states generically want to spontaneously break spatial and time reversal symmetries on the Kagomé lattice. The low energy space of mean field solutions on the Kagomé lattice shows an abundance of symmetry breaking solutions. In particular, on the 48 site Kagomé lattice, we find a novel striped phase (see Fig7.3), which is triply degenerate, breaks the three fold orientational symmetry of the lattice, but does not break time reversal symmetry. Similar states, which break translational invariance on the lattice, have been reported in a similar study on a 36 site Kagomé[10] lattice and also in a study using projected fermionic wave-functions [18] on the Kagomé lattice.

It is important to emphasize that the non-uniform Schwinger Boson methodology of 3.4 , is at present, the *only* unbiased approach to search for symmetry breaking spin liquid states on a lattice. Our method of numerical optimization is very different from the Projective Symmetry Group(P.S.G.)[2], which is used only to search for Symmetric uniform spin liquids. Our method of numerically solving the SBMFT equations does not impose any symmetry restrictions on the mean field ground state, allowing it(mean field state) to *spontaneously* break spatial or time reversal symmetries to find the lowest energy state on a given lattice. Whether such states are robust to larger lattice sizes or survive quantum fluctuations and Gutzwiller projection to yield ground states of the Heisenberg Hamiltonian (7.1) is obviously a big concern, and needs to be addressed by further numerical and theoretical advances in the field.

Finally, we showed a concrete realization of the three topological quasiparticle excitations of a Z_2 spin liquid in a numerical experiment. We found that symmetry breaking SBMFT solutions support all three kinds of topologically non-trivial particle excitations: the bosonic spinon, visons (see Fig.7.6) and a spinon-vison bound pair called a fermionic spinon (see Fig.7.7). We also calculated the energy and the stability of each kind of excitation within the method of non-uniform SBMFT (introduced in Chapter 3). In the future, it will be possible to use non-uniform SBMFT to numerically study mutual statistics and braiding properties of these particles and even tunneling between vison states.

BIBLIOGRAPHY

[1] L. Balents, Nature **464**, 199 (2010).

[2] X.-G. Wen, Phys. Rev. B **65**, 165113 (2002).

[3] F. Wang and A. Vishwanath, Phys. Rev. B **74**, 174423 (2006).

[4] Y.-M. Lu, Y. Ran, and P. Lee, Phys. Rev. B **83**, 224413 (2011).

[5] F. Wang, Phys. Rev. B **82**, 024419 (2010).

[6] T.-P. Choy and Y. Kim, Phys. Rev. B **80**, 064404 (2009).

[7] M. Lawler, A. Paramekanti, Y. Kim, and L. Balents, Phys. Rev. Lett. **101**, 197202 (2008).

[8] L. Messio, C. Lhuillier, and G. Misguich, Phys. Rev. B **87**, 125127 (2013).

[9] Y.-C. He, N. Sheng, D. and Y. Chen, Phys. Rev. Lett. **112**, 137202 (2014).

[10] G. Misguich, Phys. Rev. B **86**, 245132 (2012).

[11] B. Clark, J. Kinder, E. Neuscamman, G. Chan, and M. Lawler, Phys. Rev. Lett. **111**, 187205 (2013).

[12] S. Sachdev, Phys. Rev. B **45**, 12377 (1992).

[13] L. Messio, C. Lhuillier, and G. Misguich, Phys. Rev. B **87**, 125127 (2013).

[14] O. Tchernyshyov, R. Moessner, and S. L. Sondhi, EPL (Europhysics Letters) **73**, 278 (2006).

[15] A. Essin and M. Hermele, Phys. Rev. B **87**, 104406 (2013).

[16] U. Hizi, P. Sharma, and C. Henley, Phys. Rev. Lett. **95**, 167203 (2005).

[17] C. Castelnovo, R. Moessner, and S. L. Sondhi, Nature **451**, 42 (2008).

[18] B. Clark, J. Kinder, E. Neuscamman, G. K. L. Chan and M. J. Lawler, Phys. Rev. Lett, 187205 (2013).